Anomalous transport properties of the skyrmion compound EuPtSi

Simon Rousseau

THÈSE

Pour obtenir le grade de

DOCTEUR DE L'UNIVERSITÉ GRENOBLE ALPES

École doctorale : PHYS - Physique
Spécialité : Physique de la Matière Condensée et du Rayonnement
Unité de recherche : LNCMI - Laboratoire National des Champs Magnétiques Intenses

Propriétés de transport anormales dans le composé skrymionique EuPtSi

Anomalous transport properties of the skyrmion compound EuPtSi

Présentée par :

Simon ROUSSEAU

Direction de thèse :

Georg KNEBEL DIRECTEUR DE RECHERCHE, CEA CENTRE DE GRENOBLE	Directeur de thèse
Gabriel SEYFARTH MAITRE DE CONFERENCES, UNIVERSITE GRENOBLE ALPES	Co-encadrant de thèse
Alexandre POURRET MAITRE DE CONFERENCES, UNIVERSITE GRENOBLE ALPES	Co-encadrant de thèse

Rapporteurs :

BENOIT FAUQUE
CHARGE DE RECHERCHE HDR, CNRS DELEGATION PARIS CENTRE
ALAIN PAUTRAT
DIRECTEUR DE RECHERCHE, CNRS DELEGATION NORMANDIE

Thèse soutenue publiquement le **19 décembre 2023**, devant le jury composé de :

BENOIT FAUQUE CHARGE DE RECHERCHE HDR, CNRS DELEGATION PARIS CENTRE	Rapporteur
ALAIN PAUTRAT DIRECTEUR DE RECHERCHE, CNRS DELEGATION NORMANDIE	Rapporteur
ILYA SHEIKIN DIRECTEUR DE RECHERCHE, CNRS DELEGATION ALPES	Examinateur
SEBASTIEN BURDIN MAITRE DE CONFERENCES HDR, UNIVERSITE DE BORDEAUX	Examinateur
SOPHIE DE BRION PROFESSEURE DES UNIVERSITES, UNIVERSITE GRENOBLE ALPES	Présidente

Remerciements

Mes premiers remerciements sont adressés aux membre du jury devant lequel j'ai eu le plaisir de soutenir, présidé par Sophie De Brion; Ilya Sheikin et Sébastien Burdin comme examinateurs; Alain Pautrat et Benoît Fauqué pour leur relecture de mon manuscrit. Merci pour les discussions et questions pertinentes qui ont conclu ce chapitre de ma vie.

J'aurai également pu commencer ces remerciements par mes encadrants, ceux qui m'ont accepté en thèse, qui m'ont enseigné quasiment tout ce que je sais et avec qui c'était un réel plaisir de travailler au quotidien. Gabriel, qui m'a appris à faire mes premiers transferts d'hélium. J'aurais aimé travailler un peu plus avec toi, pas seulement lorsqu'il s'agit de mesurer en champs intenses le dimanche à 23h. Tu t'es toujours rendu disponible pour discuter malgré les milliards de choses dans ton emploi du temps, et sans toi j'imagine même pas les galères administratives. Merci pour les petits cochons en pâte d'amande qui m'ont porté chance pendant trois ans. Alexandre, qui m'a fait transférer de l'hélium tous les deux à trois jours pendant trois ans. Je te remercierai jamais assez pour les échantillons que tu as contacté, pour toutes les discussions à essayer de comprendre ce qu'est le pouvoir thermoélectrique et pour m'avoir poussé à toujours mesurer plus de choses intéressantes. Tu m'as fait confiance pour m'occuper de la manip pendant que tu gérais un master et des étudiants, mais tu es toujours resté présent pour parler physique. Georg, qui a transféré l'hélium pour moi quand j'étais en vacances. Malgré tes goûts graphiques pour le moins douteux (le jaune c'est non), je dois remercier tes connaissances, à toujours trouver la bonne publication, le bon bouquin qui contient la solution qu'on cherche. Même si tu souffles fort, d'exaspération je suppose, tu es quand même là quand il s'agit de débugger un code LabView incompréhensible le vendredi à 19h, organiser une visio avec un théoricien russe, ou tout simplement pour nous raconter la vie de Shubnikov.

Je remercie tous les gens de Imapec qui m'ont accueilli dans leur labo même si j'étais le seul à ne pas travailler sur UTe_2. Daniel qui chantonne dans les couloirs du 10.05, Pierre qui a une régularité impressionnante sur sa consommation de yaourts, Jean-Pascal qu'on a agacé continuellement à lui demander pourquoi $R = 0$ dans un supra. Je remercie particulièrement Iulian pour son expertise en cryogénie, pour faire une nouvelle tige en fibre de verre, pour refaire le mélange de la dilution au spectro, et pour re-refaire des tests de fuite sur la 18T.

Je remercie les autres occupants du 10.05, tous les voisins du groupe Lateqs, les théoriciens du GT, ceux qui s'arrêtent toujours dans le couloir pour voir quels trucs marrants on peut faire avec de l'azote au lieu de travailler.

Bien sûr je n'étais pas seul à jouer avec l'azote liquide, donc je tiens à remercier tout particulièrement Adrien qui a un don pour faire exploser les bouteilles en plastique, Nils qui n'a pas encore retrouvé tout le sel caché dans ses affaires, Timothée qui n'oubliera jamais la poule à Colin, et Julien qui apprendra un jour à toucher la cible de fléchettes. Continuez à retourner les bureaux des collègues, coller des mêmes sur les murs, faire des montages photos pétés des permanents, ou lister toutes les pâtisseries de France. Plus généralement, un grand merci à tous les thésards que j'ai eu la chance de rencontrer: Lou-Anne, Rami, Marion, Yoan, Thomas, Julia et tous les autres.

Une mention spéciale et un grand merci pour tous les gens que j'ai croisé et qui m'ont aidé de près ou de loin pendant la thèse: Alexandra, Dominique, Amélie et Marielle pour

l'administratif, Christophe et Marie-Aude comme membres du CSI, Andrei Varlamov pour son aide sur le pouvoir thermoélectrique, et Swee Kuan Goh pour m'avoir invité à Hong Kong comme collaborateur.

Finalement, j'aimerai remercier de tout mon cœur mes amis qui m'ont accompagné pendant trois ans, pour la plupart qui ont même assisté à une soutenance incompréhensible: Marie, Nathan, Eva, Paul, Emilien, Aurélie, ...

Un énorme merci à Nesrine qui m'a connu dans les moments les plus durs et les plus stressants, de la rédaction du manuscrit à la préparation de la soutenance, qui malgré ça m'a soutenu en continu, m'a changé les idées lorsque j'en avais besoin et à qui j'aurai le plaisir de rendre la pareille dans quelques temps.

Enfin, je remercie mes parents et ma soeur, ma famille, ceux qui m'ont formé depuis ma naissance et m'ont donné le goût de la logique, la curiosité, l'apprentissage, la rigueur, et sans qui je ne serais évidemment pas là. Encore mille mercis.

Abstract

In this thesis, we have studied the electrical and thermal transport properties of the non-centrosymmetric compound EuPtSi, at low temperatures and under magnetic field.
The first part of the results focuses on the low-field ($H < 5$ T) magnetic phases that are observed in EuPtSi below the ordering temperature $T_N = 4.1$ K for the three main directions $H \parallel [110]$, $H \parallel [111]$ and $H \parallel [100]$. From the angular dependence of the resistivity under magnetic field, we confirmed the presence of anomalous phases: for the direction $H \parallel [111]$ the so-called skyrmion lattice A-phase, and for the $H \parallel [100]$ direction the skyrmion-related A' and B phases. By studying these phases with various transport probes, we have established the magnetic phase diagram with precision. We have also evidenced the presence of additional anomalies at low-temperature related to the skyrmion phases. Our temperature-dependent results for the $H \parallel [111]$ and $H \parallel [100]$ evidence the metastable behavior of the A, A' and B phases under field cooling. From the peculiar metastable state for the $H \parallel [100]$ direction, further field sweeps show that both the A' and the B phases exist in the super-cooled regime with phase lines between them. From transport measurements as a function of temperature, we also show an anomalous transport in the conical ordered state.
The second part of our results focus on the Fermi surface of EuPtSi, studied with quantum oscillations in the thermoelectric power. The temperature dependence of the quantum oscillations recovers the effective mass of the carriers for each Fermi surface branch, with results comparable to the literature. From the field-dependence of the quantum oscillations, we have recovered the Dingle temperature and mean-free path of the carriers using a new analysis framework for the thermoelectric power, indicating that the latter is an extremely sensitive probe to detect quantum oscillations.

Contents

Introduction

In 2009, the observation of a magnetic skyrmion lattice (SkL) phase in MnSi [1] proved the existence of an object that has been proposed more than 40 years earlier as a model of the nucleon in nuclear physics [2]. The concept of skyrmions was then introduced in solid state physics in the 1980s. Magnetic skyrmions are topologically protected particle-like objects that are very promising for technological applications. With their small size compared to magnetic domains, magnetic memories with high information density can be devised, and individual skyrmions can be moved with low excitation currents i.e. low energy consumption. For the prospect of potential applications, skyrmions are highly sought-after and ongoing research aims to understand their fundamental properties, a lot of which are still open questions.

Although some systems with preserved inversion symmetry have also been confirmed to host skyrmions, a key ingredient for the formation of skyrmions was first found to be the lack of inversion center of the crystal structure. From the discovery of the SkL in MnSi, other compounds with the non-centrosymmetric space group $P2_13$ potentially hosting skyrmions have been looked for, one of which is EuPtSi. EuPtSi orders in the helical antiferromagnetic state with a low ordering temperature $T_N = 4.1$ K, and shows a rich phase diagram under field with different magnetic orders. The A-phase of EuPtSi for a magnetic field $H \parallel [111]$ has been confirmed to be a SkL phase in 2018, making it the first $4f$ rare-earth skyrmion compound [3]. Moreover the helical ordering vector is small, with a periodicity of 18 Å, and as such it is strongly pinned to the crystal structure. Under applied magnetic field, this induces a strong anisotropy of the magnetic phase diagram. The A-phase has been observed around the $H \parallel [111]$ direction, whereas for $H \parallel [110]$ no such phase exists. In turn, the $H \parallel [100]$ direction shows evidence of two different skyrmion-like phases, named A' and B.

The low thermal excitation needed to induce the A-phase allows it to be observed at temperatures down to 450 mK which provides a rare opportunity for the study of skyrmions close to their ground-state [4]. The A' and B phases, on the other hand, are observed in a very small angle range and down to 250 mK [5]. Their study proves to be challenging from an experimental perspective and their formation mechanism and structure has yet to be reported. Moreover, it was recently shown that it is possible to stabilize the SkL phases in a metastable state at lower temperature under magnetic field-cooling, which still needs clarification [4].
The field-temperature phase diagram of EuPtSi is investigated using electrical and thermal transport measurements at low temperature and high magnetic field for the three main directions. We have compared the anomalous features of the SkL in longitudinal and transverse resistivity with thermal conductivity and thermoelectric power. The thermoelectric power especially yields promising results, both in measurements related to the

magnetic orders and the analysis of the Fermi surface of EuPtSi through quantum oscillations.

This thesis is divided into four main parts. The first chapter consists of theoretical concepts needed to understand the experimental work of the later chapters. An introduction to the thermoelectric power and its underlying theory is presented. An emphasis is put on its sensitivity to changes in the electronic density of states and to the Fermi-surface properties. Quantum oscillations are then presented through the Lifshitz-Kosevich theory for magnetization and resistivity, and the Pantsulaya-Varlamov theory framework for the thermoelectric power. Finally, we also introduce various magnetic orderings, the concept of skyrmions and the prototypical skyrmion compound MnSi. The second chapter consists of the experimental methods used for the transport measurements of the following chapters. In the third chapter, we introduce EuPtSi in detail and present the electrical and thermal transport results we have obtained. The field-dependent measurements are first presented for the three different main directions, $H \parallel [110]$, $H \parallel [111]$ and $H \parallel [100]$ with the emphasis on the SkL A, A' and B phases. A second part then focuses on the temperature-dependent results where we study the metastable behavior of the SkL phases down to 100 mK. The fourth and last chapter presents quantum oscillations measurements in EuPtSi, mainly in thermoelectric power.

Other compounds have been studied during the period of this PhD thesis, albeit not to the same extent as EuPtSi. The main results for $MoTe_2$ are briefly presented in Appendix B.

Chapter 1

Theoretical background

In this chapter, we recall physical concepts and theoretical explanations concerning the understanding of the results in the subsequent chapters. First we will introduce thermoelectricity, the Seebeck and the Nernst coefficient and their interest as probes to study transport properties of a metallic system. We will then describe quantum oscillations in magnetization, resistivity and thermoelectric power and the corresponding theoretical analyses. Finally, we will explore low-temperature magnetic orders that will be encountered in the experimental results.

Chapter contents

1.1 Thermoelectricity

Thermoelectric coefficients are very interesting probes to study the electronic properties of a system, albeit not as common as resistivity or specific heat. In this work, we have used a large array of probes, two of which are thermoelectric coefficients, the Seebeck and the Nernst effects. This section will explain these two transport effects and how they can be used to study a system.

1.1.1 The origin of thermoelectricity

To understand how thermoelectricity works and what is actually measured through the thermoelectric coefficients, let us start by recalling well known transport concepts for the case of a one-dimensional system. Ohm's law states that an electric field $\mathbf{E}$ applied along a conductor produces a flow of charge $\mathbf{J^e}$:

$$\mathbf{J^e} = \sigma \mathbf{E} \tag{1.1}$$

with σ the electrical conductivity in $\Omega^{-1}\mathrm{m}^{-1}$. As an analogy with electricity, a temperature difference across a solid generates a heat current. The thermal current $\mathbf{J^Q}$ is linked to a temperature gradient $\nabla \mathbf{T}$:

$$\mathbf{J^Q} = -\kappa \nabla \mathbf{T} \tag{1.2}$$

κ is the thermal conductivity in $\mathrm{WK}^{-1}\mathrm{m}^{-1}$. The $-$ sign comes from the fact that heat flows from hot to cold while the thermal gradient vector points the opposite way. Both σ and κ are positive coefficients that are well defined properties of a solid body. Thermoelectricity comes from the observation by T. J. Seebeck (1821) that the application of a thermal gradient on a conducting solid produces a voltage difference.[1] Later, J-C. Peltier (1834) observed that one could induce a heating or cooling effect by injecting an electric current through a conductor. Lord Kelvin (1854) accurately described the two effects as being the same phenomenon. The existence of this phenomenon implies that the equations 1.1 and 1.2 should be modified, thus becoming:

$$\mathbf{J^e} = \sigma \mathbf{E} - \alpha \nabla \mathbf{T} \tag{1.3a}$$

$$\mathbf{J^Q} = \beta \mathbf{E} - \kappa' \nabla \mathbf{T} \tag{1.3b}$$

The first equation states that a charge current can be generated either by an electric field E or a temperature gradient ∇T [6]. The second equation means that either a temperature gradient or an electric field can induce a heat flow. Without thermal gradient, or conversely without electric field, the previous equations 1.1 and 1.2 are naturally recovered. The coefficients linking these properties are σ the electrical conductivity, α the Peltier coefficient (or thermoelectric conductivity) and κ the thermal conductivity. Linking the Seebeck and Peltier effect, β is related to α through the Kelvin relation:

$$\beta = \alpha T \tag{1.4}$$

The Seebeck coefficient S along the x direction is defined as:

$$S = -\frac{E_x}{\nabla T_x} \tag{1.5}$$

The $-$ sign reflects the opposite potential difference compared to a resistivity experiment if the entropy carriers are electrons. The Seebeck coefficient is the measure of the electric

[1] Both the Seebeck and the Peltier effect were first observed across the junction of two wires of different materials, leading to the first thermocouple. For our explanation, we will however consider a single homogeneous medium.

field generated by a thermal gradient in the absence of a thermal current. In other words, by setting $\mathbf{J^e} = \mathbf{0}$ in equation 1.3a, we obtain:

$$S = \frac{\alpha}{\sigma} \tag{1.6}$$

We can note that both the Peltier coefficient (in $\mathrm{AK^{-1}m^{-1}}$) and the electrical conductivity (in $\Omega^{-1}\mathrm{m}^{-1}$) depend on the sample dimensions. This geometrical factor with a unit of length, however, vanishes in the ratio, therefore the Seebeck coefficient being an intensive quantity.[2]

The results have been presented so far for the case of a one-dimensional system. However with the application of a magnetic field, the Lorentz force on the charged particles is perpendicular to their direction of propagation. This additional force causes the charge flow to deviate. Rewriting equations 1.1 and 1.2 and taking the transverse components of a longitudinal field and temperature gradient respectively, we then obtain the Hall effect for electricity and the so-called thermal Hall effect as its temperature analogue. It comes naturally that transverse thermoelectric effects are also observed, the Nernst and Ettinghausen effects (transverse counterparts to the Seebeck and Peltier effects respectively). [7, 8, 9]

We can then write the Seebeck coefficient as the thermoelectric tensor $\hat{S}$:

$$\hat{S} = \hat{\sigma}^{-1}\hat{\alpha} \tag{1.7}$$

Which gives:

$$S_{xx} = \frac{\sigma_{yy}\alpha_{xx} - \sigma_{xy}\alpha_{xy}}{\sigma_{xx}\sigma_{yy} + \sigma_{xy}^2} \tag{1.8}$$

If $\alpha_{xy} \ll \alpha_{xx}$ and $\sigma_{xy} \ll \sigma_{xx}$, it becomes:

$$S_{xx} = \frac{\alpha_{xx}}{\sigma_{xx}} \tag{1.9}$$

and we recover equation 1.6. By the same process, under the application of a magnetic field along z, a longitudinal thermal gradient along x gives rise to a transverse electric field along y, and the Nernst coefficient is:

$$N = S_{xy} = \frac{E_y}{\nabla_x T} \tag{1.10}$$

Experimentally, because the voltage difference is measured perpendicularly to the temperature difference, a geometric factor has to be taken into account, which was not the case for the Seebeck effect where both are measured at the same points or contacts of the sample. Given the length l and the width w of the sample, the geometric factor is $f = l/w$ and the Nernst coefficient is recovered as $N = f\frac{\Delta V_y}{\Delta T_x}$.

[2] In practice, this is ensured by measuring the temperature difference and the voltage difference at the same points of the sample.

1.1.2 The Seebeck coefficient as a transport probe

As a transport probe, the Seebeck coefficient depends on the density of states (DOS) of the charge carriers. In the case of electrons at finite temperature T, their energy distribution is given by the Fermi-Dirac distribution:

$$f(\epsilon, T) = \frac{1}{\exp\left(\frac{\epsilon-\mu}{k_B T}\right) + 1} \tag{1.11}$$

where μ is the chemical potential and k_B the Boltzmann constant. At $T = 0$ K electrons occupy all the states below $\mu = \epsilon_F$ the Fermi energy and none of the states above ϵ_F. With temperature, this distribution is broadened. The total number of electrons N_{tot} in the volume V of the solid gives the carrier density $n = N_{\text{tot}}/V$. We then have:

$$n = \int_0^\infty f(\epsilon) g(\epsilon) d\epsilon = \int_0^{\epsilon_F} g(\epsilon) d\epsilon \tag{1.12}$$

and $g(\epsilon)$ is the density of states, or the number of states per unit of energy and unit of volume. The Drude formula for the electrical conductivity gives:

$$\sigma = \frac{e^2}{3} \left[g(\epsilon) v_F^2 \tau(\epsilon) \right]_{\epsilon=\epsilon_F} \tag{1.13}$$

with v_F the electrons velocity, e the elementary charge and τ the scattering time of the electrons. The Drude formula states the conductivity as being proportional to the DOS and to the scattering term at the Fermi energy [10]. As is well described in the book by K. Behnia [6] and as such will not be explained here, in the Boltzmann picture one can link the Seebeck coefficient to the electrical conductivity using the Mott formula [11]:

$$S = -\frac{\pi^2}{3} \frac{k_B^2 T}{e} \left(\frac{\partial \ln\, \sigma(\epsilon)}{\partial \epsilon} \right)_{\epsilon=\epsilon_F} \tag{1.14}$$

By substituting equation 1.13 into 1.14, we have

$$S = -\frac{\pi^2}{3} \frac{k_B^2 T}{e} \left(\frac{\partial \ln\, g(\epsilon)}{\partial \epsilon} + \frac{\partial \ln\, \tau(\epsilon)}{\partial \epsilon} \right) \tag{1.15}$$

As such, the Seebeck coefficient is proportional to the logarithmic derivative of the DOS and the scattering term with respect to the energy at the Fermi level. Variations in the DOS will thus impact the Seebeck coefficient, making it a very good probe to detect quantum oscillations, as described in section 1.2, in order to study the Fermi surface of a metal. From the previous equation, we can see that the Seebeck coefficient depends on the temperature and the concentration of impurities through τ in the second term $\frac{\partial \ln\, \tau(\epsilon)}{\partial \epsilon}$. This term corresponds to the phonon-drag contribution and arises when the thermal gradient produces a lattice heat current in addition to the electronic current. This phonon-drag contribution thus contributes mainly with a large electron-phonon coupling. In the zero-temperature limit, however, this term can be neglected and the only contribution to the Seebeck effect remaining is the diffusive contribution $\frac{\partial \ln\, g(\epsilon)}{\partial \epsilon}$, i.e. generated by the diffusive movement of the charge carriers.

In the case of a free electron gas, ignoring the phonon-drag contribution in the low-temperature regime, the DOS becomes:

$$g(\epsilon) = \frac{1}{2\pi^2}\left(\frac{2m}{\hbar^2}\right)^{\frac{3}{2}}\epsilon^{\frac{1}{2}} \tag{1.16}$$

From equation 1.14, it is easy to see that the Seebeck coefficient is linear with temperature, and $S \to 0$ for $T \to 0$ K. The scattering-independent Seebeck coefficient is thus:

$$S = \frac{\pi^2}{3}\frac{k_B^2}{e}\frac{T}{T_F} \tag{1.17}$$

with T_F the Fermi temperature.
Considering equations 1.13 and 1.16 at the Fermi energy, with $\epsilon_F = \frac{1}{2}\frac{\hbar^2 k_F^2}{m}$, we can link the conductivity to the mean-free path $l = \tau v_F$ and the Fermi surface $S_F = 4\pi k_F^2$ with a cross-section $A = \pi k_F^2$:

$$\sigma = \frac{e^2 k_F^2 l}{3\pi^2\hbar} = \frac{l e^2 A}{3\pi^3\hbar} \tag{1.18}$$

This equation is valid in the assumption of a spherical Fermi surface and an isotropic $\tau(\epsilon) = \tau$ [12]. The logarithmic term in equation 1.14 then becomes:

$$S = -\frac{\pi^2}{3}\frac{k_B^2 T}{e}\left(\frac{1}{l}\frac{\partial \ln\, l(\epsilon)}{\partial\epsilon} + \frac{1}{A}\frac{\partial \ln\, A(\epsilon)}{\partial\epsilon}\right)_{\epsilon=\epsilon_F} \tag{1.19}$$

From this equation, we can see that variations in the Fermi surface will impact the Seebeck coefficient in a major way. If the curvature of the Fermi surface is positive, i.e. in the case of electrons, the sign of the Seebeck is negative. For holes, the Fermi surface curvature would be negative, yielding a positive Seebeck coefficient. In most metals, however, the Fermi surface is not spherical and the scattering term τ is anisotropic. While equation 1.19 is not applicable in this case, as a first approximation we can divide the Fermi surface in multiple sub-surfaces i for which the previous assumptions still apply. In equation 1.18, we then replace lA by $\sum_i l_i A_i$. For a multi-band system, the total Seebeck coefficient is then the sum of the Seebeck coefficient for all the bands i, weighted by the conductivity

$$S = \frac{\sum_i \sigma_i S_i}{\sum_i \sigma_i} \tag{1.20}$$

where $\sum_i \sigma_i = \sigma$ the total conductivity previously established.

1.1.3 A measure of the entropy per charge carrier

The picture described here is an alternative definition of the thermoelectric power that provides a good hand-wavy description of its origin[3].

A thermal gradient added to a conductor induces a desequilibrium in the system. As a response, the flow of electrons tends to re-establish the equilibrium. The thermoelectric power therefore measures the available entropy of the system without thermal gradient,

[3]This section is inspired by the book *Fundamentals of Thermoelectricity* by K. Behnia [6].

or rather the correction to heat propagation provided by the electric field countering the heat flow.

Callen interprets the Seebeck effect as the *ratio of entropy flow to particle flow in the absence of a thermal gradient* [7]. Since the heat flow does not require particle flow, the Seebeck coefficient quantifies the amount of entropy which particles can carry with no help from the thermal gradient. Since the carrier particles can be of either sign, the response can be dominated by either occupied electronic states or unoccupied ones, meaning a coefficient that can be negative or positive, respectively. This is due to the difference in carrier density, velocity and/or mean-free path above and below the Fermi level.

Additionally, other effects can give rise to entropy flow and thus contribute to the thermoelectric power. For example, spin entropy of delocalized electrons has been observed to lead to a Seebeck response in magnetic conductors [13].

1.2 Quantum oscillations

Quantum oscillations measurements are a powerful way to determine the Fermi surface of a metal. They were first measured in electrical conductivity, the Shubnikov-de Haas (SdH) effect, and shortly after in magnetization, the de Haas-van Alphen (dHvA) effect, in Bi in 1930 [14, 15, 16]. The theory for magnetization was described by Lifshitz and Kosevich (LK) in 1956 [17]. All quantities related to the density of states can show quantum oscillations [18]. This is the case of resistivity, magnetization, but also sound attenuation and magnetostriction. In this section we will explain the underlying mechanisms of quantum oscillations, the LK theory and its limitations in the case of oscillations in thermoelectric power. In keeping with the rest of the manuscript, in this section the magnetic field will be expressed as H in units of teslas for simplification.

1.2.1 Cyclotron orbit and Landau quantization

From a classical point of view, the application of a magnetic field $\mathbf{H}$ to a metal affects the motion of the charge carriers due to the Lorentz force $\mathbf{F}$. This Lorentz force is perpendicular to the direction of the carrier velocity:

$$\mathbf{F} = e\mathbf{v} \times \mathbf{H} \tag{1.21}$$

with e the charge of the electron and $\mathbf{v}$ its velocity. For a strong magnetic field, the trajectory of the carriers in the plane orthogonal to the field direction will become circular with an angular frequency $\omega_c = eH/m$, m being the carrier mass. This is called the cyclotron orbit.

As this subject is very well explained by Shoenberg [18], we will only give a brief overview. The quantum oscillations originate from the Landau quantization of the cyclotron orbits. The latter are quantized in k space, and electrons are confined into cylindrical constant-energy surfaces called Landau tubes, represented schematically in figure 1.1. For a magnetic field applied to a free electron gas along the z direction, the energy associated with the tube n is:

$$E_n = \left(n + \frac{1}{2}\right)\hbar\omega_c + \frac{\hbar^2 k_z^2}{2m} \tag{1.22}$$

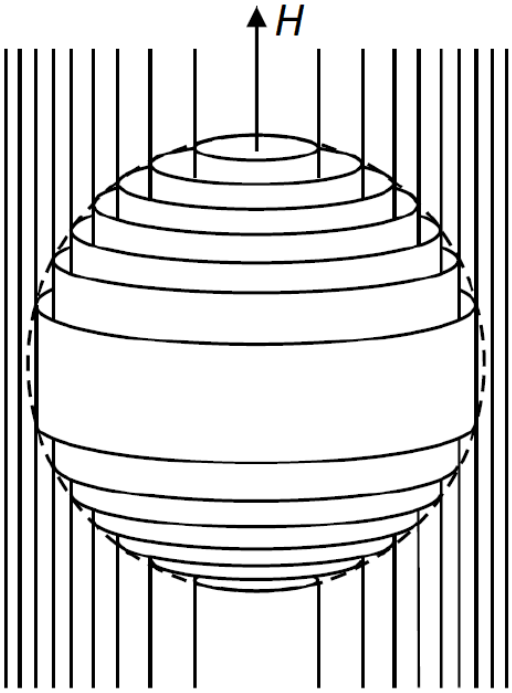

Figure 1.1: Schematic representation of the Landau tubes, i.e. the quantization of the electronic levels under a magnetic field $\mathbf{H} \parallel \mathbf{z}$, for a spherical Fermi surface.

The energy spacing between two Landau tubes n and $n+1$ is then $\hbar\omega_c$ and increases with magnetic field strength. As electrons cannot exist above the Fermi level at $T = 0$ K, when a tube crosses the Fermi level the electrons drop to the next tube. This gives rise to oscillations in the DOS at the Fermi level as a function of the inverse magnetic field. If we tune the magnetic field H and measure a physical property as a function of $1/H$ we shall observe oscillations with the periodicity:

$$\Delta\left(\frac{1}{H}\right) = \frac{2\pi e}{\hbar S} \tag{1.23}$$

This periodicity depends on the area S of the electron/hole pocket. Multiple periods, or frequencies, thus mean different orbits or different pockets, allowing to determine both the number and the sizes of the pockets in a metal.

1.2.2 The Lifshitz-Kosevich theory

The theory proposed by Lifshitz and Kosevich (1956) [17] describes oscillations in magnetization that are periodic in $1/H$ as follows:

$$\tilde{M} = \sum_p \sum_i \frac{1}{p^{3/2}} A_i \sin\left(\frac{2\pi p F_i}{H} + \phi\right) \tag{1.24a}$$

$$\text{with } A_i \propto H^{1/2} \left|\frac{\partial^2 S_i}{\partial k^2}\right|^{-1/2} R_T R_D R_S \tag{1.24b}$$

The oscillatory part of the magnetization is thus a sum over each pocket i of the amplitude A_i with frequency F_i. p is the harmonic number and $\frac{\partial^2 S_i}{\partial k^2}$ is the curvature of the Fermi surface pocket considered. The damping factors R_T, R_D and R_S, respectively the temperature damping, Dingle damping and spin-splitting, will be presented in detail subsequently.

Fermi surface curvature

The factor $\frac{\partial^2 S_i}{\partial k^2}$ corresponds to the curvature of the Fermi surface pocket. It is independent of the temperature and the magnetic field and is related to the way Landau tubes cross the Fermi surface. For a high curvature, the depopulation of the crossing Landau tube is almost continuous and the DOS at the Fermi energy will be almost constant, giving a small oscillation amplitude. On the other hand, for a low curvature such as a 2D cylindrical FS, the depopulation is abrupt and the oscillations will be large.

Spin-splitting factor

R_S is the spin-splitting damping factor. It is due to the Zeeman effect lifting the spin degeneracy of the bands under the applied magnetic field [18]. For the case of a linear Zeeman effect, the Zeeman energy is given by:

$$E_{\mathrm{Z}} = \pm g \mu_B H \tag{1.25}$$

with μ_B the Bohr magneton and g the g-factor for the conduction electrons. A spin lying parallel (antiparallel) to the magnetic field H yields a plus (minus) sign. This energy shift induces a change in the size of the Fermi surface and its cross-section, thus modifying the frequency of the corresponding oscillations:

$$F(H) = F(H=0) + \frac{m^*}{\hbar e} E_{\mathrm{Z}} \tag{1.26}$$

The Zeeman effect thus induces a splitting of a Fermi surface into two non-degenerate surfaces. The frequency measured in quantum oscillations is the back-projection at zero field of the actual frequency of the band [18] and not the actual frequency. A linear Zeeman effect will shift both frequencies by the same absolute amount, thus recovering the same frequency in the back-projection. With the assumption of equal amplitudes for the frequencies $F_\uparrow$ and $F_\downarrow$, this leads to a shift of phase ϕ_S between the oscillations from the two split Fermi surfaces, with the interference reducing the amplitude by R_S, given as:

$$R_S = \cos(\phi_S) = \cos\left(\frac{\pi p g m^*}{m_0}\right) \tag{1.27}$$

where $g = 2$ for free electrons. The value of g can be modified by spin-orbit interaction and can be calculated if the effective mass m^* is known. As R_S does not depend on either T or H, it is most often not taken into account. This R_S damping factor is valid for the case of a linear Zeeman splitting, illustrated in figure 1.2 (left). On the other hand, a non-linear field dependence of the Zeeman effect will affect the frequency observation as:

$$F_{\mathrm{obs},\downarrow\uparrow}(H) = F_{\mathrm{true},\downarrow\uparrow}(H) - H\frac{\partial F_{\mathrm{true},\downarrow\uparrow}}{\partial H} \tag{1.28}$$

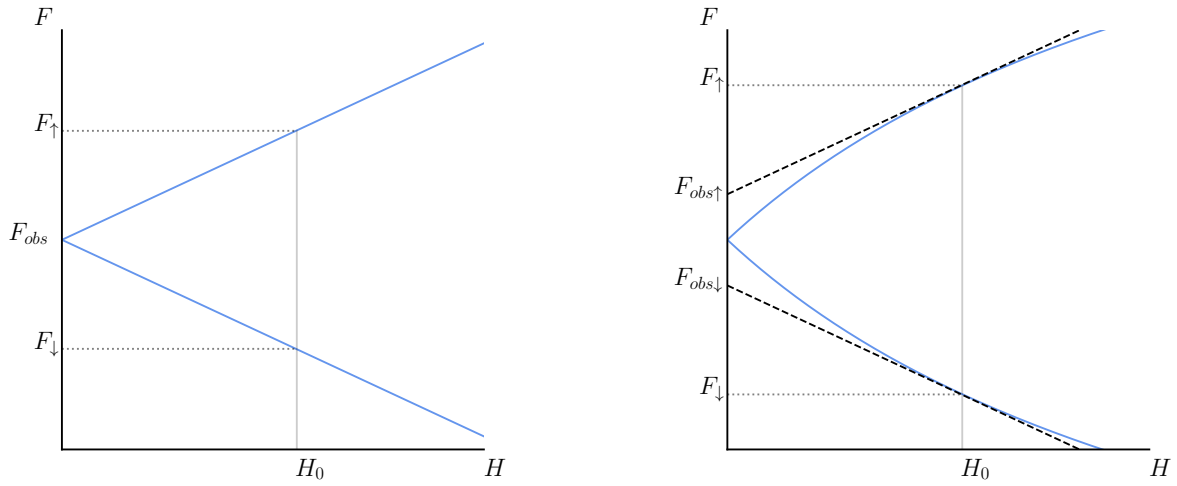

Figure 1.2: Schematic illustration of the Zeeman effect in a linear (left) and sub-linear case (right). $F_{obs\uparrow\downarrow}$ are the observed frequencies while $F_{\uparrow\downarrow}$ are the true frequencies.

The tangential back-projection at zero field thus produces two distinguishable observed frequencies, as illustrated in figure 1.2 (right). The difference between the up and down frequencies increases with the magnetic field, and the relative positions of $F_\uparrow$ and $F_\downarrow$ depend on whether the Zeeman effect is sub-linear ($F_\uparrow > F_\downarrow$) or super-linear ($F_\uparrow < F_\downarrow$).

Temperature damping factor

R_T is the temperature damping factor. As the temperature increases, the energy levels of the carriers are broadened due to the Fermi-Dirac distribution. The Fermi surface is then less well defined and Landau levels are broadened, which leads to a damping of the amplitude of the oscillations. For the case of the dHvA effect it is given as:

$$R_T(T) = A\frac{\alpha p m^* T/H_{\text{eff}}}{\sinh(\alpha p m^* T/H_{\text{eff}})} \tag{1.29}$$

with $\alpha = 2\pi^2 k_B m_0/e\hbar \approx 14.69$ T/K. m^* is the effective cyclotron mass for the branch considered. For a magnetic field range of oscillations taken between H_{min} and H_{max}, H_{eff} is given by $\frac{1}{H_{\text{eff}}} = \frac{1}{2}\left[\frac{1}{H_{min}} + \frac{1}{H_{max}}\right]$. For the calculation of R_T, the effective field should remain constant over the whole range of temperature. From the R_T factor, one can calculate the effective mass by plotting the temperature dependence of the Fast Fourier Transform amplitude A_i for a given frequency F_i and fitting it with the formula above. The maximum amplitude is at $T = 0$ K. Another common way is to use the so-called *mass plot*. Rewriting the hyperbolic sine as $\sinh(x) = \frac{1}{2}(\exp(x) - \exp(-x))$, the mass plot is:

$$\ln\left[\frac{A_i(T)}{T}(1 - \exp(-2\alpha p m^* T/H_{\text{eff}}))\right] = -\frac{\alpha p m^*}{H_{\text{eff}}}T \tag{1.30}$$

plotted as a function of T with A_i the oscillation amplitude for branch i. The effective mass m^* is then obtained self-consistently from the slope of the linear plot. The precision

of the effective mass determination naturally comes from the number of temperatures studied, which means one should measure quantum oscillations over a wide temperature range. For heavy effective masses, the slope of $R_T(T)$ is steep, and the corresponding frequency will be observed at very low temperatures only. As the mass decreases, the temperature range at which it will be observed increases.

Dingle damping factor

Impurity scattering and other effects reduce the lifetime τ of the quasiparticles [19]. It was shown by Dingle (1952) [20] that this can be taken into account as an additional temperature T_D, in kelvins, causing a broadening of the Fermi level with a Fermi-Dirac distribution $f_{FD}(T + T_D)$. The Dingle temperature is then given by:

$$T_D = \frac{\hbar}{2\pi k_B \tau} \tag{1.31}$$

This additional temperature reduces the amplitude of the oscillations with an exponential factor, the Dingle damping factor R_D given by:

$$R_D = \exp\left(-\frac{\alpha p m^* T_D}{H}\right) \tag{1.32}$$

with m^* the effective mass obtained from the temperature damping factor, and T_D the Dingle temperature. As R_D only depends on H, it can be calculated through the magnetic-field dependence of the amplitude of the oscillations. Here, H is the variable effective field H_{eff} corresponding to variable FFT windows of the oscillatory signal. For a given temperature T_0 and oscillation i, the field dependence of equation 1.24 is:

$$A_i(H, T_0) \propto H^{\frac{1}{2}} R_T(H, T_0) R_D(H) \tag{1.33a}$$

$$R_D(H) = A_i(H, T_0) H^{-\frac{1}{2}} \frac{1}{R_T(H, T_0)} \tag{1.33b}$$

where $R_T(H, T_0)$ should be taken as equation 1.29 with fixed temperature and variable field. In a similar way to the mass plot, the *Dingle plot* is obtained from equations 1.32 and 1.33, as:

$$\ln\left[A_i(H) H^{\frac{1}{2}} \sinh\left(\frac{\alpha p m^* T_0}{H}\right)\right] = -\frac{\alpha p m^* T_D}{H} \tag{1.34}$$

When plotted against $1/H$, the Dingle temperature T_D is given by the slope of the linear plot.
T_D is an effective temperature from which one can calculate the scattering lifetime τ as per equation 1.31. With the Fermi velocity $v_F = \frac{\hbar k_F}{m^*}$, the scattering lifetime is linked to the mean-free path l by:

$$l = v_F \tau \tag{1.35}$$

The Fermi wave-vector k_F is determined from the Onsager relation $F = \frac{\hbar}{2\pi e} S$ with $S = \pi k_F^2$ for a spherical Fermi surface. Equation 1.35 thus becomes:

$$l = \frac{\hbar^2 k_F}{2\pi k_B m^* T_D} = \frac{\hbar^2 \sqrt{2eF}}{2\pi m^* k_B T_D} \tag{1.36}$$

with F and m^* taken for the considered peak.

Oscillations in resistivity (Shubnikov-de Haas)

Oscillations in the resistivity (or conductivity) were the first quantum oscillations discovered, in 1930 by Shubnikov and de Haas in Bi, a few months before the de Haas-van Alphen experiment [14]. The theory, on the other hand, was understood after the Lifshitz-Kosevich theory. The difficulty in understanding the SdH oscillations comes from the many scattering mechanisms that have to be considered for the electrical resistivity. Pippard (1965) [21] simplified the understanding of the effect by taking the scattering probability as proportional to the number of states into which the electrons can be scattered [22]. This probability determines the relaxation time τ and the resistivity, and oscillates with $g(\epsilon)$ the DOS. For the first harmonic and a single band with frequency F considered, we then have:

$$\frac{\tilde{\sigma}}{\sigma} \propto \left(\frac{H}{F}\right)^{\frac{1}{2}} R_D R_T R_S \frac{\tilde{g}(\epsilon)}{g(\epsilon)} \tag{1.37}$$

with $\tilde{\sigma}$ and $\tilde{g}(\epsilon)$ the oscillatory parts of the conductivity and the DOS, respectively. The oscillatory behavior of the resistivity ρ is thus the same as for the magnetization $\tilde{M}$:

$$\tilde{\rho} = \sum_p \sum_i \frac{1}{p^{3/2}} A_i \sin\left(\frac{2\pi p F_i}{H} + \phi\right) \tag{1.38a}$$

$$\text{with } A_i \propto H^{1/2} \left|\frac{\partial^2 S_i}{\partial k^2}\right|^{-1/2} R_T R_D R_S \tag{1.38b}$$

All the damping terms R_D, R_T and R_S are the same as for the dHvA measurements.[4] Microscopic properties of the system like the effective mass m^*, the Dingle temperature T_D, scattering lifetime τ and mean-free path l are recovered from a similar analysis of the temperature and field-dependence of the oscillatory amplitude as for magnetization.

1.2.3 Quantum oscillations in thermoelectric power

Oscillations in the thermoelectric power have first been observed by Young and Fletcher in Sn, Zn and Al in 1973, 1981 and 1983 [24, 25, 26]. As presented in section 1.1, unlike resistivity or magnetization, the Seebeck coefficient is not directly proportional to the DOS, instead being proportional to its logarithmic derivative. As such, it comes naturally that S would be more sensitive to oscillations in the DOS, making them substantially larger than in some other probes. However, it also implies that the LK theory previously presented would not accurately describe oscillations in the thermoelectric power.
A simple hand-wavy argument to showcase this inaccuracy comes from the low temperature behavior of the Seebeck effect. Viewing the Seebeck coefficient as a measure of entropy per charge carrier [7], at zero temperature there is no entropy left and the Seebeck and its oscillatory part go to zero. The oscillatory amplitude then possesses a maximum at finite temperature. This is contradictory to the LK theory for which the amplitude of the oscillations is maximum at $T = 0$ K. A common way to circumvent this contradiction is to instead use the LK theory to analyze S/T, ensuring a temperature dependence of oscillatory amplitude with a 0 K maximum. However, this approach is not ideal as it is

[4] This is true as well for the H^n prefactor that depends on the probe used ($n = \frac{1}{2}$ for ρ, M, S; $n = \frac{3}{2}$ for torque magnetometry, ...) [18, 23].

not supported by theory and a proper approach is required.
Additional ways of analyzing thermoelectric power oscillations have been proposed by Trodahl [27] and Kirichenko [28], but they fail to account for the finite-temperature maximum of the amplitude. The most convincing theory that we will be using is the one established by Pantsulaya and Varlamov (PV) in 1989 [29].

Pantsulaya-Varlamov theory

The thermoelectric power contains information on both thermodynamic and transport properties of a system. As such the interpretation of the TEP is rather difficult. It is related to the electronic entropy per charge carrier, a thermodynamic property, but also to the scattering time, a transport property. Both of these can contribute to quantum oscillations under magnetic field.
Much like the case of resistivity, the oscillatory signal of the TEP is described from the analysis of the scattering of carriers, by Pippard's argument. The scattering probability is proportional to the number of states in which electrons can be scattered and so to the DOS at the Fermi level. From this, we can establish an oscillatory behavior similar to those seen previously in equations 1.24a and 1.38a. For a frequency F_i with harmonic p of the Fermi surface i, the corresponding amplitude A_i is given by:

$$A_i \propto H^{1/2} \left| \frac{\partial^2 S_i}{\partial k^2} \right|^{-1/2} R'_T R_D R_S \tag{1.39}$$

All the factors are the same as presented for the LK theory previously. From the energy dependence of the electrons relaxation, Young, Fletcher (based on a thermodynamic approach) [30] and later independently Pantsulaya and Varlamov (based on a kinetic approach), calculated the temperature damping factor R'_T of the TEP as being the derivative of the factor R_T for the Lifshitz-Kosevich theory.

$$\text{LK: } R_T(X) = A_0 \frac{X}{\sinh(X)} \tag{1.40a}$$

$$\text{PV: } R'_T(X) = A'_0 \frac{\partial R_T(X)}{\partial X} = \frac{X\coth(X) - 1}{\sinh(X)} \tag{1.40b}$$

where A_0 and A'_0 are amplitude factors independent of X. $X = \alpha p m^* T/H$, and $\alpha = 2\pi^2 k_B m_0/e\hbar \approx 14.69$ T/K, as defined previously. The maximum amplitude of the TEP quantum oscillations as a function of temperature corresponds to $X = 1.62$, or:

$$T_{\max} = \frac{0.11 H_{\text{eff}}}{p m^*} \tag{1.41}$$

The temperature dependence follows the expected behavior of the TEP in the zero-temperature limit, as $R'_T(T \to 0\text{K}) \to 0$, complying with the vanishing entropy.
Following the same principles as the LK theory presented previously, the temperature dependence analysis of the oscillations of the TEP recovers the effective mass. The complex expression for $R_T\prime$ does not, however, allow the mass plot to be traced linearly. Instead the effective mass is recovered from a self-consistent fit of expression 1.40b. Additionally, the temperature maximum yields the effective mass as per equation 1.41.

Dingle temperature

The Dingle temperature is not a systematically calculated property, and the Seebeck effect is a rather rarely used probe. As mentioned previously, the common (but incorrect) way to analyze oscillations in the Seebeck coefficient is to divide S by T, recovering a signal shape similar to what the LK theory predicts. The rare analysis of T_D from the TEP in the literature thus naturally seemed incorrect. By using the PV framework, we can consider a new approach to the field-dependence of the quantum oscillation amplitudes. From equations 1.32 and 1.33b, the Dingle damping factor for peak i at $T = T_0$ becomes:

$$R_D(H) = A_i(H, T_0) H^{-\frac{1}{2}} A_0' \frac{\sinh(\frac{\alpha p m^* T_0}{H})}{\frac{\alpha p m^* T_0}{H} \coth(\frac{\alpha p m^* T_0}{H}) - 1} = \exp\left(-\frac{\alpha p m^* T_D}{H}\right) \tag{1.42}$$

H here is given by $\frac{1}{H} = \frac{1}{2}\left[\frac{1}{H_{min}} + \frac{1}{H_{max}}\right]$, for successive field windows $[H_{min}, H_{max}]$ such that $\frac{1}{H_{min}} - \frac{1}{H_{max}}$ remains constant, i.e. each field window is of similar $1/H$ size. The amplitude A_0' and the effective mass m^* are the values recovered from the self-consistent temperature dependence fit over the whole field range. We postulate for practicality that m^* is field independent and these values are constants, although for each H value $R_T^{PV}(H, T_0)$ should be recalculated.
The modified Dingle-plot is then a linear plot of the logarithm of expression 1.42 as a function of $1/H$, and the Dingle temperature T_D is given by the slope $-\alpha p m^* T_D$.
With equations 1.31 and 1.36, we recover the scattering lifetime τ and mean-free path l for the considered frequency.

The results of the field-dependence of the TEP quantum oscillations using the PV framework are shown in section 4.3 for EuPtSi. We have compared our TEP analysis with resistivity data, both probes yielding matching results.

1.3 Skyrmions and magnetic orders

This section presents various magnetic orders as they are found in the compound studied in this work, EuPtSi. This also serves as an introduction to the complex spin textures comprising skyrmions, their formation, characterization and potential applications. MnSi, as the prototypical skyrmion compound, will be briefly presented.

1.3.1 Magnetic orders

Para-, Ferro-, Antiferro- magnetism

A ferromagnet (FM) is a material in which a spontaneous magnetization exists even in the absence of an applied magnetic field. All its magnetic moments are collinear, i.e. they lie along a single unique direction (assuming a single-domain material). Such material is characterized by its ordering temperature, the Curie temperature T_C. Below T_C, the magnetization is $M_s(T < T_C) > 0$, the spontaneous magnetization. In turn, $M_s(T > T_C) = 0$, which defines the paramagnetic (PM) state where the moments are randomly oriented.
In contrast, an antiferromagnet (AFM) is defined as having a zero net magnetization

below its ordering temperature, the Néel temperature T_N. It is the superposition of two ferromagnetic sublattices with moments anti-parallel to one another. In the simplest one-dimensional view, neighboring magnetic moments are opposite to each other.

In the PM state, the magnetic susceptibility $\chi = M/H$ can be fitted to a Curie-Weiss dependence:

$$\chi = \frac{1}{T - \theta} \tag{1.43}$$

where θ is the Weiss temperature, whose sign indicates the ground-state ordering of the studied material. For a FM, $\theta > 0$ and we expect $\theta = T_C$. For an AFM, $\theta < 0$ and $\theta = -T_N$. $\theta = 0$ corresponds to a PM material. It is important to note that the Weiss temperature is often very different from T_C or $-T_N$, as the calculation above is a rough approximation. We will not go into the details here as they can be found in the literature, for example [31].

Other orders that minimize the energy of a system can also appear, due to multiple complex origins. One such state is the helical ordering under zero field.

Helical and conical orders

Helimagnetism is a form of magnetic ordering where moments of neighboring magnetic sites arrange themselves in a spiral or helical pattern. The helical state is characterized by a magnetization:

$$\mathbf{m}(\mathbf{r}) = \mathbf{n_1}\cos(\mathbf{q_h}.\mathbf{r}) + \mathbf{n_2}\sin(\mathbf{q_h}.\mathbf{r}) \tag{1.44}$$

in real space with unit vectors ($\mathbf{n_1}$,$\mathbf{n_2}$,$\mathbf{n_3}$) [31, 32]. $\mathbf{m}$ is the reduced magnetization vector $\mathbf{m} = \mathbf{M}/|M_S|$ and $\mathbf{n}_{1,2}$ are unit vectors of the plane perpendicular to the helix pitch along $\mathbf{n_3}$. The helix is formed along the propagation vector $\mathbf{q_h}$ in reciprocal space, with moments in a plane perpendicular to the direction of $\mathbf{q_h}$. The real-space wavelength λ of the helix, or its modulation period, is $\lambda = 2\pi/|\mathbf{q_h}|$. Integrating equation 1.44 over the volume of the material (with dimensions $d \gg \lambda$) yields a total magnetization $M = 0$, so helimagnetism can be seen as a form of antiferromagnetism. The helical magnetic ordering is illustrated in figure 1.3. In the illustration, the helix has a period of 8 moments. For a long helix period, neighboring moments are almost collinear, leading to ferromagnetic-like fluctuations. For a period corresponding to two (respectively one) atomic distance, the AFM (resp. FM) order is recovered. The conical state is similar to the helical state under magnetic field H and is described by the magnetization $\mathbf{m}(\mathbf{r}) = m_1 \cdot \mathbf{n_1} + m_2 \cdot \mathbf{n_2} + m_3 \cdot \mathbf{n_3}$ with:

$$m_1 = \cos\,\phi \tag{1.45a}$$
$$m_2 = \sin\,\phi\,\cos(\mathbf{q}_H \cdot \mathbf{r}) \tag{1.45b}$$
$$m_3 = \sin\,\phi\,\sin(\mathbf{q}_H \cdot \mathbf{r}) \tag{1.45c}$$

with ϕ the conical angle between the field direction and the direction of the moments. The angle ϕ relates to $\cos\,\phi \sim (H/M_s)q_H D$ [32] with D the Dzyaloshinskii-Moriya term (introduced in the following section). As the amplitude of the field increases, the moments reorient along the field direction, as illustrated in figure 1.3. The propagation vector of

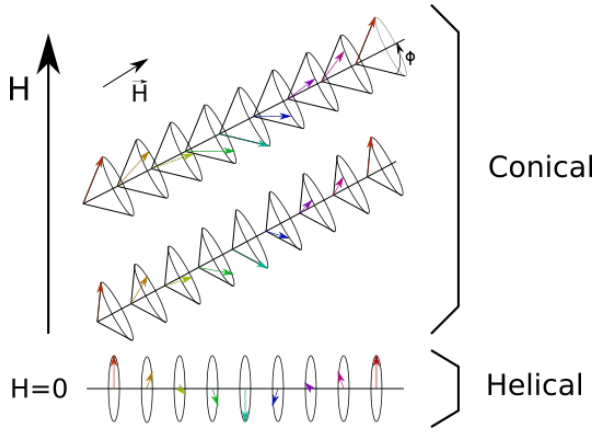

Figure 1.3: Schematic illustration of the helical and conical orders, with moments represented as colored arrows. The vertical axis represents the magnitude of the magnetic field. At zero field in the helical state, the moments are perpendicular to the pitch of the helix. Under field, in the conical state, the pitch is aligned along the field $\vec{H}$. As H increases, the moments progressively align along $\vec{H}$.

the helix usually lies in the direction of the field H, in this case along $\mathbf{n_1}$. This is the case in the prototypical compound MnSi presented in section 1.3.3. In EuPtSi however, the pitch of the helix reorients progressively along the field as well, as the crossover between the helical and the conical order is smooth.

The lack of inversion symmetry in the crystal structure leads to the existence of the helical and the conical ordering from a combination of symmetric and antisymmetric exchange interactions [33]. The former favors collinear spins while the latter favors perpendicular spin alignment.

Symmetric exchange interaction

The symmetric exchange interaction originates from the Coulomb repulsion of electrons of neighboring atoms. It is spin-dependent due to the Pauli exclusion principle. For neighboring moments $\mathbf{S}_i$ and $\mathbf{S}_j$, the Hamiltonian is given by:

$$H_{\text{ex}} = -\sum_{ij} J_{ij} \mathbf{S}_i \cdot \mathbf{S}_j \tag{1.46}$$

with J_{ij} the exchange integral between atoms i and j. Its sign yields the magnetic ordering. For $J > 0$, the system favors a FM state with parallel spins. Alternatively, for $J < 0$ the AFM state with antiparallel spins is favored.

Dzyaloshinskii-Moriya interaction

The DM interaction is an antisymmetric exchange interaction first proposed by Dzyaloshinskii (1958) [34] to explain the weak spontaneous magnetization observed in some AFM materials. Moriya (1960) [35] calculated this exchange by taking the spin-orbit coupling into account in crystals without inversion symmetry. The DM interaction is described by

the following Hamiltonian:

$$H_{\mathrm{DM}} = \sum_{ij} \mathbf{D}_{ij} \cdot \mathbf{S}_i \times \mathbf{S}_j \tag{1.47}$$

where $\mathbf{S}_i$, $\mathbf{S}_j$ are neighboring spins and the vector $\mathbf{D}_{ij}$ reflects the symmetry of the local environment of the magnetic atoms. The DM interaction requires the absence of inversion symmetry, for example in the bulk compounds of the space group $P2_13$ (e.g. MnSi [36], FeGe [37], Cu_2OSeO_3 [38], EuPtSi [39],...), or in specific multilayered compounds. The orbit of an electron depends on the spin direction, and electrons on sites without inversion symmetry minimize the crystal-field energy through the DM interaction by forming a noncollinear spin structure [33]. The energy is minimized when $\mathbf{S}_i$ and $\mathbf{S}_j$ are perpendicular to each other and their cross product $\mathbf{S}_i \times \mathbf{S}_j$ lies parallel to $\mathbf{D}_{ij}$. Inversely, for parallel $\mathbf{S}_i$ and $\mathbf{S}_j$, $H_{\mathrm{DM}} = 0$. It thus favors a rotation of the magnetization around a line of magnetic atoms. With a strong ferromagnetic exchange interaction, the generated state is a long-wavelength helical order. The neighboring spins are then slightly noncollinear. Helimagnetic ordering with a short modulation period can arise when AFM exchange interactions are dominant. The chirality of the helix is given by the sign of $\mathbf{D}_{ij}$ and is determined by the eniantomorph (right- or left-handedness) of the chiral crystal [40, 41].

1.3.2 Skyrmions

Skyrmions[5] are magnetic textures characterized by a vortex-like spin swirling. Extensive reviews on the subject can be found in the literature [41, 42, 43] and we will only give a basic introduction here.

In a 2D plane, a skyrmion is represented by a magnetic domain enclosed in a chiral

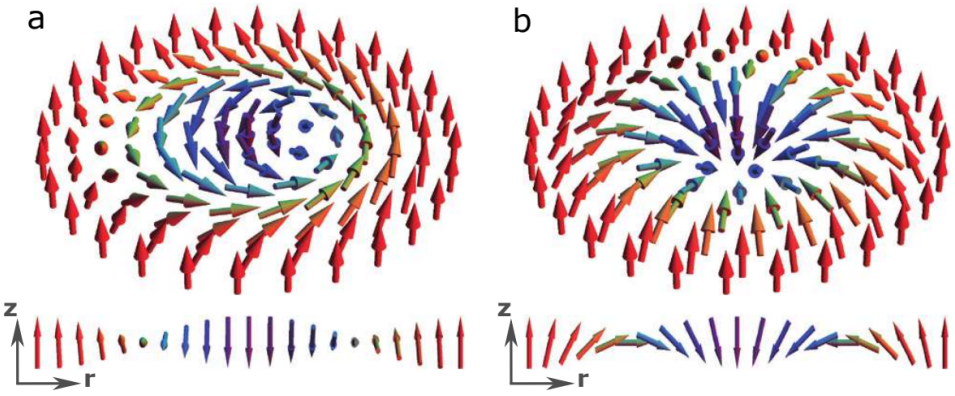

Figure 1.4: Artistic representations of 2D skyrmions of the Bloch (a) and Néel (b) types. Pictured at the bottom is a radial cut for both cases. Illustration from [44].

domain wall. In the center of the skyrmion, the magnetization points one direction while at its edge it points to the opposite direction. The magnetization undergoes a continuous rotation in one dimension when moving from the center to the periphery. Much like

[5]Strictly speaking, the concept proposed by Skyrme in 1962 [2] applies to any particle characterized by a topological integer that cannot be changed due to continuous deformations of a vector field, i.e. topologically protected. In this work we will only refer to the magnetic skyrmions.

domain walls, two types of skyrmions can be found, pictured in figure 1.4 from [44], the Bloch type (a) and the Néel type (b). In the former, the magnetization rotates along a radial axis and in the latter along a tangential axis. For each case, the bottom of the figure shows a cut across the skyrmion.

Skyrmions are characterized by their winding number $W = 1$. W counts the angle of rotation the magnetization does around the core, i.e. for a skyrmion the magnetization undergoes a complete rotation. Other spin textures have different winding number, for example $W = \pm 1/2$ for merons in which the moments are in-plane at the edge of the particle and out of plane at the center. For antiskyrmions which are similar to skyrmions but with alternating Bloch and Néel rotations, $W = -1$ [41]. The winding number, or topological charge, cannot be changed by continuous deformations and the skyrmion is thus a topologically protected texture, the stability of which yields interesting properties, especially for applications (see section 1.3.4). In bulk compounds, skyrmions are of the Bloch type due to chiral symmetry. Néel type skyrmions can be formed in heterostructured synthetic materials with interfacial DM interaction.

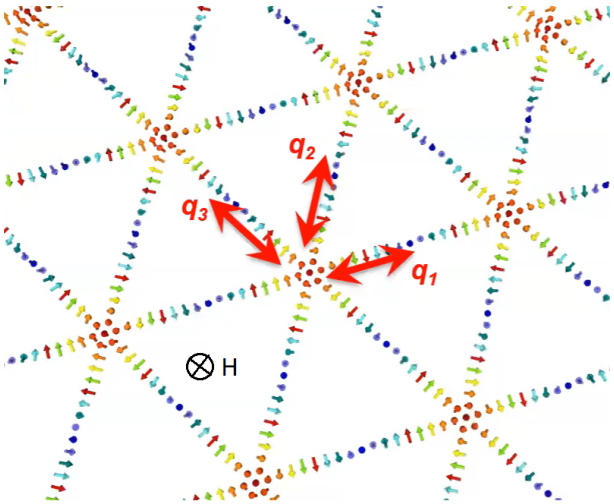

Figure 1.5: Schematic illustration of a triple-q Bloch-type skyrmion lattice, with skyrmion cores located at the crossing of the single-q helixes. The magnetic field H is out of plane. Adapted from [45].

Skyrmions are often found in a form of crystalline lattice, such as the triangular lattice in real space [41]. The system is then described in terms of the spin density wave picture by considering a triple-q state, schematically illustrated in figure 1.5, from [45]. The reduced magnetization $\mathbf{m}(\mathbf{r})$ is expressed as:

$$\mathbf{m}(\mathbf{r}) \approx \mathbf{m}_{\text{uniform}} + \sum_{i}^{3} \mathbf{m}_{q_i}(\mathbf{r} + \Delta\mathbf{r}_i) \tag{1.48}$$

with $\mathbf{m}_{q_i}$ the helical magnetization from equation 1.44 for each single q helical structure i. $\mathbf{m}_{\text{uniform}}$ is the uniform magnetization induced by the Zeeman effect, and $\Delta\mathbf{r}$ is the phase shift between each helix. In this picture, the skyrmion is a superposition of three helical structures of periodicity $\lambda \approx \lambda_{\text{helical}}$ forming an angle of 120° with one another in

the 2D plane perpendicular to the applied field. Singling out one helix from this state recovers the skyrmion cross section at the bottom of figure 1.4 (a). It is to be noted that the skyrmion lattice is formed in a 2D plane. Through translation symmetry, in the third dimension (along the field direction) the skyrmion lattice can be seen as a lattice of cylinders or vortex-like structures.
The triple-q structure of the magnetic skyrmion is experimentally observed in magnetic scattering experiments (small angle neutron scattering (SANS) and X-rays) with a characteristic hexagonal pattern in reciprocal space with a norm $|q|$, shown in the following section for MnSi in figure 1.7.

Additionally, the existence of a skyrmion lattice can be inferred from topological Hall effect (THE) measurements. Due to the spin-polarization along the magnetic texture, the conduction electrons acquire a Berry phase, which affects transport in the same way as an external magnetic field. The THE contribution is then akin to the transverse motion of the deflected electrons from the fictitious Lorentz force due to this emergent magnetic field [32]. Because the core polarization of the skyrmions opposes the applied magnetic field, the THE contribution is of opposite sign of the ordinary Hall effect. The topological Hall effect is described in more detail in section 3.2.3 along with our measurements of the Hall resistivity in EuPtSi. Additional ways of characterizing skyrmions are Lorentz transmission electron microscopy (LTEM) and magnetic force microscopy (MFM) [32].

1.3.3 The prototypical skyrmion compound MnSi

MnSi is a B20 compound with the $P2_13$ cubic structure. The $P2_13$ space group is non-centrosymmetric and chiral. It is presented for EuPtSi in section 3.1.1. As discussed previously, the lack of inversion symmetry allows the DM interaction. A competition between the latter and FM exchange interaction causes the system to order helimagnetically below the transition temperature $T_N = 29$ K. The helimagnetic ground state of MnSi with a periodicity $\lambda = 175$ Å in real space was observed in 1976 [46] and was understood as due to the competition of three hierarchical energy scales. The strongest is the FM exchange interaction, then the DM interaction. Finally weak crystal field effects pin the wave vectors along the body diagonal $H \parallel [111]$ of the cubic unit cell with the lattice parameter $a = 4.55$ Å. Upon the application of a magnetic field $H > 0.1$ T at low temperature in any direction, the system goes from a helical to a conical order. Additionally, right below the transition temperature $T_N = 29$ K, the so-called A-phase appears inside the conical phase. It is enclosed in the $H - T$ phase diagram between $H = 0.1$ and 0.2 T and spans almost 2 K, as shown in figure 1.6 (left). Moreover the A-phase appears for all field directions, indicating that the phase diagram of MnSi shows only a small anisotropy.

SANS experiments from Lebech et *al.* [48], performed with a field perpendicular to the neutron momentum transfer, showed the disappearance of the magnetic intensity upon entering the A-phase. In 2009, SANS measurements by Muhlbauer et *al.* [1] showed that in the A-phase, the scattering pattern appears in the direction of the field. The six-fold geometry in the pattern is independent of the crystal orientation and due to the triple-q structure of the triangular skyrmion lattice. An example of the six-fold intensity pattern from SANS measurements [1] in the A-phase at $T = 26.45$ K and $B = 0.164$ T is shown in figure 1.7. The right panel exhibits measurements of the topological Hall effect in MnSi by Neubauer et *al.* [49]. The ordinary and anomalous parts of the Hall effect were subtracted,

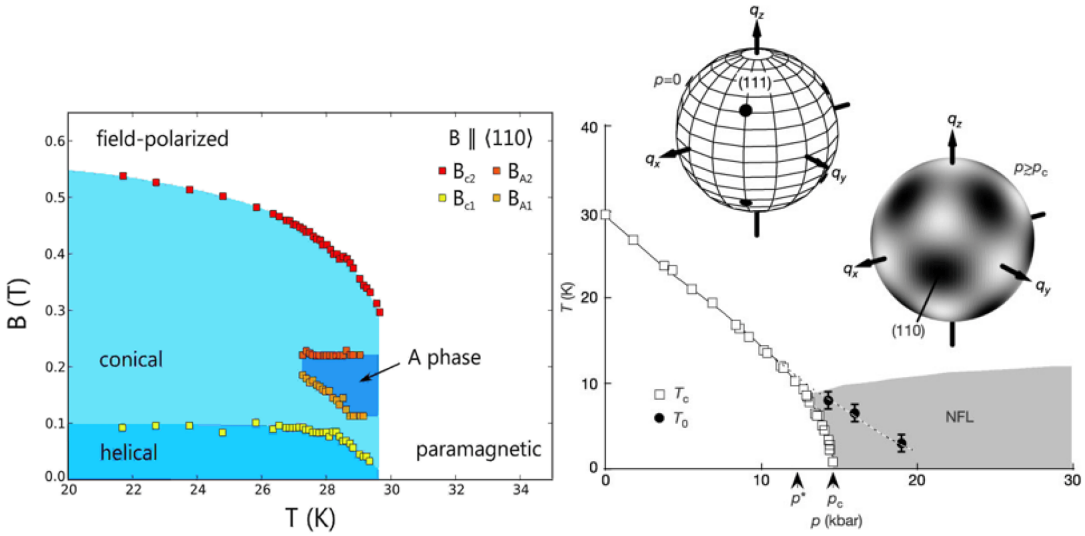

Figure 1.6: Left: magnetic phase diagram of MnSi at ambient pressure with the various phases colored for clarity, from [1]. Right: $P-T$ phase diagram of MnSi with the grey shaded area above P_C corresponding to the non-Fermi liquid regime. The T_C transition changes from second-order to weakly first order at P^*. The spheres show directions of strong elastic neutron intensity in reciprocal space at ambient pressure (left) and under high pressure below the crossover temperature T_0 (right), from [47].

and the THE is shaded, reaching up to $\Delta\rho_H \approx 5$ nΩ·cm. This small Hall contribution is due to the large size of the skyrmions of 180 Å in diameter whose core magnetization opposes the applied magnetic field and produces an emergent field proportional to the skyrmion density. This field is $H = 13.15$ T in MnSi. By comparison, the emergent field in EuPtSi with the small skyrmions of 18 Å is $H = 1105$ T. The calculations are detailed in section 3.2.3.

Additionally, a non-Fermi liquid (NFL) phase appears above the critical pressure [50, 51]. With applied pressure, the ordering temperature decreases and reaches 0 for $P >$ 14.6 kbar. The pressure-temperature phase diagram of MnSi [47] is shown in the right panel of figure 1.6. Strikingly, resistivity measurements show a clear $\rho(T) = \rho_0 + AT^{3/2}$ dependence in a temperature range of about three orders of magnitude (from 10 mK to 6 K) above the critical pressure P_C, over a large pressure range. This contrasts with the Fermi liquid T^2 behavior usually found in metals. The origin of the NFL behavior is not yet definitely understood, and is subject to discussion. A connection between the NFL state and the skyrmion lattice has been supported through topological Hall effect measurements in the NFL state [52, 53]. The observation of a THE signal in the NFL regime suggests a breakdown of Fermi liquid theory from non-trivial topological spin correlations [54].

The discovery of the SkL state in MnSi due to the non-centrosymmetric crystal structure prompted the investigation of other compounds with the $P2_13$ space group as potential skyrmion hosts. The existence of skyrmion lattices was confirmed for compounds such as FeGe through X-ray scattering measurements [37], Cu_2OSeO_3 through SANS experiments [38], and EuPtSi through THE measurements[3].

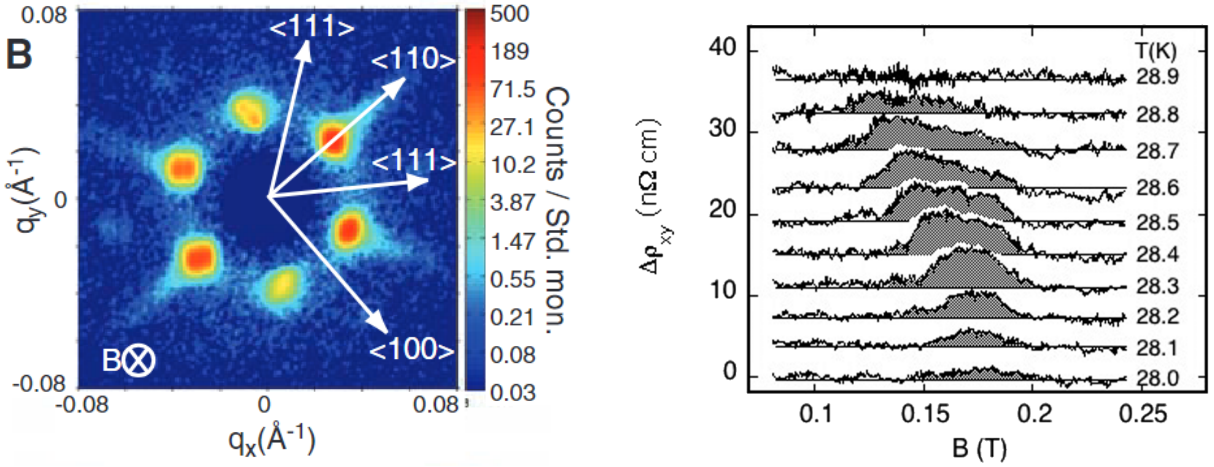

Figure 1.7: Left: six-fold intensity pattern from SANS measurement in the A-phase of MnSi, with $T = 26.45$ K and $B = 0.164$ T, from [1]. Right: Hall effect in MnSi with the ordinary and anomalous contributions removed, yielding the THE contribution shaded in grey. Curves are shifted vertically for clarity, from [49].

1.3.4 Skyrmions, not only interesting for fundamental research...

This thesis work only covers experimental observations of skyrmion lattices in EuPtSi bulk crystals. As such it does not aim to pursue applications. However, it is important to mention the possible applications that skyrmions may have, and skyrmion-based technologies, even if they are beyond the scope of this work. For more information, the reader is invited to look at the reviews by Fert et *al.* [55], Kaviraj et *al.* [42] and Everschor-Sitte et *al.* [56], which inspired this section.

Due to their potential small size in the nanometer range and their behavior as particles, skyrmions naturally are good candidates for information storage. For this, instead of lattices in bulk crystals, realizations of individual skyrmions in thin films or multi-layered heterostructures are preferred. The presence of an interface in this case is crucial in inversion symmetry breaking, to establish the DM interaction. Skyrmions have been stabilized as individual particles at room temperature in perpendicularly magnetized multi-layers, such as Ir/Co/Pt thin films, using fabrication technologies commonly used for spintronic devices [55, 57]. In these systems, individual skyrmions have been obtained with diameters down to 30 nm, which is close to what is required for applied memory devices (<10 nm) [58].

A current induced motion of an individual skyrmion can be achieved at low energy costs, due to the spin-transfer torque exerted by spin-polarized currents [59, 60]. It is the so-called skyrmion Hall effect, with a co-existence of longitudinal and transverse motion. Repulsive interaction from the edges of racetrack-like devices can limit the transverse motion, and the skyrmion can then be moved with velocities up to the 100 m/s range, with a rather low excitation current density of around $10^{10} - 10^{11}$ A/m^2, which is two orders of magnitude smaller than the current density in common racetrack memories [42].

Considering the seminal observation of magnetic skyrmions in bulk crystals in 2009, the

intense research efforts have provided a new array of potential applications, such as memories, logic devices and radiofrequency devices, to this relatively new object. It is however important to consider that many questions still remain unanswered and both fundamental and applied research are still needed before skyrmion devices can be used in everyday technologies.

Chapter 2

Experimental methods

All measurements presented in this thesis were made at very low temperatures, between 50 mK and 10 K, and high magnetic fields, up to 16 T. This chapter will present some experimental works regarding cryogenics as well as the methods used for the various measurements of the following chapters.

Chapter contents

2.1 Low temperatures and improvements on the performance of the cryostat

A large majority of the low-temperature measurements were obtained in the Pheliqs laboratory of the CEA using a homemade ^{3}He/^{4}He dilution refrigerator cryostat whose cold stages are pictured in figure 2.1. The cryostat is inserted in an Oxford Instruments Nb_3Sn superconducting coil cooled at liquid He temperature 4.2 K with a bore diameter of $\varnothing = 40$ mm, reaching up to 16 T in an area of approximately one cubic centimeter. The superconducting coil has a field-compensated zone at the mixing chamber of the cryostat. The principle of the dilution refrigerator being very well described in the literature [61, 62], it will not be presented here. It is, however, to be noted that a series of careful improvements has enhanced the cooling power of the dilution fridge, decreasing its base temperature from 100 mK on the mixing-chamber stage to 46 mK, measured with a calibrated Germanium thermometer.

The first major improvement consisted in the preparation of the right ratio of the ^{3}He/^{4}He mixture. The analysis of the ^{3}He proportion in the mixture was made with a

spectrometer and was found to be around 25%, which is higher than usually recommended [62]. By preparing a mixture consisting of 20% ^{3}He and 80% ^{4}He within the necessary volume, the mixing chamber reached temperatures below 100 mK and in a more stable manner as the cooling power was enhanced.

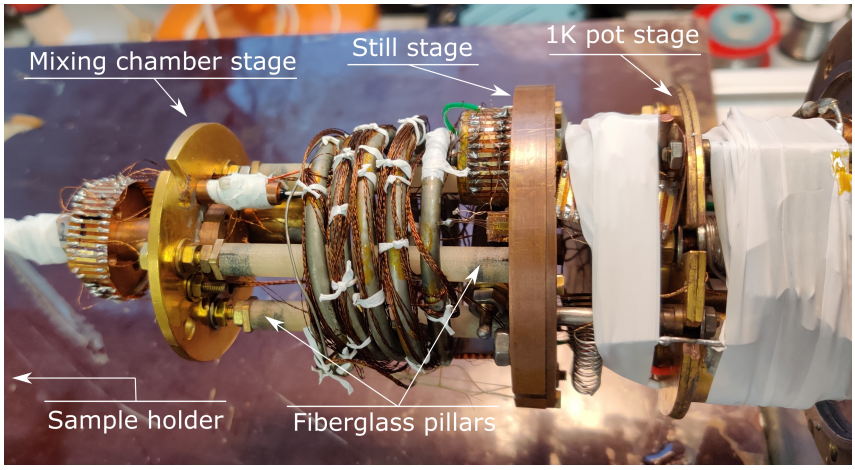

Figure 2.1: Picture of the cold stages of the ^{3}He/^{4}He dilution fridge used for most of the measurements in this work. The fiberglass pillars are 11 cm long for scale.

A second improvement on the performance of the dilution fridge was achieved by replacing the three pillars between the still stage and the mixing chamber stage, shown in figure 2.1. This change was made when the previous 10 cm long Vespel pillars broke. Fiberglass pillars have a lower thermal conductivity, around 10^{-4} Wm^{-1}K^{-1}, compared to 10^{-3} Wm^{-1}K^{-1} at 1 K for Vespel [63], which helps lowering the thermal coupling between the two stages of the fridge. The new pillars were designed to be 11 cm long with the fastening bolts and nuts, which pulls on the continuous heat exchanger enough to lessen the contact points between the spirals without compromising its function. The pillars were put in place while the alignment of the cold stages was monitored with a laser to ensure the position of the samples in the area of maximum field. The continuous exchanger was then held in place with Kevlar wires in various points to avoid further unwanted heat leaks.

Finally, another major improvement to the performance of the dilution fridge was the careful rewiring of the lower stages. All the wires between the still and the mixing chamber stages were replaced with 80 μm diameter NbTi wires in Cu matrix. These wires are superconducting for temperatures below 10 K and allow low resistivity measurements while lowering the thermal conductivity between the stages of the fridge. As all the superconducting wires are located in the area of compensated field, their critical field of approximately 10 T is never reached even during 16 T measurements.

Through the series of improvements presented above, the base temperature of the mixing chamber of the dilution refrigerator has been successfully lowered from around 100 mK to 46 mK. During measurements, with the thermal charge originating from the various thermometers, heaters and probe wiring on the sample-holder, the lowest stable sample temperature achieved is 50 mK for resistivity measurements and 85 mK for thermoelectric power measurements, as the latter involves partial heating of the sample.

The cold finger ensuring the thermal link between the mixing chamber stage of the

cryostat and the sample-holder is a massive copper rod that screws in both sides. It allows a good thermal coupling between the two. However, during measurements in the dilution regime, the effective regulation temperature of the sample-holder cannot exceed 800 mK, as the mixing chamber is thus heated above 700 mK, above the ^{3}He/^{4}He phase separation, and the mixture cannot condensate inside. To avoid this problem a second cold finger shown in figure 2.2 has been designed. A fiberglass rod with a brass strip running along

Figure 2.2: Cold fingers ensuring the thermal link between the cold stages of the cryostat and the sample-holder. Top: copper rod. Bottom: fiberglass with a brass strip along its length, held in place by copper pieces, allowing the sample-holder to reach $T = 6$ K without leaving the dilution regime. Both heat sinks are wrapped in Teflon tape to protect the wires from the sharp edges.

its length limits the coupling between the sample-holder and the cryostat. The brass strip of cross section 10 mm $\times$ 1 mm is locked in place by copper pieces that connect the rod to each side. This setup works well for resistivity measurements and allows continuous measurements with a regulation between 75 mK and 6 K, without leaving the dilution regime and keeping the mixing chamber below the He phase separation temperature.
Because of the small amount of power needed to regulate the temperature, this heat sink cold finger can be used only in resistivity measurements. The thermal gradient constantly needed to measure thermoelectric coefficients heats the sample-holder more than the mixing chamber can absorb, and the lowest effective temperature achievable with such a setup reaches around 500 mK.

The two sample-holders that were used in this work are presented in figure 2.3. The holder on the left is used for resistivity and Hall effect measurements and consists of a copper plate on top of a parallelepipedic copper mass. The samples are placed at the center on top of the plate. The sample-holder on the right is used for thermoelectric power measurements. The massive cylindrical silver block is prolonged by a silver pillar on which the samples are placed. The various elements of the thermoelectric power sample-holder will be described below. Both sample-holders are temperature-regulated by a RuO_2 thermometer of $R_{300K} = 1$ kΩ calibrated between 40 mK and 7 K and a resistive heater, both glued with General Electric varnish to the mass of the sample-holder. 50 μm diameter copper wires connect the sample-holder to the cryostat along the cold finger heat sink.

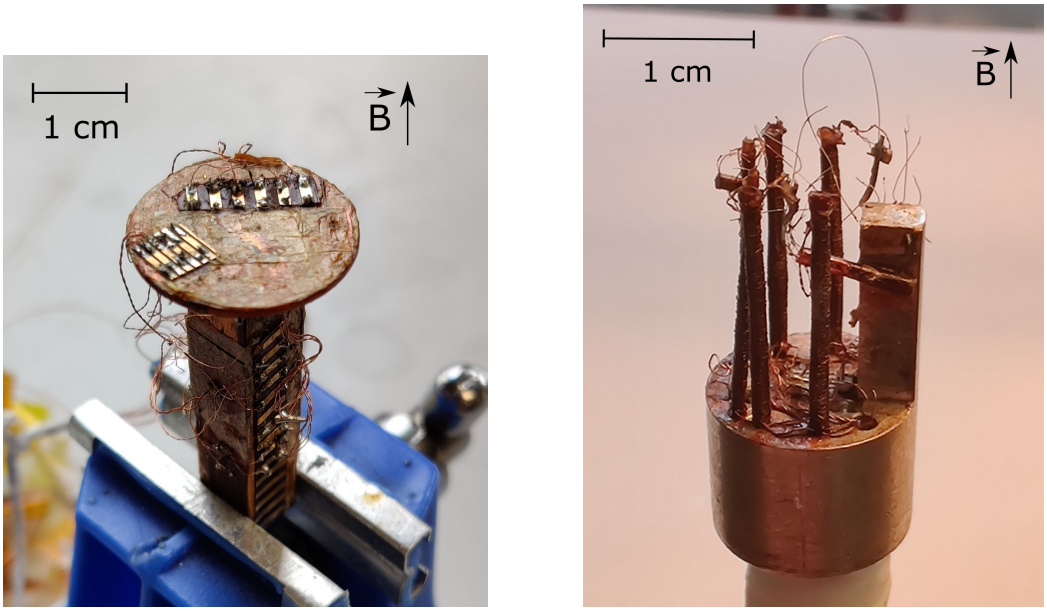

Figure 2.3: Sample holders used in low-temperature and high magnetic field measurements for resistivity (left) and thermoelectric power (right).

2.2 Resistivity and Hall effect measurement

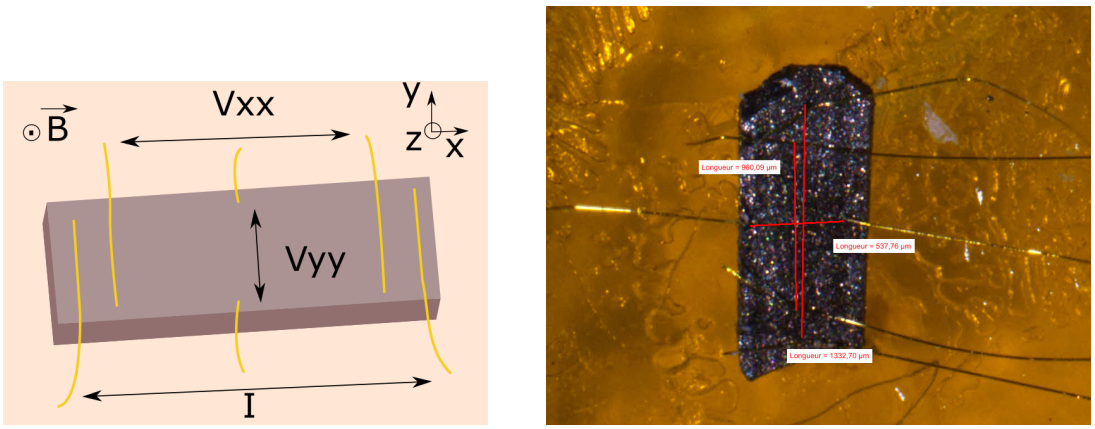

Figure 2.4: Left: schematic representation of the electrical contacts on the sample for resistivity and Hall effect measurements. Right: picture of a EuPtSi sample ($H \parallel [111]$ sample # 2) from above with resistivity and Hall effect contacts. For both figures, the magnetic field is applied normal to the flat face of the sample.

We measured the resistivity using the common AC four-point probe method, schematically represented in the left panel of figure 2.4 and pictured in the right panel for a sample of EuPtSi $H \parallel [111]$, with four gold wires of 15 μm diameter spot-welded to the sample. Two additional wires in the transverse configuration are used for Hall effect measurements. The sample is glued on top of an insulating square of paper to the copper sample holder with General Electric varnish. This allows a good thermal coupling of the sample to the cold finger of the fridge without grounding it.

The AC current is applied by a SR830 lock-in amplifier delivering a 1 V voltage through a 10 kΩ resistance (i.e. a current of 100 μA) at a frequency of 17.530 Hz. The measurement voltage V_{xx} is amplified by a factor 100 with a room-temperature transformer and read on the same lock-in amplifier.
For Hall effect measurements, a similar method is used with the addition of a second transformer and lock-in amplifier synchronized with the first to measure the voltage across the two additional transverse contacts. The transverse voltage is measured for positive and negative magnetic fields of same amplitude and sweep rate. The addition of the two signals (symmetric part) recovers the longitudinal resistivity in case of misalignment, and the subtraction (antisymmetric) is the Hall voltage. The longitudinal and transverse resistivity are then obtained by

$$\rho_{xx} = \alpha \frac{V_{xx}}{I_{xx}}$$
$$\rho_{xy} = \alpha_H \frac{V_{yy}^{+} - V_{yy}^{-}}{2I_{xx}}$$

with $\alpha = \frac{wt}{l}$ and $\alpha_H = t$ being the geometrical factors of the sample for longitudinal and transverse measurements, with w the width, t the thickness and l the length of the sample respectively.

2.3 Magnetization measurements with a Faraday balance

Some magnetization measurements presented in this work were obtained with a Faraday balance setup in the LNCMI laboratory. A precise review of the principles of the Faraday balance can be found in ref. [64] and will not be explained in detail here. The setup is cooled in a Variable Temperature Insert (VTI) reaching temperatures between 1.3 K and 6 K by controlling the liquid He flow and the evaporating pressure inside the VTI. The VTI is itself inserted into a superconducting coil reaching fields up to 16 T. Low pressure ($\approx$ 1 mbar) exchange gas around the sample chamber ensures the temperature stabilization between the latter and the VTI. In the chamber, the sample is fixed with vacuum grease onto a floating metallic platform. The platform is attached with four meander-like arms, allowing elastic vertical displacement along the z direction, as shown in the right panel of figure 2.5. Changes of magnetization are recovered through the capacitive coupling of the platform with the fixed holder. A Ni permanent magnet with a conical shape induces a field gradient in the area where the platform and the sample sit. The samples measured are small enough to consider the field gradient homogeneous in the sample. This measurement system is valid only for $H_{\text{app}} \gtrsim 1$ T corresponding to the saturation of the gradient-inducing magnet.
A schematics for the measurement setup is presented in figure 2.5, taken from [64]. Under a magnetic field gradient $\frac{dH_z}{dz}$, the sample will feel a force and move vertically due to its magnetization M_z, thus changing the value of the measured capacitor C within the linear regime ($\Delta C << C$) as per

$$\Delta z \approx \Delta C \propto F_z \propto M_z \frac{dH_z}{dz} \tag{2.1}$$

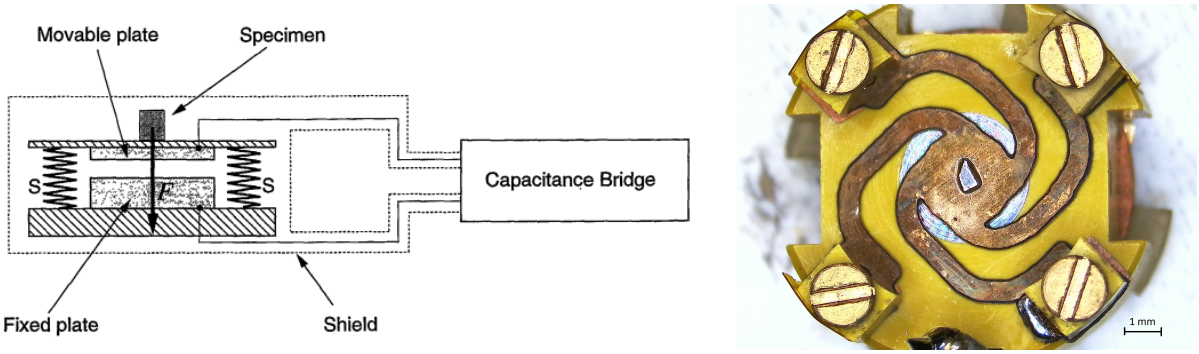

Figure 2.5: Left: principle of the measurement setup. The magnetic force $F \parallel H$ the applied field. The meander-like contacts are represented as springs S. The permanent Ni magnet inside the fixed plate is not shown here. From [64]. Right: picture of the platform with the EuPtSi sample for $H \parallel [110]$ at the center.

with Δz the displacement and F_z the force on the sample along the z direction. The capacitance is measured with a high precision Andeen-Hagerling capacitance bridge with a resolution of a few pF. Depending on the magnitude of the expected magnetization, the platform chosen is more or less rigid. For EuPtSi, as is presented in the following chapters, reaching a high value of $M \approx 7\ \mu B/f.u.$ at saturation, the force experienced by the sample in the field is large, causing a large vertical displacement. As such, the platforms used are quite rigid in this case.
It is important to note that this realization of a Faraday balance is also sensitive to torque effects, i.e. a non-vertical movement of the sample will also change the measured capacitance. Hence, for a given compound, only the easy magnetization axis can be accurately measured, which is the $H \parallel [110]$ direction for EuPtSi. For other field orientations, the measured ΔC will be the resulting effect of a convolution of both ΔM_z and torque effects.

Because the value of the capacitance depends on the sample, the platform used, the rigidity and composition of the latter, the absolute value of the magnetization is hard to determine and a specific calibration is needed. Where applicable, in this work, we have determined the value by comparing the Faraday balance data with commercial SQUID device measurements, in the saturation region of our signal. On the other hand, for quantum oscillation measurements of the dHvA (de Haas-van Alphen) effect, only relative changes of the magnetization signal hold information, and the absolute value is not needed.

2.4 Thermoelectric coefficients measurement

2.4.1 Measurement setup

The Seebeck coefficient S, the Nernst coefficient N, and the thermal conductivity κ are measured simultaneously using the "one heater - two thermometers" technique, with the setup shown schematically in figure 2.6. One end of the sample is glued with conductive silver paste to the heat sink, while the rest of the sample is free and surrounded by vacuum. The longitudinal thermal gradient is established by a heater connected to the side of the sample opposite the heat sink cold finger.

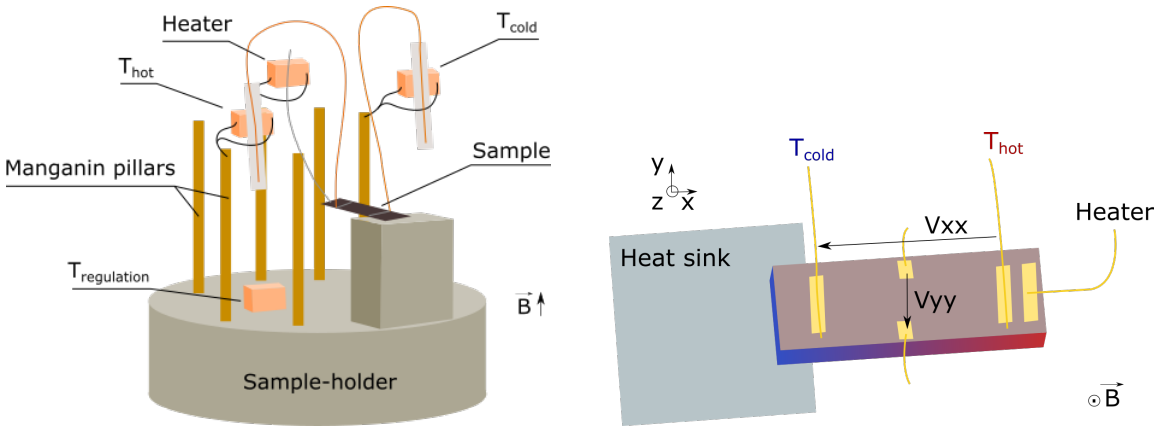

Figure 2.6: Schematic representation of the thermoelectric coefficients measurement setup (left). Close-up from above on the sample contacts with the thermal gradient applied between the heater side in vacuum and the silver heat sink (right). Temperature and longitudinal voltage V_{xx} are taken from the same contacts on the sample.

The thermometers used to measure the temperature gradient are commercial RuO_2 chips with a room-temperature value of $R_{300K} = 1$ kΩ, and $R_{4K} \approx 3.5$ kΩ. A silver strip pasted to the RuO_2 is used for thermalization between the thermometer and 15 μm gold wires spot-welded to the sample. Both thermometers have been calibrated between 75 mK and 6.5 K, and show a negligible magnetoresistance of the order of 1 % at 16 T. The temperature measurements are acquired through a MMR3 device, which allows measurements of three resistors in parallel, with low readout current ($< 10^{-7}$ A) to avoid heating the thermometers in vacuum. The heater used is a commercial RuO_2 chip with $R_{300K} = 3$ kΩ. An electrical current of the order of a few micro amperes at low temperature is applied to the heater, generating heat through the Joule effect. A gold wire spot-welded to the sample and silver-pasted to the heater allows the heat flow.

With the setup described above, it is necessary for the heater and the thermometers to be well decoupled from the copper block sample holder, to ensure that most of the power from the heater goes to and through the sample and that the thermometers accurately recover the sample temperature. To avoid a heat leak between them and the sample holder, the electrical wiring is made through 30 μm diameter manganin wires about 30 cm long that are coiled around capton tubes. These wires have very low thermal conductivity at low temperature ($\approx 10^{-1}$ $WK^{-1}m^{-1}$ at 1 K compared to $\approx 10^{2}$ $WK^{-1}m^{-1}$ for copper) and have a typical overall electrical resistance $R = 250$ Ω. Similar wires are used to recover the Seebeck and Nernst voltages.

At low temperatures, the thermal gradient induced in the sample is of the order of 3 % of the regulation temperature ($\Delta T/T \approx 3$ %). This gradient has to be small to avoid non-linearity in the response of the system. The order of magnitude of the Seebeck coefficient in metals is about 1 μV/K. With $T = 100$ mK and $\Delta T = 3$ mK, this leads to a Seebeck voltage of the order of 3 nV. To avoid noise and parasitic signal coming from multiple welds at various temperatures, the copper wires used to measure the thermoelectric coefficients are direct between the 1K pot stage and the analog DC nanovoltmeters. The nanovoltmeters work on battery in order to avoid noise due to the power grid. The ends of the copper wires are pressed into the Cu knobs inputs of the nanovoltmeters to get an electrical contact without welds. The analog nanovoltmeter signal is then read and

acquired through Keithley voltmeters. This method allows us to have a noise level below 0.5 nV in our signal.

Thermal conductivity κ measurements are performed at the same time and using the same setup as thermoelectric measurements. In addition to the two thermometers mentioned above, a multimeter measures the voltage V_H across the heater used to induce the thermal gradient. By multiplying the voltage and the heating current I_H, the heating power is recovered. Using Fourier's law of heat conduction, κ (in $\mathrm{WK^{-1}m^{-1}}$) is

$$\kappa = \alpha' \frac{P}{\Delta T} = \alpha' \frac{I_H \times V_H}{\Delta T} \tag{2.2}$$

with $\alpha' = \frac{1}{\alpha}$ the geometrical factor, $\alpha = \frac{\omega t}{e}$ the same factor as for resistivity measurements.

2.4.2 Measurement protocol

Thermoelectric coefficient measurements (Seebeck, Nernst and thermal conductivity) need to be performed in a specific protocol depending on whether the variable parameter is the magnetic field or the temperature. By inducing a temperature gradient in the sample, it makes measuring a reference temperature of the sample quite tricky, which is why it is important to measure all the thermometers before and after turning the heater on. All the data obtained for field sweeps thermoelectric measurements are made according to the following steps:

1. Zero field and regulation temperature without gradient
2. Zero field with gradient
3. Continuous field sweep with the applied gradient
4. Fixed target field and gradient after the sweep
5. Fixed target field and regulation temperature without gradient

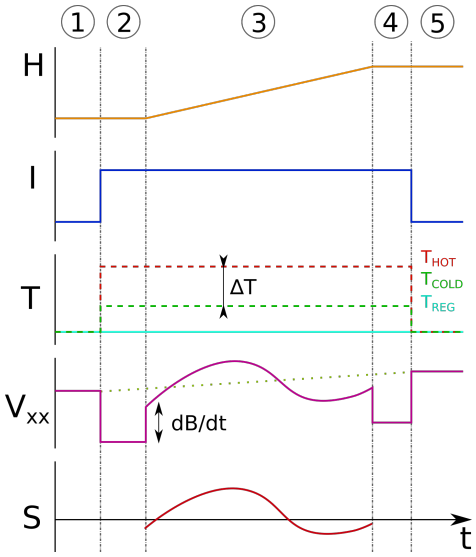

Figure 2.7: Schematic representation of the measurement protocol for the thermoelectric power.

A schematic typical field sweep measurement of the thermoelectric power is presented in figure 2.7 where the numbers correspond to the steps described previously. V_{xx} is the raw longitudinal voltage signal measured with the nanovoltmeters, as the difference between the potentials of the cold and the hot contact. During field sweeps measurements, a voltage V_{emf} proportional to dH/dt appears due to the electromotive force by the sweeping magnetic field. The amplitude of this voltage is constant for a fixed sweep rate and is removed by comparing the signal before and after the beginning of the sweep. To obtain the

Seebeck coefficient, a value of thermoelectric voltage without applied current (dotted line in figure 2.7) is subtracted from the signal. This value can be seen as a linear background signal $V_0^{\Delta T=0}$ that, once removed, allows us to recover a value of $S = 0$ µV/K without gradient. To ensure this background value is linear at all fields, measurements in field steps are also regularly performed with fixed temperature. For various magnetic fields along the range of interest, mean values of the thermoelectric signal and thermometers are taken with and without gradient.
Following this protocol, the Seebeck signal S during field sweeps is recovered:

$$V_{\text{signal}}(H) = V_{xx}(H) - V_0^{\Delta T=0}(H) - V_{\text{emf}}\left(\frac{dH}{dt}\right)$$

$$S(H) = -\frac{V_{\text{signal}}^{\Delta T\neq 0}(H)}{\Delta T} = \frac{V_{T_{\text{cold}}} - V_{T_{\text{hot}}}}{T_{\text{hot}} - T_{\text{cold}}}$$

with the minus sign due to measuring in opposite convention from the resistivity.
For measurements with temperature as the variable parameter and a fixed magnetic field, temperature sweeps are not possible since the thermal gradient needs to change for each temperature. Instead, the measurements are done in steps along the temperature range of interest. For each reference temperature without gradient, a heating current is estimated to keep a constant ratio $\Delta T/T \approx 3\%$. The temperature of the thermometers and the thermoelectric voltage are measured with and without the applied gradient. Once stabilized, the mean values are taken as one data point at temperature $T_{\text{mid}} = (T_{\text{hot}} + T_{\text{cold}})/2$.

As thermal conductivity measurements are performed at the same time as thermoelectric power measurements, the protocol is the same.

Nernst coefficient measurements are performed with the same protocol as for the Seebeck coefficient. As it is the transverse coefficient, much like the Hall effect with regard to resistivity, the Nernst voltage is obtained by subtracting positive and negative magnetic fields measurements of identical amplitude and sweep rate. The positive and negative fields are interpolated for similar absolute value.

2.5 Quantum oscillation analysis

The Fermi surface of a metal holds a lot of information regarding the properties of the material and the charge carriers. There are only a few ways to directly measure the Fermi surface, for example through ARPES measurements [65]. The mapping of the Fermi surface can also be done by determining the period of quantum oscillations under a sweeping magnetic field, if the sample quality allows it. As was described in chapter 1.2, various measurement quantities exhibit quantum oscillations at low temperature and high magnetic field. In this work, such oscillations have been observed in resistivity, magnetization and thermoelectric coefficient measurements. In order to be accurately compared and studied, it is important to follow a similar protocol for each analysis. All the data treatment was performed using Python codes that have been developed for the purpose of this work.
To analyze the quantum oscillations, a Fast Fourier Transform (FFT) routine is used. The FFT is performed on a field window $[H_{\text{min}}, H_{\text{max}}]$ that is the same for all data of a

particular sample. The effective magnetic field H_{eff} for the window is given by

$$H_{\text{eff}} = \left[\frac{1}{2}\left(\frac{1}{H_{\text{min}}} + \frac{1}{H_{\text{max}}}\right)\right]^{-1} \tag{2.3}$$

On this field window, the signal is interpolated in units of $1/H$ to recover the periodicity of the oscillations. The FFT calculation will yield frequencies in units of magnetic field, in tesla. A polynomial background whose order is determined by the shape of the signal is subtracted from the data to filter out low frequencies and a Hanning window is applied to the oscillatory signal to reduce the white noise background in the frequency spectrum [66]. Figure 2.8 shows the data treatment applied to a raw signal until the calculation

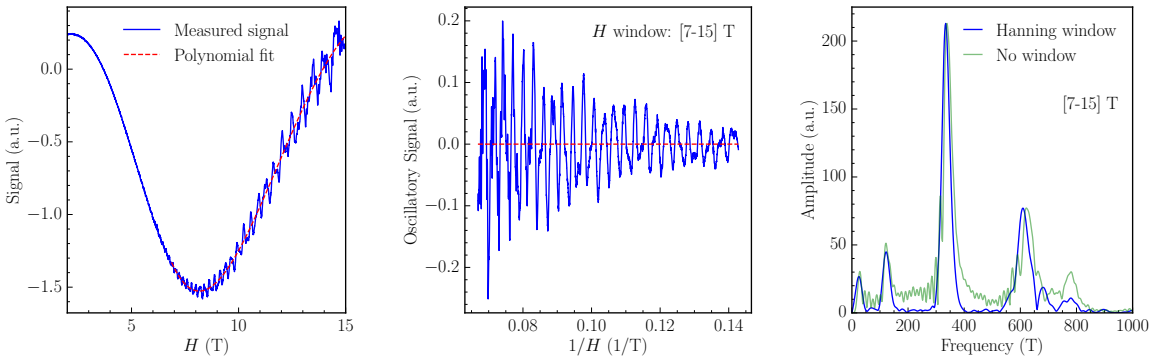

Figure 2.8: Left: Measured signal with quantum oscillations (blue), fitted with a polynomial function (red). Center: Oscillatory part of the signal taken between 7 and 15 T with the polynomial background removed, as a function of $1/H$. Right: FFT spectra obtained with a Hanning window (blue) and without (green).

of the FFT. Each frequency observed in the FFT spectrum corresponds to the extremal cross-section of a carrier pocket of the Fermi surface or an harmonic of the fundamental frequency. A study of the angular dependence of the amplitudes yields information about the Fermi surface topology but has not been done for this work. Studies of the field dependence of the amplitude allows to recover the Dingle temperature which gives information on the mean-free path of the carriers. The temperature dependence of the amplitude of each frequency is analyzed to recover the effective mass of the charge carriers. We can note that the absolute value of the peak amplitudes does not hold interesting information, only the relative amplitude for various temperatures is relevant. For Shubnikov-de Haas (SdH) and de Haas-van Alphen (dHvA) oscillations, respectively in resistivity and magnetization, the amplitude of each frequency with respect to temperature will be maximum at low temperatures. The *curve_fit* python package is used to compute the parameters of the Lifshitz-Kosevich (LK) formula and yield the effective mass m^* in units of m_0 the free electron mass. For oscillations in thermoelectric power, however, the amplitudes will reach a non-zero temperature maximum and the Pantsulaya-Varlamov (PV) formula is used, as was described in section 1.2.3.

Additionally, the effective mass can be recovered from the temperature maximum of the amplitudes $T_{max} = \frac{0.11 H_{\text{eff}}}{p m^*}$. As the position of the peak depends inversely on the effective mass, high effective masses will shift the position of the peak to lower temperatures

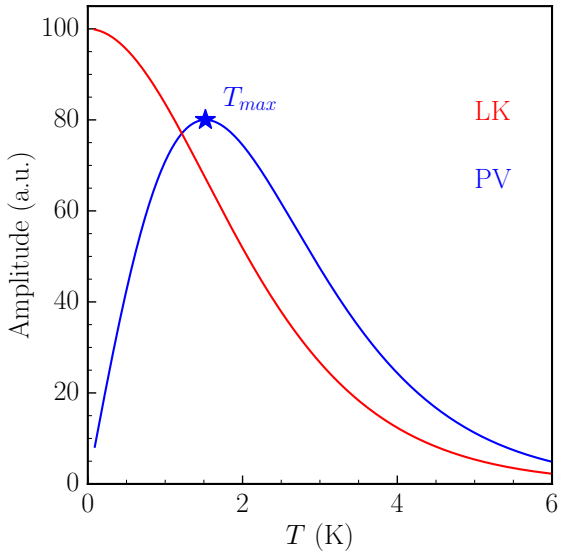

Figure 2.9: Schematic view of the Lifshitz-Kosevich (red) and the Pantsulaya-Varlamov (blue) formulas used to fit the temperature dependence of the amplitudes of each frequency peak of the FFT spectrum. The maximum T_{max} of the PV fit is indicated by a star.

and the slope will be sharper. A schematic example of the LK and the PV fits is provided in figure 2.9 for the same effective carrier mass. The maximum of the PV fit is indicated by a star.

Chapter 3

Study of the skyrmion lattice phases of EuPtSi

In this chapter, we present the thermodynamic and transport measurement of the various magnetic phases of EuPtSi at low temperature and under magnetic field. We will focus on the skyrmion lattice (SkL) phases present at low field (H<5 T). Quantum oscillations experiments performed above 5 T will be presented in the next chapter. The three main orientations of EuPtSi, namely $H \parallel [110]$, $H \parallel [111]$ and $H \parallel [100]$ have been studied using resistivity, Hall effect, thermal conductivity and thermoelectric power. In the $H \parallel [110]$ direction, the compound remains in the conical state at all fields below the field-polarized transition. For $H \parallel [111]$, the so-called A-phase is observed. In the $H \parallel [100]$ direction, two distinct phases A' and B, exist. While these phases are closed in the $H - T$ phase diagram, by performing field-cooled experiments they can be observed as metastable states down to temperatures much lower than expected.

Chapter contents

3.1 Introduction to EuPtSi

3.1.1 State of the art

In 2009, the skyrmion lattice was evidenced in MnSi [49]. The realization of this exotic magnetic texture initiated the search of other skyrmion-hosting compounds, especially in non-centrosymmetric compounds of the space group $P2_13$, the same as MnSi. One such compound is EuPtSi, whose skyrmion lattice was found by Kakihana et *al.* in 2018 [3] with the evidence of an anomalous behavior in the Hall resistivity. This makes EuPtSi the first $4f$ rare-earth based example in which a skyrmion lattice has been detected. In this section, EuPtSi is introduced along with the main results found in the literature.

Rare-earth systems and Eu-based compounds

Rare-earth based metallic compounds possess various interesting properties pertaining to the field of strongly correlated electron physics [31, 39]. These physical properties are due to the electronic configuration for lanthanides, $4d^{10}4f^n5s^25p^65d^16s^2$ (with a Kr core) and $n = 0 - 14$. The $4f$ electrons with a local moment give rise to magnetism. As there is no overlap of wave functions between the $4f$ electrons, a direct magnetic interaction does not occur. Instead, the magnetic order is driven by indirect interactions mediated by the spins of conduction electrons, the so-called Ruderman-Kittel-Kasuya-Yosida (RKKY) interaction. In turn, the Kondo interaction causes a coupling of the localized spin of the magnetic impurity and the spin of the conduction electron, leading to a screening of the magnetic moment and thus the suppression of the magnetic ordering. The competition

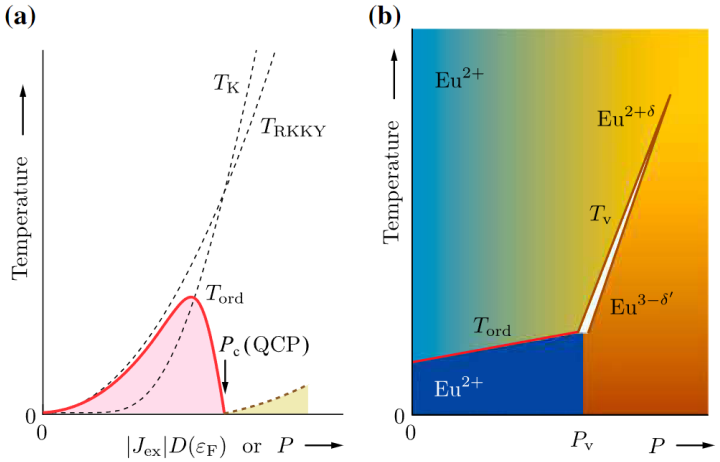

Figure 3.1: (a) Doniach phase diagram showing the suppression of the magnetic ordering temperature T_{ord} with pressure P. Below T_{ord} (shaded in pink) is the magnetic ordered region. T_K and T_{RKKY} are the Kondo and the Ruderman-Kittel-Kasuya-Yosida temperatures, respectively. P_C is the critical pressure corresponding to the quantum critical point (QCP). Above P_C is the quantum critical region (shaded). (b) $P-T$ phase diagram representing the valence transition in Eu compounds. T_V is the first-order valence transition temperature and P_V is the pressure at which the first-order valence transition appears. From [39].

between the RRKY interaction and the Kondo interaction at low temperature is represented by the Doniach phase diagram in figure 3.1 (a) (from [39]) as a function of pressure P or $|J_{ex}|D(\epsilon_F)$ with the magnetic exchange interaction J_{ex} between the $4f$ and the conduction electrons, and $D(\epsilon_F)$ the electronic density of states at the Fermi energy. The RRKY interaction dominates at low pressure (or small $|J_{ex}|D(\epsilon_F)$), whereas the Kondo interaction dominates at higher pressure (or large $|J_{ex}|D(\epsilon_F)$) and the ordering temperature T_{ord} is suppressed, leading to a quantum critical point (QCP) at the pressure P_C. In the quantum critical region, heavy-fermion states appear at low temperature where novel states such as unconventional superconductivity have been observed, for example in some Ce compounds [67].
For most rare-earth atoms, the $4f$ electrons are in a trivalent state. For compounds based on Ce and Yb at opposite ends of the $4f$ rare-earths group, the hybridization between the $4f$ states and the conduction electrons is not negligible. These systems are prototype systems to be well described by the Doniach phase diagram presented above. Some rare-earths such as Eu, Sm, Tm and Yb, however, can be in a divalent state in compounds. Most Eu-based compounds are found in the divalent $4f^7$ state corresponding to the half-filled $4f$ shell, and we have $L = 0$ and $S = J = 7/2$ with L, S and J the orbital, spin and total angular momentum respectively. A valence instability between the divalent Eu^{2+} and the trivalent Eu^{3+} ($4f^6$, non-magnetic, with $S = L = 3$, $J = 0$), due to the small energy difference between the two states [68], often leads to a first-order valence transition under pressure. This is illustrated in figure 3.1 (b) from [39], with T_V the first-order valence transition temperature and P_V the pressure at which the first-order valence transition appears. The pressure-temperature phase diagrams of several Eu compounds have been studied by Onuki et *al.* [39]. Only a few Eu-based compounds show Doniach-like phase diagrams where the magnetic ordering can be suppressed continuously with pressure. EuPtSi, the compound studied here at ambient pressure, is divalent and is far from any magnetic or valence instability.

Crystal structure

EuPtSi is a cubic chiral compound of the Ullmannite-type (NiSbS-type) with the space group $P2_13$ (No. 198), T^4, crystallographic point group 23 (Schoenflies symmetry group T). Of the five cubic crystallographic point groups, this group has the lowest symmetry. As all cubic systems, it possesses four three-fold rotation axes along body diagonals ([111]), but four-fold rotation axes are absent along the main axes ([100]). This point group instead has two-fold rotational symmetry along its main axes. As such, EuPtSi lacks spatial inversion symmetry and mirror symmetry. This allows chirality of the crystal structure. A schematic representation of the point group from ref. [10] is shown in the left panel of figure 3.2, with the triangles on the sides of the cube representing the symmetries and the chirality.
EuPtSi has an equiatomic composition (1:1:1 stoechiometry) with 4 of each atom per unit cell. The unit cell parameters with atomic sites positions and nearest neighbors distances for each atom is reported in table 3.1, partially adapted from [69]. Within the cubic cell with lattice parameter $a = 6.4336$ Å, four Eu atoms form a tetrahedron. Each Eu atom is shared by three equilateral triangles with sides of 3.9404 Å, in three dimensions, forming the so-called trillium lattice. The trillium lattice is similar to the network of Mn atoms in MnSi. The structure of EuPtSi is illustrated in the central panel of figure 3.2 from [69],

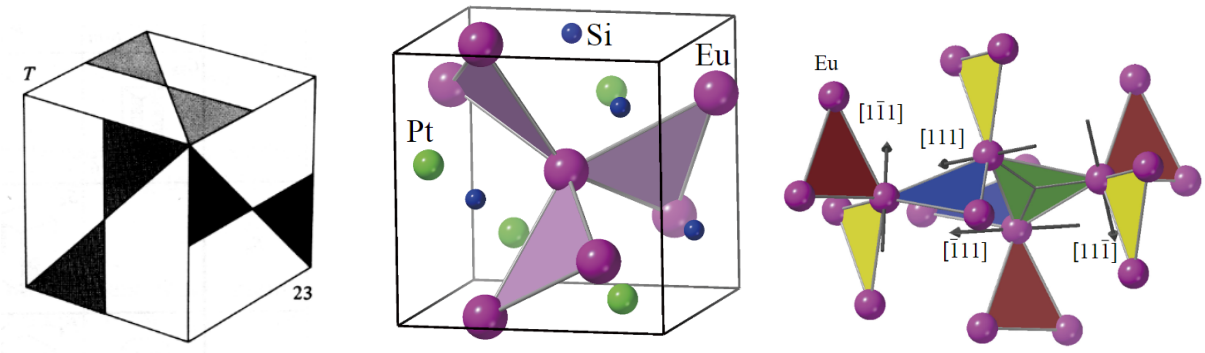

Figure 3.2: Left: crystallographic point group 23 (T). Painted triangles represent the chirality of the cubic system and its symmetries, from [10]. Center: cubic unit cell of EuPtSi with the trillium lattice colored. Eu atoms are purple, Pt atoms in green and Si atoms in blue. Right: corner-sharing of the trillium lattice, showing only the Eu atoms. Threefold symmetry axes are indicated. Center and right figures are from [69].

and the right panel depicts the corner-sharing equilateral triangles forming the trillium lattice. The threefold symmetry axes are indicated by arrows. This complicated structure is the cause of chirality in EuPtSi.

Atom	Wyckoff site	x	1^{st} neighbors (Å)	2^{nd} neighbors (Å)
Eu	$4a(x,x,x)$	0.36989	3.94044	5.94919
Pt	$4a(x,x,x)$	0.08627	4.00133	6.56370
Si	$4a(x,x,x)$	0.6614	3.99250	5.54322

Table 3.1: Atomic positions and nearest neighbors distances in EuPtSi, with lattice parameter $a = 6.4336$ Å, adapted from [69].

The Ullmannite-type compounds have garnered a lot of interest for the theoretical aspect of frustrated magnetism [70, 71, 72]. EuPtSi was thus studied for this prospect, and was found to have a lot of similarities with MnSi with the cubic B20 crystal structure and the same space group as EuPtSi. MnSi is presented in section 1.3.3.

Magnetic fluctuations in the PM domain

When EuPtSi was first synthesized in 1990 by Adroja et *al.* [73], the metallic compound was found to be paramagnetic down to nearly 4 K. From ^{151}Eu Mössbauer studies on polycrystal samples, the authors observed an onset of magnetic ordering at 4.2 K. Like MnSi, EuPtSi orders in a helical structure at low temperature. Because helimagnets have no total magnetic moment, it can be seen as a form of antiferromagnetism, which was the conclusion of the works by Franco et *al.* who measured a Néel temperature $T_N = 4.1$ K through specific heat and magnetic susceptibility measurements [74]. This ordering temperature is quite low compared to previously known Eu-compounds with magnetic ordering temperatures ranging from 10 to 100 K [75, 76, 77, 78]. The low-temperature magnetic ordering is a common feature of geometrically frustrated magnetic systems, for example the triangle lattice, honeycomb lattice, Kagomé lattice, and in the case of EuPtSi the

trillium lattice [72, 70].

The first order nature of the transition is evidenced by the sharp specific heat peak,

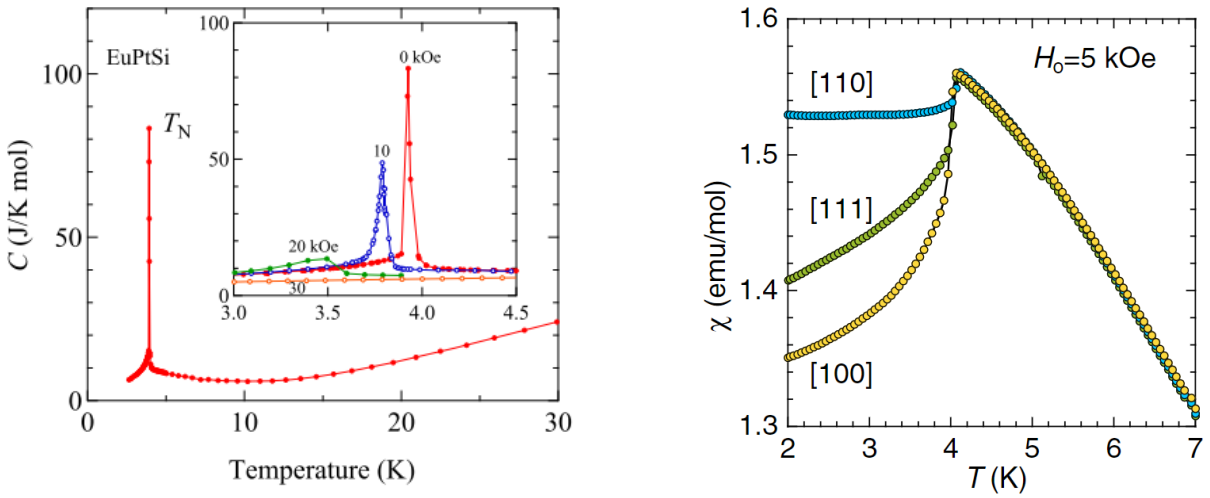

Figure 3.3: Left: temperature dependence of the specific heat for $H \parallel [111]$ with the T_N transition for various magnetic fields in the inset. From [79]. Right: temperature dependence of the magnetic susceptibility for the main three crystallographic direction, emphasizing the PM/helimagnetic transition at T_N=4.05 K. From [4].

and steep drops of resistivity and susceptibility, as shown in figure 3.3, from [79] and [4]. Additionally, hysteretic features are observed in the temperature dependence of thermal expansion. The broadening of the magnetic ordering transition with increasing magnetic field could be due to a change from field-induced first order to second order. Calculations of magnetocaloric entropy (MCE) scaling by Mishra et *al.* [80] indicate the possibility of a tricritical point at $H_{app}^{TCP} = 2.75$ T and $T^{TCP} = 3.2$ K for the [111] direction, above which the T_N/H_C transition becomes second order. This result has been supported by magnetization measurements from Sakakibara et *al.* [81].

In EuPtSi, the magnetization goes to 0 at zero field, which is a feature of AFM ordering. However, as seen in figure 3.4 from [39] the susceptibility follows a Curie-Weiss law at high temperature (> 50 K), with a Weiss temperature $\theta \approx 7 - 11$ K indicating predominantly FM correlations in the PM regime. As such, there are competing FM and AFM exchange interactions. Close to T_N, $\chi(T)$ data show a slow decrease upon warming, with a much weaker Curie-Weiss behavior.

A critical slowing down of the magnetic fluctuations has been evidenced by muon spin relaxation and nuclear magnetic resonance (NMR) by Higa et *al.* [82]. At zero field, the fluctuations may be ferromagnetic-like, but the Weiss temperature $\theta \approx 4$ K measured by the Knight shift in NMR changes sign to negative at about 1.2 T, indicating antiferromagnetic fluctuations.

The magnetic entropy at T_N is only about half the $R\ln 8$ expected for the 7/2 spin of Eu^{2+}. Extending far above T_N, the tail in the specific heat remains large and evidences that a substantial amount of entropy is carried by the magnetic fluctuations in this region, as shown by NMR. These strong magnetic fluctuations originate from the Dzyaloshinskii-Moriya (DM) interaction due to the absence of inversion symmetry in the crystal structure of EuPtSi, as described in section 1.3. Despite the absence of orbital moments in EuPtSi,

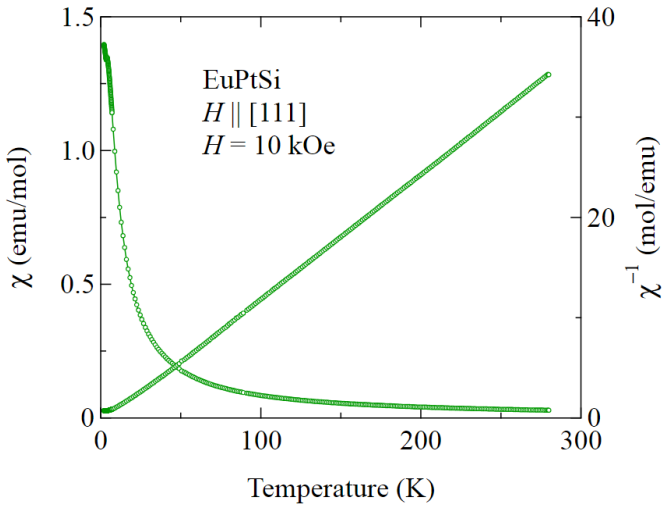

Figure 3.4: Susceptibility and inverse susceptibility for $H \parallel [111]$ as a function of temperature between 300 K and 2 K, from [39], emphasizing the low-temperature of the magnetic ordering and the positive Weiss temperature, leading to a FM-like coupling.

a DM interaction is still present because the Pt $5d$ states, which are subject to strong spin-orbit interaction, play a significant role in the RKKY exchange between Eu moments [35, 83]. The DM interaction is the source of the helimagnetism of EuPtSi.

Helimagnetic ground state and conical order

The multi-domain helical ordering ground state of EuPtSi is evidenced by single crystal neutron diffraction from Kaneko et *al.* [83] and resonant X-ray scattering from Tabata et *al.* [84]. Magnetic reflections at zero field and low temperature are described by the q-vectors $q_0 = (\pm\delta_1, \pm\delta_2, \pm\delta_3)$ with $\delta_1 = 0$, $\delta_2 = 0.2$ and $\delta_3 = 0.3$, as well as the cyclical permutations of q_0. Permutations of a vector $(\delta_3, \delta_2, \delta_1)$ have not been observed, emphasizing the symmetry of the crystal structure with a single-handedness chirality. Additionally, a first order commensurate-incommensurate 'lock-in' transition is observed in single crystal neutron diffraction at $T_N^* \approx 2.5$ K, with $\delta_1 \approx 0.04$ above T_N^* in the incommensurate region and $\delta_1 = 0$ below T_N^* [83]. However, this 'lock-in' transition relates to a very small change in entropy, hence this transition has not been detected in bulk or transport measurements.
From the q-vectors, the periodicity of the helix, or characteristic length in real-space can be calculated with $\xi = 2\pi/|q|$ where $|q| = 0.36(2\pi/a)$ and $a = 6.4336$ Å the cubic lattice parameter. The obtained value is ξ =18 Å, which is ten times smaller than the helical periodicity of MnSi, at 180 Å. This small value corresponds to only seven Eu^{2+} spins forming a period of an helix, schematically, indicating the strong coupling of the helical state to the underlying crystal lattice. The short period explains the strong AFM behavior of EuPtSi compared to the nearly FM behavior of MnSi in which neighboring moments are nearly collinear.

As is usual for compounds with a helimagnetic ground state, under an applied magnetic field, the magnetic ordering of EuPtSi may change to a conical order. Additionally,

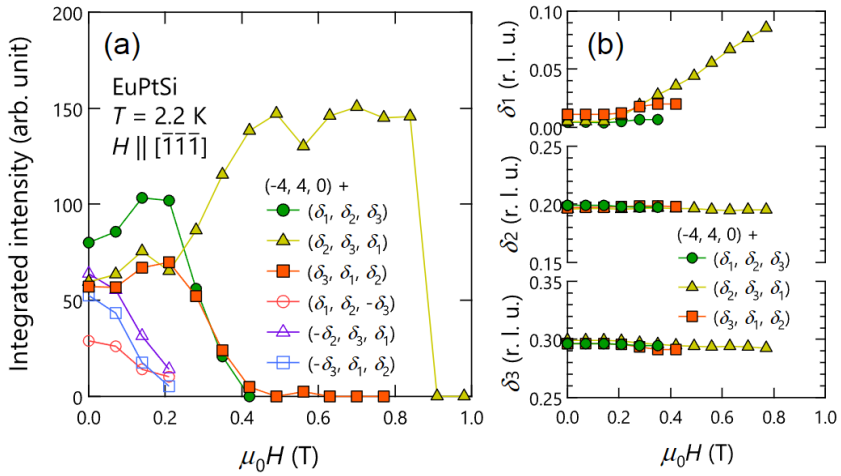

Figure 3.5: Field dependence of the resonant X-ray scattering (a) integrated intensity of the magnetic peaks of the q vectors $(\pm\delta_1, \pm\delta_2, \pm\delta_3)$, (b) the components δ_1, δ_2 and δ_3. The measurements are made at 2.2 K with $H \parallel [\bar{1}\bar{1}\bar{1}]$ between 0 and 1 T, from [84].

the multi-domain single-q structure turns to a single-domain single-q [84]. Under field, only the domains with the smallest angle between the helix pitch and the magnetic field direction are favored, thus only the helical vector q_H close to $\pm\mathbf{H}$ remains. This is shown in figure 3.5 with the field dependence of the integrated intensities of the propagation vectors for $H \parallel [\bar{1}\bar{1}\bar{1}]$ below 1 T, measured at 2 K. From the left panel, one can see that above 0.2 T, only three of the six q-vectors $q = (\pm\delta_1, \pm\delta_2, \pm\delta_3)$ are populated, and only one remains above 0.4 T.
The transition between the multi-domain and the single-domain regimes coincides with the helical-to-conical crossover in EuPtSi, at the transition hereafter referred to as H_D. In the conical region, the helix described by q_H, which was affixed to the lattice due to crystal symmetries, becomes unpinned and is expected to progressively align along the field direction. This is different from MnSi in which the helix pitch reorientation along the field direction in the conical order occurs swiftly. The right panel of figure 3.5 shows the field dependence of the components δ_i of the q-vectors. In the conical order, as the field increases, δ_1 increases and q_H tends to align along $H \parallel [\bar{1}\bar{1}\bar{1}]$. For EuPtSi, H_D is around 0.1 T near T_N and slightly increases for lower temperatures, reaching close to 0.5 T at 0.1 K. In the following results, we will assign the magnetic ordered phase for fields higher than the helical region as conical, for simplicity.

In addition to the reorientation of the helix along the field, for increasing field strength, the DM interaction is suppressed and the magnetic moments align along the magnetic field as well, as described in section 1.3.1, until the transition H_C to the paramagnetic state. The H_C transition for EuPtSi happens at around 2.5 T at low temperatures.

Skyrmion lattice A-phase

Like MnSi, for the $H \parallel [111]$ direction EuPtSi exhibits a skyrmion lattice phase located at the border of the PM region, enclosed in the conical phase between the fields H_{A1} and H_{A2}. It was dubbed the A-phase with reminiscence to MnSi by Kakihana et *al.* who observed it in magnetization M, resistivity ρ and Hall effect ρ_H measurements. The latter

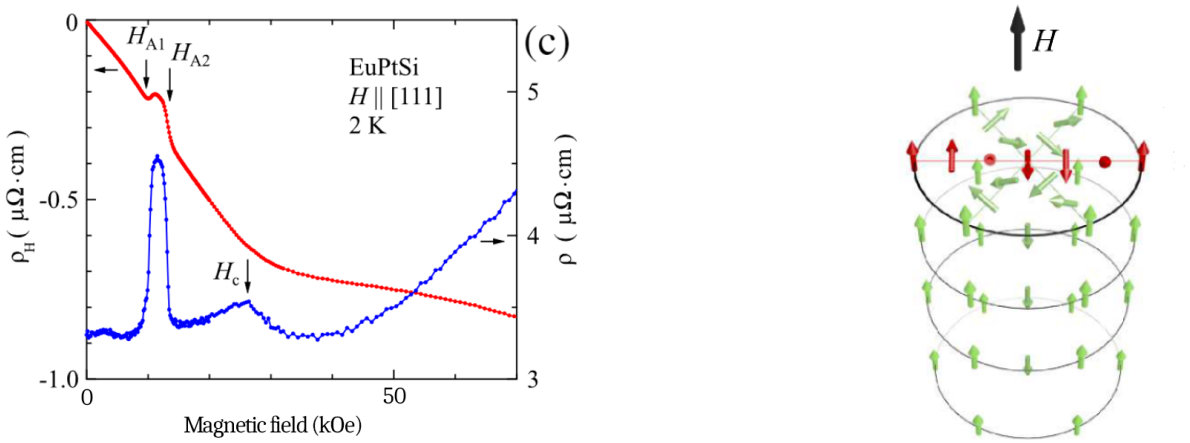

Figure 3.6: Left: Hall resistivity (red) and magnetoresistance (blue) for $H \parallel [111]$ at T=2 K, with current $J \parallel [11\bar{2}]$ from [3]. Right: schematic representation of the triple-q ordering perpendicular to the field H, from [39]. A single-q helix is shown in red for clarity.

two are shown in the left panel of figure 3.6, from [3]. In the Hall effect, the anomalous peak structure of the A-phase is not accurately described by the usual $\rho_H = R_0 H + R_S M$ relation, with the first term being the ordinary term and the second the so-called anomalous term proportional to the magnetization. As such the topological Hall effect was proposed to describe the A-phase, in a fashion similar to MnSi. In MnSi the A-phase exists between 0.1 and 0.2 T and extends over a temperature range of 1 K, between 28 and 29 K, see figure 3.7 (right). In contrast, the $H-T$ phase diagram of EuPtSi for the $H \parallel [111]$ direction extends over a much larger range, both in field and in temperature, with evidences of the A-phase as low as 0.45 K, between 0.75 and 1.4 T. The EuPtSi and MnSi phase diagrams are shown in figure 3.7, from [4] and [49].

The A-phase in EuPtSi is described by the triple-q order with $q_1 = (-0.29, 0.09, 0.20)$, $q_2 = (-0.20, 0.29, -0.09)$ and $q_3 = (0.09, 0.20, -0.29)$, schematically represented on the right panel of 3.6, from [39]. The results are confirmed from both neutron and resonant X-ray scattering [83, 84]. The triple-q structure forms a hexagonal lattice of skyrmions in the plane orthogonal to the magnetic field direction, with a modulation period of 17.8 Å in agreement with the helical q-vector periodicity.

Anisotropic phase diagram

An additional difference between MnSi and EuPtSi comes from the anisotropy of the $H-T$ phase diagram. In MnSi, the A-phase SkL is found to exist in the whole field region whereas for EuPtSi the magnetic phase diagram is highly anisotropic. For the $H \parallel [111]$ direction which lies along the body diagonal of the cubic structure, the A-phase has already been presented, see figure 3.7 (left). For the hard-magnetization axis $H \parallel [100]$, on the other hand, two different phases dubbed A' and B are observed with very close resemblance to the A-phase. The phase diagram for the $H \parallel [100]$ direction is shown in figure 3.8, from [4]. For the easy-magnetization axis $H \parallel [110]$, however, the system remains in the helical/conical state below T_N.

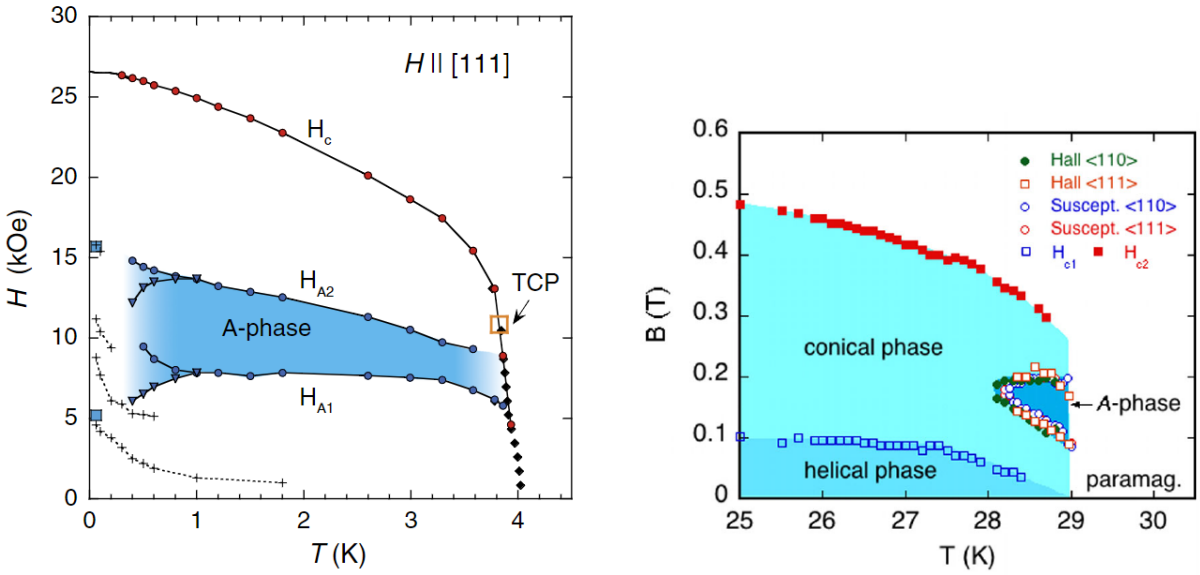

Figure 3.7: Left: $H-T$ phase diagram for EuPtSi $H \parallel [111]$ from magnetization measurements. TCP indicates the tricritical point. The conical ordering lies below H_C and in the unshaded region around the colored A-phase. From [4]. Right: $H-T$ phase diagram for MnSi from [49].

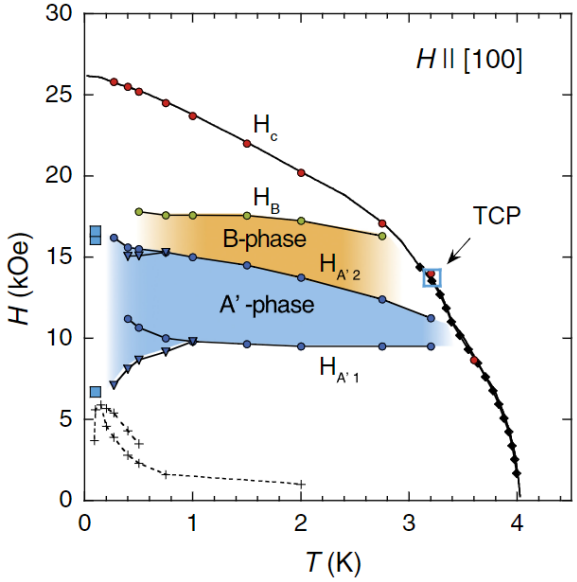

Figure 3.8: $H-T$ phase diagram for the $H \parallel [100]$ direction obtained by magnetization measurements, with the colored A'- and B-phases. TCP indicates the tricritical point. From [4].

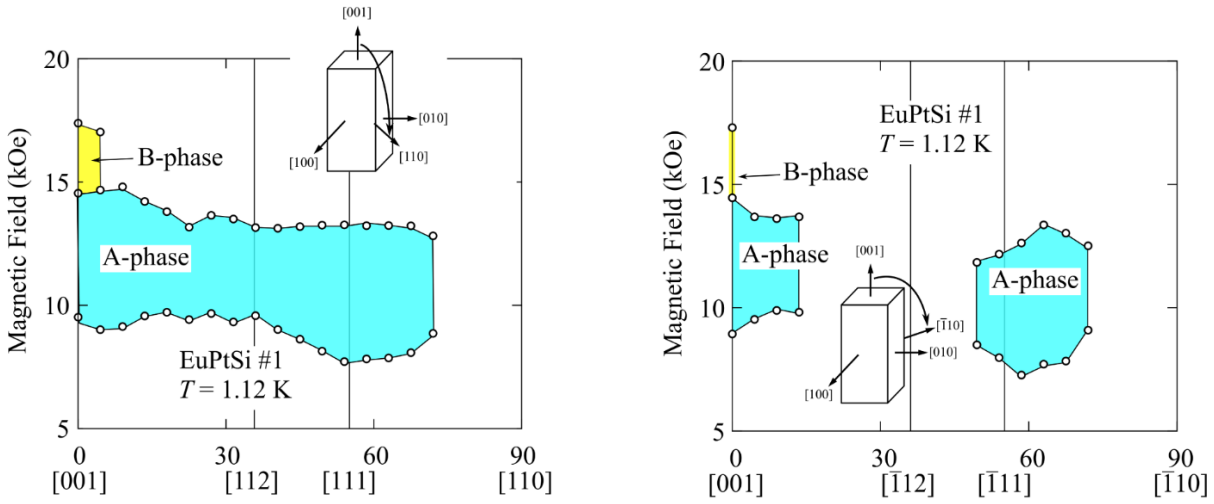

Figure 3.9: Angular dependence of the A and B phases for magnetic fields rotated as per the schematics, [001]→[110] (left) and [001]→[$\bar{1}$10] (right). From [5].

The anisotropy of the $H-T$ phase diagram of EuPtSi has been confirmed through resistivity [85] and ac susceptibility [5] (shown in figure 3.9 at 1.12 K) measurements. The A-phase is found to exist in a 20° range around the [$\bar{1}$11] direction, whereas a rotation from the [111] to the [001] direction shows the presence of the A-phase for all angles. As such, no phase line has been observed between the A-phase and the A' phase for $H \parallel [001]$ as of yet. The B-phase is only observed for a few degrees along $H \parallel [001]$. The magnetic phase diagram for this direction is shown in figure 3.8, from [4]. The angular dependence of the $H-T$ phase diagram will be presented in more detail along with our own results in section 3.2.1.

This strong anisotropy contrasts heavily with MnSi and might be due to the small skyrmion size, hence a strong coupling of the SkL with the crystal lattice. The Eu atoms forming an individual skyrmion are arranged in a complicated structure, which might not correspond to a lower energy state than the conical ordering for some directions, like $H \parallel [110]$ [39]. By contrast, in MnSi with the very large skyrmions, the crystal lattice is considered continuous, and any direction can be considered for the formation of the SkL. The q-vectors of the zero-field helical order are threefold symmetric around the [111] axis and twofold symmetric around [100]. The vector (0.2,-0.3,0) and its cyclical permutation are nearly perpendicular to [111] and very close to the triple-q vectors of the A-phase. As such, the SkL phase is easily formed for this direction. For the [100] axis, four q vectors are perpendicular to the field direction, which could explain the formation of the A'- and B-phases. The [110] direction is, however, far from the symmetry axis, leading to no SkL phase. Due to the RKKY magnetic interaction, the anisotropy in EuPtSi is also determined by the anisotropy of the Fermi surface, which will be detailed in chapter 4.

Motivation for this thesis

The work presented in this thesis aims to deepen the understanding of EuPtSi through precise low temperature measurements as functions of T, H and angle of the resistivity,

Hall effect, as well as thermoelectric power and thermal conductivity. By using a dilution refrigerator and a low-noise measurement setup, we have investigated the three main axes [110], [111] and [100], shedding new light on the anomalous behavior of the A, A' and B phases. The resistivity measurements allow us to probe the various phases at low-temperature (down to 90 mK). The Hall resistivity measurements confirm the topological Hall effect in the three skyrmion or skyrmion-related phases. Finally the thermoelectric power and thermal conductivity measurements, which have never been performed in this system, evidence the presence of new energy scales at high field in addition to the low field ($H < H_C$) features.

3.1.2 Sample characterization

All the samples used in this work were provided by the laboratory of Y. Ōnuki (University of the Ryukyus, Okinawa, Japan) and were cut by D. Aoki (Tohoku University, Oarai, Japan). The single crystals were grown by the Bridgman method using Mo crucibles as described in ref. [3, 79]. The starting compound PtSi is arc-melted, and Eu and crashed pieces of PtSi with 1.2:1 composition are sealed in Mo-crucibles. This mixture is then heated up to 1480°C in Ar gas atmosphere before slow cooling to room temperature.

The samples are thin slabs with rectangular shapes. For most of this work (with the exception of the angular dependent measurements), the field is oriented orthogonal to the large flat face. The electrical current (for resistivity and Hall effect measurements) or temperature gradient (for thermal conductivity and thermoelectric coefficients measurements) are applied along the length of the sample, i.e. perpendicular to the magnetic field. A schematics is shown in chapter 2, and a picture of a sample contacted for resistivity measurements can be found in figure 2.4. We have measured the electrical resistivity between 300 K and 2 K in a Physical Property Measurement System (PPMS). These measurements are completed by data obtained in a dilution refrigerator down to 50-90 mK to recover the residual resistivity ratio RRR$=\frac{\rho_{300K}}{\rho_0}$ with ρ_0 being the resistivity extrapolated to zero kelvin. The zero-field cooling measurements of $\rho(T)$ for three samples are shown in figure 3.10. The samples are named after the direction orthogonal to the large flat face i.e. the orientation of the applied magnetic field. The inset shows a close-up of the low temperature (< 5.5 K) zero-field cooling for the $H \parallel [111]$ sample #2, obtained in the dilution refrigerator setup down to 90 mK.

The samples are presented in table 3.2 with the corresponding crystal orientations, current direction, RRR and demagnetizing coefficient (detailed in the next section). For some samples, the RRR has not been determined. This can happen when a sample breaks for example. The RRR is an indication of sample quality for a metal, with a high RRR indicating a high quality or purity. This can be seen in chapter 4 as only the sample with the best RRR ([100] #2) features quantum oscillations in the resistivity (Shubnikov-de Haas effect). Unless specified otherwise, the experimental results presented hereafter are obtained with samples [110]#1, [111]#2 and [100]#2.

$H \parallel$	Sample	$J \parallel$	RRR	N
[110]	# 1	[100]	-	0.787
[111]	# 1	[$\bar{1}$01]	-	0.812
[111]	# 2	[$\bar{1}\bar{1}$2]	24	0.920
[100]	# 1	[011]	-	0.817
[100]	# 2	[011]	32	0.851
[100]	# 3	[001]	12	0.797

Table 3.2: Samples of EuPtSi, labeled after the field direction. Columns are: direction of the current J, residual resistivity ratio RRR and demagnetizing coefficient N.

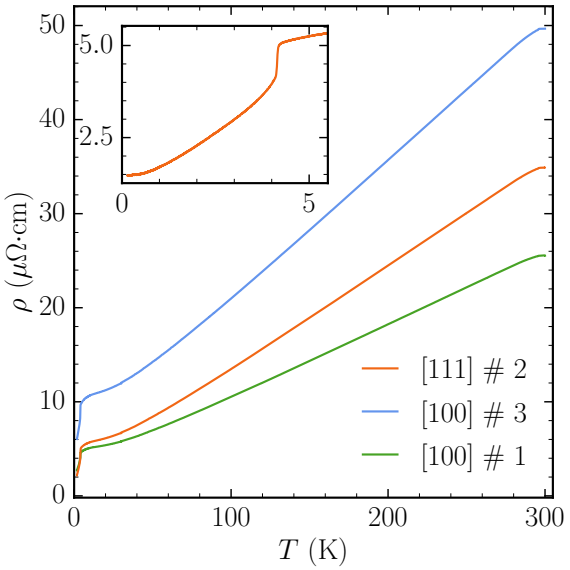

Figure 3.10: $\rho(T)$ measurements between 300 K and 2 K for three samples, under zero-field cooled conditions in the PPMS. Inset: $\rho(T)$ between 5.5 K and 90 mK for the [111] #2 sample in a dilution setup.

3.1.3 Demagnetizing field correction

EuPtSi orders helimagnetically below $T_N = 4.05$ K. For $T<T_N$, under applied magnetic field H_{app}, the magnetization M increases near-linearly until H_C where it saturates. The increase of $M(H)$ corresponds to the canting of the spins under applied magnetic field. The spins are fully oriented along the field direction at H_C, entering the field-polarized paramagnetic state. The magnetization measurements at various temperatures for $H \parallel$ [100] are shown in the left panel figure 3.11. At $T = 2$ K, $H_{C,\text{app}} = 3.2$ T and M saturates at a value of $M_{\text{sat}} \approx 7\ \mu_B$/Eu. As temperature increases, the saturation transition becomes less sharp. The measurements were performed in a SQUID device (MPMS by Quantum Design) and are limited to $H_{\text{app}} = 5$ T and $T > 2$ K. It is to be noted that from these measurements, the A- and B-phases are difficult to determine. To ensure that the saturation is reached, we have performed magnetization measurements up to 16 T in a Faraday balance system, as described in section 2.3. For the Faraday balance, torque effects also induce a displacement of the platform and so the samples should only be measured along their easy magnetization axis to avoid any confusion. The right panel of figure 3.11 thus corresponds to the [110] direction. It is to be noted that above 4-5 T, the field dependence of the magnetization has been reported to be isotropic [4]. The saturation value M_{sat} is thus the same for all orientations. M_{sat} is represented as a dotted line in the right panel of the figure. We can note that for all temperatures, 90% of the saturation magnetization is reached at 7 T. Because the value $M_{\text{sat}} = 7\ \mu_B/f.u.$ is large, the effective magnetic field H differs from the applied magnetic field H_{app} by a demagnetizing factor, taking into

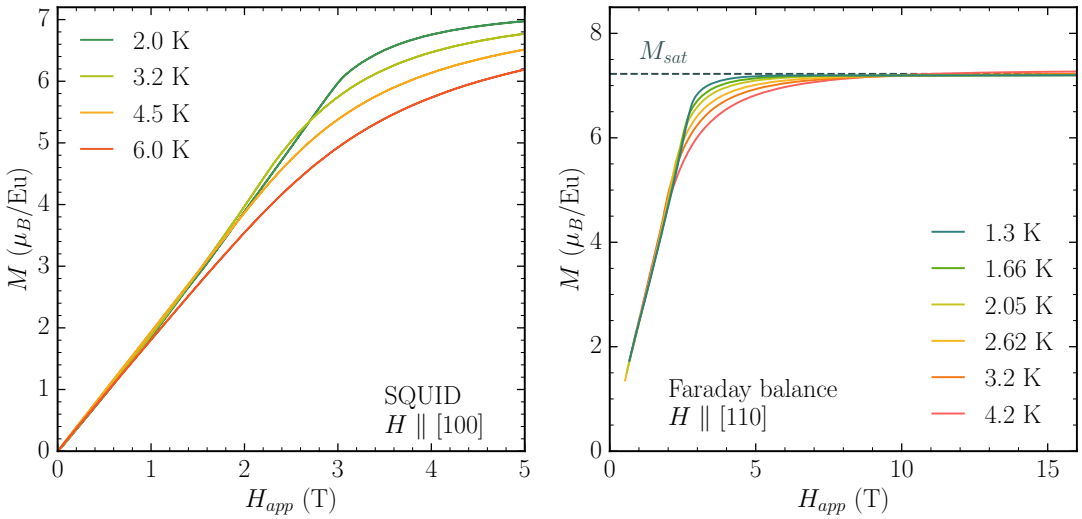

Figure 3.11: Left: $M(H)$ between 2 and 6 K for an applied field H_{app} up to 5 T along the [100] direction, measured in a SQUID device. Right: $M(H)$ measured with a Faraday balance up to $H_{\text{app}} = 16$ T along the [110] direction. The dotted line indicates the saturation magnetization M_{sat}.

account the internal field. The effective field[1] is given by

$$H = H_{\text{app}} - NM \tag{3.1}$$

with N the demagnetizing coefficient. This coefficient depends only on the geometry or shape of the sample. For an infinitely large thin film in the xy-plane with $\vec{H} \parallel \vec{z}$, $N_z = 1$, $N_x = N_y = 0$. For a sphere $N = \frac{1}{3}$. For a parallelepipedic sample, a formula for approximating the demagnetizing coefficient is

$$N \approx \frac{4ab}{4ab + 3c(a+b)} \tag{3.2}$$

with sample dimensions $2a \times 2b \times 2c$ for $H_{\text{app}} \parallel c$, supposing a uniform field inside the sample [86]. For the samples used in this work, this gives values of N between 0.8 and 0.9 for each sample described in section 3.1.2. By comparing the low-temperature phase diagram obtained for a given direction with the literature, we have empirically determined the N coefficient value of a few samples, which are in good agreement with the values obtained with equation 3.2. From equation 3.1 using the magnetization measurements previously shown, we can re-normalize the magnetic field. The temperature variation of M has been shown to have very little impact on the correction, and we have used the 2 K SQUID curve, extrapolated up to 16 T along the Faraday balance measurements.

The correction is shown in figure 3.12 as a function of the applied magnetic field for different values of the demagnetizing coefficient N. H_{app} corresponds to the uncorrected field, i.e. N=0, a linear dependence with a slope of 1. The corrected field H re-normalized by the magnetization separates from the uncorrected one linearly until ≈ 3.2 T where

[1] Strictly speaking, the *magnetic flux density* in tesla is $B = \mu_0(H_{\text{app}} + (1-N)M) = \mu_0(H+M)$, and the *magnetic field strength* H is in amperes per meter. For the sake of convenience, we will be ignoring the vacuum permeability $\mu_0 = 4\pi \times 10^{-7}$ Tm/A, therefore referring to H from eq. 3.1 in tesla.

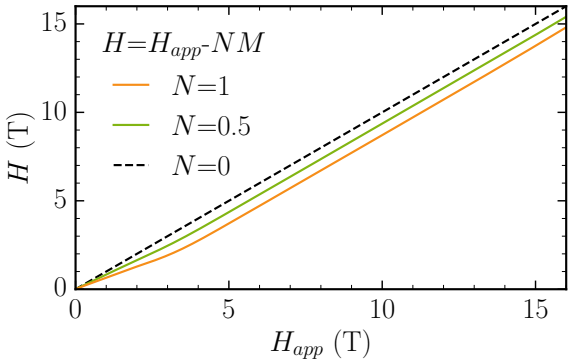

Figure 3.12: Comparison between the applied field H_{app} and the corrected field H for different values of the demagnetizing coefficient N up to 16 T.

the magnetization saturates. At $\approx$ 3.2 T, the correction represents $\approx$ 30% of the field amplitude, making the correction non-negligible. For fields corresponding to a mostly saturated magnetization, i.e. $H > 4$ T, the correction is constant. With the experimental setup used most in this work with an applied field up to 16 T and $N \approx 0.9$ for all samples, the effective field is thus limited to around 15 T. The rest of this work will subsequently refer to the corrected magnetic field as H in teslas.

3.2 Field-dependent measurements on EuPtSi

In this section, we will discuss the field-dependent measurements. The angular dependence of the magnetic phase diagram at 1.75 K in resistivity ρ is first presented, before the results for the three main directions using ρ, the Seebeck coefficient S, the Nernst coefficient N, the thermal conductivity κ and the Hall resistivity ρ_H between 0.1 and 6 K, for fields up to 15 T.

3.2.1 Angular dependence of EuPtSi

Unlike MnSi and other $B20$ compounds, the $H-T$ phase diagram of EuPtSi is strongly anisotropic, as discussed in section 3.1.1. For MnSi, the skyrmion lattice A-phase exists in the middle of the conical order below T_N irrespectively of the magnetic field orientation only in a small temperature range of about 1 K below T_C. In contrast, for EuPtSi the A-phase exists only around [111], [$\bar{1}$11] and equivalent directions. The [100] direction presents two different phases A' and B. The [110] direction does not show such phases at low temperatures. To clarify the angular dependence of EuPtSi, we have measured the field-dependence of the resistivity ρ for two samples in a PPMS with a rotation setup.
Given the symmetries of the crystal structure, it is important to note that the directions [100], [010] and [001] are equivalent, as they are produced by three-fold rotational symmetries along the body diagonals. The lack of four-fold symmetry along the main crystallographic axes, however, forces a distinction between the body diagonals. The directions [111], [$\bar{1}\bar{1}$1] and [$\bar{1}$1$\bar{1}$], for example, are equivalent, but are not equivalent to [$\bar{1}$11], [11$\bar{1}$] and [1$\bar{1}$1]. Similarly, [110] is equivalent to [$\bar{1}\bar{1}$0] and not to [1$\bar{1}$0]. This is a direct consequence of the low symmetry of the crystal structure. With these equivalences in

mind, the angular measurements subsequently presented have been labeled accordingly and in a manner convenient for visual representation. It is important to note that from resistivity measurements, directions such as [111] and [$\bar{1}$11], that are not equivalent, are not discernible without the angular dependence.

The angular dependence of $\rho(H)$ at 1.75 K is shown in figure 3.13 (a), for applied fields up to 5 T. All data shown here are for continuous increasing positive field sweeps. Between each measurement at 1.75 K, we have heated the sample to 5 K, above T_N, to ensure the zero-field cooling condition was maintained for the whole process. The measurements are made with the sample [111]#2, with 0 degrees corresponding to $H \parallel$ [111]. The current is applied along the [$\bar{1}\bar{1}$2] direction, corresponding to the length of the sample. The axis of rotation is the [$\bar{1}$10] direction. The rotation sequence is schematically represented in figure (b) by a dashed blue arrow ⓐ, along with the main crystallographic directions. Figure 3.13 (c) shows the angular phase diagram taken from the measurements in (a).
For all angles, at zero field, the system is in the helical state until the transition H_D that occurs around 0.1 T for all angles. Between H_D and H_C, the system is supposedly in the conical order with the single domain single-q. Above H_C, the moments are mostly oriented along the applied magnetic field direction and the system is in a field-polarized paramagnetic state.
The A-phase visibly exists from $\approx$ -3° to $\approx$ 15° around the $H \parallel$ [111] direction. In the A-phase, the resistivity is strongly enhanced from the additional scattering due to the skyrmion lattice. We have determined the best alignment of the sample with $\theta = 0°$ corresponding to the highest value of the transition H_C, but a misalignment of a few degrees can not be excluded as only a one-axis rotator is used. Because the demagnetizing field correction depends on the sample geometry, which itself depends on the angle of the sample, we show the resistivity as a function of the applied (uncorrected) field.
As EuPtSi has a cubic structure, body diagonals on opposite sides of a face are equivalent and separated by 109.4°, which explains the presence of the A-phase at 95° and higher. For these large angles, the field is applied mostly along the current direction and the skyrmion lattice phase corresponds to a decrease in resistivity, which is coherent with the measurements from Takeuchi et *al.* [85]. This is explained by the relative angle between the q-vectors of the ordered phases and the current direction. Since the population of the different domains of the q-vectors changes along the field direction above H_D, the variation of angle between the field and the current changes the sign of the resistivity signal in the ordered phases [87].
For angles between 45° and 58°, $\rho(H)$ shows the opening of two phases. For $45 < \theta < 50°$, the two phases are positive bumps in resistivity. For $50 < \theta < 58°$ the lower-field phase turns negative, and the higher-field phase disappears at $\theta > 58°$. These two phases are the A'- and B-phase around the $H \parallel$ [001] direction.
So far, we have only discussed figure 3.13 (a) and (c) with respect to the main crystallographic directions. As is evident from the colored arrows and dots, transitions corresponding to the A-phase have actually been observed for the entire continuous range of angles. For all the angles that have not been mentioned above, however, the transitions are very small and not visible without zooming. The isotropic A-phase shows up as a rounded bump with an amplitude reaching values as small as 0.01 $\mu\Omega$·cm above the conical signal background for $\theta = 32°$. This value is only about 3 times bigger than the noise

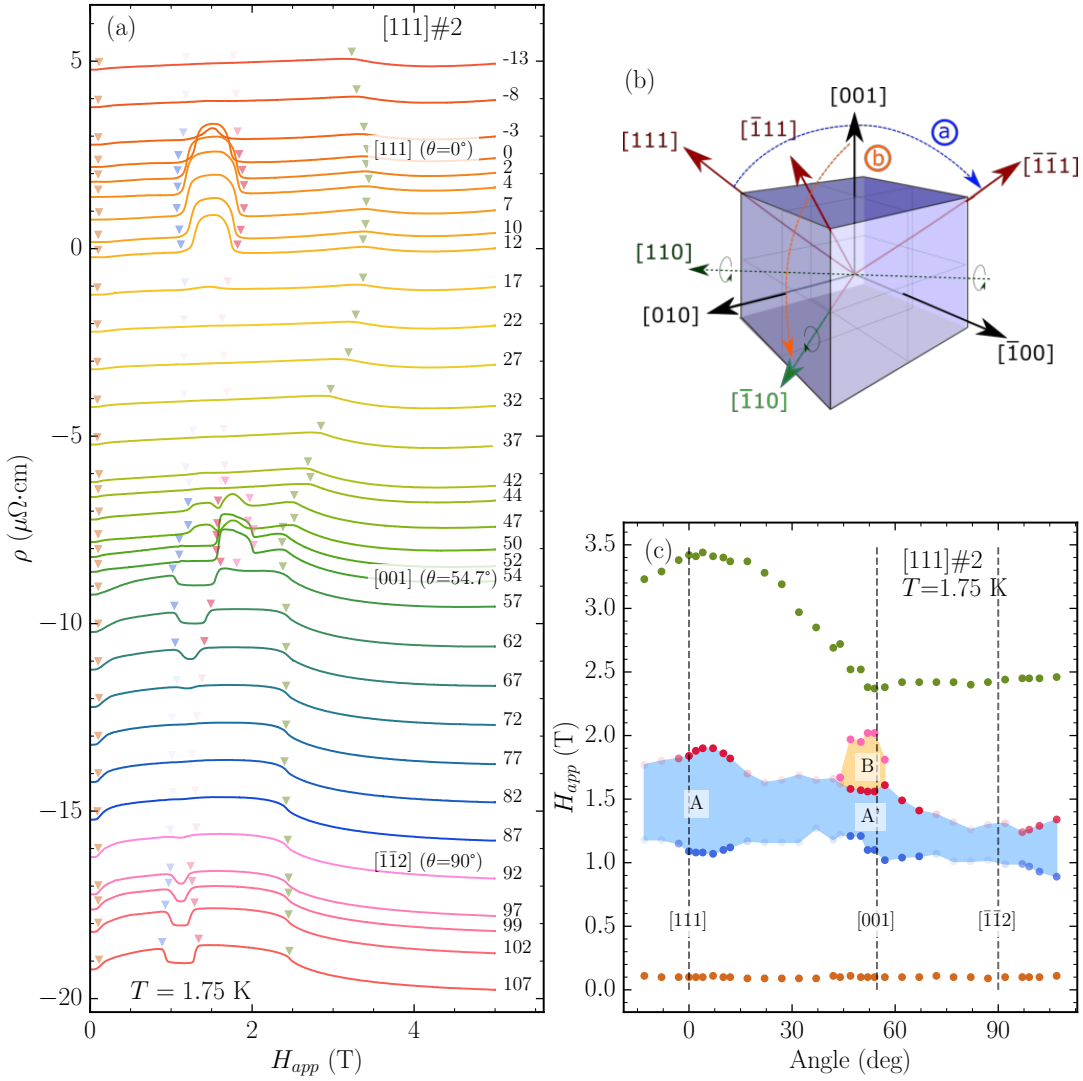

Figure 3.13: (a): $\rho(\theta)$ for applied fields up to 5 T between $H \parallel [111]$ ($\theta = 0°$) and $H \parallel [\bar{1}\bar{1}2]$ ($\theta = 90°$). Data are shifted vertically proportionally to the angle by -0.2 $\mu\Omega$·cm. Colored triangles indicate the respective transitions from which the angular phase diagram in (c) is determined, with H_D (brown), H_{A1} (blue), H_{A2} (red), H_B (pink) and H_C (green) in order of increasing field. (b): simplified cubic cell indicating the principal direction. The blue arrow is the rotation ⓐ performed in (a). Red arrows are the directions evidenced in (a). The orange arrow is the rotation sequence ⓑ from figure 3.14. (c): angular phase diagram from the $\rho(\theta)$ measurements. Colored transition fields correspond to the arrows in (a). Color strength of the transition markers correlate to the size of the anomaly in the ρ data.

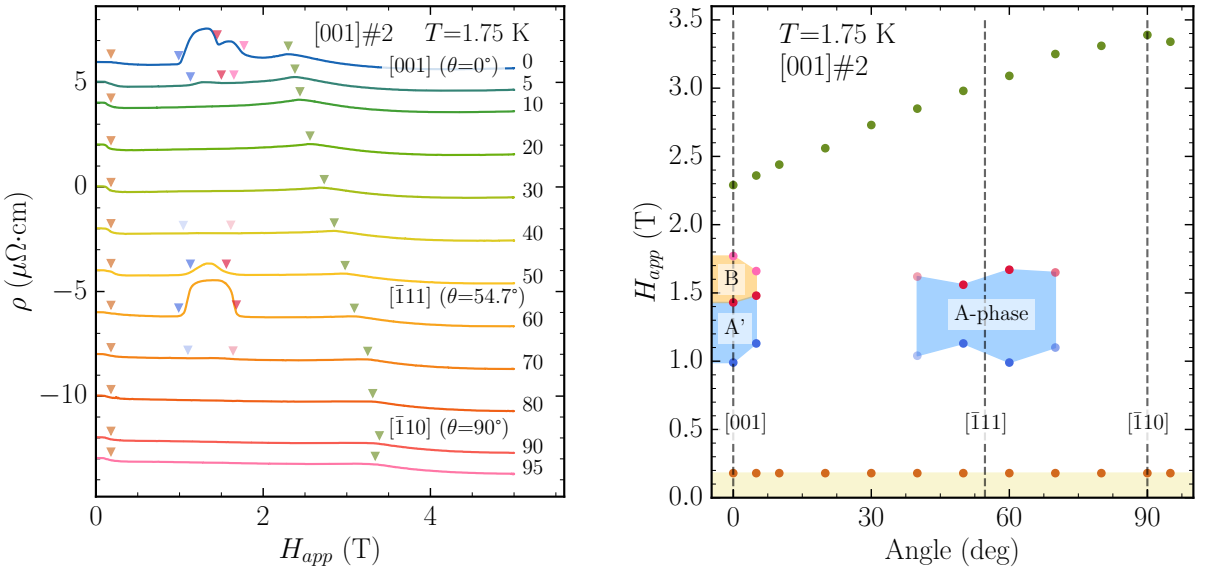

Figure 3.14: Left: $\rho(\theta)$ up to 5 T between $H \parallel [001]$ ($\theta = 0°$) and $H \parallel [\bar{1}10]$ ($\theta = 90°$), following the rotation ⓑ from schematics 3.13(b). The rotation axis is [110]. The data is shifted vertically by -0.2 $\mu\Omega$·cm per degree. Right: corresponding angular phase diagram with colored A-, A'- and B-phases. Transitions are indicated as triangles on the left and circles on the right, with H_D (brown), H_{A1} (blue), H_{A2} (red), H_B (pink) and H_C (green) in order of increasing field.

level of the measurement setup. For comparison, at the $\theta = 4°$ direction, the amplitude of the A-phase is 1.2 $\mu\Omega$·cm. A comparison between the $\theta = 4°$ data (with the largest anomaly between H_{A1} and H_{A2}) and the $\theta = 32°$ data (with the smallest anomaly) is shown in appendix A. The transition fields are thus indicated in figures (a) and (c) with the color strength of the arrows/dots reflecting the height of the transitions. For this specific rotation, the A-phase and the A'-phase are therefore connected and exist in a wide angle range as no phase line has been observed between these two phases.

The second angular dependence, performed on the sample with the large flat face corresponding to the [100] direction #2, is presented in figure 3.14 with the same protocol as the previous measurement. Because the [100] and the [001] are equivalent, for the purpose of this section the directions have been labeled following the schematics 3.13(b), in which this rotation is ⓑ in orange, with the rotation axis being [110] which is also the direction of the current. The current is thus always applied perpendicular to the field. For this rotation [001] → [$\bar{1}$10], the $H \parallel [\bar{1}11]$ direction corresponds to an angle $\theta = 54.7°$. The A-phase is only observed for $40 < \theta < 70°$ and is not connected to the A'-phase found for $\theta < 10°$. The B-phase is observed only within a 5° angular range of the $H \parallel [001]$ direction.
Due to the particular symmetries and chirality of the crystal structure of EuPtSi, the A- and A'-phases appear to be continuously connected for certain axes, and different for others. Future microscopic experiments have to determine the magnetic structure. In the rest of this work, as we study the low-temperature transport properties of EuPtSi with fixed angle, the denomination A-phase will be used for the [111] direction, and A'-phase

for the [100] direction where the B-phase also exists.

3.2.2 Results for $H \parallel [110]$

We have seen in the previous section that the A-phase and the A'- and B-phases lie in the $H \parallel [111]$ and $H \parallel [100]$ directions respectively. The $H \parallel [110]$ direction, on the other hand, does not present similar features. As such, while the $H \parallel [110]$ direction might not be as exciting as the other two, it presents the opportunity to study the system in the helical/conical order. By comparing the [110] direction with the others, it can be used as a sort of background to understand how the exotic magnetic orders impact the system. With this idea in mind, we have studied the $H \parallel [110]$ direction of EuPtSi with an array of different probes at various temperatures and under magnetic field.

Resistivity measurements

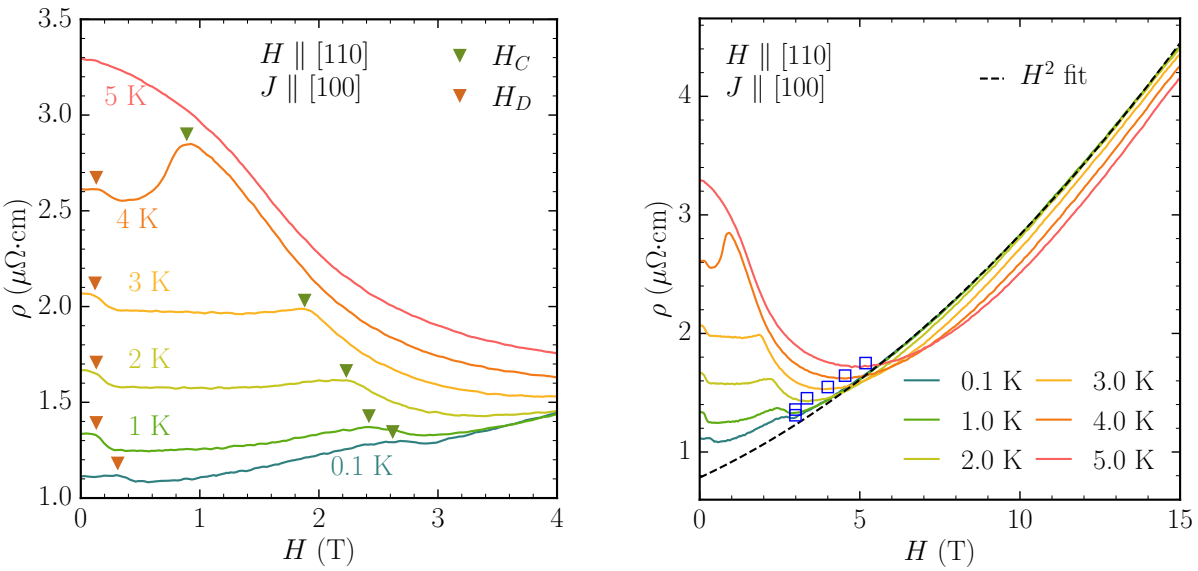

Figure 3.15: Resistivity as a function of magnetic field for temperatures between 0.1 and 5 K up to 4 T (left) and 15 T (right). Transitions H_D (brown) and H_C (green) are indicated as arrows on the left graph. The black dotted curve on the right is a $\rho \propto H^2$ fit on the 1 K data and the blue squares indicate the minimum of the curves due to the cross-over.

The field dependence of the resistivity for EuPtSi $H \parallel [110]$ is presented in figure 3.15 for temperatures between 0.1 and 5 K, $H < 4$ T (left graph) and $H < 15$ T (right graph). The measurement is performed with current $I = 0.5$ mA with $J \parallel [100]$. Above $T_N = 4.05$ K in the paramagnetic state, the magnetoresistance is negative up to 4 T. Below T_N the system is in the helical order at zero field. Under applied field, a transition H_D from the multi-domain helical state into the single-domain conical state is observed around 0.1 T as a step with a slight decrease in resistivity. In the conical state, $\rho(H)$ remains almost constant or increases slightly at low temperature until the transition H_C between the conical order and the paramagnetic state occurs. H_C appears as an abrupt

shoulder-like change of slope that goes to lower fields as the temperature is increased. Finally, H_C reaches 0 T for $T_N = 4.1$ K.
From sweeps in the low-field region, we can see that the magnetic field reduces ρ. The magnetoresistance is negative in the low-field region below $H = 3$ T at 2 K and below 4 T at 5 K. This is a strong contrast from the conventional magnetoresistance expected in compensated metals [88]. Only above $H = 3 - 5$ T the magnetoresistance increases quadratically with magnetic field, recovering the usual behavior of a compensated metal with only closed orbits. In this high-field region, shown in the right panel of figure 3.15, the resistivity increases in H^2 for all temperatures, reaching a similar value close to 4.5 $\mu\Omega$·cm at 15 T. This is also true for the $H \parallel [111]$ and [100] directions presented in the next sections. The full curves at all temperatures measured are available in appendix A.

Close to the ordering transition field at low temperatures, the field suppresses the magnetic fluctuations, reducing ρ in that region. As T and H increase, the transition between the suppressed ρ regime and the quadratic increase regime gets a broad crossover, as shown from the magnetization measurements in section 3.1.3. The cross-over between the two regimes is indicated by a blue square. The criterion chosen is the minimum of the $\rho(H)$ data in this region. At higher temperatures ($T > 5$ K, not shown here), the negative magnetoresistance behavior decreases as the system is progressively further away from the ordering temperature. A similar behavior of magneto-resistance suppression at low field has been observed in MnSi [89] and comes from magnetic fluctuations dominating the resistivity close to the transition, which in MnSi is in the vicinity of $T_N = 29$ K. In the conical state, as the applied field increases, the progressive canting of the moments towards a ferromagnetic-like ordering leads to a reduction in spin fluctuations scattering the conduction electrons. The suppression of the spin-fluctuations has been evidenced by NMR measurements under magnetic field [82]. At higher fields, the cyclotron motion of the conduction electrons causes the enhancement of scattering proportional to H^2, and the temperature variation of ρ becomes very small while the Eu $4f$ electrons are fully localized.
Figure 3.16 shows the temperature dependence $\rho(T)$ for fields between 0 and 3 T (left panel) at low temperature, and for fields up to 15 T (right panel). Dots in the left panel indicate points taken for decreasing temperatures and lines for increasing temperatures. No hysteretic behavior is observed between the two. Increasing T-steps only are shown in the right panel. The transition T_N (corresponding to H_C for $\rho(H)$) is seen as an abrupt decrease below 4.05 K. The strong slope below T_N is a feature of the first-order nature of the transition. The hysteresis of the transition at zero field is not observed here but is clearly visible in specific heat measurements [79]. The transition temperature decreases under field and is not visible above 2.6 T. In the helical state below 3.5 K at zero field, the resistivity scales as $\rho(T) \propto T^{1.65}$. A similar power law T^n with $1.65 < n < 1.91$ is observed for all fields in the conical order ($H < H_C \approx 2.6$ T), n increasing with increasing field. This is emphasized in figure 3.17 where $\rho(T^2)$ is shown with the same data as the previous figure. All curves are shifted with $\rho(T = 0.1\text{ K}) = 0$. This contrasts from the typical $n = 2$ metallic ground-state behavior. This anomalous behavior is reminiscent of the non-Fermi liquid (NFL) phase in MnSi in which ρ scales as $T^{3/2}$ above its critical pressure [50, 51]. The reason for this unconventional behavior is not yet well understood and does not follow the expected behavior of a FM or AFM metal with dominant electron-magnon scattering.

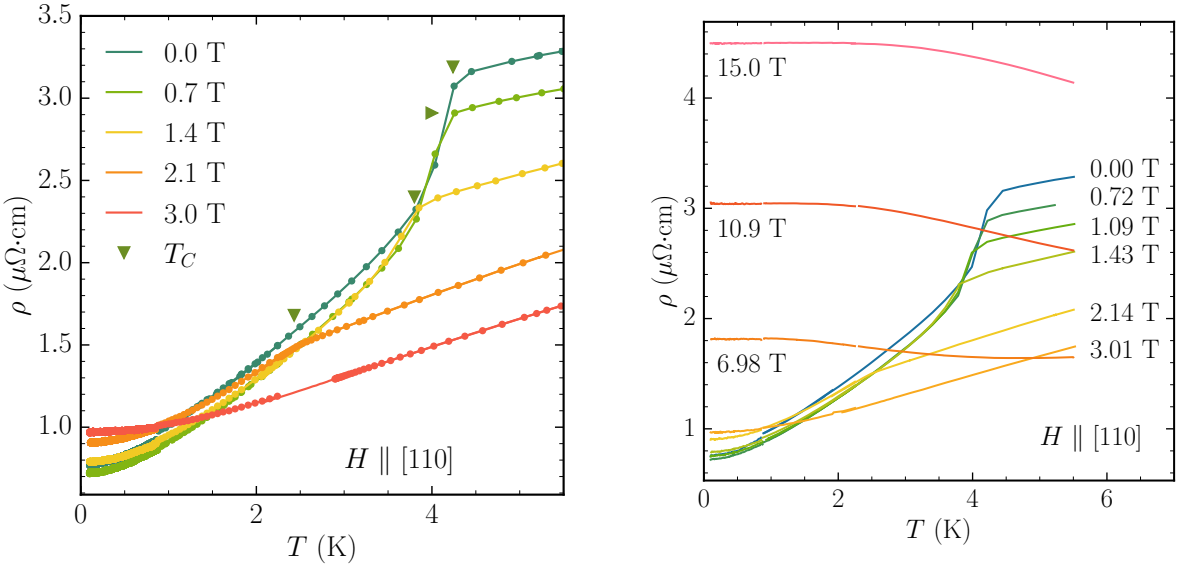

Figure 3.16: Temperature dependence of ρ for fields $H \parallel [110]$ between 0 and 3 T (left) and between 0 and 15 T (right), up to 5.5 K. Green arrows on the left panel indicate the $T_C \equiv H_C$ conical/PM transition. At 0 T, $T_C = T_N = 4.1$ K.

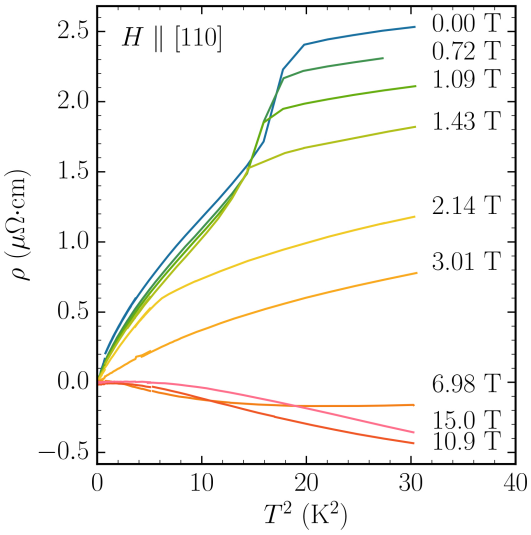

Figure 3.17: Temperature dependence of the resistivity as a function of T^2 for fields up to 15 T in the $H \parallel [110]$ direction, between 0.1 and 5.5 K. Curves are shifted vertically with $\rho(T = 0.1 \text{ K}) = 0$. Note the crossings of the 6.98, 10.9 and 15 T curves.

For MnSi, the NFL phase is observed for pressures $P > 14.6$ kbar. For this pressure, the long-range magnetic ordering is suppressed with T_N reaching 0 K, and the NFL behavior has been measured between 30 mK and 6 K [54, 53]. Observations of the topological Hall effect in MnSi under pressure supports a connection between the skyrmion lattice and the NFL state. In EuPtSi, as the field increases and the spin fluctuation scattering diminishes, $\rho(T)$ becomes flatter in the low temperature region (< 2 K), eventually becoming mostly constant for $H > 4$ T. For higher fields and temperatures, as shown on the right panel of figure 3.16 and figure 3.17, $\rho(T)$ decreases. The temperature dependence at high magnetic fields clearly indicates that it is dominated by the cyclotron motion of the electrons, as $\rho(T)$ decreases with increasing temperature and a H^2 field dependence is observed, as described previously.

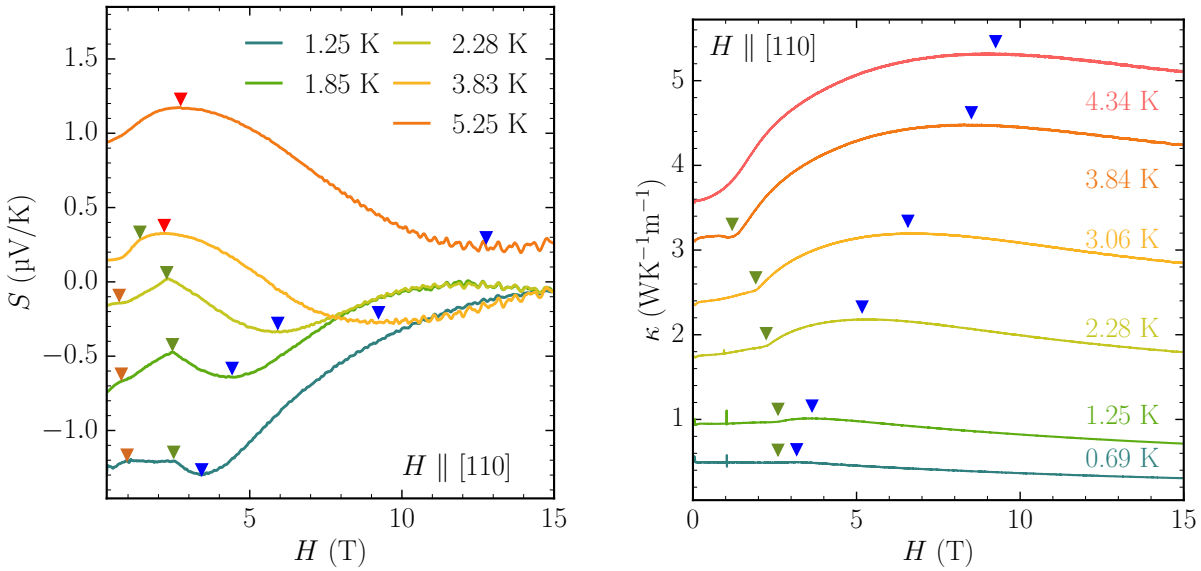

Figure 3.18: Field dependence of the Seebeck coefficient S (left) and the thermal conductivity κ (right) for various temperatures. The transition H_C is indicated by green arrows and H_D by brown triangles. The positions of local minima (maxima) in S are represented by blue (red) arrows. Maxima in κ are in blue.

Seebeck and thermal conductivity measurements

Figure 3.18 (left) shows the field dependence of the Seebeck coefficient up to 15 T. The transition H_C is clearly visible in the thermoelectric power. Interestingly, we can observe the presence of a local minimum at 3.5 T for $T = 1.25$ K, increasing in temperature until 5.25 K where it is located at $H = 13$ T. In a similar fashion, a local maximum grows from $H_C = 1.7$ T at 3.5 K and remains almost constant for higher temperatures. Additionally, for fields $H > 7$ T, quantum oscillations are visible. These will be treated in chapter 4 and will not be investigated here.
The right panel of figure 3.18 shows the thermal conductivity κ under magnetic field. In the conical state, $\kappa(H)$ remains mostly constant and above H_C one observes an increase that is enhanced with temperature. The thermal conductivity can usually be understood as the sum of the phonon component κ_p, the electronic component κ_e, and the magnetic

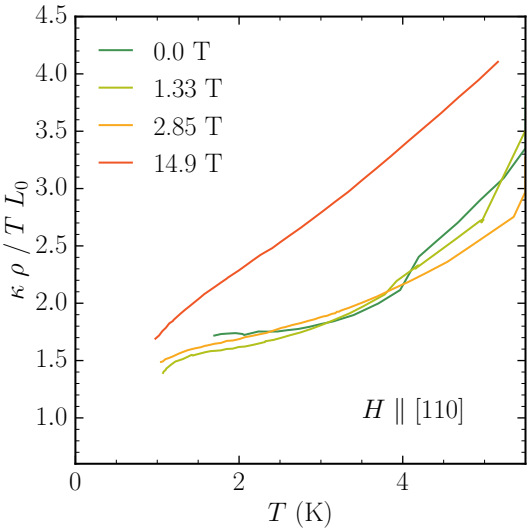

Figure 3.19: Temperature dependence of the Wiedemann-Franz law $(\kappa\rho)/(TL_0)$ for fields of 0, 2, 4 and 16 T. κ is the thermal conductivity, ρ the longitudinal resistivity and $L_0 = 2.44 \times 10^{-8}$ W·Ω·K^{-2} is the Lorentz number.

component κ_m [90, 91]:

$$\kappa = \kappa_p + \kappa_e + \kappa_m \tag{3.3}$$

In the ferromagnetic-like FP-PM state above H_C with all the moments oriented along the field, the magnetic component does not contribute to κ. The electronic component κ_e can be found from the Wiedemann-Franz (WF) law:

$$\kappa_e \rho = L_0 T \tag{3.4}$$

with L_0 =2.44×10^{-8} W·Ω·K^{-2} the Lorentz number. Figure 3.19 shows the validation of the WF law, with $\kappa\rho/TL_0$ as a function of temperature at various fields extrapolating to 1 in the low-temperature limit. From the WF plot, we can see that at 15 T only the electronic component of κ plays a part with an almost linear temperature dependence. At lower fields, on the other hand, κ_p and κ_m should be taken into account. As the WF law holds in this system, the feature of the crossover between the PM and the FP-PM regime in the resistivity should also appear in the thermal conductivity. The maximum in κ is denoted by blue arrows in the right panel of figure 3.18.
From an experimental point of view, the thermal conductivity $\kappa = \alpha\frac{P}{\Delta T}$ is a measurement of the heating power P needed to induce a gradient ΔT across the sample, normalized by the geometric factor α. We can note that the maxima are mainly due to minima in the thermal gradient. As κ is measured at the same time and with the same setup as the thermoelectric power Seebeck coefficient $S = \frac{\Delta V}{\Delta T}$, with a constant heater power during the field sweep, it is natural that the extrema in κ are found in S as well. Indeed, as can be seen by the blue circles and crosses in the right panel of figure 3.20, the local minima in S and the local maxima in κ coincide. The Seebeck voltage ΔV also features both minima and maxima, proving that these anomalies are not due to inaccuracies in the temperature measurement setup, and that the high-field feature is related to the crossover between the PM and the FP-PM regime.

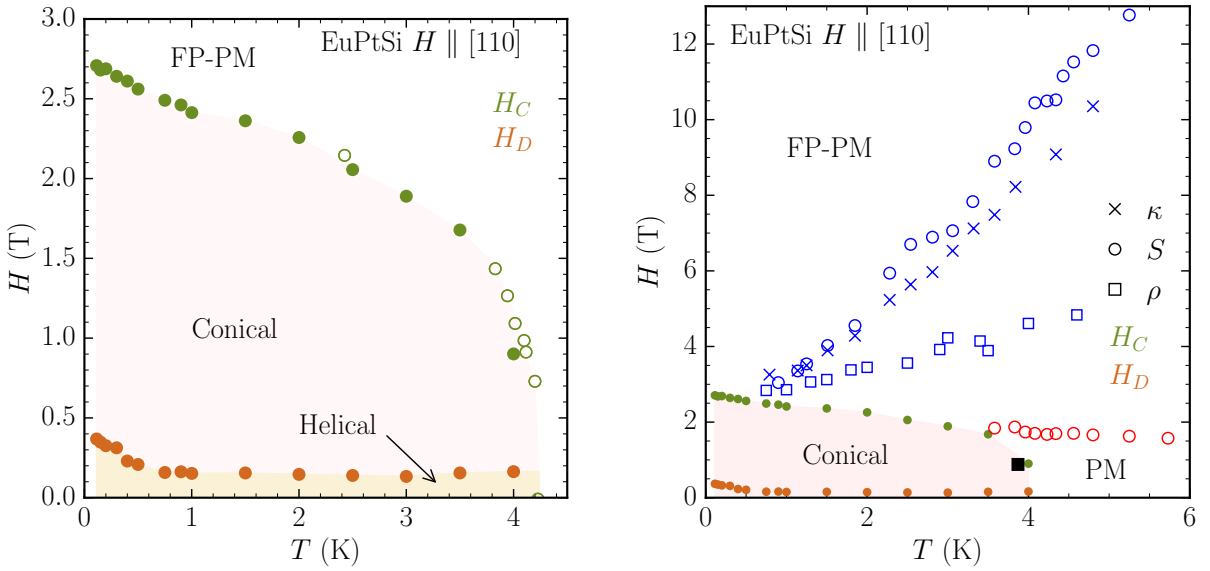

Figure 3.20: $H - T$ phase diagram of EuPtSi for the $H \parallel [110]$ direction. Left: obtained with resistivity measurements, full (open) circles being from $\rho(H)$ ($\rho(T)$). Right: extended phase diagram from ρ measurements (full dots), with additional features of S (open circles), κ (crosses) and ρ (squares). The red line corresponds to local maxima in the Seebeck data, while the blue one corresponds to minima and maxima in S and κ, respectively. The black square is the tricritical point determined in [81].

From the measurements presented above, we can determine the $H - T$ phase diagram, shown in figure 3.20 on the left. Full circles indicate transitions from the $\rho(H)$ measurements and open circles from $\rho(T)$. The helical order lies below the H_D transition line. Between H_D and H_C is the conical order and above is the field-polarized, or field-induced ferromagnetic state, unshaded. We can note that the works of Sakakibara et *al.* have evidenced the presence of a tricritical point (TCP) in EuPtSi [81]. This shows in dM/dT measurements as the change from a symmetric peak to an asymmetric one at $T_{\mathrm{TCP}} = 3.87$ K and $H_{\mathrm{TCP}} = 0.88$ T, broadening with field. The right panel of figure 3.20 shows the same phase diagram as on the left with full dots, extended to 6 K and 13 T. As the H_C transition is observed for the same fields for all probes, only the resistivity data is shown for this transition for the sake of visual clarity. The red (blue) circles correspond to the local maxima (minima) observed in the $S(H)$ data, while blue crosses correspond to maxima in $\kappa(H)$. The blue squares are minima in $\rho(H)$. The blue line rising from the H_C transitions at low temperature seems to agree with the reorientation of the magnetic moments under applied magnetic field. Above the blue line, the system lies in the field-polarized state. The variations between the different probes may be attributed to the criterion chosen, and emphasize the width of the crossover. On the other hand, the line of red dots from maxima in the $S(H)$ signal might be the indication of a short range magnetic order in the paramagnetic state. It might be related to the tricritical point found in ref. [81], marked on figure 3.20 (right) with a black square, although the maxima in $S(H)$ join H_C at 1.7 T and 3.5 K, which is at a significantly higher field.

From the study of the low temperature phase diagram for the $H \parallel [110]$, we have confirmed that no SkL phase exists for this direction. For ρ, S and κ the conical order yields a flat or linear field dependence, and the three probes are in good agreement for the H_D and H_C transitions. The absence of the A-, A'- and B-phases allows us to recover a 'background' signal to understand the other directions better. Additionally, S also features anomalies at higher temperature, which might be related to new energy scales of the system.

3.2.3 Results for $H \parallel [111]$

We now turn our focus to the $H \parallel [111]$ direction of EuPtSi, with the A-phase reminiscent of the one in MnSi. Since its discovery, the A-phase has been confirmed to be a SkL phase with triple-q ordering and $q_1 = (-0.29, 0.09, 0.20)$, $q_2 = (-0.20, 0.29, -0.09)$ and $q_3 = (0.09, 0.20, -0.29)$ [3, 83]. The skyrmions form a triangular lattice in real-space with the characteristic length 18 Å in the plane perpendicular to the magnetic field. While this A-phase is well documented in the literature, the resistivity measurements shown in this section allow us to draw a more precise magnetic phase diagram. Other probes will be presented, such as the Hall resistivity with the topological Hall effect (THE) arising from the skyrmion lattice, and thermoelectric measurements.

Resistivity measurements

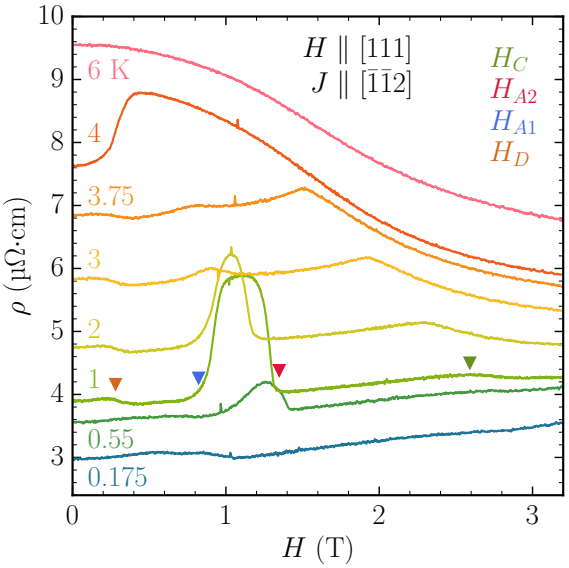

Figure 3.21: Field variation of ρ at various temperatures above 0.175 K, for increasing magnetic field sweeps between 0 T and 4.5 T along the [111] direction. The 0.175 K curve is shifted vertically by -0.5 $\mu\Omega$·cm for clarity. Transitions are indicated by colored arrows on the 1 K data.

Figure 3.21 shows $\rho(H)$ of EuPtSi in the [111] direction for a wide range of temperatures between 0.175 K and 6 K, with a current $J \parallel [\bar{1}\ \bar{1}2]$ of 0.5 mA. Four transitions can be observed and tracked along the temperature range. The first transition H_D occurs

around 0.25 T as a downwards step and corresponds to the transition from the multi-domain helical state to the single-domain conical state. At low temperatures $T < 1$ K, H_D increases, reaching 0.5 T at 0.175 K. For these temperatures, the anomaly is really small in the $\rho(H)$ data and the transition field is recovered from the derivative of the signal, indicating that it is not a well defined transition but a crossover [84]. The A-phase appears as a large bump between the transitions H_{A1} at 0.8 T and H_{A2} at 1.3 T. The amplitude of $\rho(H)$ in the A-phase reaches close to 2 $\mu\Omega$·cm at 1 K. In turn the A-phase is not observed for temperatures below 0.45 K. At temperatures approaching $T_N \approx 4.05$ K, H_{A2} decreases closer to $H_{A1} = 0.8\ T$. As the anomaly corresponding to H_C grows, the signal from the A-phase diminishes and the transition fields are recovered from the derivative of $\rho(H)$. Above 3.75 K, the A-phase transitions become indistinguishable from H_C, the transition from the conical state to the paramagnetic state, as H_C drops to 0 T at $T = T_N$.

In the A-phase, the enhancement of the resistivity is due to additional scattering of the carriers on the skyrmion lattice. The skyrmions act as scattering centers for the conduction electrons, due to a local emergent magnetic field. It is speculated from measurements in MnSi that the ρ response in the A-phase is naturally the superposition of the signal due to the SkL order and the signal from the conical order background [92]. Ignoring the presence of the A-phase, the resistivity for the $H \parallel [111]$ direction is very similar to the $H \parallel [110]$ direction previously observed. We can note a slight difference in the slope of $\rho(H)$ in the conical order, from a flat field-dependence for the [110] direction to a small increase of the order of 0.25 $\mu\Omega$·cm/T for the present direction at all temperatures. This slope may be related to the depopulation of the multiple domains comprising the helical ordering, as only the domains with q close to the field direction remain in the single-domain conical order. The q-vectors in the helical state are closer to the $H \parallel [110]$ direction than the $H \parallel [111]$ direction, with $q = (0.2, 0.3, 0)$. The reorientation of the single-domain single-q conical order along the field would correlate with the slight increase in $\rho(H)$. Even with this small slope it is reasonable to assume that the conical background can be fitted linearly, hence the large signal in the A-phase being solely due to the SkL.

For fields $H_C < H < 4$ T, the resistivity is reduced with increasing field, with the detailed explanation already given for the previous direction. For fields $H > 4$ T (additional curves can be found in appendix A), $\rho(H) \propto H^2$ and the curves become mostly indistinguishable above 7 T for all temperatures as previously described for $H \parallel [110]$, with the cyclotron motion of the electrons increasing the scattering. No oscillations of the Shubnikov-de Haas effect were observed in the resistivity, even at 15 T.

The data from figure 3.21 have all been acquired for increasing field sweeps, at a rate of 0.1 T/min. The sweep rate has been confirmed not to have a strong influence on the data. On the other hand the field sweep direction matters, as hysteretic features of the transitions can be observed, evidencing their first-order nature, as shown in figure 3.22. Colored open triangles correspond to the H_{A1} and H_{A2} transitions for the H-down sweep at 0.6 K. The hysteresis of the H_C transition (not shown here) has not been observed for any temperature, suggesting a second-order of the transition. However, as was described for the previous orientation, resistivity measurements have not been able to confirm the order of the H_C transition. The hysteresis of the H_D transition, on the other hand, is shown for the 1 K data. During decreasing field sweeps, the transition H_D is not observed

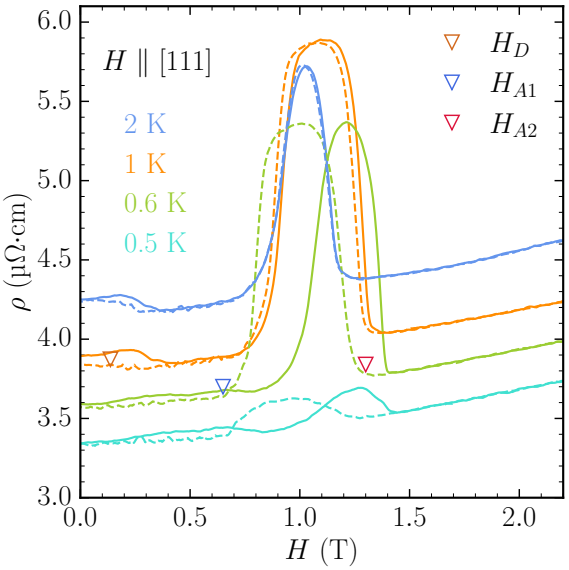

Figure 3.22: Comparison between increasing (full lines) and decreasing (dashed lines) $\rho(H)$ field sweeps for $T = 2$, 1, 0.6 and 0.5 K. The hysteretic features of the transitions H_{A1} and H_{A2} are shown for the $T = 0.6$ K data with open triangles. The hysteretic H_D transition is shown on the 1 K data. The $T = 0.5$ K data was shifted by -0.2 $\mu\Omega$·cm for clarity, and the 2 K data by -0.5 $\mu\Omega$·cm.

below 1 K as the system remains in the conical order. A similar observation has been made in magnetization measurements [4]. The helical order is recovered at $H = 0$ and H_D is observed again if a decreasing field sweep is subsequently followed by an increasing field sweep. The transitions delimiting the A-phase, namely H_{A1} and H_{A2}, are shifted to lower fields when the latter is decreased. Above $T = 1$ K, the increasing and decreasing field sweeps yield similar results. The hysteresis of the A-phase only opens for lower temperatures until the A-phase disappears around $T = 0.45$ K.

From the $\rho(H)$ measurements presented above, we can determine the $H - T$ phase diagram of EuPtSi for the $H \parallel [111]$ direction in figure 3.23. The colored markers correspond to the transitions indicated in figure 3.21. Full squares are data taken from increasing field sweep measurements and full circles are from increasing temperature sweeps in the regions where the transition lines become vertical. Open triangles denote the decreasing field sweeps. The measurements of $\rho(T)$ used here will be shown at a later point in section 3.3 where we evidence measurements of a metastable A-phase under field-cooling. The A-phase is enclosed in the $H-T$ phase diagram and spans a large temperature range from 0.45 K to 4 K. For the whole temperature range, the transitions H_{A1} and H_{A2} almost do not evolve with field. Below 1 K however, the two transition lines follow the field sweep direction as the phase closes upwards for increasing fields and downwards for decreasing fields. The H_D transition from the helical to the conical order also increases below 1 K for measurements with increasing magnetic field, reaching ≈ 0.5 T at 0.2 K.

The phase diagram is naturally very reminiscent of MnSi, but let us highlight a significant difference in the normalized range of the A-phase between the two compounds. In MnSi it spans about 1 K at 29 K ($\approx 3\%$) whereas in EuPtSi it spans 3.65 K at 4 K

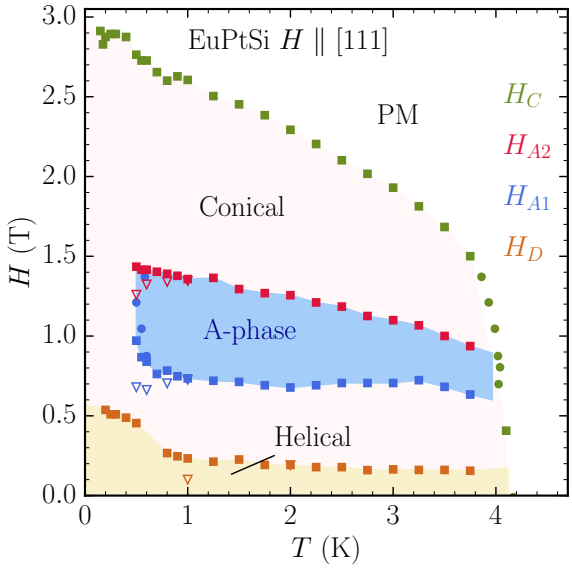

Figure 3.23: Magnetic phase diagram obtained for the [111] direction by resistivity measurements. Full squares (open triangles) are transition fields from increasing (decreasing) field sweeps. Circles denote transitions obtained by increasing temperature sweeps of ρ.

($\approx 91\%$). Furthermore, reaching such low temperatures, it has potential to provide good insights on the physical properties of a SkL close to its ground state. Additionally, the A-phase of EuPtSi exists for a field range of $\approx 0.5 - 0.75$ T, compared to less than 0.1 T for MnSi.

Thermoelectric coefficients and thermal conductivity measurements

As shown in figure 3.24, the field dependencies of S, κ, N and ρ, from top to bottom, all show clear evidence of the A-phase. The comparison is made for a temperature close to 1.75 K (1.68 K for S, κ, N measured simultaneously and 1.75 K for ρ). The four measurements were made in similar conditions on sample #1 with increasing sweeps at 0.1 T/min. The four transitions at low field are indicated with vertical dotted lines. The slight discrepancies may come from a possible misalignment of a few degrees between the ρ and the S setup. The H_D transition between the helical and the conical orders is not observed in thermoelectric measurements for this direction.
For fields $H < 0.2$ T, the superconducting magnet and flux jumps induce random noise on the signal, both in the thermoelectric voltage and the temperature gradient. The $S(H)$ signal corresponding to the A-phase is similar to that of the resistivity as it is a well defined enhancement of the Seebeck coefficient amplitude, reaching up to 0.25 μV/K at 2 K. The same is true for the Nernst signal, albeit with a lower and more noisy signal. Inversely, the thermal conductivity κ in the A-phase decreases by up to 1.75 $\mathrm{WK^{-1}m^{-1}}$. The magnetic skyrmion lattice ordering thus induces additional scattering which limits both electrical and thermal transport.

$S(H)$ measurements at low temperatures ($T < 1$ K) are contaminated by the presence of a large background signal that increases as temperature lowers, making it very hard to extract the intrinsic behavior. This is developed in more detail in appendix A. The

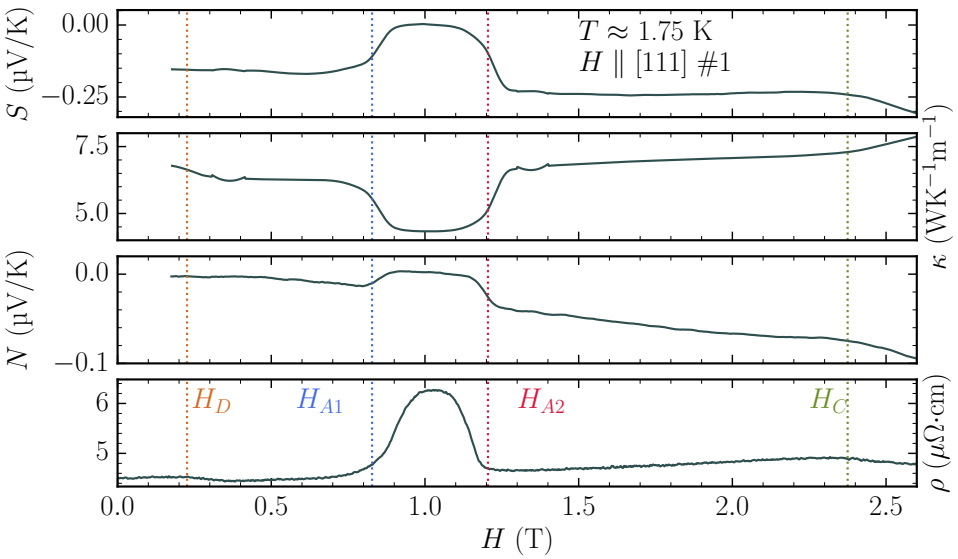

Figure 3.24: Comparison of the field dependence of S, κ, N and ρ for $H \parallel [111]$, at $T \approx 1.75$ K. Transition fields H_D, H_{A1}, H_{A2} and H_C are indicated with colored vertical lines. Measurements done on sample #1.

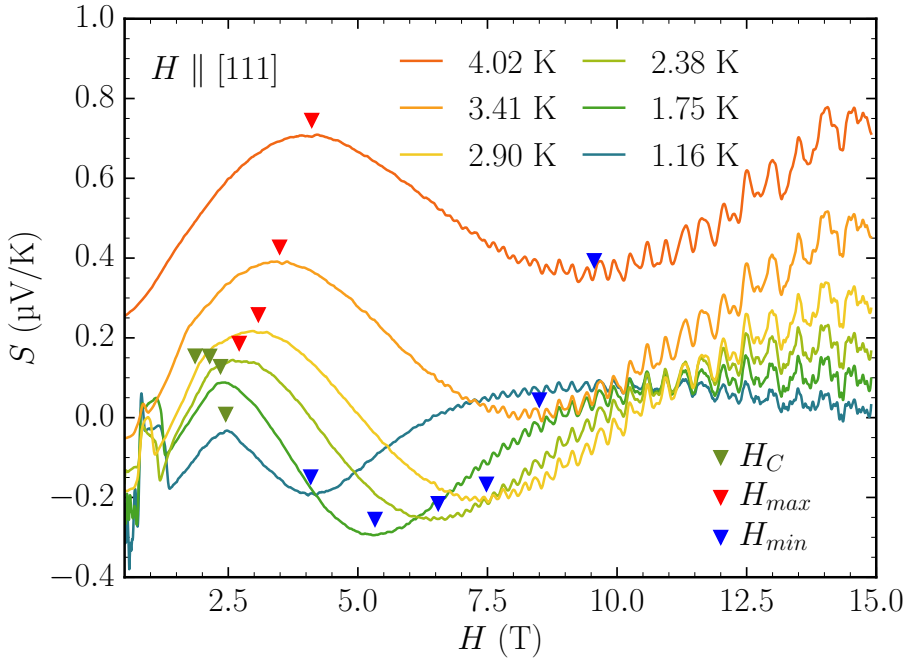

Figure 3.25: Field dependence of the Seebeck coefficient in the whole field region, between $T = 1.2$ and 4 K measured in continuous sweeps. Quantum oscillations are visible above 6 T. Colored arrows correspond to anomalies H_C, H_{max} and H_{min}. Measured on sample #2.

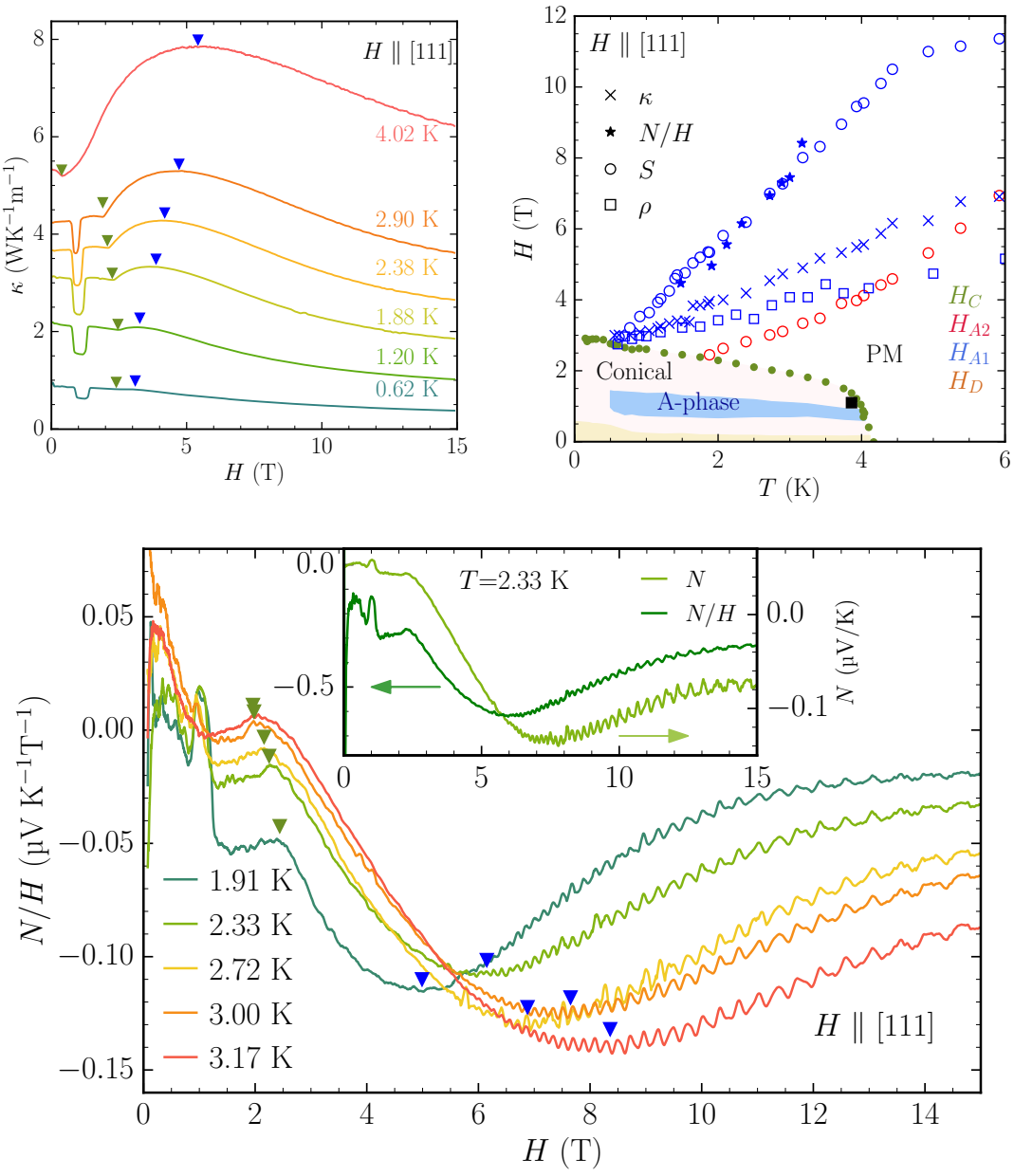

Figure 3.26: Top left: $\kappa(H)$ between 0.6 and 4 K up to 15 T, measured on sample #2. Green arrows indicate the H_C transition and blue arrows indicate the local extrema. Right: $H-T$ phase diagram from ρ (full dots) extended to 6 K and 12 T, with extrema from κ (crosses), N (stars), S (circles) and ρ (squares). The black square is the tricritical point determined in [81]. Bottom: N/H field dependence between 1.9 and 3.2 K up to 15 T, for sample #1. Inset: comparison between N (right axis) and N/H (left axis) at 2.33 K.

data shown in figure 3.25 from H-sweeps for sample #2 is thus limited to 1 K. For lower temperatures, instead of continuous field sweeps, we have performed step-by-step measurements, reducing the noise level and the background by increasing the averaging time. Hence we successfully followed the A-phase features down to 0.45 K. Similarly to the $H \parallel [110]$ direction, the $S(H)$ behavior exhibits clear maxima (red arrows) and minima (blue arrows) increasing both in field and in temperature. The maxima grow from the H_C anomaly (green arrows) at 2.5 K above which the two become distinguishable. Interestingly, as was discussed for the previous orientation, these energy scales are observed both in the ΔV and the ΔT part of the Seebeck coefficient. The thermal conductivity κ, on the other hand, shows a local maxima that is only due to variations in ΔT, see the blue arrows in figure 3.26 (top left). Contrarily to the $H \parallel [110]$ direction, the maxima in $\kappa(H)$ and the minima in $S(H)$ do not coincide as T or H increase. The same is true for the Nernst signal $N(H)$, presenting a minimum, as seen in the inset of the bottom panel of figure 3.26. It is more meaningful, however, to consider the coefficient N/H. Much like for the Hall effect (described in the next section), at high fields $H > H_C$ where the magnetization is mostly saturated, the Nernst coefficient has a linear-in-H component [6, 93]. From the N/H field-dependence the minimum falls along the S data. Their agreement is very good, especially considering that they come from two different samples.
All probes exhibit an anomaly rising from H_C at the same point of 0.6 K and 2.9 T but follow different critical lines, as shown in figure 3.26 (top right panel). Their crossing point is similar to the $H \parallel [110]$ direction one, and is in agreement with the cross-over from the PM to the FP-PM regime that is clearly observed in $\rho(H)$ (blue squares). On the other hand, the maximum in S (red) appears at 1.8 K and 2.2 T, which is much higher than was the case for $H \parallel [110]$, and crosses the κ maximum line at 6 K and the ρ minimum line at 4 K. The existence of a tricritical point was determined from magnetization in ref. [81] at $H_{\mathrm{TCP}} = 1.1$ and $T_{\mathrm{TCP}} = 3.86$ K, as shown in the top right panel of the figure 3.26 by a black square. The TCP thus exists at much lower field and higher temperature than the starting point of the $S(H)$ maxima critical line. The energy scales observed in the Seebeck coefficient are therefore assumed to not be connected to the existence of a TCP.

Topological Hall effect in the A-phase

In general, the Hall effect is understood as being the sum of two components, the ordinary Hall effect (OHE) and the anomalous Hall effect (AHE). It empirically follows the relation

$$\rho_H = R_0 H + R_S M \tag{3.5}$$

with the first term being the OHE with R_0 the ordinary Hall coefficient[2], and the second term the AHE with R_S a scaling factor. The OHE is dependent on the carrier density $n = (R_0 e)^{-1}$ and scales linearly with the magnetic field [94]. The origin of the AHE, on the other hand, is still a source of controversy and has been for decades [95]. From a simple approach, two different left-right asymmetric scattering processes that scale with the magnetization M are usually considered. The first is the incoherent skew scattering, for which we expect $R_S \sim \rho$ the longitudinal resistivity [96, 97]. The second is the coherent skew scattering, for which $R_S \propto \rho^2$ [98].

[2]Maintaining the convention applied to the rest of this work, the vacuum permeability μ_0 is ignored to have H in teslas.

A third component, the so-called topological Hall effect (THE) can be observed for skyrmion compounds and can be used as a tool to study the phase relationship of the helices forming the triple-q ordering and the topological properties of the SkL, such as the chirality and the winding number [99, 100]. The THE arises from the Berry phase acquired by conduction electrons along the spin-polarization of the magnetic texture [49, 101, 102]. The Berry phase affects charge transport in a similar way as an external emergent magnetic flux does, and the THE corresponds to the transverse motion of conduction electrons by this emergent field, akin to a Lorentz force. EuPtSi provides the rare occasion to ob-

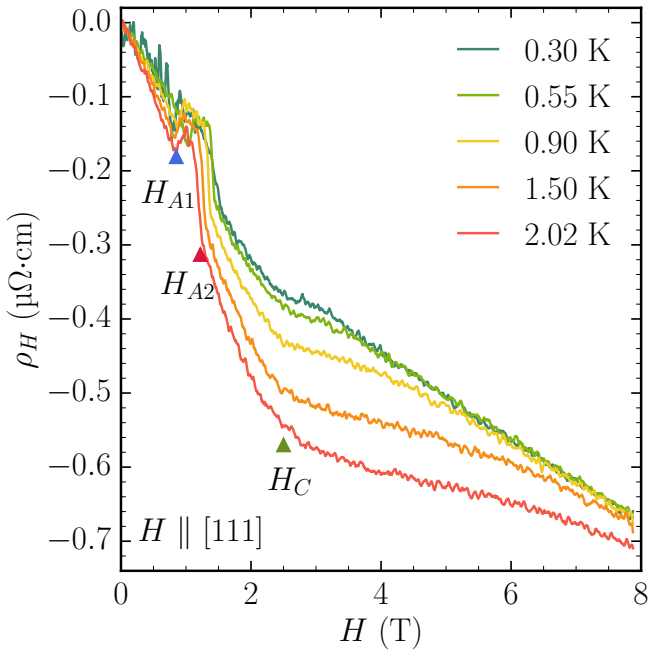

Figure 3.27: Hall resistivity for $H \parallel [111]$ for temperatures between 0.3 and 2 K. Colored arrows indicate the H_{A1}, H_{A2} and H_C anomalies on the 2 K curve.

serve all three types of Hall components simultaneously in the same system [3]. We have performed Hall resistivity measurements for $H \parallel [111]$ and $J \parallel [\bar{1}\bar{1}2]$ of 0.5 mA according to the protocol described in chapter 2. Field sweeps have been performed for both positive and negative field direction at the same sweeping rate of 0.1 T/min. The sweeps are performed subsequently without changing the temperature regulation. The Hall resistivity signal is then obtained by taking the antisymmetric combination of the two measured signals $\rho_{xy}(H > 0)$ and $\rho_{xy}(H < 0)$. The field dependence of the Hall resistivity is presented in figure 3.27 for various temperatures. The anomalies corresponding to H_{A1}, H_{A2} and H_C are annotated for the $T = 2$ K data with colors as per the $H - T$ phase diagram (see figure 3.23). The H_D transition at low field is not observed due to flux jumps in the superconducting magnet which are prominent in decreasing fields below ≈ 1 T. On the other hand, the A-phase is clearly evidenced by an additional contribution to the Hall effect forming a peak structure between H_{A1} and H_{A2}. The sign of the A-phase signal is opposite the sign of the global Hall signal, yielding a positive contribution in an otherwise negative signal due to electrons dominating the transport.

Figure 3.28 (left) shows the three components to the Hall effect fitted to the $T = 1$ K

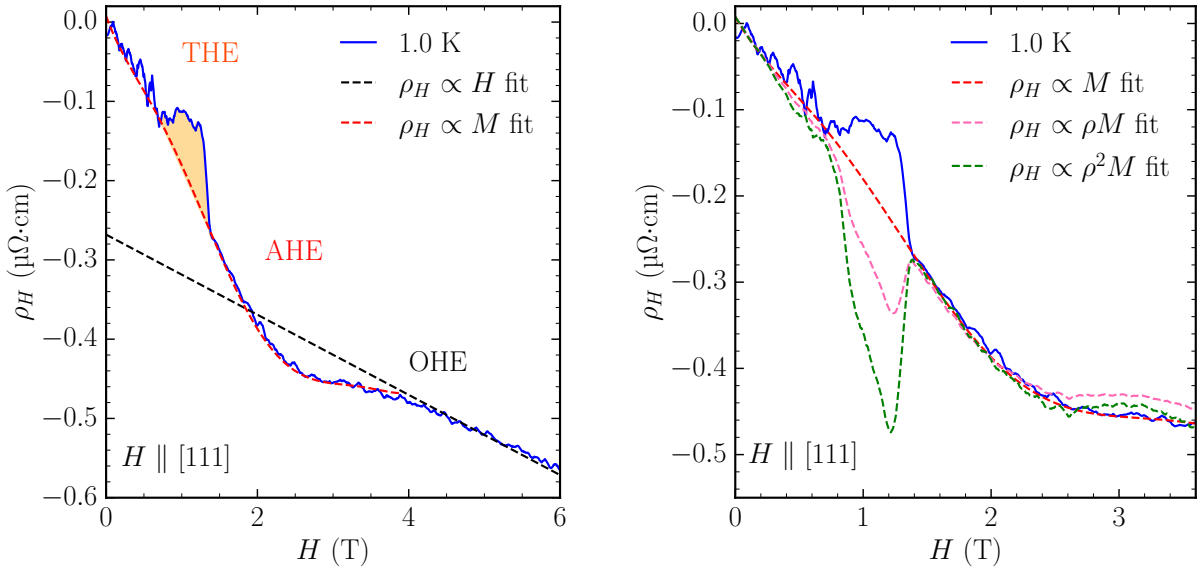

Figure 3.28: Left: the three contributions to the Hall effect represented simultaneously on the 1 K data. The THE in the A-phase is the colored orange region. Right: fittings of the 1 K data with three different AHE models $\rho_H \propto \rho^n M$, with ρ the longitudinal resistivity, M the magnetization and $n = 0 - 2$. $n = 1$ corresponds to the incoherent skew scattering process and $n = 2$ to the coherent skew scattering process.

data. The Anomalous Hall Effect (AHE) is described by a $\rho_{xy} \propto M$ law, with a negative sign to concord with the negative Hall effect. Following magnetization, the AHE is mostly linear at low fields until saturation, as shown by the red dashed line. $M(H > H_C)$ is saturated for all temperatures, thus the AHE being constant. For increasing temperatures, the saturation transition H_C is broadened and the saturated AHE is observed at higher fields. The Ordinary Hall Effect (OHE) which is described by a $\rho_H \propto H$ behavior is visible for fields $H > H_C \approx 2.5$ T at low temperature ($H > 5$ T at 2 K). The OHE dominates at high fields and gives rise to a linear signal, as shown by the black dashed line. Due to the AHE previously described, the OHE does not reach zero at zero field. By fitting the high-field data between 6 and 15 T with a first order polynomial $ax + b$, we obtain a value $|R_0| = 0.051$ $\mu\Omega$·cm/T. In a very simplified approach, as only one charge carrier is taken into account, the corresponding carrier concentration is $n = (|R_0|e)^{-1} = 1.23 \times 10^{22}$ cm^{-3}, which is within the expected range for a metal. Attempts to fit the AHE term with $\rho^2 M$ and ρM dependencies due to side-jump and skew scattering respectively, shown in figure 3.28 (right), have been unsuccessful to describe the peak structure of the A-phase, much like the works by Kakihana et *al.* [3]. The magnetization data are from SQUID device measurements, as presented in section 3.1.3, and corresponds to the $H \parallel [100]$ direction. It is important to note that no strong anomalies are observed in our $M(H)$ data, giving a linear fit (dashed red curve) between H_{A1} and H_{A2}. Besides the A-, A'- and B-phases, the magnetization is mainly isotropic for a given temperature. Data from the literature, in agreement with our own, indicates that the features of the SkL phases are rather small and would explain neither the shape not the magnitude of the ρ_H feature. Hence we can use our $H \parallel [100]$ $M(H)$ measurements to approximate the AHE term in the fittings. For the $\rho^2 M$ and ρM fits (dashed green and pink respectively), ρ is the resistivity mea-

surement already presented. For both cases, the fitting of the A-phase gives a negative additional contribution instead of a positive one.
The A-phase contribution is thus not due to the AHE and is the expression of a third Hall effect contribution, the so-called Topological Hall Effect (THE).

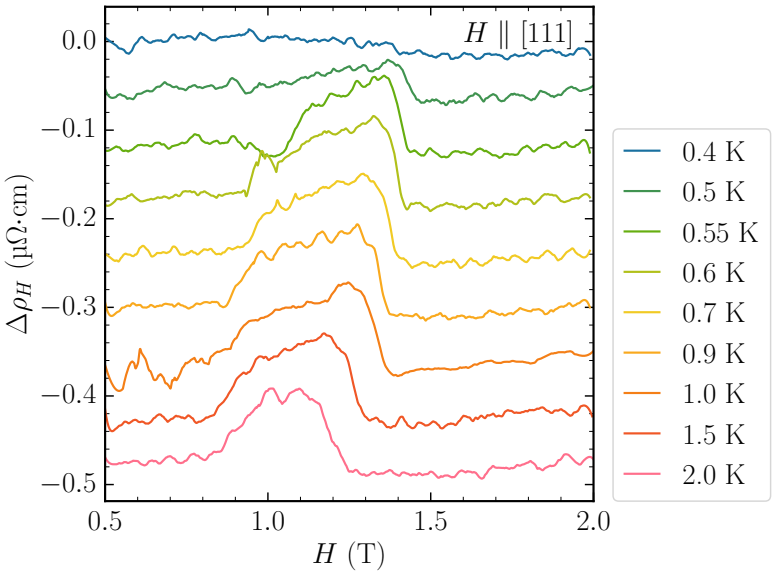

Figure 3.29: Topological Hall resistivity, i.e. Hall resistivity with OHE and AHE contributions removed, centered on the A-phase. Curves are shifted vertically for clarity.

In figure 3.29, we have fitted the Hall resistivity linearly between 0.5 T and 2 T in the conical phase, thus removing the OHE and the AHE contribution. The data shown are shifted vertically. In this view the only remaining contribution is the THE due to the skyrmion lattice in the A-phase, which reaches a maximum of $\Delta\rho_H = 0.1$ $\mu\Omega$·cm at 0.6 K, taken between the maximum and the mean values at the transitions. The disappearance of the anomaly below 0.5 K is in good agreement with the phase diagram previously measured. Along their motion, conduction electrons are affected by an emergent magnetic field based on the skyrmions of the A-phase. Considering the spin polarization of the electrons to follow the spin texture adiabatically, the additional THE signal can be expressed as

$$\Delta\rho_H^{THE} \approx P R_0 H_{\text{eff}} \tag{3.6}$$

with R_0 the ordinary Hall constant previously measured, P the local spin polarization of the conduction electrons and H_{eff} the emergent magnetic field [49, 102]. P comes from the Berry phase collected by the carriers, it is maximum $P = 1$ for a fully polarized system and minimum $P = 0$ for vanishing polarization for which there is no THE. In between the two cases, the polarization is given by $P = \mu_{spo}/\mu_{sat}$ the ratio of the ordered magnetic moment μ_{spo} in the A-phase and the saturated magnetic moment μ_{sat}. The former is taken from a zero-field linear extrapolation of the magnetization measurements by Sakakibara et *al.* [4] and we use the value $\mu_{spo} = 0.7$ μ_B. The saturated magnetic moment is the free Eu moment $\mu_{sat} = 7$ μ_B, yielding $P = 0.1$. The emergent field is $H_{\text{eff}} = -\Phi_0\Phi$ with $\Phi_0 = h/e$ the flux quantum for a single electron and Φ is given by the skyrmion density. For an hexagonal skyrmion lattice, the reciprocal and real-space

lattice vectors have lengths $2\pi/\lambda_S$ and $\lambda_S/\sin(2\pi/3)$ respectively, with $\lambda_S = 18$ Å the wavelength or periodicity of the helical state near T_N [103]. The size of the unit cell of the skyrmion lattice is thus $\lambda_S^2/\sin(2\pi/3)$. The obtained emergent magnetic field is

$$H_{\text{eff}} = -\frac{h}{e}\left(\frac{\sqrt{3}}{2\lambda_S^2}\right) \approx -1105 \text{ T} \tag{3.7}$$

with the negative sign indicating that H_{eff} opposes the applied magnetic field. By comparison, the emergent field from the skyrmion lattice in MnSi is evaluated at -13.15 T. The difference of two orders of magnitude is explained by the small size of the skyrmions in EuPtSi, an order smaller than in MnSi.
From equation 3.6, with $|R_0| = 0.051$ $\mu\Omega$·cm and the values of P and H_{eff} given above, we obtain a theoretical estimate of a THE in EuPtSi with a magnitude $\Delta\rho_H^{THE} = 0.56$ $\mu\Omega$·cm. Compared to the measured value of 0.1 $\mu\Omega$·cm, the theoretical value is in reasonable agreement, and both are much larger compared to MnSi with $\Delta\rho_H^{THE} = 4$ nΩ·cm [49]. The large THE in EuPtSi is thus related to the small size of the skyrmions, which produce a very large local effective field opposing the applied field. The motion of the conduction electrons is affected, leading to a contribution to the Hall effect opposite the ordinary contribution.

3.2.4 Results for $H \parallel$ [100]

The $H \parallel$ [100] direction of EuPtSi presents two distinct magnetic phases next to one another in the conical order of the $H - T$ phase diagram. From the angular dependence of the resistivity presented in section 3.2.1, we have seen that the B-phase exists only close to the main crystallographic axes [100], [010] and [001]. The A'-phase, in turn, can be followed along the body diagonal of the cubic structure and links to the A-phase seen for the $H \parallel$ [111] direction. A rotation along the other body diagonal, however, shows a distinction between the A'-phase and the A-phase for $H \parallel [\bar{1}11]$. From experimental observations, the A'- and B-phases look similar in nature to the A-phase, however the detailed magnetic structure has yet to be reported for these phases. Because the structures are next to each other in the $H - T$ phase diagram, the possibilities of phase-mixing between a SkL and a conical phase, or two SkLs with differing parameters, exist.

Resistivity measurements

The field-dependence of the resistivity is shown in figure 3.30 (left) for fields below 3.5 T and temperatures ranging between 0.1 K and 4 K. The right panel shows the same measurements with additional temperatures between 0.1 and 6 K, up to 15 T. The resistivity at high field follows the same H^2 dependence as for the other orientations, highlighted by the dotted black line in the right panel of the figure, and will not be detailed further here. The similarity with the $H \parallel$ [111] direction is evident for the anomalies corresponding to the transitions H_D and H_C, respectively from the helical to the conical state and from the conical to the PM state. We can note that the H_D transition corresponds to an increase in ρ whereas it was a decrease for the other orientations. For this field and current orientations, the magnetic fluctuations increase the scattering in the conical state with respect to the helical state. In the conical state, $\rho(H)$ increases almost linearly with H, similarly to

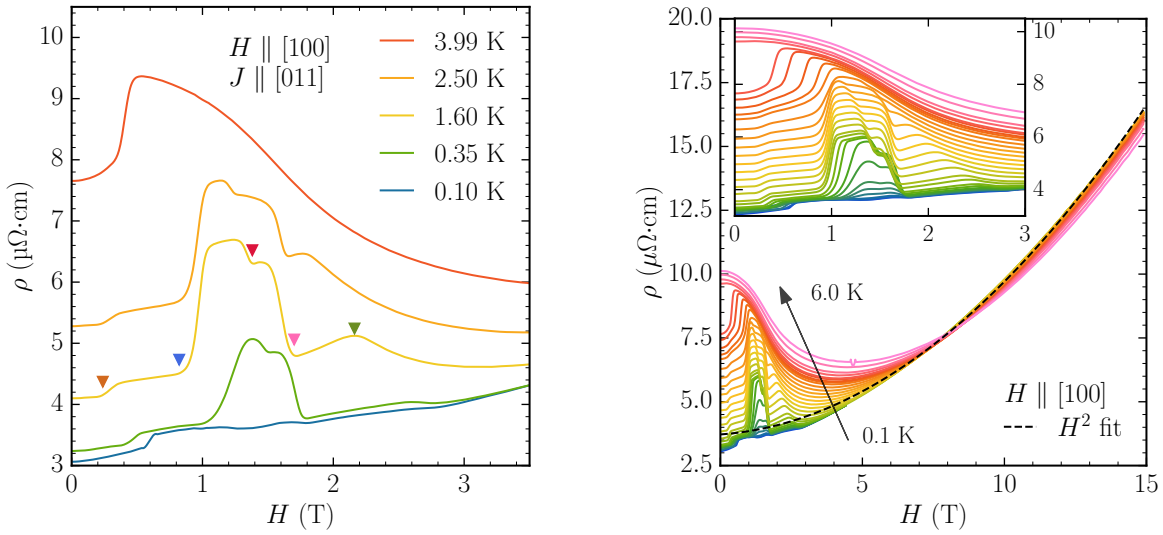

Figure 3.30: Left: $\rho(H)$ for $H \parallel [100]$ between 0 and 3.5 T. Colored arrows denote the anomalies corresponding to transitions H_D, H_{A1}, H_{A2}, H_B and H_C in the order of increasing field. Right: $\rho(H)$ up to 15 T for temperatures between 0.1 and 6 K with the $\rho \propto H^2$ fit in dotted line. The inset shows a close-up between 0 and 3 T.

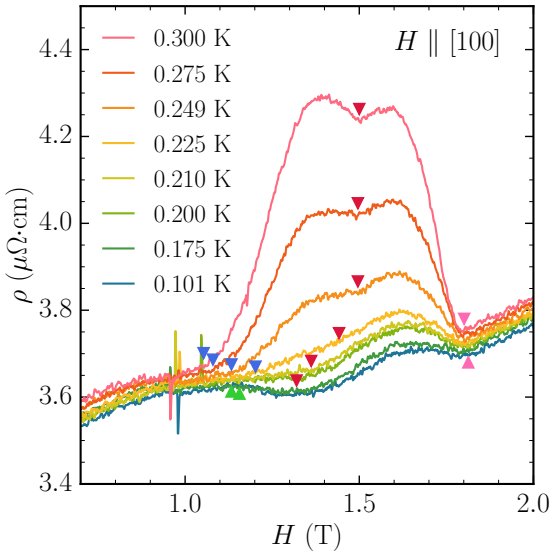

Figure 3.31: $\rho(H)$ for $H \parallel [100]$ for $T \leq 0.3$ K, in the conical order between 0.7 T and 2 T. The triangles indicate the anomalies H_{A1} (blue), H_{A2} (red), H_B (pink). H_{A1} disappears below 0.225 K as the A-phase closes. H_{A2} and H_B are observed at all temperatures. Below 0.225 K, a previously unreported anomaly is observed around 1.15 T, indicated by green triangles.

the other direction [111] and [110]. Between $H_{A1} \approx 0.9$ T and $H_{A2} \approx 1.5$ T, the A'-phase is formed and $\rho(H)$ is enhanced by up to 2 $\mu\Omega$·cm at 2 K. The H_{A2} transition between the two phases is a downwards step, as the B-phase is less resistive. $H_B \approx 1.75$ T is the upper field limit to the B-phase. Contrarily to the [111] direction where the A-phase disappears below 450 mK, for $H \parallel [100]$, both phases exist at lower temperatures, down to 250 mK. At $T = 0.3$ K, both phases reach around the same value of resistivity $\rho = 4.3$ $\mu\Omega$·cm. Below 0.3 K, the A'-phase reaches lower values than the B-phase, as the A-phase visibly closes at higher temperature than the B-phase.

With the low noise level of our measurement setup, we have evidenced anomalies linked to the SkL phases down to our lowest available temperatures, around 100 mK, as shown in figure 3.31. Below 0.3 K, the resistivity in the A'- and B-phases rapidly diminish with temperature. The transition H_{A1} from the conical order to the A'-phase increases as the temperature decreases, reaching ≈ 1.2 T at 0.225 K where the A'-phase disappears. The H_{A2} transition, however, decreases rapidly below 0.22 K, reaching a wide minimum of ρ at 1.32 T for $T \leq 0.2$ K. On the other hand, the transition H_B between the B-phase and the conical order is unchanged and clearly visible at all temperatures. The presence of H_{A2} and H_B at all temperatures seems to indicate that the B-phase persists at much lower temperature than the A'-phase.
At $T = 0.1$ K the B-phase bump has a height of only ≈ 0.1 $\mu\Omega$·cm, or 5 % of the maximum value at 2 K. The width of the B-phase, on the other hand is greatly increased, as can be seen in the low temperature phase diagram of figure 3.33. The large shift of H_{A2} upon closing of the A'-phase may be an indication of a mixing of the two phases at higher temperature. For temperatures above 0.225 K, the B-phase signature in the resistivity may be partially hidden by the large signal from the A'-phase.
Additionally, for temperatures below 0.225 K, $\rho(H)$ decreases with a slight change of slope around 1.15 T, indicated by green triangles in figure 3.31. This previously unreported anomaly can be tracked from the closing of the A'-phase but does not line-up with the H_{A1} critical line. Our precise low temperature measurements of the resistivity thus seem to indicate that interesting spin textures still exist in the field range of the SkL phases at very low temperature.
Comparing the results of increasing and decreasing field sweeps as per figure 3.32, we can evidence the first-order nature of the transitions H_{A1}, H_{A2} and H_B. The hysteresis is only visible for temperatures below 1 K, as was the case for the [111] direction. Interestingly, for increasing field sweeps the width of the A-phase decreases with temperature, whereas for decreasing field sweeps, the width becomes larger as H_{A1} lowers from 1 T to 0.6 T. The opposite is observed for the B-phase, closing with decreasing fields as H_B lowers to 1.5 T at 0.2 K.
The hysteresis of the various transitions are shown in the $H - T$ phase diagram in figure 3.33, with full squares (open triangles) for increasing (decreasing) fields. Dots in the phase diagram are the corresponding anomalies observed in $\rho(T)$ measurements presented in section 3.3.3. As there are essentially two phase diagrams due to the hysteresis, on the low temperature diagram on the right, the two are superimposed with colored areas for the increasing fields and hatched regions for the decreasing fields. The H_D transition hysteresis is not observed below 0.5 K as it reaches fields below 0.1 T for which the superconducting magnet induces noise on the signal. The additional anomaly found at

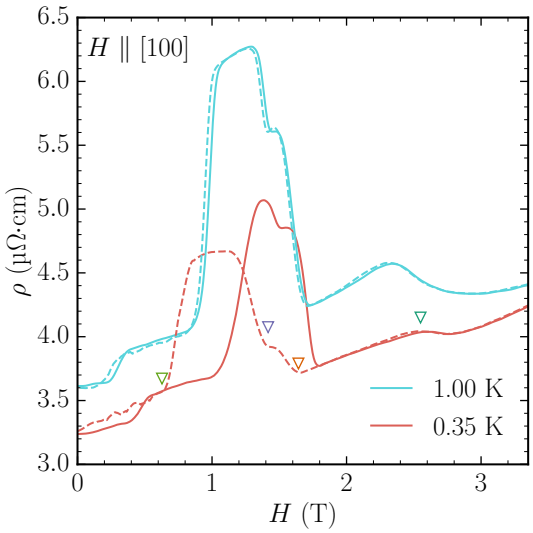

Figure 3.32: $\rho(H)$ measurements in increasing (full lines) and decreasing (dashed lines) fields for $H \parallel [100]$. Colored arrows indicate transitions H_{A1}, H_{A2}, H_B and H_C for the 0.35 K decreasing field sweep data, with colors corresponding to the phase diagram (see figure 3.23).

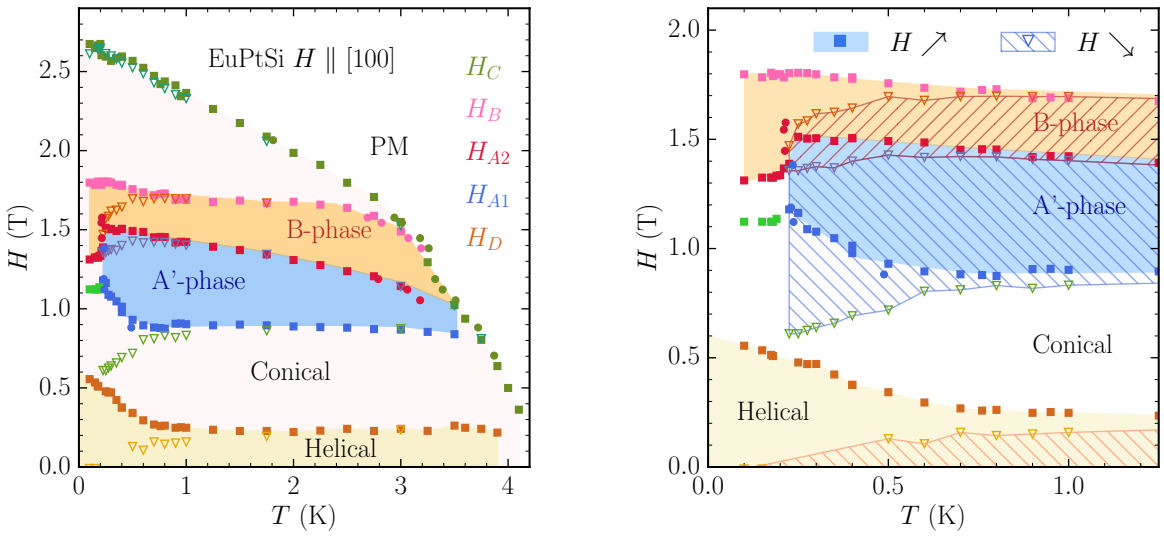

Figure 3.33: Magnetic phase diagram obtained for the [100] direction by resistivity measurements. Full squares (open triangles) are anomalies from increasing (decreasing) field sweeps. Full circles are anomalies from $\rho(T)$ (see section 3.3.3). Colored areas indicate the various magnetic structures. Green squares around 1.1 T below 0.25 K indicate the newly found anomaly from $\rho(H)$ measurements (see figure 3.31). Left: up to 4 K and 3 T. Right: up to 1.25 K and 2 T. Hatched areas correspond to the decreasing-field phase diagram.

low temperature (see figure 3.31) is evidenced on the phase-diagram close-up as green squares around 1.1 T. It follows from the H_{A1} transition after the A-phase closes below 0.225 K and is seen in increasing field sweeps only. It might be too small to be measured in decreasing fields, or disappear altogether in a similar way to the B-phase. As for the nature of the anomaly, resistivity measurements do not allow to draw more conclusions. The observation of the anomaly is reproducible and it is observed even more clearly from the field dependence of the metastable SkL phases presented in the next section.
Future $\rho(H)$ measurements with an experimental setup allowing lower temperatures would help clarify the results presented here, in combination with probes that can discern the precise magnetic structures in the various regions of the phase diagram.

Topological Hall effect in the A' and B phases

We have performed Hall resistivity measurements for the $H \parallel [100]$ direction following the same protocol as in section 3.2.3 for the previous orientation. A field sweep rate of 0.1 T/min was used for both positive and negative field sweeps at fixed temperature. The

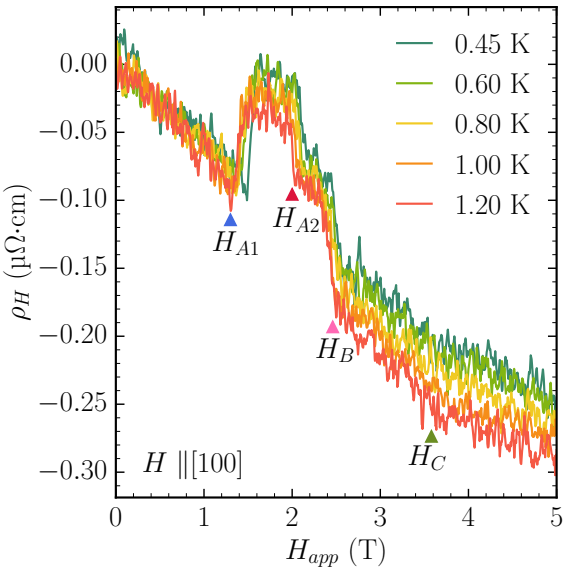

Figure 3.34: Hall resistivity for $H \parallel [100]$ for temperatures between 0.45 and 1.2 K, for applied fields between 0 and 5 T. Colored triangles indicate the H_{A1}, H_{A2}, H_B and H_C anomalies on the 1.2 K data.

field dependence of the Hall resistivity is shown in figure 3.34 between 0 and 5 T of applied (uncorrected) magnetic field, for temperatures between 0.45 and 1.2 K. The anomalies corresponding to the transitions H_{A1}, H_{A2}, H_B and H_C are indicated by colored triangles on the 1.2 K data. The A'-phase between H_{A1} and H_{A2} is evidenced by a large positive contribution. The B-phase between H_{A2} and H_B also yields a positive contribution to ρ_H, smaller in amplitude than the A'-phase. As was the case for the $H \parallel [111]$ direction, the Ordinary Hall Effect (OHE) can be fitted from measurements above 5 T (not shown here) in which the Anomalous Hall Effect (AHE) is constant, as the magnetization reaches saturation. Magnetization measurements as shown in section 3.1.3 are unable to explain the magnitude or the sign of the anomalies due to the presence of the A' and B phases.

As such, the anomalies are likely to be due to the Topological Hall Effect (THE). The

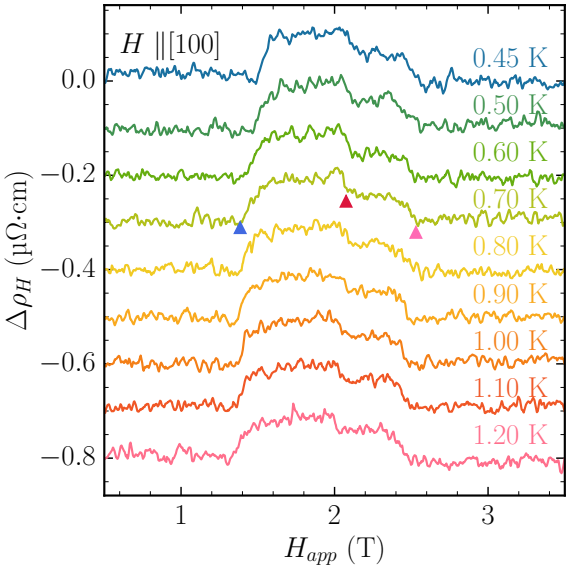

Figure 3.35: Topological Hall resistivity, i.e. Hall resistivity with OHE and AHE contributions removed, centered on the A' and B phases. Colored triangles indicate the H_{A1}, H_{A2} and H_B transitions in order on increasing field. Curves are shifted vertically for clarity.

isolated THE is presented in figure 3.35 after fitting the Hall resistivity data linearly between 0.5 and 3 T. The transitions H_{A1}, H_{A2} and H_B in order of increasing field are indicated by colored triangles on the 0.7 K data. The data are shifted vertically for clarity. The A'-phase yields an amplitude maximum of $\Delta\rho_H = 0.1$ $\mu\Omega$·cm at 0.7 K and the B-phase an amplitude maximum of $\Delta\rho_H = 0.07$ $\mu\Omega$·cm at 0.8 K. For the $H \parallel [100]$ direction, scattering experiments have yet to reveal the structure of the A' and B phases, whether they are SkL, multi-q structures, etc. As such, the amplitude of the effective emergent magnetic field produced by the magnetic structure and opposing the applied field cannot be estimated as per equation 3.7. A theoretical estimate of the THE with which to compare our measurements is thus not obtainable yet. Nevertheless, this new observation of the THE for both magnetic phases of the $H \parallel [100]$ direction still points to evident similarities between the A' and B phases and the confirmed skyrmion lattice A-phase for $H \parallel [111]$. Future scattering experiments would allow a more precise study of these skyrmion-related phases.

Thermoelectric measurements

For this field direction, continuous $S(H)$ measurements evidence clear quantum oscillations due to the high residual-resistivity-ratio of the sample $RRR = 32$, as shown in figure 3.36 (a). However, at low temperature $T < 1.3$ K, the Seebeck signal is difficult to measure in continuous field sweeps due to the rise of a large background signal which we could not identify. This background does not occur in field step measurements (blue dots in the figure), which correspond to the real Seebeck signal. Additional data in continuous field sweeps is presented in appendix A. The anomalies corresponding to the A'- and B-

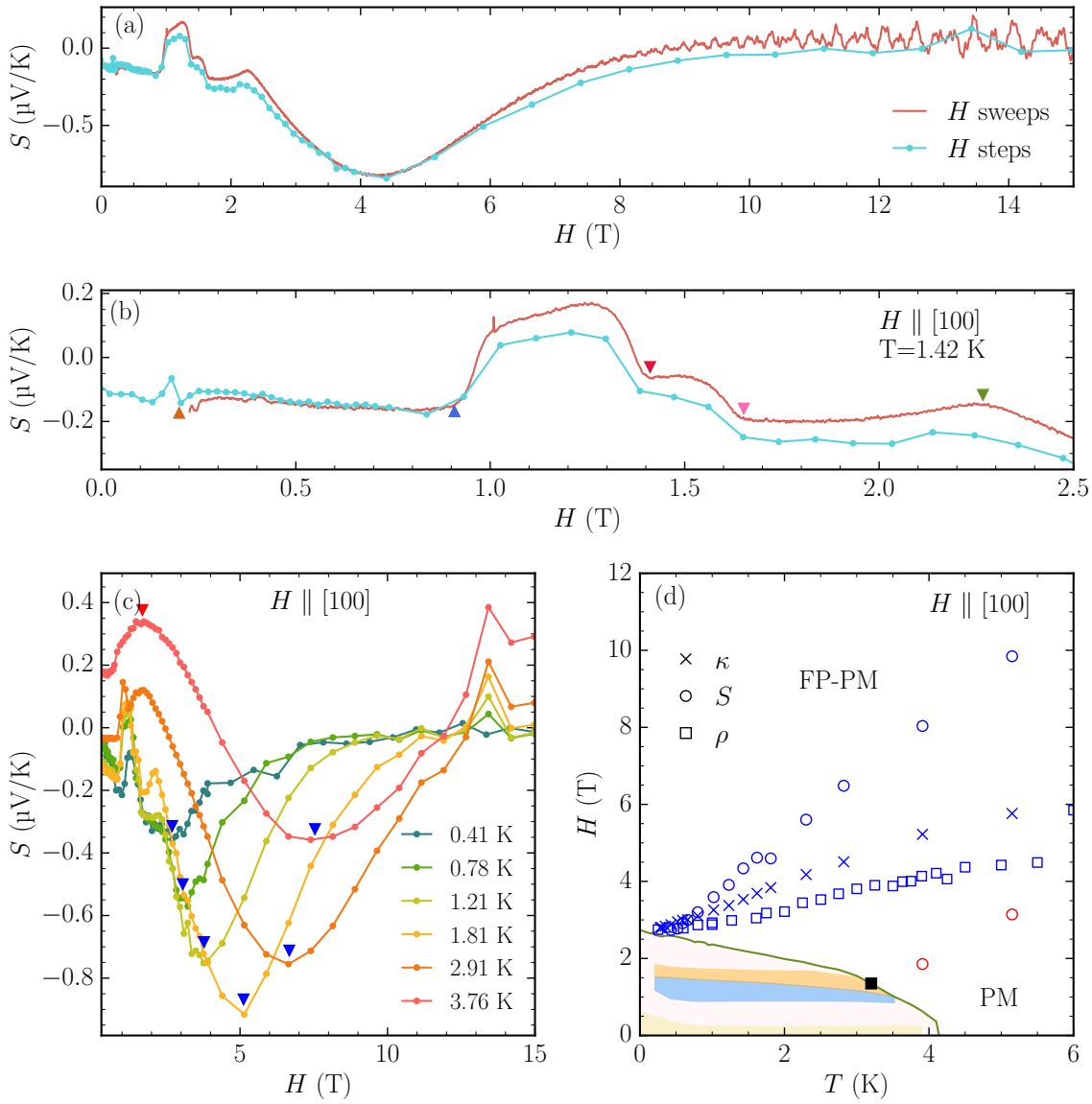

Figure 3.36: (a), (b): comparison between $S(H)$ measurements with continuous H-sweeps (red) and H-steps (blue) at 1.42 K, between 0 and 15 T (a) and between 0 and 2.5 T (b). Arrows in (b) correspond to the transitions H_D, H_{A1}, H_{A2}, H_B and H_C in order of increasing field. (c): Seebeck signal measured by H-steps for temperatures between 0.4 and 3.8 K over the whole field range (the data points are linked for clarity). Arrows indicate the extrema reported in (d). (d): extended phase diagram with the extrema from $S(H)$, $\kappa(H)$ and $\rho(H)$ (circles, crosses and squares, respectively). The black square indicates the position of a tricritical point from ref. [81].

phase are easily evidenced (3.36 (b)) and match very well the $\rho(H)$ measurements. Both phases yield large positive contributions with sharp transitions. Much like in resistivity, the A'-phase is larger than the B-phase in the Seebeck coefficient, reaching 0.14 μV/K at its largest for $T = 1.4$ K, compared to 0.7 μV/K for the B-phase.
We also report the presence of high-field energy scales coherent with the previous two orientations. The minimum in the Seebeck signal extends linearly with T and H from the conical to FP-PM transition at around 2.8 T and 0.5 K, and has been followed up to 10 T at 5 K. The thermal conductivity also presents a maximum related to the same energy scales (not shown here), with the extrema in both probes presented in the extended $H - T$ phase diagram 3.36 (d) with the minima in resistivity measurements. These field and temperature scales clearly mark the crossover to the fully polarized paramagnetic state.
The local maxima in the $S(H)$ data, on the other hand, have only been observed for two temperatures for this orientation, and are denoted by red circles in the figure 3.36 (d). Interestingly, contrarily to the previous orientations (see figures 3.20 (right) for $H \parallel [110]$ and 3.26 (top right) for $H \parallel [111]$), in the $H \parallel [100]$ direction the maximum in $S(H)$ seems to form a critical line coinciding well with the tricritical point determined by Sakakibara et *al.* in [4]. For this orientation magnetization measurements in the literature yield $H_{\mathrm{TCP}} = 1.35$ T and $T_{\mathrm{TCP}} = 3.2$ K, indicated by a black square in the figure. Further studies with more data would help clarify the relation between the TCP and the Seebeck coefficient anomalies. The clear quantum oscillations visible in figure 3.36 (a) are analyzed in detail in the next chapter.

For the field direction $H \parallel [100]$ of EuPtSi, the previously established phase diagram shows magnetic phases down to 0.1 K. The Seebeck coefficient measurements, however, could only be performed above 0.4 K, even with H-steps. Nevertheless, the Seebeck effect has proven to be a powerful probe picking up on magnetic transitions due to the formation of skyrmion lattices, large quantum oscillations invisible in resistivity, and indications of the spin polarization of the FP-PM state.
In this section, we have seen the field dependence of the ordered phases of EuPtSi below the Néel temperature for the three main crystal orientations. We have recovered the $H-T$ phase diagram and shown the hysteretic features of the A-, A'- and B-phases. We have also measured the topological Hall effect in the A, A' and B phases, and evidenced the cross-over between the PM and the FP-PM regimes from various transport probes. From precise low-temperature resistivity measurements, we have also evidenced the existence of the B-phase down to 0.1 K and a possible indication of a mixing of the A'- and B-phases. We also report the presence of a new anomaly rising at around 1.1 T below 0.25 K for the $H \parallel [100]$ direction. This anomaly is only observed for $H \parallel [100]$ and can be assumed to be connected to the existence of both the A'- and B-phases as it is not observed for $H \parallel [111]$.

3.3 Metastable skyrmion lattice phases under field cooling

We will now study the temperature dependence of the transport properties of EuPtSi. For the sake of clarity, anomalies in the temperature dependence corresponding to transitions from the $H-T$ phase diagram will be named as per their field equivalent, for example $T_{A1} \equiv H_{A1}$. As the $H \parallel [110]$ direction has no skyrmion lattice (SkL) phase, $\rho(T)$ measurements have already been presented in section 3.2.2 and no anomalous magnetic structures or hysteretic behaviors were observed between increasing and decreasing temperature sweeps. For the directions $H \parallel [111]$ and $H \parallel [100]$, on the other hand, decreasing temperature sweeps yield different results in the transport properties whether the magnetic field is applied first (i.e. field-cooling conditions) or not (zero-field cooling). With specific cooling conditions depending on the magnetic history, SkL phases can be created in temperature ranges different from those seen thus far. The resulting phases are then called metastable phases and the metastability evidences the topological robustness of the skyrmion lattices [104].
The metastable behavior of SkL phases in EuPtSi and in MnSi from the literature is first presented, followed by our own results for the $H \parallel [111]$ and $H \parallel [100]$ directions, extending the respective phase diagrams down to the lowest temperatures available in our measurements.

3.3.1 State of the art

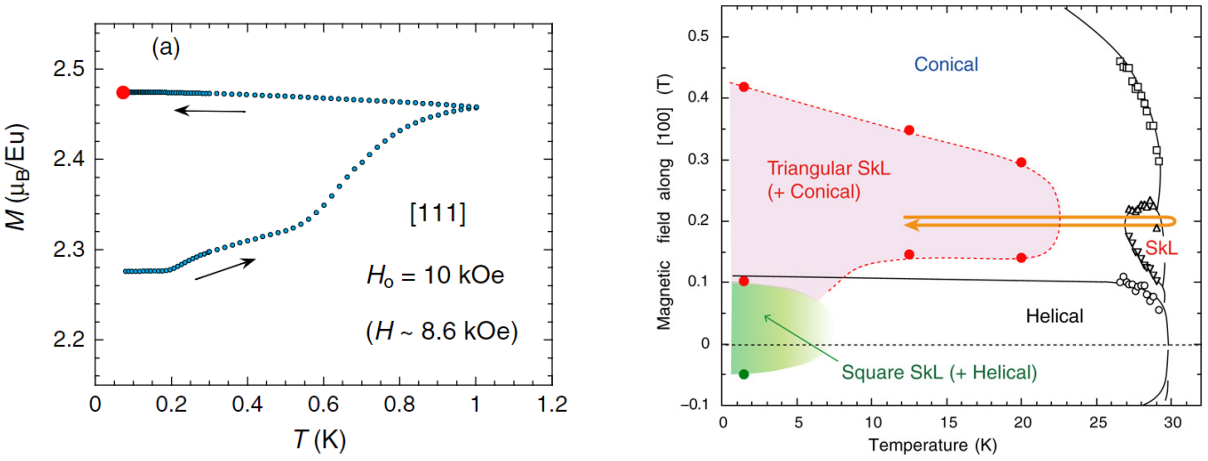

Figure 3.37: Left: $M(T)$ measurements of EuPtSi from [4]. H_0 is the magnetic field applied at 60 mK before the T-sweeps, and H is the renormalized field due to the demagnetizing correction, respectively. The arrows indicate the direction of the temperature sweeps, and the red dot is the end of the sweep in the metastable A-phase. Right: $H-T$ phase diagram of MnSi from field-cooling Small-Angle Neutron Scattering (SANS) measurements, from [105].

The difference in the behavior of the magnetization between increasing and decreasing temperature sweeps below 1 K for $H \parallel [111]$ in EuPtSi has been highlighted by Sakakibara

et *al*. Their results are shown in figure 3.37 (left), from [4]. A magnetic field of 0.86 T is applied at 60 mK after zero-field cooling (ZFC). Upon heating, the transition from the conical state to the A-phase occurs at around 0.5 K (the first step in figure 3.37 possibly corresponds to a q domain reorientation), with a value of $M = 2.6\ \mu_B$/Eu at 1 K.

Upon field cooling (FC), the magnetization retains a value close to that in the A-phase, without showing any form of transition back to the conical order even at 60 mK. This suggests the metastable behavior of the SkL phase. Subsequent field sweeps at low temperature (not shown here) indicate a tilted plateau structure similar to the A-phase signature, and discontinuous jumps back to the conical order for fields corresponding to the extrapolated values of the critical lines of the transitions H_{A1} and H_{A2} in the $H-T$ phase diagram. This metastable A-phase has been confirmed to be stable for at least 10^4 s at low temperature. Similar observations are reported in the same article for the A'-phase for $H \parallel [100]$.

A metastable SkL is also observed in MnSi [105, 106], however rapid quenching at 700 K/s was needed, whereas even slow FC in EuPtSi results in the metastable SkL state. The $H-T$ phase diagram of MnSi obtained with FC is reported in figure 3.37 (right), from [105].

Many other systems exhibit metastable SkL phases. In EuPtSi, the SkL phases are formed at unusually low temperatures in the normal state. As such, the possibility of obtaining a metastable skyrmion lattice state at low temperature provides a rare opportunity to study the ground-state properties of such phase. At the time of writing this thesis, the magnetization measurements from Sakakibara et *al*. are the only reported observations of this behavior in EuPtSi, and only cover the A- and A'-phases, respectively for the [111] and the [100] directions. There have been no report of similar results from transport probes, and no observation of the metastable B-phase.

3.3.2 Metastable A-phase for $H \parallel [111]$

Measurements of $\rho(T)$ are presented in figure 3.38 for various fixed magnetic fields applied along the [111] direction. For each measurement, the magnetic field is applied at low temperature after ZFC, therefore keeping the system in the helical/conical state. The data were then acquired by sweeping the temperature continuously from 0.25 K to 6 K, and then back to 0.25 K. For a visual aid, the temperature sweeps are reported on the phase diagram in figure 3.39 as horizontal lines with colors corresponding to figure 3.38. T sweeps at zero field recover the behavior similar to the $H \parallel [110]$ direction, with the step-like transition at $T_N = 4.05$ K, indicating the ordering of the spins and therefore the reduction of magnetic scattering of the conduction electrons. The transition corresponding to H_C for field sweeps decreases with field and fits very well the critical line in the phase diagram. A non-Fermi liquid (NFL) behavior is observed in the conical state, with $\rho(T) \propto T^n$ with $n = 1.55$ at zero field and $n \neq 2$ in the conical state, similarly to the $H \parallel [110]$ direction. The analysis of the NFL behavior is shown in more detail in appendix A, as this section focuses on fields corresponding to the A-phase, $H_{A1} \approx 0.8$ T $< H < H_{A2} \approx 1.3$ T.

Increasing temperature $\rho(T)$ shows the sharp transition from the conical state to the A-phase at 0.45 K for $H = 1.21$ T. The conical state is recovered at higher temperature, before the pronounced transition from the conical to the field-polarized paramagnetic state

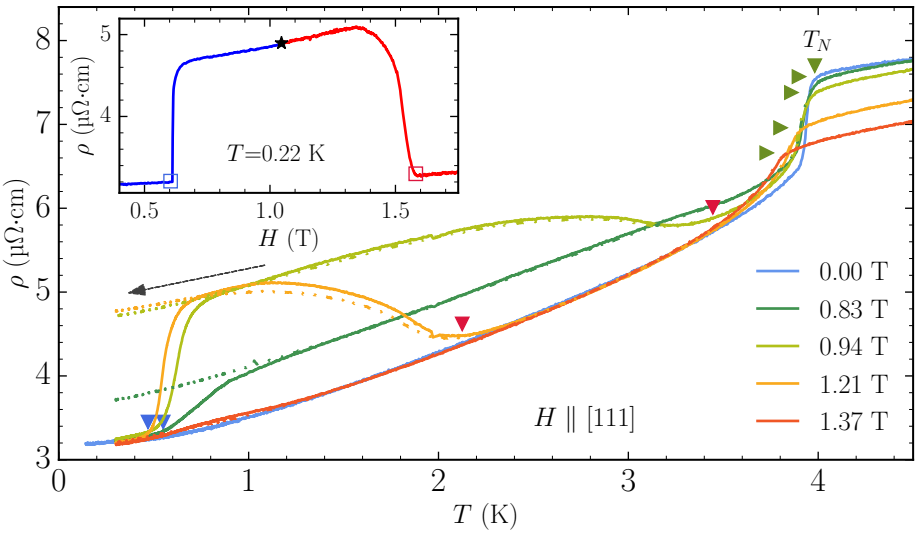

Figure 3.38: Temperature dependence of ρ for various fixed magnetic fields along the [111] direction after initial ZFC. Solid lines (dotted lines) denote increasing (decreasing) temperature sweeps between 0.25 K and 4.5 K. The blue triangles indicate the entering into the A-phase, and red triangles indicate transitions back to the conical state. Green triangles denote the H_C transitions (T_N at 0 T). The black arrow shows the decreasing T-sweep in the metastable A-phase. Inset: field sweeps performed from the metastable state at 0.22 K, with the starting point at 1.04 T indicated by a star. Open squares indicate the sharp transitions back to the conical state and are reported on the phase diagram in figure 3.39.

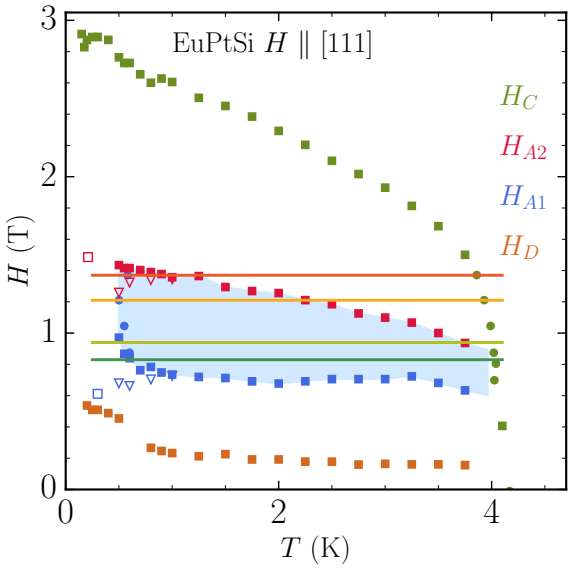

Figure 3.39: $H-T$ phase diagram of EuPtSi for $H \parallel [111]$, from figure 3.23 with additional horizontal lines indicating temperature sweeps from fig. 3.38. Open squares are the H_{A1} and H_{A2} transitions from the metastable A-phase to the conical state.

at around 4 K. The amplitude of ρ in the A-phase is in agreement with the field-dependent measurements. In equilibrium conditions, the SkL phase is stabilized by thermal fluctuations at finite temperature [1]. This temperature of 0.45 K is very low compared to $T_N = 4.05$ K, around 10 %, which implies that the free energy of the A-phase is only slightly different from that of the conical state [4].

During field cooling (indicated by the black arrow), no transition is observed below 1 K, indicating that the A-phase is stable down to lowest temperatures. This implies that the super-cooled metastable SkL state persists down to temperatures much lower than expected, down to the lowest temperatures available in our setup. In the metastable A-phase, ρ decreases with a $\rho(T) \propto T^{1.3\pm0.1}$ dependence, from the value at 1.3 K. The existence of this metastable phase means that the free energy difference between the conical and the SkL state is rather small. When thermal agitation is sufficiently low, the system remains in the SkL state instead of transitioning back to the conical state, emphasizing the stability of the SkL state in the super-cooled regime.
After attaining the metastable SkL state, a field sweep as shown in the inset of figure 3.38 at $T = 0.22$ K shows the A-phase for a large field range, between 0.6 and 1.55 T. The H_{A1} and H_{A2} transitions from the metastable state correspond to their respective critical lines at lower temperatures, as indicated by open squares on the phase diagram fig. 3.39. The metastable A-phase is thus strongly irreversible against a field sweep. Subsequent field sweeps cannot recover the metastable state and the FC protocol has to be repeated in this case.
To make sure the various magnetic states below T_N had no part in the metastable behavior of the A-phase, we have performed field coolings down from the paramagnetic state well above 4 K. This metastable A-phase state can be obtained under field-cooling independently of the magnetic history and whether the system is first heated at zero field or under field. The resistivity value obtained after field-cooling is the same for decreasing temperature sweep rates of 1 K/h and 3600 K/h, from $T > 4$ K and $1 < T < 4$ K. We have also confirmed the stability of this metastable state with respect to time, with no change in ρ for at least up to 72 hours (not shown here). It shows that the super-cooled A-phase has an extremely slow dynamic.
Measurements of the temperature dependence of the Hall effect are presented in figure 3.40, with the black arrow indicating the decreasing sweep direction. The T sweep rate is the same and the field is first applied at low temperature, similarly to the longitudinal resistivity protocol described above. In agreement with the longitudinal resistivity data, the metastable A-phase is kept at low temperature with the hysteresis opening at around 1.2 K at 1.21 T. The high temperature of the hysteresis opening might be due to slight differences in the positive and negative sweeps, shifting the sweep-up and -down curves.

Using a protocol similar to the ρ measurements previously described, we have measured the temperature dependence of S and κ for the [111] direction, shown in figure 3.41, left and right, respectively. Continuous temperature variation between 0.25 K and 6 K is not possible with our setup for these probes, and the measurements were made in two sets, above and below 1 K. This does not matter as we have seen with ρ that the metastable A-phase does not depend on whether the field is applied at low T or not. Seebeck coefficient measurements follow an almost flat temperature dependence in the A-phase close to 0 μV/K. The $T_C \equiv H_C$ anomaly is a very small bump at all fields.

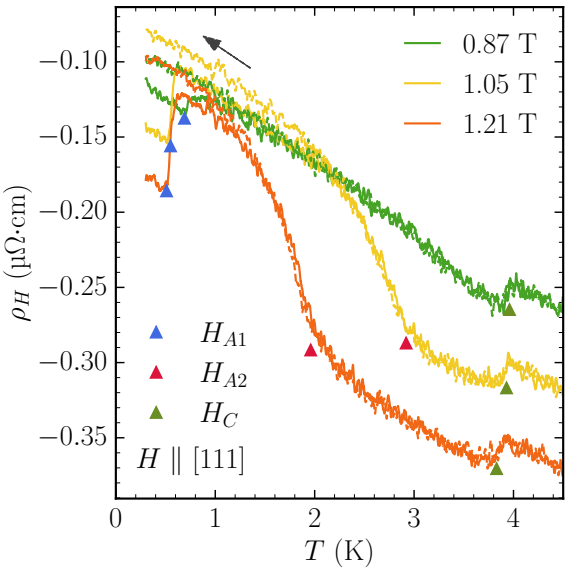

Figure 3.40: Temperature dependence of the Hall resistivity for fields corresponding to the A-phase. Colored triangles indicate the transitions H_{A1} (blue) upon entering the A-phase, H_{A2} (red) between the A-phase and the conical order, and H_C (green) between the conical and the PM orders. The black arrow indicates the decreasing T sweep. Upon field-cooling, the transitions H_{A1} is not observed as the system remains in the metastable A-phase.

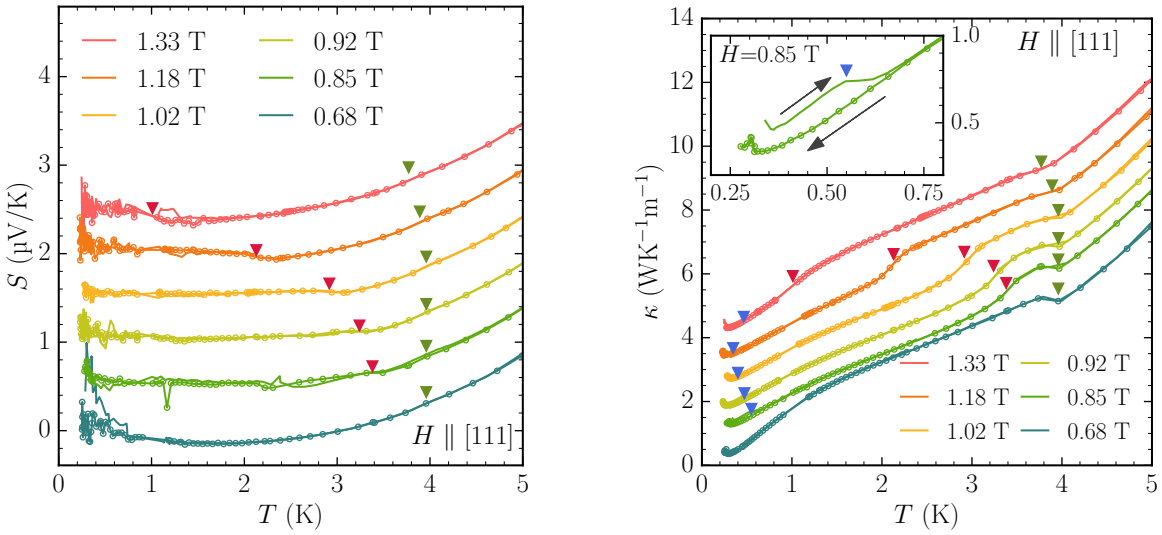

Figure 3.41: Temperature dependence of the Seebeck coefficient (left) and thermal conductivity (right) at various fixed fields and below 5 K. Data is acquired in two ranges, for $T < 1$ and $T > 1$ K. Increasing T data is in full lines and decreasing T in linked circles. For both probes the curves are shifted vertically with respect to the 0.68 T data. The inset for κ shows the temperature hysteresis due to the metastable A-phase at 0.85 T, with the black arrows indicating the T-sweep direction. No hysteresis is seen in the $S(T)$ data. Colored triangles in both figures indicate the crossing of transition lines from the phase diagram, H_{A1} in blue, H_{A2} in red and H_C in green.

In the conical and PM orders, the temperature dependence of the Seebeck coefficient is indistinguishable. To measure the Seebeck coefficient at such low temperatures, we have reduced the temperature gradient, which also reduced the voltage signal drastically, yielding very noisy $S(T)$ measurements below 1 K. As such we have not observed the metastable A-phase with this probe. Thermal conductivity measurements, on the other hand, exhibit a clear distinction between increasing and decreasing temperature behavior. This is shown in the inset of figure 3.41 (right). The transition from the conical state to the A-phase around 0.4 K manifests by a decrease in κ, indicated by blue triangles in the figure. An increase of similar size is measured at higher T, when recovering the conical state (red triangles), i.e. crossing the H_{A2} transition line. The H_C transition (green triangles) follows a change of slope as κ increases rapidly with T in the paramagnetic state. Under field cooling, κ decreases with the same slope as in the A-phase with no evidence of a transition back to the conical state, again implying the super-cooled metastable state.

As a recap, we have successfully observed the metastable behavior of the SkL A-phase for EuPtSi $H \parallel [111]$ using both a transport probe (ρ) and a thermodynamic probe (κ). The agreement with the magnetization measurements in the literature is very convincing [4]. To ensure the lack of influence of the magnetic history on our results, we have performed field-cooling down from the paramagnetic state and under various conditions. The metastable state is robust in time and exists as a continuation of the $H-T$ phase diagram down to 90 mK instead of 450 mK expected from the field dependence.

3.3.3 Metastable A'- and B-phases for $H \parallel [100]$

For the magnetic field applied parallel to the [100] direction, the A' and B skyrmion lattice phases exist down to 250 mK, as already discussed in section 3.2.4. From the field dependence described previously, we actually have found anomalies in the resistivity down to lower temperatures. From the temperature dependence of ρ, using the same protocol as for the [111] direction, we will see that our results point to the existence of an additional magnetic phase or the coexistence of both A' and B phases.

The temperature dependence $\rho(T)$ for $H \parallel [100]$ is presented in figure 3.42 for increasing (full lines) and decreasing (dashed lines) temperature sweeps between 0.1 and 4.1 K for different fields. Colored triangles indicate the different transitions observed in the $H-T$ phase diagram shown in figure 3.33: H_{A1} in blue, H_{A2} in red, H_B in pink and H_C in green. For each measurement, the field is first applied at 0.1 K with a slow sweep rate of 0.05 T/min to avoid heating due to eddy currents. The data shown were acquired in two segments $0.1 < T < 0.85$ K and $0.8 < T < 4.2$ K, at 1 and 3 K/h, respectively. The power-law dependence of $\rho(T)$ in the conical state and the step-like increase at T_C at low fields are similar to the previous field directions (not shown here).
At $H = 0.88$ T, close to the border between the A'-phase and the conical state, a very small increase in $\rho(T)$ occurs at $T \approx 0.5$ K, indicating a transition from the conical state to the A'-phase. At this field, the transition H_{A1} is almost horizontal on the phase diagram (as seen schematically in the inset of figure 3.42), and the distinction between the A'-phase and the conical order is hard to define above 1 K. The sharp step-like transition at 3.7 K into the PM state, however is clear. On cooling, a small hysteresis opens around

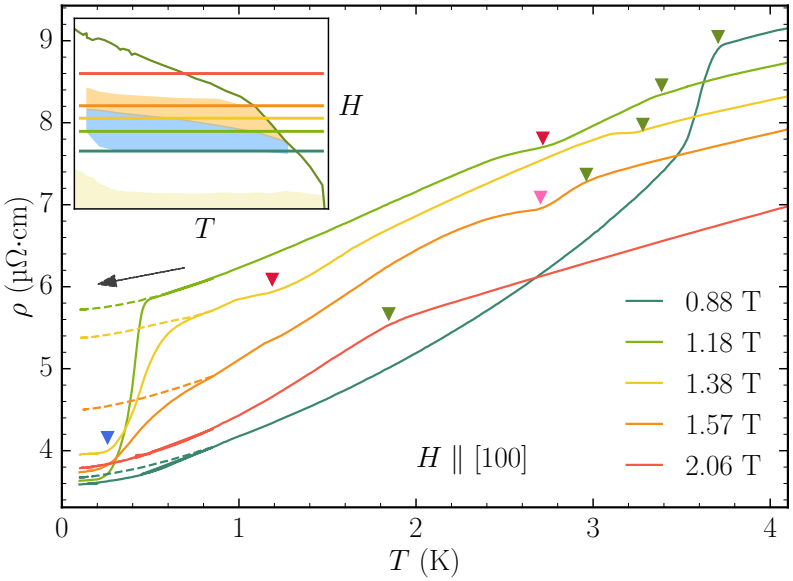

Figure 3.42: $\rho(T)$ measurements for $H \parallel [100]$ between 0.1 K and 4.1 K for different fields. Increasing T is plotted in full lines and decreasing fields in dashed lines. Colored triangles indicate transitions in the $H-T$ phase diagram from figure 3.33 (H_{A1} in blue, H_{A2} in red, H_B in pink and H_C in green). The inset represents the T-sweeps at different magnetic fields schematically on the phase diagram.

0.75 K, indicating that the A'-phase can be super-cooled.
At $H = 1.18$ T, the system enters the A'-phase at 0.25 K upon heating with a very sharp transition. At 2.7 K, a dip in the resistivity indicates the crossing of the H_{A2} transition from the A'- to the B-phase. In this temperature range, however, both SkL phases have very small resistivity signatures, as already seen in figure 3.30. The transition into the PM regime is observed as a change of slope at $T_C = 3.4$ K. On cooling at 1.18 T, the temperature hysteresis opens at 0.45 K, with no observation of the transition from the A'-phase back to the conical order. Instead, the resistivity forms a slanted plateau indicating the metastable A'-phase.
At $H = 1.38$ T, the system enters the A'-phase on heating at 0.25 K. At this field, the crossing between the A'- and the B-phase (H_{A2} transition line) occurs at 1.2 K with $\rho(T)$ showing a dip in amplitude. No hysteresis is observed between the two phases upon heating and cooling. With further heating, the system then remains in the B-phase until $T_C = 3.3$ K where ρ decreases in the B→PM transition. At this field, cooling shows a temperature hysteresis opening at 0.65 K as the system stays in a metastable SkL state with $\rho(0.1\text{ K}) = 5.35$ $\mu\Omega$·cm.
At $H = 1.57$ T, the system remains in the B-phase upon heating from 0.25 K to 2.7 K. The conical state is recovered between the transition H_B (pink triangle) at 2.7 K and the transition $T_C = 3$ K. The transitions in this temperature range are broad, as the transition lines are almost horizontal on the phase diagram (schematically recalled in the inset of figure 3.42). Cooling at $H = 1.57$ T shows a hysteresis opening around 0.85 K, highlighting the metastable B-phase in a similar fashion as the A' metastable phase described previously.

At $H = 2.06$ T, the system stays in the conical ordering until the transition H_C into the PM regime at 1.9 K. No hysteretic behavior is observed between heating and cooling at this field.
From the temperature sweeps, one can recover the various phases of the $H-T$ phase diagram in good agreement with the $\rho(H)$ measurements. Because the A'- and B-phases lie horizontally on the phase diagram, the transitions are broad but nonetheless visible. Both phases indicate a clear temperature hysteresis in $\rho(T)$ at lower temperatures ($T < 1$ K), which is highlighted in figure 3.43.

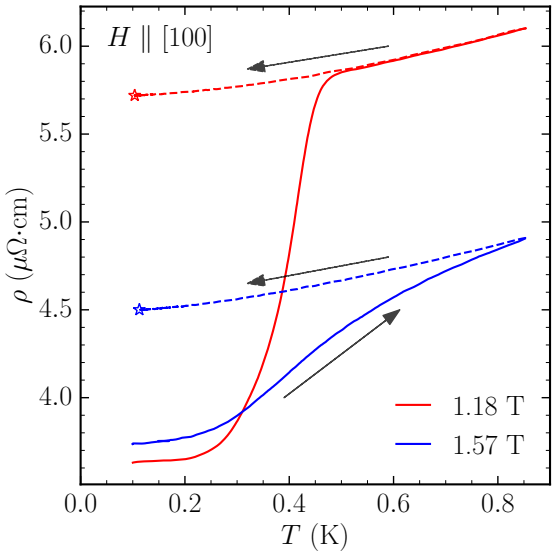

Figure 3.43: $\rho(T)$ measurements for $H \parallel [100]$, between 0.1 K and 0.85 K. Increasing T is plotted in full lines and decreasing fields in dashed lines. Stars indicate the end of the T-sweeps in the metastable A'-phase at 1.18 T (red) and metastable B-phase at 1.57 T (blue).

The distinction between the two SkL phases in $\rho(T)$ lies in the width of the low-temperature transition during the heating process. As seen in figure 3.43, for the A'-phase at $H = 1.18$ T, the transition at ≈ 0.25 K is narrow, with a width of $\Delta T = 0.15$ K, from 3.7 to 5.8 $\mu\Omega$·cm. The transition into the B-phase also starting at ≈ 0.25 K for $H = 1.57$ T is much wider with $\Delta T > 0.5$ K and only reaches 4.8 $\mu\Omega$·cm at 0.85 K. Upon field-cooling, the system remains in a metastable state with a resistivity slightly decreasing from the height of the transition, reaching 5.7 $\mu\Omega$·cm for the super-cooled A'-phase ($H = 1.18$ T), and 4.5 $\mu\Omega$·cm for the super-cooled B-phase ($H = 1.57$ T). The stars indicate the end of the temperature sweeps.

After field-cooling the system as described previously, we have performed slow field sweeps from the metastable states at around 0.11 K. The following example details the complete measurement protocol:

- Zero field cooling down to $T = 0.11$ K.

- H-sweep from 0 T to 1.18 T at 0.05 T/min, $T = 0.11$ K.
- T-sweep from 0.11 K to 0.85 K at 1 K/h, $H = 1.18$ T (solid red curve of figure 3.43).
- T-sweep from 0.85 K to 0.11 K at 1 K/h, $H = 1.18$ T (dashed red curve of figure 3.43), ending at the red star in the metastable A'-phase.
- H-sweep from 1.18 T to 0.5 T or from 1.18 T to 2 T at 0.05 T/min, represented in figure 3.44 (left) starting from the red star, with the field direction indicated by arrows. Other starting points (stars) are naturally obtained using a similar protocol with a different field.

The results are shown in figure 3.44 with the starting points of the H-sweeps indicated by stars and black arrows denoting the field sweep direction.

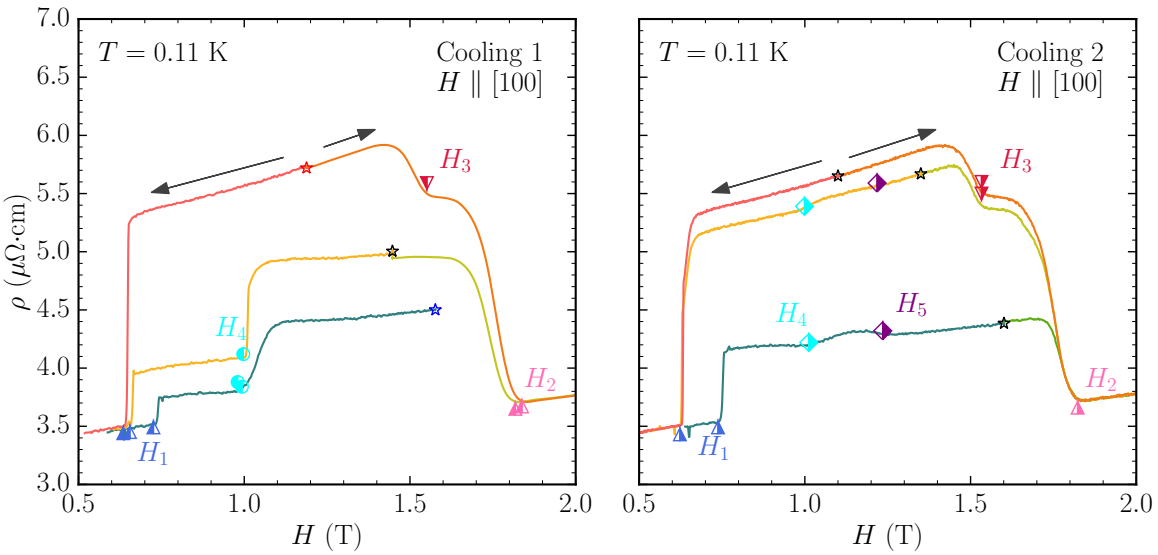

Figure 3.44: Field dependence of ρ from the metastable A'- and B-phases induced by field cooling, for temperatures close to 0.11 K. The two graphs correspond to two different measurements in similar conditions with the same sample. Black stars indicate the starting point of the H-sweeps (1.45 T on the left panel, 1.1, 1.35 and 1.6 T on the right panel), and the direction of the sweep is given by the black arrows. The red and blue stars at 1.18 and 1.57 T on the left panel are reported from figure 3.43. Anomalies in the metastable H-sweeps are labeled with numbers from 1 to 5.

We have performed two series of measurements. The experimental setup was heated back to room-temperature between the two. Both coolings were operated successively under identical conditions with the same sample and same contacts, at different times.
Let us start with the first cooling, on the left panel of figure 3.44. The red and blue stars correspond to the T sweeps shown in figure 3.43, at 1.18 and 1.57 T respectively.
From preparing the system in the metastable A'-phase at 1.18 T at 0.11 K, a subsequent decreasing field sweep shows a tilted plateau ending with a sharp transition at $H_1 = 0.65$ T (blue triangle). This anomaly corresponds to the edge of the critical line of H_{A1} for decreasing fields and indicates the system leaving the super-cooled phase and

recovering the conical order. Starting at the same point but with an increasing sweep yields two consecutive anomalies. At $H_3 = 1.5$ T (red triangle) the resistivity decreases from the metastable A'-phase to the metastable B-phase. One can note the similarity in $\rho(H)$ behavior with H-sweeps in the SkL phases at equilibrium at higher temperature in section 3.2.4. A second transition at $H_2 = 1.8$ T (pink triangle) shows the B→conical transition, in agreement with the H_B transition line from the phase diagram.
After preparing the system in between the metastable A'- and B-phases at 1.45 T (black star), increasing field sweeps also show the H_2 anomaly at 1.8 T. Decreasing field sweeps show two anomalies at $H_4 = 1$ T and $H_1 = 0.65$ T (light blue circles and dark blue triangles, respectively). These two anomalies are also observed in decreasing field sweeps from the metastable B-phase (starting at the blue star at 1.57 T).
The fields corresponding to the previously mentioned anomalies H_{1-4} are reported as half-filled circles on the low-temperature phase diagram in figure 3.45, with the numbering as a visual aid. The bottom panel of figure 3.45 shows the same phase diagram as the top panel, split between anomalies observed in increasing field sweeps (left) and decreasing field sweeps (right), for visual clarity. Anomalies denoted H_1, H_2 and H_3 in the metastable region all fit very well to the low-temperature continuation of the critical lines in the equilibrium phase diagram. As such, we have $H_1 \equiv H_{A1}$ for decreasing fields, $H_2 \equiv H_B$ for increasing fields, and $H_3 \equiv H_{A2}$ between A' and B for increasing fields. The presence of H_3 around 1.5 T instead of 1.35 T may be an indication of the metastable A'-phase partially drowning the signal of the metastable B-phase, as we observed in $\rho(H)$ measurements (see figure 3.31).
The downwards step in $\rho(H)$ at H_4 in figure 3.44 could be attributed to the transition B→A' between the two metastable phases, however the anomaly occurs at lower fields than expected. In fact, one would expect the transition B→A' around 1.35 T as a continuation of H_{A2} measured in decreasing fields. Instead, H_4 occurs very close to the newly found anomaly around 1.1 T from $\rho(H)$ measurements (see figure 3.31), depicted as green squares in the low temperature phase diagram.
From this first cooling measurement, we can conclude that despite the system having remained in only one phase during the metastable state preparation, one can also detect the other metastable phase. The amplitude of the resistivity in the FC induced metastable phases is much higher than otherwise observed during field sweeps after ZFC, proving their metastability. Both the A'-phase and the B phase are thus very stable with respect to temperature fluctuations. With respect to field, on the other hand, the super-cooled phases both disappear once the critical fields are reached (H_1 for decreasing sweeps and H_2 for increasing ones), and subsequent field variations cannot recover the metastable phases. Only the field cooling process allows the creation of such metastable phases.

In order to further study the anomaly H_4, we have then performed a second measurement using the same protocol, the results of which are on the right graph of figure 3.44. Placing the system in the metastable A'-phase at 1.1 T, we recover the same behavior as for the first cooling, with the transitions $H_1 \equiv H_{A1}$ for a decreasing field sweep, $H_3 \equiv H_{A2}$ and $H_2 \equiv H_B$ for an increasing field sweep.
A decreasing sweep starting at 1.35 T in the metastable A'-phase, however, shows additional anomalies at $H_5 = 1.3$ T (purple diamond) as a small increase and at $H_4 = 1$ T (blue diamond) as a downwards step in the metastable A'-phase. With the system pre-

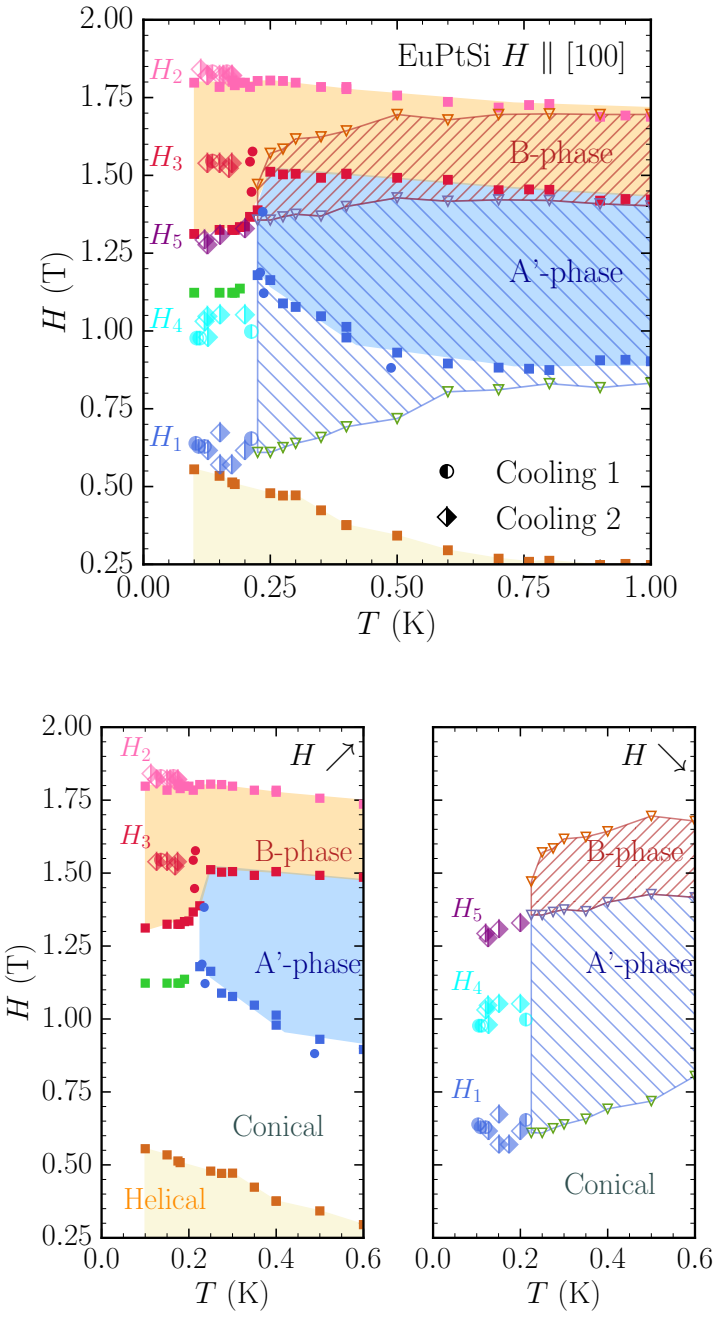

Figure 3.45: Top: low temperature $H-T$ phase diagram for EuPtSi H ∥ [100] from H-sweeps measurements, from figure 3.33. Full squares (open triangles) are transitions from increasing (decreasing) H-sweeps in the 'normal' state, and the shaded (hatched) areas are the A'- and B-phases. Green squares at 1.1 T correspond to the additional anomaly from low temperature H-sweeps (see figure 3.31). Full circles are transitions from $\rho(T)$ measurements. Anomalies in the H-sweeps from the metastable states are represented with half-filled circles (1st cooling) and diamonds (2nd cooling), with the same numbering as in figure 3.44. Bottom: same phase diagram as the top panel, between 0 and 0.6 K, split between the anomalies observed in increasing field sweeps (left) and decreasing field sweeps (right) both in the 'normal' and the metastable state.

pared in the metastable B-phase at 1.6 T, a decreasing field sweep indicates a clear bump between $H_5 = 1.35$ T and $H_4 = 1$ T, and a sharp transition from the metastable phase to the conical state at $H_1 = 0.75$ T (blue triangle). It is to be noted that small field fluctuations from the superconducting magnet are enough to destroy the fragile metastable states, sometimes causing the H_1 anomaly to be observed at slightly higher fields than 0.65 T, highlighting the strong field-irreversibility of the super-cooled phases.
The transitions H_1, H_2 and H_3 are in agreement with the previous cooling. The bump between H_4 and H_5, on the other hand, lies in the phase diagram between the decreasing H_{A2} transition line and the green line from the newly found anomaly. Because the amplitude of the resistivity is similar before and after the bump, one could imagine the coexistence of two different magnetic phases. Both anomalies H_4 and H_5 being observed in a decreasing field sweep starting from the A' metastable phase may indicate that the amplitude of the A'-phase could have drowned the H_5 anomaly in the first cooling measurement.

The two different data sets performed under the same conditions yield different results. As of the time of writing, we have not been able to explain these discrepancies. However, the two measurements do coincide with the $H - T$ phase diagram. In keeping with the $H \parallel [111]$ direction results for the metastable A-phase, the various anomalies in the metastable states for $H \parallel [100]$ lie in the continuation of critical lines at lower temperature. Despite the resistivity not allowing much insight in the microscopic nature of the different phases, our measurements suggest the existence of an additional low-temperature phase that is visible in the metastable state and otherwise hidden by the amplitude of ρ in the equilibrium state. The low-temperature $H - T$ phase diagram of EuPtSi for this field direction yields four different results whether the variables (H and T) are swept up or down, in combination of one another. Unfortunately, so far there have been no reports of neutron or X-ray scattering experiments that would clarify the magnetic orders in the A'- and B-phases.

3.4 Conclusion

In this chapter, we have studied the transport properties of the recently discovered skyrmion host EuPtSi in its ordered magnetic phases below T_N, namely the helical, conical and skyrmion-related phases, as well as in the paramagnetic and field-polarized states. For the $H \parallel [110]$ direction for which no skyrmion lattice phase has been reported, we have measured an anomalous temperature dependence of the resistivity $\rho(T) \propto T^n$ with $n < 2$ in the conical phase below the H_C transition. We have also evidenced the presence of additional energy scales in the paramagnetic state through Seebeck coefficient and thermal conductivity measurements. These energy scales might be related to the field polarization of the magnetic moments and to the presence of a tricritical point in the H_C transition.

For the $H \parallel [111]$ direction, we have measured the anomalous scattering induced by the skyrmion A-phase with ρ, S, N, κ and ρ_H. In the Hall resistivity in particular we have confirmed the signature of the topological Hall effect due to the emergent field induced by the triple-q skyrmion lattice.

From resistivity measurements in the $H \parallel [100]$ direction with the two skyrmion-related phases A' and B, we have prolonged the phase diagram with evidence of the B-phase persisting down to 0.1 K. We have highlighted the presence of a new anomaly at

low temperatures, which might be related to the mixing of various ordered phases. Our temperature-dependent measurements in the A' and B phases show the low-temperature metastable behavior of both phases and indicate a shared formation mechanism as both metastable states can be induced from the preparation of the system in either one of them. The field dependence of ρ in the metastable phases confirms our observations of an additional structure at low temperature.

Chapter 4

Quantum oscillations in the thermoelectric power of EuPtSi

In the previous chapter, we have studied the low-field magnetic phases of EuPtSi below the conical/paramagnetic transition. We will now study the Fermi surface of EuPtSi with quantum oscillations measurements in the thermoelectric power. As a transport probe with a high sensitivity to changes in the density of states, the thermoelectric power is a very powerful tool to detect quantum oscillations. We have thus observed the various Fermi surface pockets of the system and recovered effective cyclotron masses for each pocket for the three main orientations. We have also investigated the field-dependence of the quantum oscillation amplitude. We will introduce a new analysis framework allowing us to recover parameters such as the Dingle temperature and the mean-free path from the observation of quantum oscillations in the thermoelectric power.

Chapter contents

4.1 State of the art - Fermi surface of EuPtSi

As EuPtSi has already been presented in the beginning of chapter 3, in this section we will ignore the low-field ($H < 5$ T) properties of the compound and focus instead on the Fermi surface properties. Indeed quantum oscillations are observed in high magnetic field sweeps ($H > 5$ T in EuPtSi), meaning the compound remains in the field-polarized paramagnetic state for these measurements. Most of the information on the Fermi surface of EuPtSi found in the literature comes from Kakihana et *al.* [5]. In their work, they measured quantum oscillations in the ac-susceptibility, the so-called de Haas-van Alphen (dHvA) effect, while rotating the sample to cover the angular dependence of the dHvA frequencies. The sample used for dHvA measurements in that work has a residual resistivity ratio $RRR = 30$.
The typical Fast Fourier Transform (FFT) spectrum of EuPtSi for the $H \parallel [100]$ direction, from [5], is shown in figure 4.1 for a field window of 8-13.5 T. As revealed by the angular

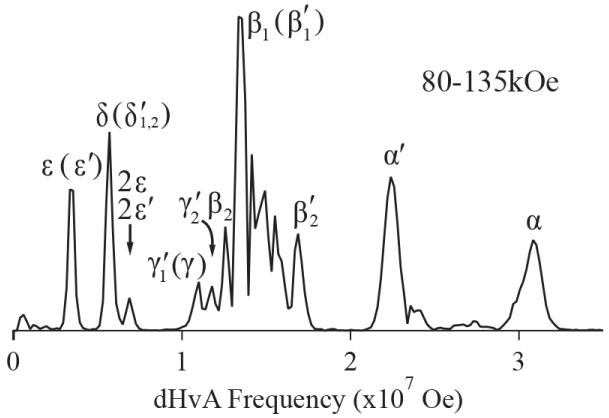

Figure 4.1: FFT spectrum for EuPtSi $H \parallel [100]$, with labels corresponding to theoretical calculations performed on SrPtSi. From [5].

dependence of the dHvA frequencies shown in figure 4.2, all the Fermi surfaces are closed in the whole-field region. The quantum oscillation frequencies are related to the extremal cross sections S_F of the corresponding Fermi surfaces via the Onsager relation

$$F = \frac{\hbar}{2\pi e} S_F \tag{4.1}$$

with $\hbar$ the reduced Planck constant and e the electron charge. A flat angular dependence such as for the ϵ and δ branches means the Fermi surface is spherical. The higher frequency branches, corresponding to the main Fermi surfaces (of larger cross-sections) such as β and α are corrugated nearly-spherical Fermi surfaces.

As shown in the right of figure 4.2 (a)-(b) from ref. [5], theoretical calculations are in good agreement with the experimental dHvA results, albeit with systematically over-estimated frequencies. These calculations were performed on the reference compound SrPtSi, which unlike EuPtSi is a non-4f compound, with the lattice parameter for the

cubic structure assumed to be the same $a = 6.4336$ Å.

The theoretical calculations place the α and α' branches at the Γ point of the cubic Brillouin zone and the other branches at the R point. The α and α' branches correspond to the electron bands 121 and 122 respectively and the others are hole bands. The theoretical Fermi surfaces are shown in figure 4.2 (c), from ref. [5].

The volumes of electron and hole Fermi surfaces are equal because EuPtSi is a compensated metal with four formula units in the unit cell. The $'$ notation for the frequencies means the Fermi surfaces would become degenerate for a centrosymmetric crystal structure. The splitting of, for example α and α', occurs because of the cubic chiral nature of the crystal. The splitting of Fermi surfaces due to non-centrosymmetry will be developed further ahead.

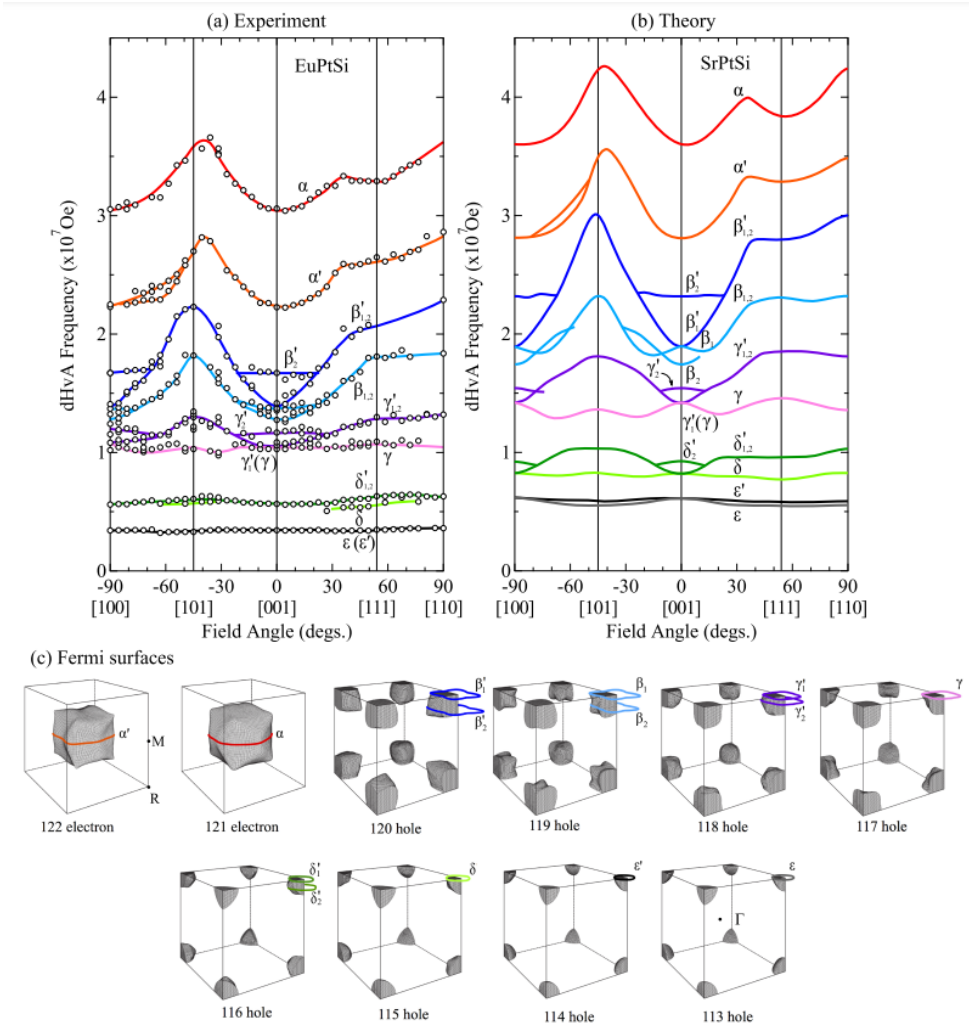

Figure 4.2: Angular dependence of dHvA frequencies from (a) experimental measurements and (b) theoretical calculations performed on SrPtSi. (c) Theoretical Fermi surfaces of EuPtSi and corresponding carrier bands for $H \parallel [100]$. Colored contours represent the extremal cross-sections from the angular dependence. From [5].

The angle-dependence of the frequencies of the dHvA FFT spectrum recovers the shape of the various Fermi surfaces, while the temperature dependence of the oscillations amplitude allows calculations of the effective mass of the carriers for each frequency. For the Lifshitz-Kosevich framework, the amplitude of the oscillations in susceptibility is given by

$$A_i \propto H^{1/2} \left| \frac{\partial^2 S_i}{\partial k^2} \right|^{-1/2} R_D R_T R_S \tag{4.2}$$

with A_i being the amplitude of the dHvA oscillations for branch i, R_T the thermal damping factor, R_D the Dingle reduction factor and R_S the spin damping factor. The various terms have been defined in section 1.2. The factor corresponding to the curvature of the Fermi pocket $\frac{\partial^2 S_i}{\partial k^2}$ does not depend on either the magnetic field or the temperature, and does not affect the following analysis. The cyclotron mass m_i^*, or effective mass, defined as

$$m^* = (\hbar^2/2\pi)\frac{dS}{d\epsilon} \tag{4.3}$$

is then obtained self-consistently by the mass plot, the plot of the natural logarithm of the thermal damping factor R_T. The masses from the dHvA measurements are in good agreement with the theoretical calculations, both will be presented along with the results of this work in the following sections for the main three orientations of EuPtSi.

Another information inferred from quantum oscillations measurements is the Landau level broadening corresponding to the lifetime broadening which can be calculated with the Dingle reduction factor R_D from the field-dependence of the oscillations. The Dingle temperature T_D can be obtained with a similar protocol as the cyclotron mass using the so-called Dingle plot. This analysis has not been reported for EuPtSi in the literature.

From the cyclotron masses, however, the splitting energy for two branches has been deduced, both experimentally and theoretically. The splitting energy of the Fermi surface is due to the antisymmetric spin-orbit interaction. A non-uniform lattice potential from the crystal structure induces an effective magnetic field and the splitting can be regarded as the Zeeman energy that arises from the interaction between this effective magnetic field and the spin of the conduction electron under zero magnetic field [107, 108]. The splitting energy of the two dHvA branches α and α' is calculated by combining the equations 4.3 and 4.1. For a small splitting energy of the conduction electrons, $\frac{dS}{d\epsilon}$ becomes $\frac{\Delta S}{\Delta \epsilon}$ and equation 4.1 becomes

$$\Delta F = (\hbar/2\pi e)\Delta S \tag{4.4}$$

which leads to the splitting energy

$$\Delta\epsilon = \frac{\hbar e}{m^*}|F_+ - F_-| \tag{4.5}$$

where $F_\pm$ are the frequencies in teslas of the two branches. m_c^* is taken as the mean value between the masses of the two split branches. These branches that are found theoretically with frequencies $F_\alpha = 3.611$ kT and $F_{\alpha'} = 2.820$ kT, have a splitting energy $\Delta\epsilon_{\text{thr}} = 1410$ K for $m_c^* = 0.752\ m_0$. For dHvA measurements, a value $\Delta\epsilon_{\text{dHvA}} = 1200$ K is found [5].

This value of the splitting energy is quite large, due to the spin-orbit coupling of the Pt $5d$ electrons. These mainly contribute to conduction electrons. This antisymmetric

spin-orbit interaction contribution to the splitting of Fermi surfaces is due to the non-centrosymmetric crystal structure. For centrosymmetric compounds such as $EuCd_{11}$ and $EuGa_4$ with tetragonal structures [109, 110], the spin-orbit coupling of the Cd and Ga electrons is smaller, hence a smaller splitting energy of 470 and 560 K, respectively.

The analysis of the Fermi surface of EuPtSi has so far only been performed experimentally with the ac-susceptibility. No reports of oscillations in resistivity, the Shubnikov-de Haas (SdH) effect, or other probes have been presented. As such we have performed thermoelectric power measurements. The temperature-dependence aims to confirm the validity of the results while the field-dependence recovers information not yet measured about the Fermi surface of EuPtSi such as the scattering lifetime and mean-free path of the carriers.

4.2 Temperature dependence of the quantum oscillations

Quantum oscillations have only been reported through the dHvA experiment in EuPtSi. The thermoelectric power, being proportional to the derivative of the density of states is a very powerful probe in this case. It is interesting to note that both the longitudinal and the transverse thermoelectric signals exhibit clear quantum oscillations. Both probes can be used to recover the effective mass of the charge carriers. The comparison between the Nernst and the Seebeck coefficient is first presented. We will then discuss the temperature dependence of the amplitude of the oscillations and the analysis of the carrier masses for each observed Fermi surface. The results in thermoelectric power measurements will be presented for the three main directions of EuPtSi, with the $H \parallel [111]$ direction first, followed by the [110] and the [100] directions. Our attempt to measure the dHvA effect for the [110] direction will also be presented. Finally we will review the recently measured oscillations of the Shubnikov-de Haas effect for the $H \parallel [100]$ direction.
The measurements presented in this chapter have been performed with the setup described in chapter 2, with a $^3He/^4He$ dilution fridge insert in a superconducting coil. The thermoelectric power measurements were made using nanovoltmeters for the voltage and a MMR3 device for the thermometer readout. The temperature range available is 0.1 K to 6 K, for applied magnetic fields up to $H_{app} = 16$ T. Because of the non-negligible demagnetizing coefficient, as described in section 3.1.3 of the previous chapter, the effective magnetic field reaches up to $H = 15$ T. The field is swept continuously at a rate of 0.1 T/min. The rate of the field sweep has been confirmed not to have an influence on the quality of the signal. The samples used in this chapter are the same as for the previous chapter 3.

4.2.1 Effective mass analysis for the $H \parallel [111]$ direction

Due to the nature of thermoelectric measurements, the range of temperature available is limited. The thermal gradient applied to the sample makes the average temperature T_{mid} rise. This effect is further enhanced by the high thermal conductivity of EuPtSi of the order of 1 $WK^{-1}m^{-1}$ at zero field and 1 K. In order to reach a thermal gradient $\Delta T/T \approx 3\%$, the heating current needed is rather high. As such, for this orientation,

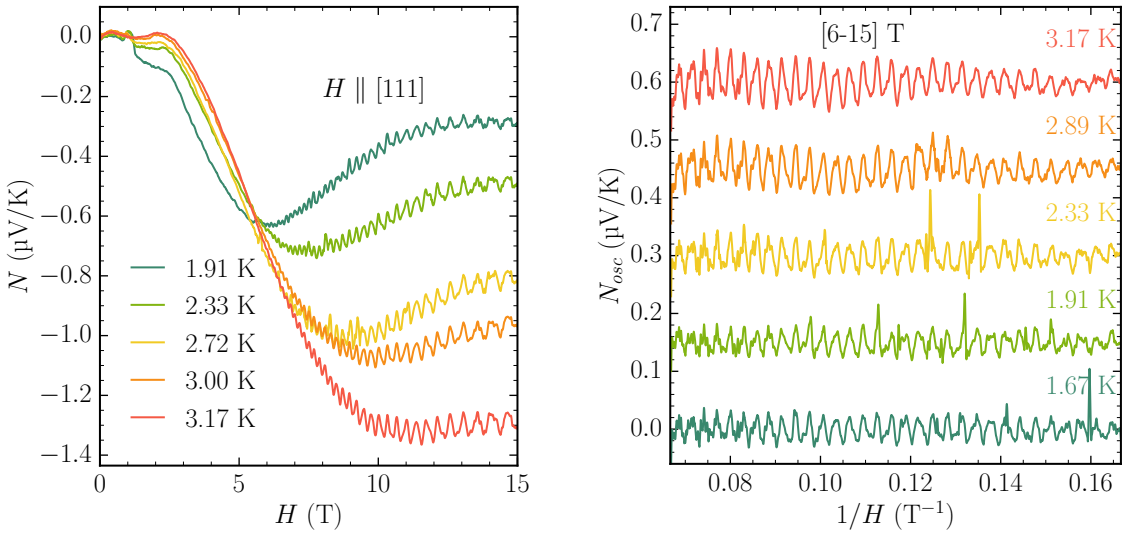

Figure 4.3: Left: Nernst coefficient up to 15 T for $H \parallel [111]$. Right: oscillatory part of the Nernst coefficient, in units of $1/H$ for a field window of 6 to 15 T. Oscillatory signals are shifted vertically for clarity.

the lowest mean temperature $T_{mid} = (T_{hot} + T_{cold})/2$ for which thermal stability has been achieved over the whole field range is 0.55 K. On the other hand, as described in section 1.2.3, unlike most other quantum oscillation probes, the maximum of the amplitude of the oscillations is not at 0 K as S goes to zero but is achieved for a finite value. This behavior is fitted by the Pantsulaya-Varlamov formula (see section 1.2.3). The transverse thermoelectric coefficient, or Nernst signal for EuPtSi $H \parallel [111]$ for temperatures between 1.67 K and 3.17 K is shown in figure 4.3, on the left. The presence of quantum oscillations in the Nernst coefficient becomes evident above 6 T for the whole range of temperatures depicted.
On the right of figure 4.3 is the oscillatory part of the Nernst signal between 6 and 15 T after subtracting a polynomial fit to this field window. The oscillatory signal is plotted as a function of the inverse of the magnetic field $1/H$. The Nernst signal is very small, with an amplitude range of only 1.4 μV/K. With the polynomial background removed, the amplitude of the oscillations reaches only 100 nV/K from peak to peak. By looking at the oscillatory part of the Nernst coefficient over the temperature range, it becomes clear that there are more than one frequency in the signal. The main frequency with the larger period in units of $1/H$ becomes larger in amplitude as the temperature increases. This is indicative of a Fermi surface with a low effective mass, as the Pantsulaya-Varlamov formula will reach its maximum for a high temperature $T_{max} = 0.11\frac{H_{\text{eff}}}{m^*}$, with H_{eff} the mean effective field for the FFT. Superimposed on this main frequency, below 0.08 T^{-1} a higher frequency becomes apparent. Interestingly, a higher frequency also appears above 0.14 T^{-1} where the main frequency is not large enough to eclipse the other frequencies.

The field-dependence of the Seebeck coefficient for EuPtSi $H \parallel [111]$ up to 15 T is presented in the figure 4.4. Below 4 T are the features of the magnetic phases of EuPtSi described in chapter 3. We can note that quantum oscillations occur above around 5 T for all the temperatures depicted. The right figure shows the oscillatory signal in units

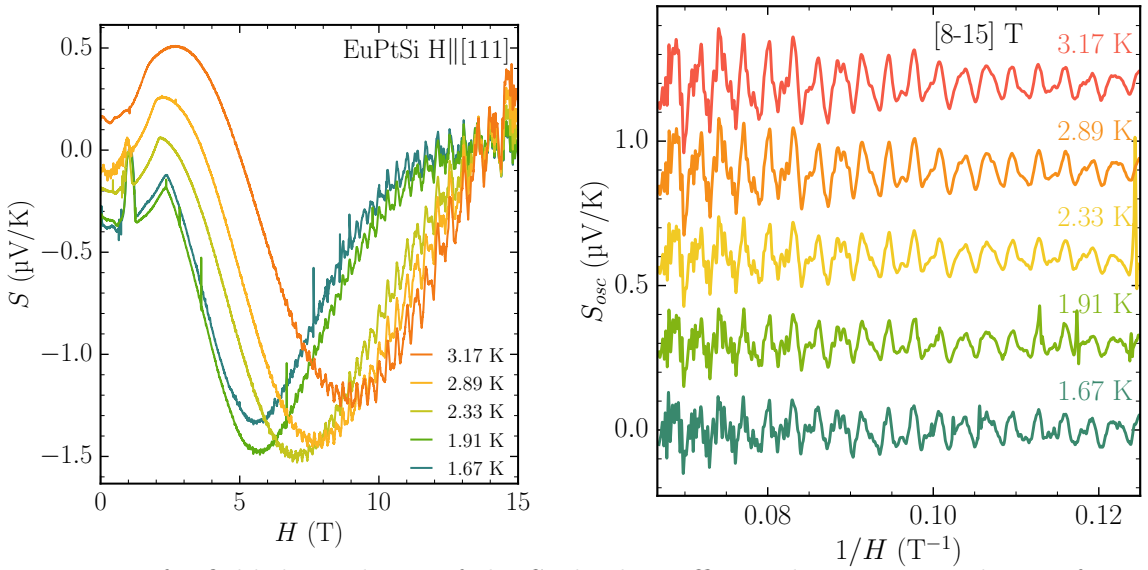

Figure 4.4: Left: field dependence of the Seebeck coefficient between 0 and 15 T for $H \parallel [111]$. Right: Oscillatory part of the Seebeck taken between 8 and 15 T in units of $1/H$. Oscillatory signals are shifted vertically for clarity.

of $1/H$, corresponding to a raw signal between 8 and 15 T for the same temperatures as the figure on the left. A polynomial background of order 3 has been subtracted from the Seebeck signal to isolate its oscillatory part. Similarly to the transverse signal presented previously, the longitudinal thermoelectric coefficient exhibits clear quantum oscillations, reaching a peak-to-peak amplitude of 350 nV/K for an overall signal between -1.5 and 0.5 μV/K. Much like for the Nernst coefficient, the oscillations in the Seebeck coefficient show the influence of a main frequency with a large amplitude reaching its maximum at higher temperatures. An additional higher frequency becomes clear for high fields, or below 0.9 T^{-1}. So far, both the longitudinal and the transverse thermoelectric coefficients clearly show quantum oscillations in the system. Both transport probes can be used to study the Fermi surface of EuPtSi. Having isolated the oscillatory part of their respective signals, we can calculate the Fast Fourier Transform for both and compare them.

Figure 4.5 shows a comparison between the FFT spectra obtained for the Seebeck and the Nernst coefficients for $T = 1.91$ K. The FFT is calculated in a field range [8-15] T for $H \parallel [111]$. The frequencies are given in teslas. Because the amplitude of the Nernst signal is much smaller than the Seebeck, in order to compare their respective FFT, both spectra have been normalized according to the amplitude of the largest peak corresponding to the ϵ pocket with $F_\epsilon = 336$ T, labeled as per the literature. We can note that both the longitudinal and the transverse thermoelectric coefficients recover the frequencies expected for the [111] direction of EuPtSi as per dHvA measurements. The width and the relative amplitude of the peaks for both probes are of a similar order, however, they tend to be slightly lower with the Nernst measurements, as evidenced with the $F_\delta = 615$ T peak whose amplitude reaches only 80 % of the Seebeck amplitude. The signal-to-noise ratio of the Nernst FFT spectrum is slightly lower, which means that the higher frequencies with lower amplitude are easier to observe in the Seebeck signal. This is important since higher frequency pockets correspond to higher effective mass carriers in EuPtSi, and the temper-

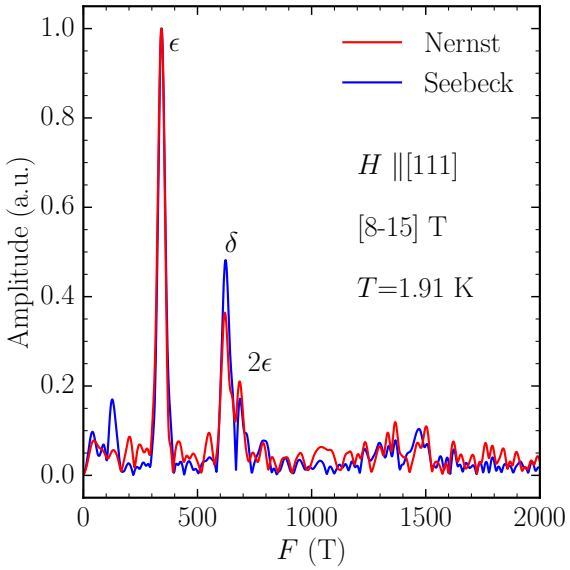

Figure 4.5: Fast-Fourier Transform (FFT) of the Seebeck (blue) and Nernst (red) signals of EuPtSi $H \parallel [111]$ calculated on a [8-15] T field window for $T = 1.91$ K, shown between 0 T and 2000 T. Both FFT are normalized according to the $F_\epsilon = 336$ T peak maximum amplitude.

ature dependence of these amplitudes will drop at a faster rate, making their observation more difficult. Additionally, measuring the Nernst coefficient with our measurement setup means sweeping the magnetic field both in the positive and the negative direction, while keeping the temperature constant. As such, both the quantum oscillations analysis and the practical measurement process indicate that the Seebeck is a more favorable probe for this system. These results are consistent over the whole temperature range evaluated. In the work presented ahead, the emphasis will thus be put on the oscillations in the Seebeck.

As can be seen in figure 4.4, the quantum oscillations start for fields as low as 5 T for the temperature range studied. However the oscillations have a very low amplitude at first and increase with the magnetic field. In order to obtain the best precision on the FFT calculations, it is important to choose the right field window in which the FFT is applied. Figure 4.6 shows a close-up of the ϵ peak at $F_\epsilon = 336$ T of the FFT spectrum obtained for different field windows on the same Seebeck field sweep measurement at $T = 1.91$ K. For clarity, each curve has been shifted horizontally by an arbitrary value, as the frequency shifts slightly between different field windows due to the non-linear Zeeman effect. This aspect is given more attention in section 4.3 and will not be described here.
By comparing the [6-12] T and the [6-15] T results, it becomes clear that a higher upper bound will give better results. This is to be expected as the number of oscillations increase and the amplitude gets larger with the applied magnetic field, and is consistent with our observation of the field dependence of the Seebeck coefficient. Next we can focus on the lower bound of the field window, and note that limiting the field window widens the peak, thus losing some frequency resolution. On the other hand, the height of the peak reaches a maximum for a FFT calculated on a [8-15] T window, corresponding to an effective field $H_{eff} = [\frac{1}{2}(\frac{1}{H_{min}} + \frac{1}{H_{max}})]^{-1} = 10.43$ T. This field window of maximum amplitude is

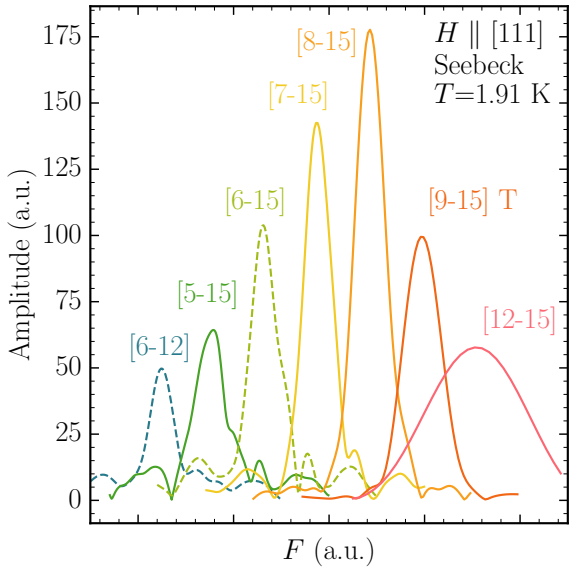

Figure 4.6: Comparison of the field windows (in tesla) used to calculate the FFT spectra of the Seebeck coefficient quantum oscillations at $T = 1.91$ K. The ϵ peak ($F_\epsilon = 336$ T) for $H \parallel [111]$ is shifted horizontally for each window. Dotted (full) lines correspond to upper (lower) bound comparisons.

the same even for high frequency pockets with small amplitudes. As a good compromise between frequency resolution and amplitude height, the [8-15] T window will subsequently be used in the rest of the analysis of the temperature dependence of quantum oscillations in EuPtSi for the direction $H \parallel [111]$.

Figure 4.7 shows the temperature dependence of the amplitude (in arbitrary units) of the oscillations in Seebeck for $H \parallel [111]$. As previously described, the field window used is [8-15] T. The FFT spectrum is recalled in the top left corner and each subsequent graph corresponds to one of the labeled peaks (noted in the top left corner of each graph). The red circles are the maximum amplitude of the peak taken from the spectrum of corresponding temperature, and the blue lines are the Pantsulaya-Varlamov fitting curves from which the effective mass is calculated:

$$R_T|_{PV} = A\frac{\frac{\alpha p m^* T}{H_{\text{eff}}}\coth(\frac{\alpha p m^* T}{H_{\text{eff}}}) - 1}{\sinh(\frac{\alpha m^* T}{H_{\text{eff}}})} \tag{4.6}$$

The temperature damping factor fitting function recalled in equation 4.6 from [29] is computed along the peak amplitudes for the range of temperature 0.55 K to 6 K. It returns two parameters, A and m^* respectively the amplitude and the effective mass of the PV fitting function. For most peaks the amplitude corresponds very well to the experimental data. Only the $F_{\gamma'} = 1.276$ kT does not quite match the shape of the data points, especially at low temperatures. From the temperature of maximum amplitude $T_{max} \approx 2$ K for this frequency, a mass of 0.6 m_0 is found. As the frequency of each peak increases, T_{max} decreases, from 3.5 K for F_ϵ to 1.4 K for F_α, as the effective cyclotron masses of the carriers increase.

The effective masses for each corresponding peak are reported in table 4.1, along

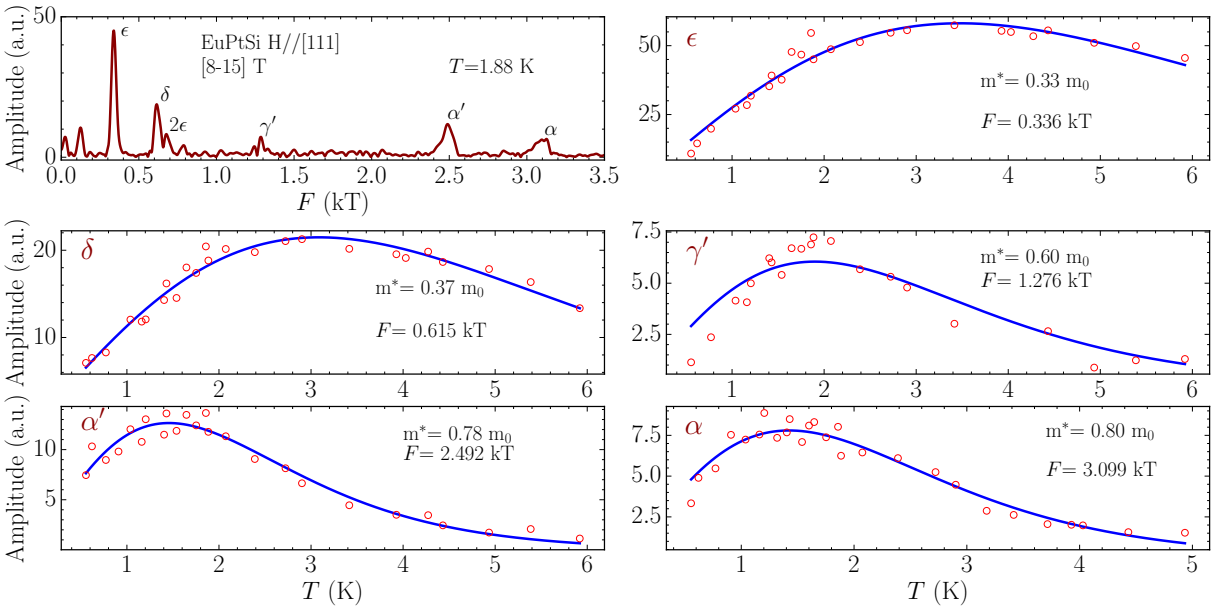

Figure 4.7: Temperature dependence of the amplitude of quantum oscillations and effective masses m^* for EuPtSi $H \parallel [111]$ obtained with a PV fitting function. Each graph corresponds to a frequency as per the FFT spectrum depicted in the top left for $T = 1.88$ K and a [8-15] T field window. Frequencies are expressed in kT and masses in units of m_0 the free electron mass.

EuPtSi $H \parallel [111]$							
This work			dHvA from [5]		SrPtSi theoretical calculations		
Branch	F (kT)	m_c^* (m_0)	F (kT)	m_c^* (m_0)	Branch	F (kT)	m_c^* (m_0)
α	3.099	0.80	3.29	1.03	α	3.847	0.743
α'	2.492	0.78	2.65	0.99	α'	3.293	0.777
					$\beta'_{1,2}$	2.793	0.797
$\beta_{1,2}$			1.81		$\beta_{1,2}$	2.313	0.700
$\gamma'_{1,2}$	1.276	0.60	1.30		$\gamma'_{1,2}$	1.850	0.588
γ			1.09		γ	1.454	0.484
$\delta'_{1,2}(\delta)$	0.615	0.37	0.63	0.36	$\delta'_{1,2}$	0.960	0.323
					δ	0.777	0.281
$\epsilon(\epsilon')$	0.336	0.33	0.35	0.27	ϵ'	0.586	0.229
					ϵ	0.555	0.221

Table 4.1: Effective carrier masses m_c^* and the corresponding frequencies F for EuPtSi $H \parallel [111]$. The results of dHvA experiments by Kakihana are recalled, as well as the theoretical masses calculated for the non-$4f$ reference compound SrPtSi [5].

with the masses measured with the dHvA effect from the literature and the theoretical ones calculated for the non-4f reference compound SrPtSi [5]. Frequencies labeled with indexes 1, 2, for example $\delta'_{1,2}$ correspond to different extremal cross sections of the same carrier pocket, δ'. The results of our Seebeck coefficient measurements are in good agreement with the dHvA experiments from the literature. The frequencies are clearly assigned and the effective mass calculations are of the same order. The theoretical calculations done on SrPtSi overestimate the frequencies measured experimentally. For higher frequencies, namely the α and α' branches, masses extracted from thermoelectric measurements seem to be in better agreement with the theory than the dHvA measurements, whereas the lower frequency results tend to deviate a bit more. The $\gamma'_{1,2}$ branch at 1.276 kT has been successfully observed for both probes, and the mass found in our calculations is in good agreement with the theory. The dHvA experiments have also identified two additional frequencies that have not been observed in this work, namely $F_\gamma = 1.09$ kT and $F_{\beta_{1,2}} = 1.81$ kT. For these frequencies, the carrier effective mass has not been measured experimentally yet. The splitting energy $\Delta\epsilon$ is calculated by taking the difference in frequency and the mean of the two measured effective masses as per equation 4.5. For the α and α' Fermi surfaces, we experimentally obtain $\Delta\epsilon^{exp} = 1030$ K, which is of the same order as the theoretical calculation of $\Delta\epsilon^{th} = 980$ K with masses 0.743 m_0 and 0.777 m_0, and the dHvA results of $\Delta\epsilon^{dHvA} = 900$ K with masses 0.99 m_0 and 1.03 m_0.

The analysis of quantum oscillations in the Seebeck coefficient provides a good transport counterpart to the ac-susceptibility measurements. The frequency results especially confirm the Fermi surface pockets observed using the dHvA effect, and the effective mass calculations are also in good agreement. Some pockets have not been observed by either this work or the dHvA experiment, which might be due to the sample lacking quality. This aspect is emphasized clearly in the next section for the $H \parallel [110]$ direction.

4.2.2 Results for $H \parallel [110]$

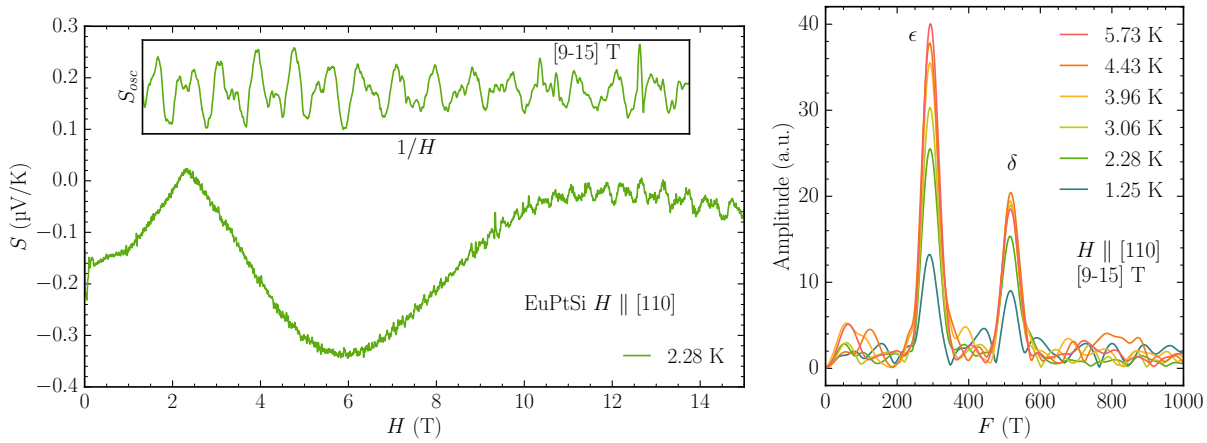

Figure 4.8: Left: field dependence of the Seebeck coefficient for EuPtSi $H \parallel [110]$ for $T = 2.28$ K. Inset: oscillatory part of the Seebeck taken between 9 and 15 T. Right: FFT spectra of the oscillations in the Seebeck $H \parallel [110]$ for temperatures between 1.25 and 5.73 K, for a field window [9-15] T.

By using the same method as for the $H \parallel [111]$ direction, we now study the oscillations in thermoelectric power for the $H \parallel [110]$ direction of EuPtSi. It is to be noted that the RRR for the sample with orientation $H \parallel [110]$ used in this section has not been successfully determined. The field-dependence of the Seebeck coefficient is shown in the left of figure 4.8 for $T = 2.28$ K, for a magnetic field up to 15 T. The sharp slope change at 2.5 T corresponds to the transition from the conical ordered state to the field-polarized paramagnetic state, as described in section 3.2.2. Likely due to the quality of the sample, measurements at low temperatures $T < 1$ K are very noisy and, while they visibly featured quantum oscillations, the background noise rendered the FFT analysis untreatable. As such, the field sweeps were performed for temperatures between 1 K and 6 K which is the upper limit of our measurement setup. For the whole temperature range measured, oscillations start to be stronger than the noise level at around 7 T, however, by studying various field-windows for the analysis of the quantum oscillations as was done in figure 4.6 for the $H \parallel [111]$ direction, better results were achieved for a [9-15] T range, corresponding to an effective field $H_{\text{eff}} = 11.25$ T. The oscillatory part of the signal after subtracting a polynomial background is shown in the inset of figure 4.8 in units of 1/T. Corresponding FFT spectra for this field window are shown in the same figure on the right-hand side graph for six different temperatures between 1.25 K and 5.73 K. Only two frequencies appear in the FFT spectrum, independently of the temperature and the field range. The corresponding Fermi surface branches are ϵ and δ at $F_\epsilon = 291$ T and $F_\delta = 517$ T. Since the Fermi surface of EuPtSi is almost isotropic it is presumable to find similar frequencies as in the $H \parallel [111]$ direction, the lack of peaks at higher frequencies can thus be attributed to the low quality of the sample. This is further indicated by the high noise level of the FFT reaching almost 50 % of the amplitude of the peaks at low temperature. By focusing on the ϵ peak of the FFT spectrum, we can see that the amplitude of the peak increases with T in the whole temperature range measured. The δ peak on the other hand reaches a maximum amplitude around 4 K. The analysis of the temperature dependence of the

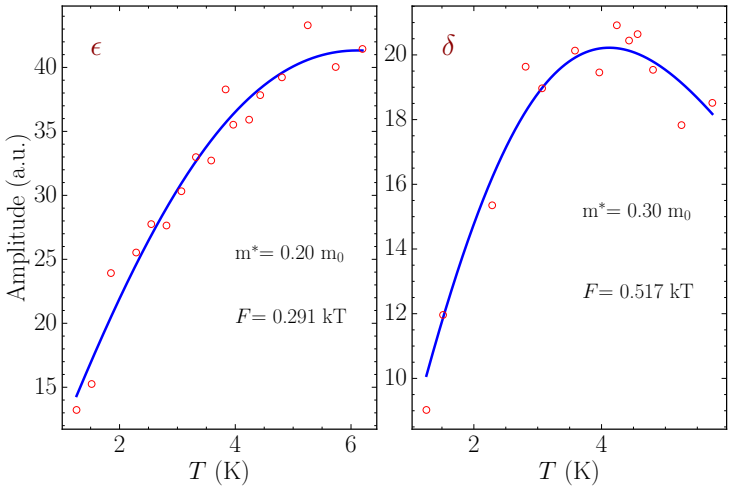

Figure 4.9: Temperature dependence of the amplitude of quantum oscillations and effective masses m^* for EuPtSi $H \parallel [110]$ obtained with a PV fitting function. The left graph corresponds to the ϵ branch and the right to the δ branch. Frequencies are expressed in kT and masses in units of m_0 the free electron mass.

amplitude of the quantum oscillations is shown in figure 4.9 for the two peaks described

above. According to the PV fitting function (in blue) the maximum amplitude of the ϵ peak on the left is barely reached at $T_{max} = 6.1$ K. A high temperature correlates to a small effective mass $m^* = 0.20\ m_0$. For the δ peak, we obtain $m^* = 0.30\ m_0$ for $T_{max} = 4.05$ K. We compare the effective masses from our Seebeck measurements to the dHvA results found in the literature [5] in table 4.2.

EuPtSi $H \parallel [110]$							
This work			dHvA from [5]		SrPtSi theoretical calculations		
Branch	F (kT)	m_c^* (m_0)	F (kT)	m_c^* (m_0)	Branch	F (kT)	m_c^* (m_0)
α			3.60	0.7	α	4.250	0.888
α'			2.70	0.99	α'	3.489	0.931
$\beta'_{1,2}$			2.23		$\beta'_{1,2}$	3.000	0.810
$\beta_{1,2}$			1.82	0.90	$\beta_{1,2}$	2.327	0.727
$\gamma'_{1,2}$			1.30	0.84	$\gamma'_{1,2}$	1.813	0.583
$\gamma_{1,2}$			1.03	0.63	$\gamma_{1,2}$	1.360	0.401
$\delta\prime_{1,2}(\delta)$	0.517	0.30	0.61	0.44	$\delta'_{1,2}$	1.032	0.360
					δ	0.832	0.357
$\epsilon(\epsilon')$	0.291	0.20	0.33	0.34	ϵ'	0.589	0.227
					ϵ	0.555	0.211

Table 4.2: Effective carrier masses m_c^* and the corresponding frequencies F for EuPtSi $H \parallel [110]$. The results of dHvA experiments by Kakihana are recalled, as well as the theoretical masses calculated for the non-4f reference compound SrPtSi [5].

It is clear from the dHvA results that higher frequencies are expected to be observed, but as both the Seebeck effect and the observation of quantum oscillations are highly dependent on the sample quality, this is not surprising that we could not detect them. Based on the only two frequencies observed in this work for the $H \parallel [110]$ direction, it is difficult to conclude on the agreement of our results with the literature ones. Measurements on a higher RRR sample would allow clearer results. Compared to the $H \parallel [111]$ direction, the Fermi surface pocket frequencies seem to be shifted to lower values. The effective masses extracted from our measurements are in good agreement with the theoretical calculations, and are within a 1.5 factor of dHvA results. The limitations of our experimental setup do not allow measurements at temperatures higher than ≈ 6 K, which would help to locate the maximum amplitude of the ϵ peak with higher precision. However, based on the dHvA results, an effective mass of 0.34 m_0 and the effective field $H_{\text{eff}} = 11.25$ T used in our FFT measurements would result in a maximum amplitude at $T_{max} = 3.64$ K, which does not fit our data points. Similarly, for the δ pocket, the maximum amplitude with $m^* = 0.44\ m_0$ corresponds to $T_{max} = 2.8$ K, which is close to 1 K lower from what our measurements suggest. In turn, our measurements of the effective masses correspond within 20 % to the theoretical calculations done on the reference compound SrPtSi [5].

4.2.3 dHvA experiment for $H \parallel [110]$

Using the Faraday balance setup described in section 2.3, we have measured the dHvA effect for the $H \parallel [110]$ direction. As it is the easy magnetization axis, it is the only direction we can measure with this setup since torque effects should be avoided as they

cannot be separated from the longitudinal displacement. The field dependence of M is presented in figure 4.10 (left) for 6 temperatures between 1.3 K and 4.2 K. The inset shows the oscillatory part of the signal between 8 and 15 T plotted in units of 1/T. The oscillatory part is fitted between 11 and 15 T and the background is removed. Figure 4.10 (right) shows the FFT signal calculated for a [11-15] T field-window for the same data-set. At various points in the $M(H)$ signal, jumps in the measurement can be seen,

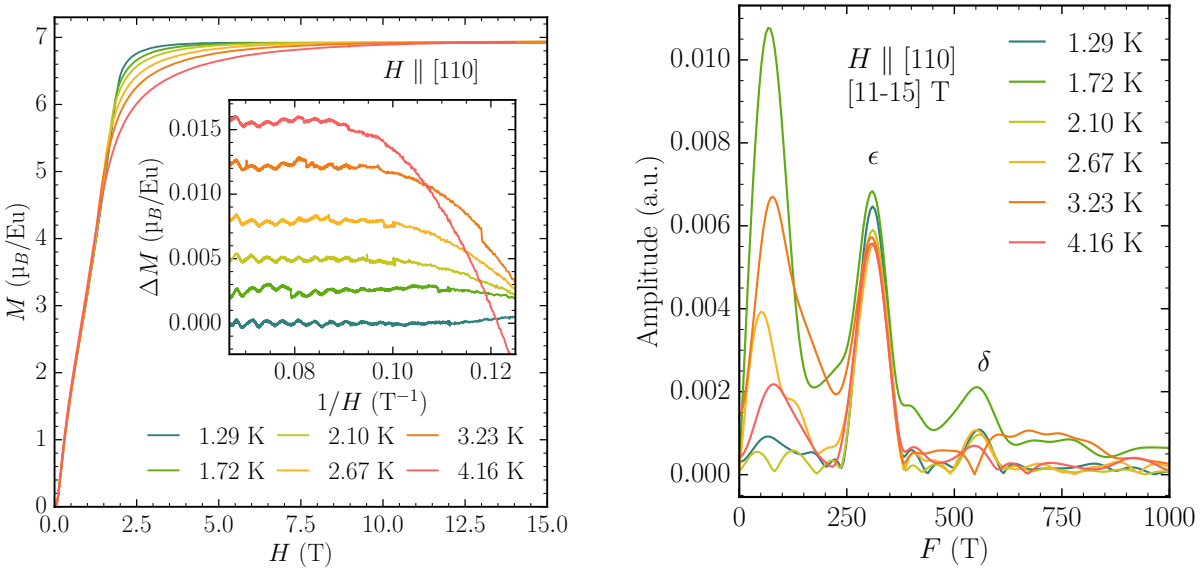

Figure 4.10: Left: field dependence of the magnetization M for EuPtSi $H \parallel [110]$ at various temperature. Inset: oscillatory part of M with a background removed between 11 and 15 T, shifted vertically. Right: FFT spectra from the $M(H)$ measurements for a [11-15] T field-window.

for example at 0.078 T for the 1.72 K data. The reason for these jumps is experimental but difficult to be identified in detail. While they seemingly do not affect the frequencies of the signal in the FFT calculation, the discontinuities at the jumps increase the noise level. This is evidenced at $T = 1.72$ K with a FFT background noise reaching $\approx 40\%$ of the ϵ peak signal at $F_\epsilon = 310$ T. Similarly the δ peak at $F_\delta = 556$ T is affected by the background noise. This makes the amplitude analysis and thus recovering the effective mass impossible for this data-set. Additionally, a low-frequency ($F \approx 50 - 100$ T) peak is observed due to the background subtraction of the $M(H)$ signal. The higher-frequency peaks $F > 1000$ T have not been observed for these measurements. Nevertheless, the two frequencies measured are in good agreement with the results presented in table 4.2.
The crystal used for the $M(H)$ measurement is the same as for the Seebeck measurements. The RRR for this crystal is unknown but from the results previously mentioned this is not the best quality crystal, which explains the lack of resolution of the FFT signal, and the absence of peaks above 1000 T.

4.2.4 Results for $H \parallel [100]$

Using the same protocol as for the previous two orientations, we have measured quantum oscillations in the thermoelectric power for the $H \parallel [100]$ direction of EuPtSi. The Seebeck

coefficient field dependence is shown in the left of figure 4.11 for $T = 1.61$ K for a magnetic field up to 15 T. Compared to the other orientations, the signal is very evident with a noise level of the order of 2 nV/K for oscillations reaching a peak-to-peak amplitude of 20 nV/K at 15 T. This can be attributed to the quality of the sample with $RRR = 32$. The optimal field-window for analyzing the quantum oscillations is [8-15] T. The oscillations start around 7 T for all temperatures. The oscillatory part of the Seebeck coefficient is plotted in the left inset of figure 4.11 as a function of $1/H$. By calculating the FFT of

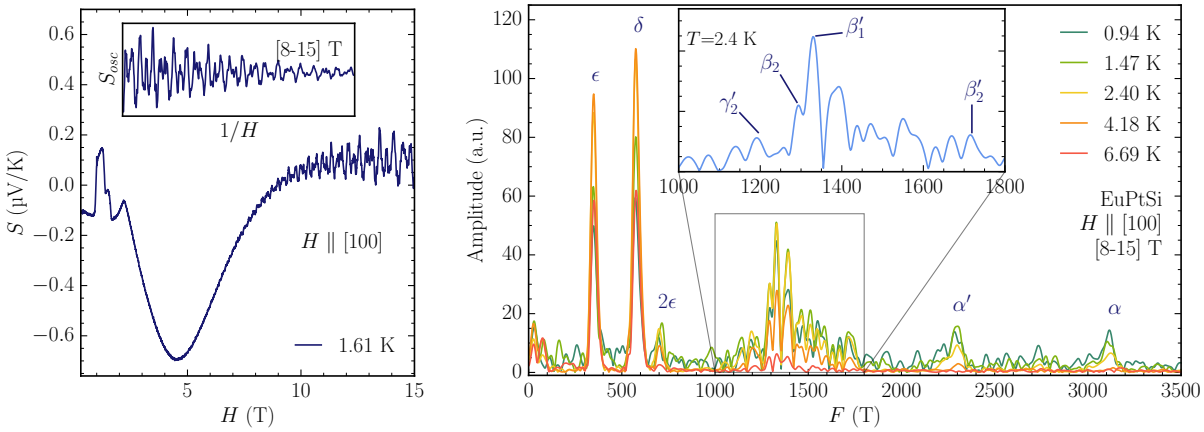

Figure 4.11: Left: Seebeck field dependence for $T = 1.61$ K for the $H \parallel [100]$ direction. Inset: Oscillatory part of the Seebeck taken between 8 and 15 T as a function of $1/H$. Right: FFT spectra of the Seebeck $H \parallel [100]$ signal for temperatures between 0.94 and 6.69 K. The peaks are labeled as per ref. [5]. Inset: close-up between 1000 and 1800 T for the $T = 2.40$ K spectrum.

the Seebeck coefficient for a [8-15] T field window for all temperatures, we obtain the spectra shown in the right figure 4.11. For all considered frequencies, the peaks are rather well defined, showcasing the quality of the signal for this sample. The smearing of the peaks located between 1200 and 1600 T (right inset of figure 4.11) is due to the closeness of the frequencies and the lack of frequency resolution of the FFT calculations. For the temperatures displayed, we can note that as the peak frequencies increase, the maximum amplitude shifts to lower temperatures, indicating increasing effective masses. From the comparison with the dHvA measurements in table 4.3, with the exception of γ'_1, each peak is clearly identified and is within the expected values. Each Fermi surface branch has been fitted with the Pantsulaya-Varlamov formula, and the temperature dependence of the oscillations for every peak is shown in figure 4.12. Despite the very small amplitude of the peaks γ'_2, β'_2, α' and α, the fitting of the data points with the PV formula indicates clear maxima from which the effective masses can be calculated. As was observed for $H \parallel [111]$, the values of effective mass deduced from the Seebeck coefficient are found between the dHvA values and the theoretical values calculated for SrPtSi. Similarly to the $H \parallel [111]$ direction, the splitting energy $\Delta\epsilon$ can be calculated for the branches α and α', giving $\Delta\epsilon_{exp} = 1320$ K. This value is located between the dHvA experiment $\Delta\epsilon_{dHvA} = 1200$ K, and the theoretical calculation $\Delta\epsilon_{thr} = 1410$ K.

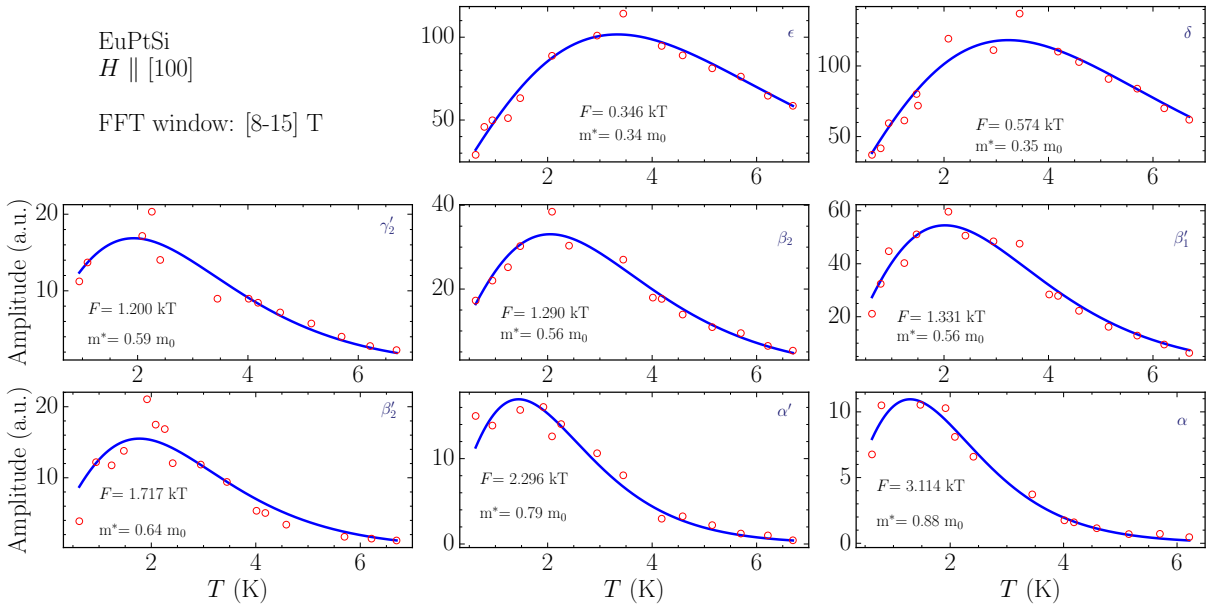

Figure 4.12: Temperature dependence of the amplitude of quantum oscillations and effective masses m^* for EuPtSi $H \parallel [100]$. Each graph corresponds to a different branch indicated in the top right corner. Blue curves correspond to PV fits calculated on the red data points. Frequencies are expressed in kT and masses in units of m_0 the free electron mass.

EuPtSi $H \parallel [100]$							
This work			dHvA from [5]		SrPtSi theoretical calculations		
Branch	F (kT)	m_c^* (m_0)	F (kT)	m_c^* (m_0)	Branch	F (kT)	m_c^* (m_0)
α	3.114	0.88	3.09	0.96	α	3.611	0.771
α'	2.296	0.79	2.25	0.88	α'	2.820	0.733
β_2'	1.717	0.64	1.68	0.81	β_2'	2.319	0.626
$\beta_1'(\beta_1)$	1.331	0.56	1.35	0.70	$\beta_1'(\beta_1)$	1.896	0.521
β_2	1.290	0.56	1.26	0.65	β_2	1.752	0.506
γ_2'	1.200	0.59	1.17	0.60	γ_2'	1.544	0.45
$\gamma_1'(\gamma)$			1.09	0.64	$\gamma_1'(\gamma)$	1.423	0.422
					δ_2'	0.924	0.317
$\delta_1'(\delta)$	0.574	0.35	0.61	0.44	$\delta_1'(\delta)$	0.826	0.269
$\epsilon(\epsilon')$	0.346	0.34	0.33	0.34	ϵ'	0.610	0.253

Table 4.3: Effective carrier masses m_c^* and the corresponding frequencies F for EuPtSi $H \parallel [100]$. The results of dHvA experiments by Kakihana are recalled, as well as the theoretical masses calculated for the non-$4f$ reference compound SrPtSi [5].

4.2.5 Oscillations in resistivity

For some reason, unknown at the time, the quantum oscillations in EuPtSi that are easily measured using the dHvA experiments were not observed at all in transport probes. This is what prompted us to measure the Seebeck coefficient of the system as explained previously. Besides the higher sensitivity to changes of the density of states of the thermoelectric power, the fact that resistivity measurements, the so-called Shubnikov-de Haas (SdH) effect did not show quantum oscillations remained a mystery. It is, however, known that the SdH effect is difficult to observe in metals with large carrier concentration [22]. The sample with $RRR = \frac{\rho_{300K}}{\rho_{0.2K}} = 32$ with the large face along the $H \parallel [100]$ direction eventually produced quantum oscillations, solving this mystery. The (simple) explanation actually is the quality of the samples measured [18].

The field dependence of the longitudinal resistivity for various temperatures between 1 and 4 K is shown in the top left of figure 4.13. All data are fitted with a second order polynomial background calculated for the 4.5 K curve (shown in inset), subtracted for clarity. The uncorrected curves can be found in appendix A. Because of the very small amplitude of the oscillations, they are nearly impossible to spot with the naked eye on the $\rho(H)$ data without background subtraction. The FFT calculations are performed for a [10-14.8] T window and the spectrum is shown in the top right of figure 4.13. Only the first two branches with $F_\epsilon = 0.355$ kT and $F_\delta = 0.586$ kT are observed. Merging peaks between 1.3 and 1.5 kT that would correspond to the γ and β branches are visible but cannot be further used to deduce the cyclotron masses. The frequencies of the first two peaks are in good agreement with the dHvA experiments as well as the Seebeck measurements.
The Lifshitz-Kosevich formula corresponding to the temperature damping factor R_T used both in dHvA and SdH effects is:

$$R_T|_{LK} = A\frac{\alpha p m^* T/H_{\text{eff}}}{\sinh(\alpha p m^* T/H_{\text{eff}})} \tag{4.7}$$

Using this formula to fit the amplitudes in the bottom of figure 4.13 yields masses $m^* = 0.35\ m_0$ for the ϵ peak and $0.37\ m_0$ for the δ peak. This corresponds to the Seebeck measurements of $0.34\ m_0$ and $0.35\ m_0$, respectively, and is in better agreement than the dHvA results reported in table 4.3 from Kakihana et *al.* [5].

Because of the lack of resolution of the oscillations in the resistivity measurements compared to the thermoelectric power, they have not been pursued further. A better sample of $RRR > 32$ would allow for more qualitative measurements. The observation of the ϵ branch in resistivity data can however be used as a benchmark to validate the Dingle temperature measurements from the field-dependence analysis of the oscillations in the thermoelectric power, presented in the following section.

4.3 Field dependence of the quantum oscillations

The systematic study of the temperature dependence of the amplitude of quantum oscillations in the Seebeck coefficient has allowed us to observe Fermi surface pockets of

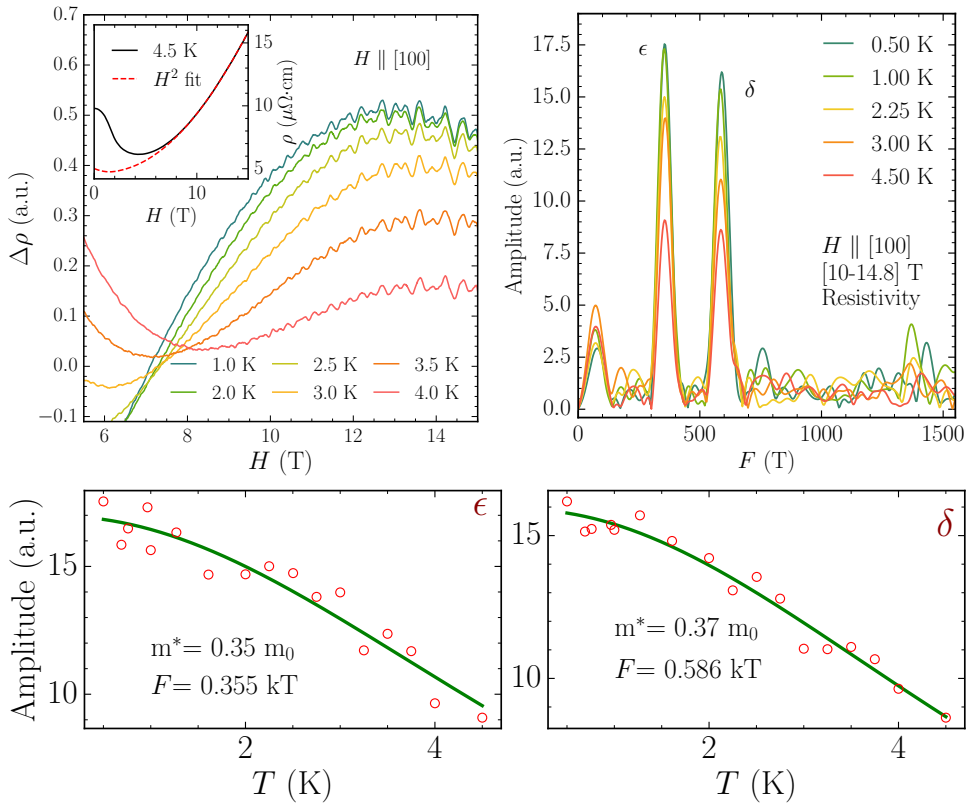

Figure 4.13: Top left: Oscillations in the field dependence of the resistivity for $H \parallel [100]$, with a H^2 background removed. Inset: H^2 polynomial background fitted between 8 and 15 T. Top right: FFT spectra obtained from the resistivity signal for a [10-14.8] T window, for $H \parallel [100]$, for temperatures between 0.5 and 4.5 K. Bottom: temperature dependence of the oscillations amplitude (red), fitted with the Lifshitz-Kosevich formula (green) for the ϵ and δ peaks.

EuPtSi and recover appropriate values of the carrier effective masses. We have provided an alternative to the susceptibility in the form of a transport probe sensitive enough to pick up quantum oscillations. As such, we have shown the relevancy of the thermoelectric power in this system and the validity of the Pantsulaya-Varlamov formula for this probe. Using the Pantsulaya-Varlamov framework, we will now study the field dependence of the quantum oscillation amplitudes to recover the Dingle damping factor R_D, the Dingle temperature T_D, the scattering lifetime τ and the mean-free-path l of the charge carriers for EuPtSi, comparing it with the well-established framework for the analysis of SdH experiments.

4.3.1 Dingle temperature calculations

With the calculated effective masses, we can now turn our focus to the field-dependence of the oscillations, and the calculation of the Dingle temperature T_D using the Pantsulaya-Varlamov theory. The Dingle temperature calculations will be presented for the $H \parallel [100]$ direction.

From the FFT spectra obtained previously, we can see that the oscillation signal in EuPtSi is made of a complex mixing of various frequencies. Because the peaks of the FFT are close both in frequency and in amplitude, analyzing the field dependence of the oscillations is not as straight-forward as the temperature dependence. To accurately compare FFT amplitudes over varied field ranges, it is important to maintain a comparable parameter, i.e. the number of oscillations per studied field windows. As the oscillations are periodic in $1/H$, taking a window of fixed length in inverse of the field suffices. For the ϵ branch, we have isolated the corresponding oscillations to fix the window as a number of periods. To do so we separated the FFT signal for a given temperature into a sum of the various frequency peaks by successively removing the amplitude of the other peaks. We then performed an inverse Fourier transform (iFFT), therefore obtaining a sinusoidal oscillatory signal for the ϵ branch.

The sine wave for the ϵ branch with a frequency of 346 T is shown in figure 4.14 (left). For comparison, the sine wave is superimposed on the Seebeck oscillatory signal for $T = 2.25$ K. Analysis over a various number of periods n_{osc} have provided better results for $n_{osc} = 8$, i.e. for 9 consecutive sine peaks. Over a 8-15 T range, the 13 field windows each containing 8 consecutive periods, are plotted in color, with the cross corresponding to the effective field value H_{eff} for each window. We can then calculate the FFT of the Seebeck signal for each field window. The resulting FFT for six field windows is shown in the right panel of figure 4.14. The first window [8.07-9.85] T corresponds to $H_{\text{eff}} = 8.91$ T, and so on until [11.3-15] T for $H_{\text{eff}} = 12.78$ T. The shift in frequency with respect to H_{eff} is due to a non-linear Zeeman effect and will not be considered here. Instead, the frequency used for the following calculations is the one from the FFT spectrum over the entire field range as calculated for the temperature dependence of the oscillations.

The field dependence of the ϵ branch has also been calculated from the resistivity data. Because of the limited field window on which the oscillations are visible, the number of effective fields H_{eff} for this probe is reduced to only eight values between 10 and 14.8 T.

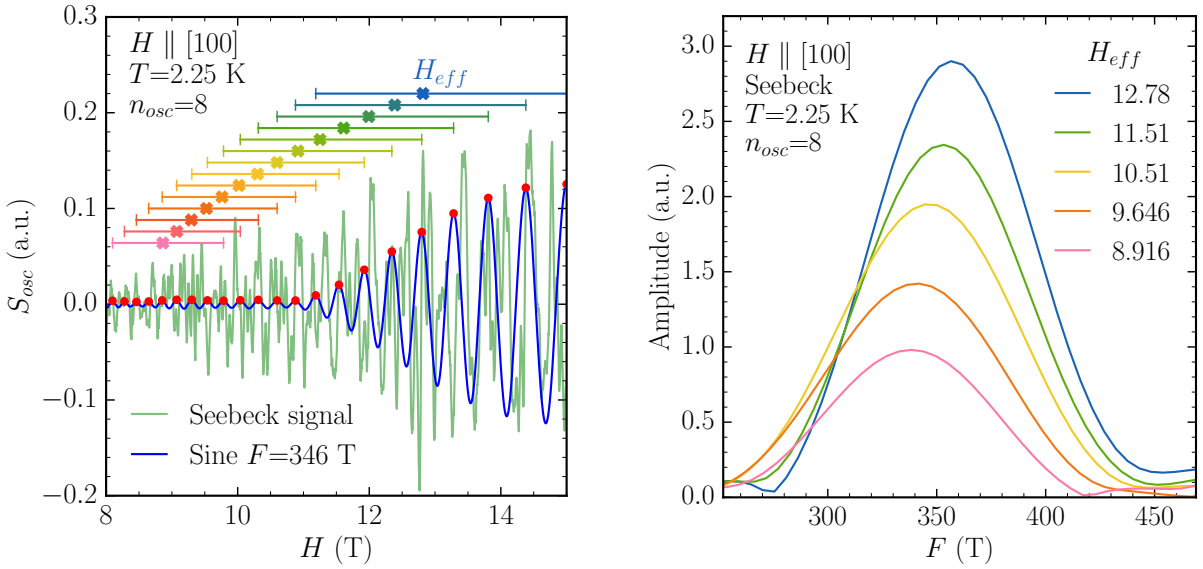

Figure 4.14: Left: sine wave corresponding to the isolated $F_\epsilon = 346$ T peak superimposed on the Seebeck oscillatory signal at $T = 2.25$ K, in units of H, between 8 and 15 T. Field windows for 8 consecutive periods are illustrated in the upper part, with the cross denoting the value of H_{eff} for this field window. The periods are taken between the peaks (red dots) of the sine wave. Right: FFT calculation of the Seebeck signal at $T = 2.25$ K for various field windows of 8 periods, centered on the ϵ peak.

Taking the maximum amplitude of the peak for various effective fields, we can now recover the Dingle temperature T_D from which we obtain the scattering lifetime τ and the mean-free path l.

As discussed in section 1.2.3, the amplitude $A_\rho(T, H)$ of quantum oscillations in resistivity for a given frequency is:

$$A_\rho(T, H) \propto R_T(T) R_D(H) \tag{4.8}$$

The temperature dependence of the oscillations provides the thermal damping factor R_T, and the Dingle damping factor R_D is given by:

$$R_D = \exp\left(\frac{-\alpha p m^* T_D}{H}\right) = \frac{A_\rho(H)}{H^{\frac{1}{2}} R_T} \tag{4.9}$$

In the Lifshitz-Kosevich theory framework, with the temperature damping factor recalled in equation 4.7, the Dingle temperature is obtained by the slope $-\alpha m^* T_D$ of the so-called Dingle plot, $\ln[A_0 H^{-\frac{1}{2}} \sinh(\alpha p m^* T/H)]$ as a function of $1/H$. For the resistivity measurements, the SdH effect which is accurately described using the LK theory framework [22], this is straightforward.

As we have seen previously, however, the LK theory falls short when it comes to analyzing the quantum oscillations for thermoelectric power, and instead the PV formula fits the experimental data much better. With R_T the Pantsulaya-Varlamov formula, from equations 4.6 and 4.9, the Dingle plot becomes:

$$\ln\left[A_0 H^{\frac{-1}{2}} \frac{\sinh(\frac{\alpha p m^* T}{H})}{\frac{\alpha p m^* T}{H}\coth(\frac{\alpha p m^* T}{H}) - 1}\right] = -\frac{\alpha p m^* T_D}{H} + Cst \tag{4.10}$$

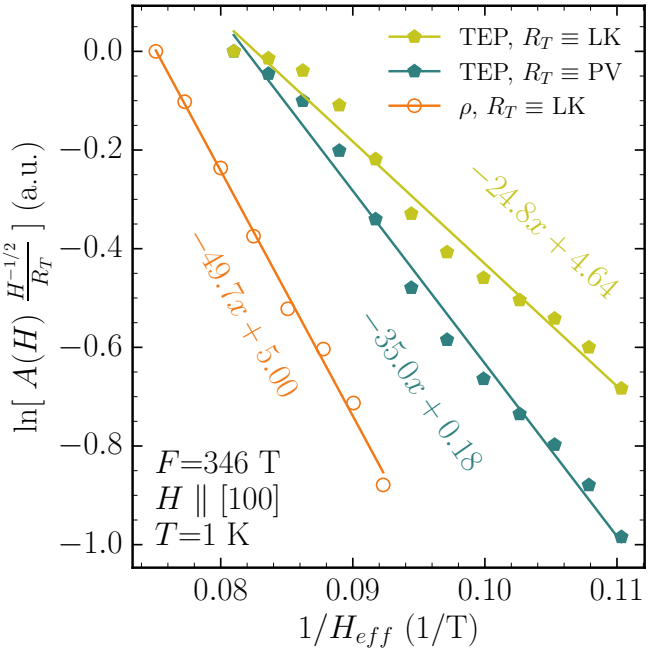

Figure 4.15: Dingle plot for the $F_\epsilon = 346\ T$ branch in Seebeck (TEP) and resistivity at $T = 1$ K. R_T is replaced by either the LK (green and orange) or the PV (blue) temperature damping factor. The $ax+b$ polynomial fit (solid lines) is indicated for each data-set, with $a = -\alpha p m^* T_D$. Data is shifted vertically for clarity.

where T is the temperature of the data, m^* is the effective mass obtained from the temperature dependence analysis and A_0 is the amplitude of the peak for the H_{eff} considered. p is the harmonic number of the peak, which is 1 in the case of the ϵ branch. The accordingly modified Dingle plot is shown in figure 4.15. The resistivity measurements are fitted with the temperature damping factor R_T from the LK framework. A comparison of the LK and PV frameworks is performed for the Seebeck measurements. The plots shown are made on $T = 1$ K data.

The Dingle plots produce a linear fit $ax + b$. The ordinates b do not yield information and have been voided for all three fits for visual clarity. Instead the information is deduced from the slope $a = -\alpha p m^* T_D$. For ρ with the LK theory framework, we obtain $a = -49.68$. For a mass $m^* = 0.35\ m_0$, this yields $T_D = 9.58$ K. The thermoelectric power analysis performed with the PV framework gives $a = -35.03$, and $T_D = 6.99$ K. The two values are of similar order. Because of the difference in quality of the signal, the accuracy of the results is difficult to evaluate. Nevertheless the comparison of the LK theory and the PV theory experimentally validate the use of the latter to analyze quantum oscillations. For comparison, the LK theory applied to the Seebeck effect yields $T_D = 4.50$ K, which is less than half the value expected from the resistivity calculations.
This analysis of the Dingle damping factor for the ϵ branch has been performed for various temperatures, the results of which are presented in the following section, as well as the analysis of the other Fermi surface pockets.

4.3.2 Scattering lifetime and mean free path calculations

The Dingle temperature T_D can be seen as an additional temperature encompassing the broadening of the Fermi level caused by impurity scattering or other effects reducing the lifetime of the carriers. From the Dingle temperature we obtain the scattering lifetime τ, assuming it does not depend on energy, with the relation:

$$\tau = \frac{\hbar}{2\pi k_B T_D} \tag{4.11}$$

The scattering lifetime is linked to the mean free path l by:

$$l = v_F \tau \tag{4.12}$$

with $v_F = \frac{\hbar k_F}{m^*}$ the Fermi velocity. The Fermi wave-vector k_F is determined from the Onsager relation $F = \frac{\hbar}{2\pi e} S$ with $S = \pi k_F^2$ for a spherical Fermi surface. This relation is valid for EuPtSi since all the Fermi surfaces are spherical (or nearly so). Equation 4.12 thus becomes

$$l = \frac{\hbar^2 \sqrt{2eF}}{2\pi m^* k_B T_D} \tag{4.13}$$

F and m^* taken for the considered peak.

The results for the ϵ branch are presented in table 4.4 for resistivity and thermoelectric power for four temperatures, $T \approx 1$ K, 2.25 K, 3.50 K and 4.1 K. From the temperature dependence of figure 4.12 for the thermoelectric power, these temperatures correspond to respectively a minimal amplitude, approaching the peak at $T_{max} = 3.4$ K, at the peak, and after the peak. In turn, the resistivity amplitude decreases continuously with temperature, as featured in figure 4.13. For all four temperatures, the values of T_D, τ and l

ρ $H \parallel$ [100], ϵ branch			
T (K)	T_D (K)	τ (10^{-13} s)	l (Å)
1.00	9.58	1.27	432
2.25	9.03	1.35	458
3.50	8.18	1.49	507
4.10	7.69	1.58	539

TEP $H \parallel$ [100], ϵ branch			
T (K)	T_D (K)	τ (10^{-13} s)	l (Å)
0.93	6.99	1.74	605
2.25	6.15	1.98	688
3.44	5.00	2.43	846
4.17	4.20	2.89	1007

Table 4.4: T_D, τ and l results from the field dependence of quantum oscillations for the ϵ branch $H \parallel$ [100] at various temperatures, for resistivity (left) and thermoelectric power (right), using the LK and PV frameworks respectively.

are of similar order and similar temperature behavior for both the LK framework Dingle damping analysis and the PV framework one. As the results strongly depend on the previous calculations of the temperature dependence, the deviation between the two probes can originate from variations of the effective mass, the frequency and the temperature damping factor R_T fitting function. Due to its very small signal, the resistivity is not the best suited probe to compare the Seebeck to, dHvA data would allow for a more accurate comparison.

The uncertainties on the results may also explain the temperature variations of our results. From a classical point of view, it comes naturally that the mean-free path should decrease with increasing temperature, as thermal agitation increases the rate of scattering. As carriers perform their cyclotron motion under applied magnetic field, a large mean-free path means the amplitude of the associated oscillation is also large. At low temperatures, the amplitude is mostly due to impurity scattering, which leads to high quality samples having better oscillatory signals, and the mean-free path should not vary too much [10]. As such, the values of l recovered from our measurements can indicate the order of magnitude ($l \approx 500$ Å for ϵ) but the precise value should be determined by other means.
A similar analysis of the ϵ branch for the $H \parallel [111]$ direction yields similar results, albeit slightly higher, of $1000 < l < 1300$ Å for $3.3 < T_D < 4.2$ K for temperatures between 1 and 3 K. Due to its small oscillatory amplitude, the $H \parallel [110]$ direction has not been successfully analyzed.

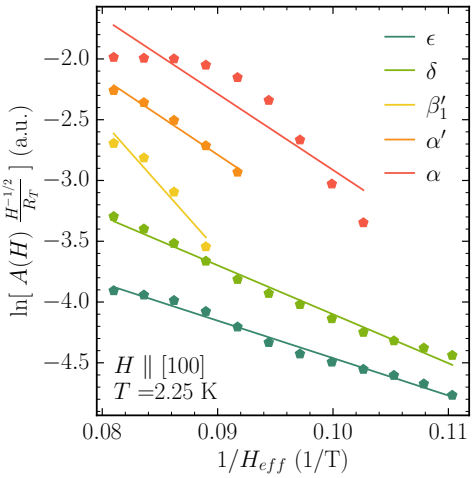

Figure 4.16: Dingle plot from Seebeck measurements with $R_T \equiv$PV at $T = 2.25$ K for 5 Fermi surfaces.

S $H \parallel [100]$, $T = 2.25$ K				
Branch	F (kT)	T_D (K)	τ (10^{-13} s)	l (Å)
ϵ	0.346	6.15	1.98	688
δ	0.571	7.79	1.56	676
β_1'	1.337	11.27	1.08	390
α'	2.280	4.78	2.54	858
α	3.119	4.23	2.87	1016

Table 4.5: T_D, τ and l results for 5 Fermi surfaces of EuPtSi from Seebeck measurements $H \parallel [100]$ at $T = 2.25$ K. The results are calculated from the slope of the linear fits from figure 4.16

The same analysis method of the Dingle damping factor, yielding information on the scattering time and mean-free path, can be performed for the other Fermi surfaces of EuPtSi on the $H \parallel [100]$ sample. However, as the resistivity oscillations are very small, only the ϵ branch analysis has been successful and thus cannot be compared with the Seebeck coefficient.
For the thermoelectric power with a better signal, the Dingle plot with the PV framework is shown in figure 4.16 for $T = 2.25$ K, with FFT windows of 0.028 T^{-1}, corresponding to 10 oscillations of F_ϵ. As quantum oscillations are all periodic in $1/H$, this window was used for all frequencies considered. The results of the scattering lifetime and mean-free path for all five branches are summarized in table 4.5. The five branches considered correspond to the first-harmonic frequencies $F_\epsilon = 0.346$ kT, $F_\delta = 0.571$ kT, $F_{\beta_1'} = 1.337$ kT, $F_{\alpha'} = 2.280$ kT and $F_\alpha = 3.119$ kT. The frequency values are taken from the FFT analysis over the whole [8-15] T field range.

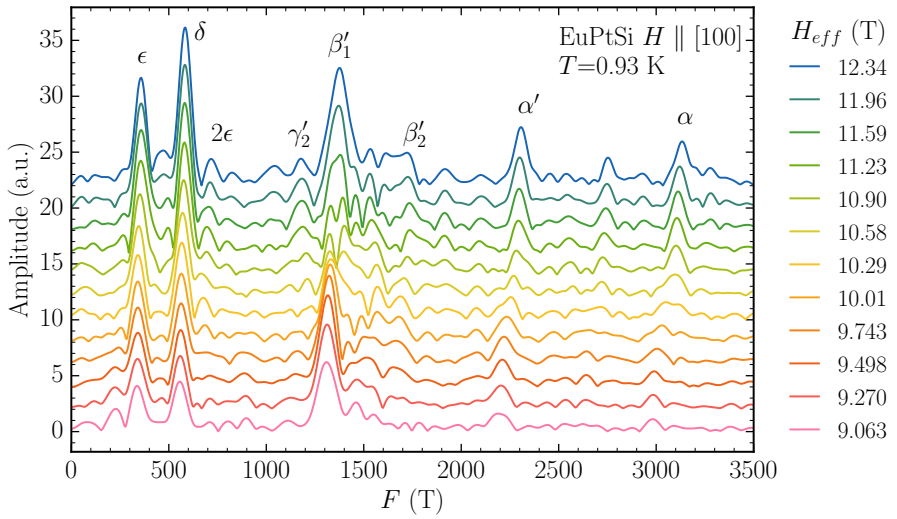

Figure 4.17: FFT calculations on the Seebeck $H \parallel [100]$ for windows of $1/H_{\text{eff}} = 0.028$ T^{-1} over a field range of [8-15] T, at $T = 0.93$ K. Curves are shifted vertically for clarity.

From the Dingle plot, we can conclude that the analysis works well for the ϵ and δ Fermi surface pockets. The amplitude of the other branches could only be analyzed for higher fields or low $1/H$ windows, as various processes affect the field dependence of the oscillations. The full FFT spectra for all the effective fields H_{eff} is shown in figure 4.17 for $T = 0.93$ K. For all values of H_{eff}, the ϵ and δ branches are well defined, and their amplitude varies linearly with H_{eff}.
For the β_1' branch, the peak is well defined only for the highest fields as other frequencies like γ_2' and β_2' mix in the signal for $H_{\text{eff}} < 11$ T. For lower effective fields, the various frequencies produce a singular peak with varying amplitude.
The α' and α peak amplitudes first decrease along H_{eff} before increasing again. This non-linearity can be seen in the Dingle plot where the α branch points cannot be fitted with an $ax+b$ dependence in $1/H_{\text{eff}}$. Additionally, the frequencies for these two pockets are shifted non-linearly to lower values as H_{eff} decreases, with $\Delta F_\alpha \approx 130$ T between the highest and lowest H_{eff}. The frequency shift is not taken into account in the Dingle temperature calculations, as it is most likely due to a non-linear Zeeman effect, as described in section 1.2.2. The additional frequency observed at around $F = 2750$ T is an harmonic with $F = \frac{F_{\alpha'}+F_\alpha}{2}$. As such, the values presented in table 4.5 are less accurate for the branches of higher frequencies. A similar observation has been made for the $H \parallel [111]$ direction, with only the ϵ, α' and α branches yielding results. For this direction we obtain values of $l_\epsilon = 1040$ Å, $l_{\alpha'} = 870$ Å and $l_\alpha = 860$ Å at $T = 1$ K, with linear amplitudes only for the first few higher H_{eff} values.

4.4 Conclusion

Quantum oscillations are a very powerful probe for characterizing the Fermi surfaces. For EuPtSi, we have successfully compared dHvA results from the literature with thermoelectric power measurements. We have performed the temperature-dependent analysis for each observable Fermi surface branches and recovered the effective carrier masses us-

ing the Pantsulaya-Varlamov theory framework, yielding consistent results. We have also made field-dependent calculations, developing a new way of recovering the Dingle temperature, scattering lifetime and mean-free path using thermoelectric power measurements. We have compared these results with resistivity measurements and confirmed that sample quality was the reason for other works not observing the SdH effect in this system.
The angular dependence of the oscillations recovers the topology of the Fermi surface but has not been further explored in this work as the literature already provides an exhaustive analysis both experimentally and theoretically. A further analysis of the spin damping factor and the non-linearity of the Zeeman effect can provide better insight into the carrier properties of EuPtSi for higher frequency Fermi surfaces.

Conclusion

Since the evidence of a realization of magnetic skyrmions in MnSi in 2009, other compounds have been investigated as potential skyrmion hosts, one such compound being EuPtSi with the A-phase SkL for the [111] direction confirmed in 2018. In this work, EuPtSi has been investigated for the main three direction, [110], [111] and [110], using transport measurements at low temperatures (down to 90 mK) and high magnetic field (up to 16 T).

We have established the magnetic phase diagram for the three directions, confirming the presence of the A phase for $H \parallel [111]$ and the A' and B phases for $H \parallel [100]$. The skyrmion lattice A-phase enhances the conduction electron scattering, giving rise to an additional contribution to the resistivity. The emergent field induced by the spin texture of the A-phase causes the so-called topological Hall effect whose large amplitude relates to the very small size of the skyrmions at 18Å. With field cooling, a temperature hysteresis of the A-phase opens and the phase can be maintained at very low temperatures, emphasizing the low thermal fluctuations needed to stabilize the skyrmion lattice. The metastable A-phase is strongly irreversible with field.

Our measurements in the $H \parallel [100]$ direction show a strong resemblance between the A' and B phases with the previously described A-phase. It appears that the signature of the A, A' and B phases are very similar in the different transport probes we have used, underlying the fact that microscopically these phases seem to be very similar, all three yielding a topological Hall effect contribution. Nevertheless, the question whether or not the A' and B phases are skyrmion lattice phases is still open. Neutron scattering experiments will help answer it. Precise low-temperature resistivity measurements evidence the presence of anomalies linked to the magnetic textures down to 100 mK, which could point to a mixing of magnetic phases. Upon field-cooling, we show that both phases can be extended in metastable states. In that particular state, both phases are created simultaneously from the same mechanism, evidencing the relation between the two. More interestingly, a previously unreported additional structure can be seen in the metastable region.

Despite the low-temperature limitations of the thermoelectric power, the latter proves to be a powerful probe in EuPtSi. The magnetic phases have been clearly observed and are consistent with other probes. Additionally, the Seebeck coefficient evidences two energy scales in the paramagnetic and field-polarized paramagnetic states.

At higher fields, we have performed quantum oscillations measurements with the thermoelectric power and measured the various Fermi surface pockets. For each one, the effective cyclotron mass was extracted from the temperature dependence of the oscillations amplitude using the Pantsulaya-Varlamov theory, with results in agreement with the

dHvA measurements in the literature. We have also analyzed the field dependence of the oscillations and, in doing so, developed a new framework for the calculation of the Dingle temperature using the thermoelectric power. The scattering lifetime and mean-free path of the carriers was calculated, and we evidenced a non-linear Zeeman effect for the higher frequency pockets.

EuPtSi is an exciting metallic system that has yet to be completely understood. Further measurements of its magnetic properties at low-temperature could lead to new insights into ground-state skyrmion physics.

Appendix A

Additional data measured on EuPtSi

To avoid redundancy and to not overcrowd this manuscript, not all the data measured on EuPtSi have been presented thus far. This appendix shows more exhaustive measurements of the resistivity from the angular dependence and for the $H \parallel [110]$ and the $H \parallel [111]$ directions, as well as low-temperature measurements of the field-dependence of the Seebeck coefficient.

A.1 Additional resistivity measurements

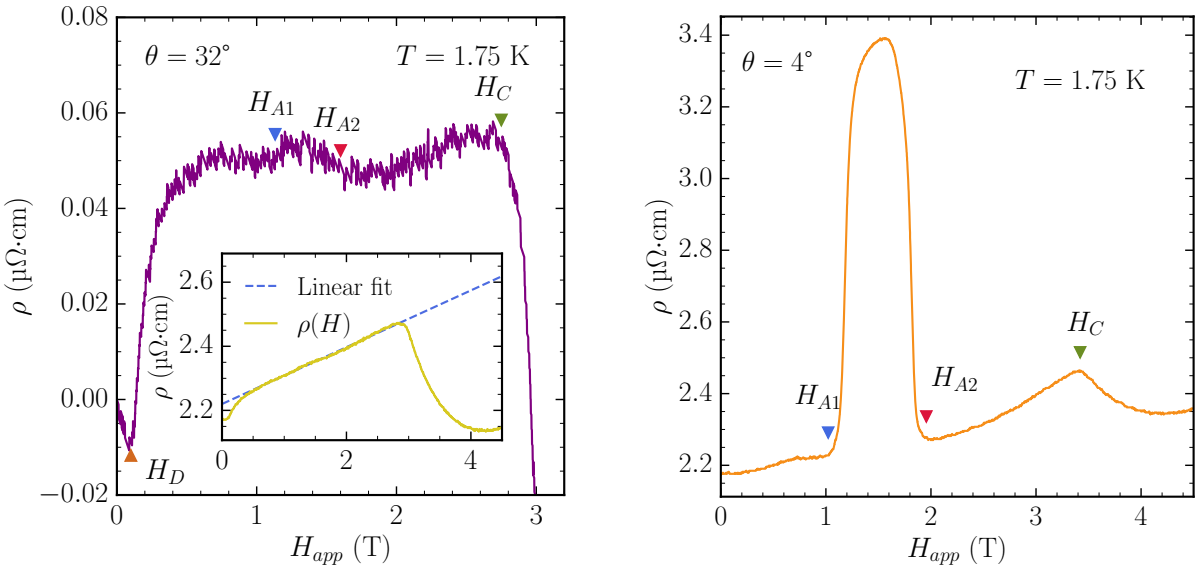

Figure A.1: Resistivity measurements at $T = 1.75$ K as a function of the applied (uncorrected) field, for two angles $\theta = 32°$ (left) and $\theta = 4°$ (right). θ is the angle of the magnetic field direction with respect to the $H \parallel [111]$ direction (see figure 3.13). Colored triangles indicate the various anomalies. On the left panel, a linear fit in the conical region between 0.5 and 2.7 T has been removed for clarity, with the full signal and the linear fit shown in the inset.

Figure A.1 shows a close-up of two curves from the angular dependence of the resistivity (see figure 3.13), at $T = 1.75$ K between 0 and 5 T of applied (uncorrected) field

with θ denoting the angle of the field direction with the $H \parallel [111]$ direction, in a rotation from $H \parallel [111]$ ($\theta = 0°$) to $H \parallel [\bar{1}\bar{1}1]$ ($\theta = 109.4°$). The left panel, with $\theta = 32°$ shows the $\rho(H)$ data with a linear fit removed in the conical order between 0.5 and 2.7 T, for clarity. The inset shows the full signal and the linear fit. This direction corresponds to the smallest height of the anomaly between H_{A1} and H_{A2}. By comparison, the right panel shows the $\theta = 4°$ curve, with the A-phase at the maximum height for this temperature. Figure A.2 shows $\rho(H)$ data for $H \parallel [110]$ between 0 and 12 T for temperatures between

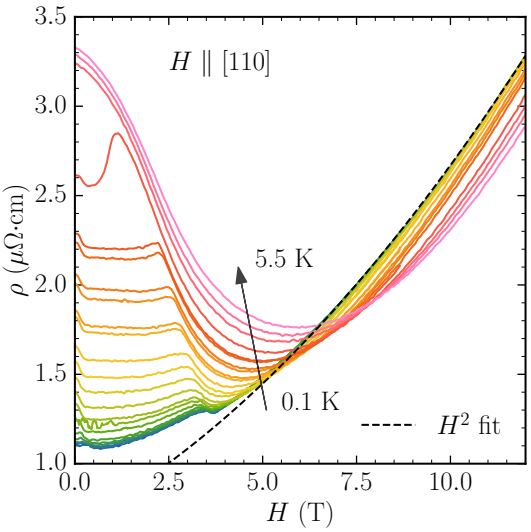

Figure A.2: $\rho(H)$ for $H \parallel [110]$ for temperatures between 0.1 and 5.5 K (indicated by the black arrow), up to 12 T. The black dotted line indicates the H^2 fit on the 0.1 K data.

0.1 and 5.5 K. The dotted line corresponds to a $\rho \propto H^2$ fit calculated on the 0.2 K data between 7 and 15 T.
Figure A.3 (left) shows $\rho(H)$ data for $H \parallel [111]$ between 0 and 15 T for temperatures between 0.2 and 6 K, with the inset showing a low-field close-up for five temperatures across the whole range. The data in the left panel are smoothed with a Savitzky-Golay filter to reduce excess noise. The right panel shows similar measurements between 0 and 8 T performed on the same sample. The difference between the two data-sets comes from the drastic improvement on the dilution refrigerator measurement setup described in chapter 2. The base temperature has been improved from 0.2 to 0.1 T, and the noise level was reduced by a factor 10. Besides these differences, the two sets are in good agreement. As such, $\rho(H)$ measurements from the second set were only made up to 8 T for most temperatures.
Figure A.4 (left) shows the temperature dependence of the resistivity between 0.1 and 5.5 K for fields $H \parallel [111]$ between 0 and 15 T. Fields corresponding to the A-phase ($0.8<H<1.3$ T) are not shown here. In the helical state $H < H_D = 0.25$ T, $\rho(T)$ follows a power law $\rho(T) \propto T^n$ with $n = 1.55$. In the conical state, $n = 1.75$ at 1.4 T and increases to close to $n = 2$ with higher H. However, as the field is increased, the temperature range at which the conical state is observed diminishes and the power-law fittings become unprecise above 2 T. The right panel shows the same data plotted as a function of T^2, emphasizing the $n \neq 2$ non-Fermi liquid behavior in the conical state. A T^2 dependence is

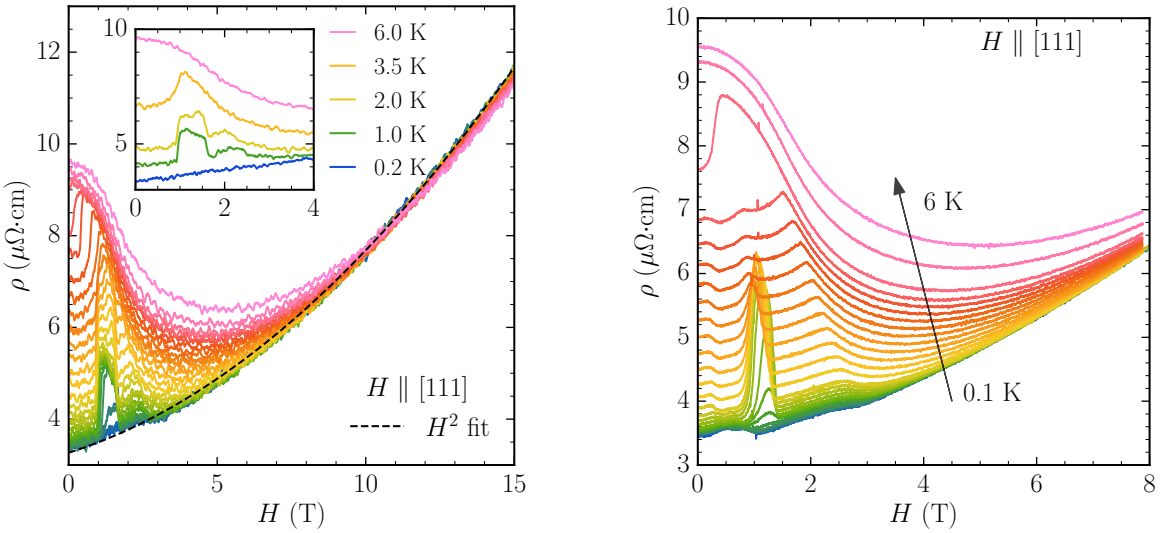

Figure A.3: $\rho(H)$ for $H \parallel [111]$ from two different measurements before (left) and after (right) improving the low-temperature setup. The data is shown between 0.2 and 6 K, up to 15 T on the left and between 0.1 and 6 K up to 8 T on the right. The inset on the left panel is a close-up between 0 and 4 T for five temperatures, emphasizing the presence of the A-phase. Note that the data on the left have been smoothed to reduce the noise level while the data on the right have not been modified.

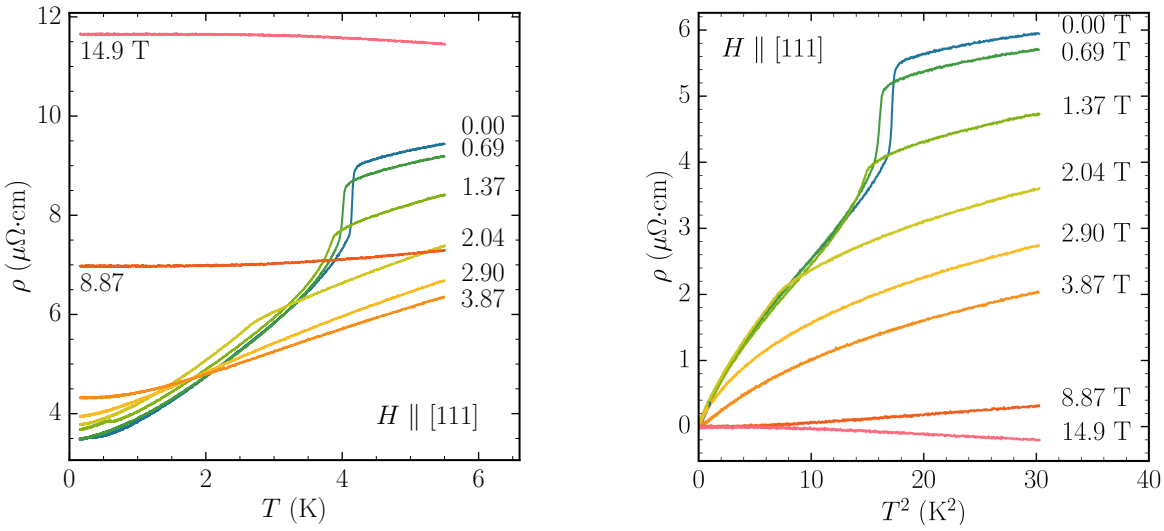

Figure A.4: ρ for $H \parallel [111]$ as a function of T (left) and T^2 (right) for various applied fields and between 0.1 and 6 K. The curvature of the low-temperature resistivity in the T^2 plot emphasizes the non-Fermi liquid behavior in the conical state. For higher fields such as 14.9 T, the resistivity is mostly temperature-independent at low temperature.

recovered around 9 T, which corresponds to the recovery of the H^2 behavior in the $\rho(H)$ data as well.

A.2 Low-temperature Seebeck measurements

A large part of the interesting behavior of EuPtSi is found at low temperature. In order to measure the thermoelectric power, a thermal gradient is needed, which can impede the performance of the measurement setup at low temperatures. This section illustrates the difficulty of measuring the Seebeck coefficient in continuous field sweeps, and the reason H-steps were preferred in some of the results from chapter 3. From the $S(H)$

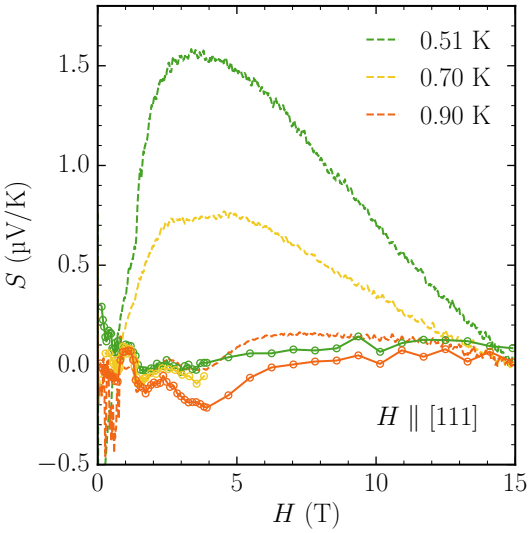

Figure A.5: $S(H)$ for $H \parallel [111]$ at T =0.5, 0.7 and 0.9 T from field sweeps (dotted) and H-steps (linked circles).

measurements at low temperatures ($T < 1$ K) we have observed the presence of a large background signal that increases as temperature lowers, as shown in figure A.5 for the $H \parallel [111]$ direction. The continuous field sweeps are represented in dotted lines. This background signal affects the voltage measurements and is present even without applied thermal gradient, for the three field directions studied. Reaching more than ten times the signal amplitude, this makes the observation of Seebeck features at low temperature much harder in continuous measurements.
While the presence of the A-phase can be traced as low as 0.5 K even with the background signal, the noise level drastically increases for this range. Inducing a significant temperature gradient ($\Delta T/T \approx 3\%$) heats the sample as a whole despite the heat sink provided by the mixing chamber of the dilution refrigerator setup. Reducing the gradient allows lower temperatures but also significantly lowers the signal level. The signal-to-noise ratio reaches close to 1 below $T = 0.6\ K$.
To attenuate the effect of the background signal and the increase in noise level, we preferred field-steps measurements (linked circles in the figure). For each discrete field values, the Seebeck coefficient is calculated with an appropriate thermal gradient. By increas-

ing the averaging time, the noise level can be reduced. Since the Seebeck is calculated separately for each field value, the background signal is removed. In turn the discrete field values loses precision to determine the exact transition fields, as well as quantum oscillations. H-steps measurements have been shown to fit the continuous field sweeps very well for $T > 1$ K, validating the use of this method.

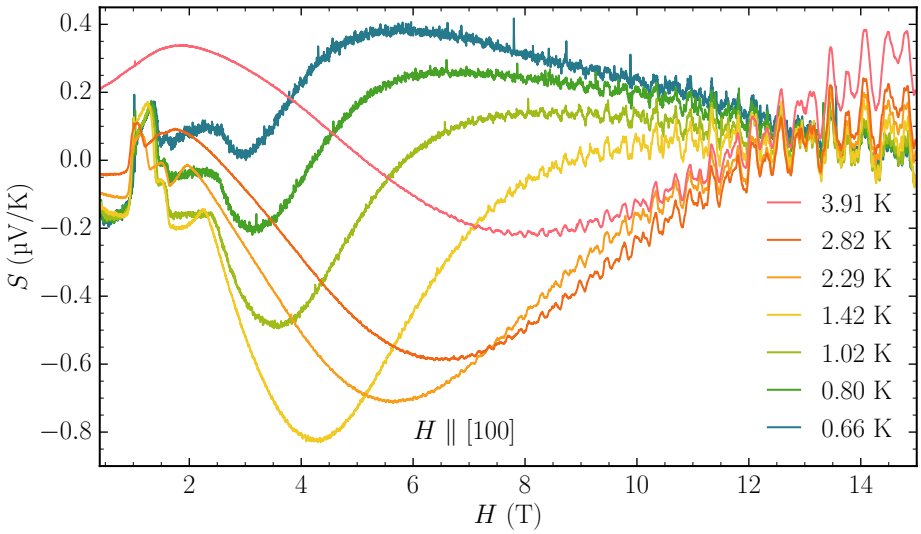

Figure A.6: $S(H)$ for $H \parallel [100]$ between 0.3 and 15 T, for temperatures between 0.66 and 3.91 K, made in continuous field sweeps.

Figure A.6 shows $S(H)$ data for the $H \parallel [100]$ direction in continuous field sweeps between 0.3 and 15 T, for temperatures between 0.66 and 3.91 K. For $T < 1.42$ K, one can see the influence of the background signal previously described with the rise of a large positive contribution, compared to the H-steps measurements shown in figure 3.36 from section 3.2.4. We can note the increasing noise level as well. Nevertheless, the A'- and B-phases are clearly visible at low-field. At high-field, the quantum oscillations are visible for all temperatures.

Appendix B

Quantum oscillations in $MoTe_2$

$MoTe_2$ is one of the compounds other than EuPtSi that I have studied during this PhD thesis. In this section, the measurements of quantum oscillations in the thermoelectric power, resistivity and magnetization will be presented. The theory and principles of quantum oscillations, especially in the thermoelectric power, have already been developed in section 1.2, and chapter 4 shows the results for EuPtSi. As such, this section will only cover the results for $MoTe_2$.

Why $MoTe_2$?

Conventionally, band theory classifies materials as insulators, semiconductors or metals based on the presence (or not) and the size of an energy gap between the conduction band and the valence band [10]. Semimetals are characterized by a weak overlap in energy between the valence band and the conduction band at particular points of the Brillouin zone, the most prominent example being graphene (2D) [111]. The 3D equivalent of graphene is the topological semimetal, grouping Dirac semimetals (Cd3As2, Na3Bi...) and Weyl semimetals (TaAs, NbAs ...) [112]. The particular points of the Brillouin zone, for which the conduction and valence bands are touching, are called Weyl nodes (or Dirac points). Near these points, the energy dispersion as a function of the electronic wave vector k is linear in the three directions of space forming Dirac cones. The rich physics of these materials comes from the presence of these Weyl nodes around which the electron wave function will acquire a topological phase or Berry phase (Weyl fermions). Topological aspects are eagerly looked for because they produce new phenomena such as topological surface states. They are also expected be used for future applications in spintronic and quantum transport [113, 114].

$MoTe_2$ has been predicted to be a type-II Weyl semimetal [115, 116], with Weyl points touching at the boundary between electron and hole pockets in the Fermi surface. Angle-resolved photoemission spectroscopy (ARPES) measurements have observed Weyl points and Fermi arcs in $MoTe_2$, in agreement with the prediction of density functional theory (DFT) [117, 118, 119]. From the DFT calculations, large hole pockets are predicted but had not been observed in quantum oscillations measurements. The works of Hu et *al.* [120] show the appearance of new frequencies in the Shubnikov-de Haas (SdH) Fast Fourier Transform (FFT) spectrum. The spectrum is shown in figure B.1 taken from [120]. The first peaks are α and β with frequencies $F_\alpha = 226$ T and $F_\beta = 263$ T, corresponding to

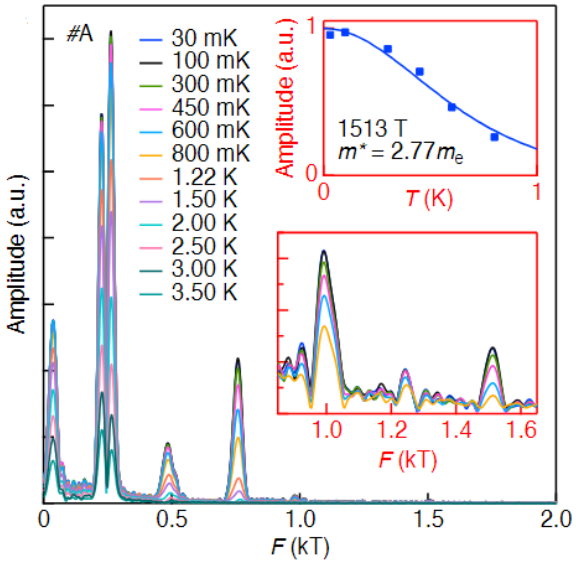

Figure B.1: Shubnikov-de Haas FFT spectra for temperatures between 30 mK and 3.5 K, calculated between 8 and 13 T. The lower inset shows a close-up of the spectra between 0.85 and 1.65 kT for temperatures between 30 and 800 mK, with a FFT calculated between 9 and 13 T. The upper inset shows the amplitude of the 1513 T peak as a function of temperature. From [120].

the electron pockets. These peaks are well documented in the literature [121, 114, 122]. Other frequencies observed are $F_\gamma = 484$ T, $F_\delta = 758$ T, and $F_{2\beta} = 518$ T, the latter being the second harmonic of the β peak with $F_{2\beta} \approx 2 \times F_\beta$.
The works of Hu et *al.* also report the observation of two higher frequencies, 988 T and 1513 T, shown in the inset of the figure. These frequencies will be referred to as F_1 and F_2 in this work. From the frequencies alone, it can be noted that F_1 is close to $2 \times F_\gamma$ or $F_\gamma + F_{2\beta}$. F_2 is close to $2 \times F_\delta$. However, the effective masses calculated are $m_1 = 1.50\ m_0$, and $m_2 = 2.77\ m_0$, which seem to exclude the possibility of the frequencies being harmonics, with $m_\gamma = 1.37\ m_0$ and $m_\delta = 1.99\ m_0$, significantly more than half the masses of the higher frequencies [123]. As such, these newly observed frequencies are candidates for being the hole pockets theoretically expected.

dHvA and SdH experiments

Using the Faraday balance setup described in section 2.3, we have performed a de Haas-van Alphen-type experiment. The field dependence of the magnetization signal M is shown on the left panel of figure B.2 for three temperatures, 1.37 K, 2.6 K and 4.07 K between 0 and 16 T. Quantum oscillations are clearly visible above 6 T. We have also performed the SdH experiment down to 0.11 K, and $\rho(H)$ for five temperatures between 0.2 and 2 K is shown in the right panel of figure B.2. The resulting FFT spectra for both probes are shown in figure B.3, with the peaks labeled as per [120]. The window used for the FFT calculation is [6-16] T for the magnetization and [10-16] T for the resistivity, which were determined to be the best windows, respectively, using the same protocol as described in chapter 4 for EuPtSi.

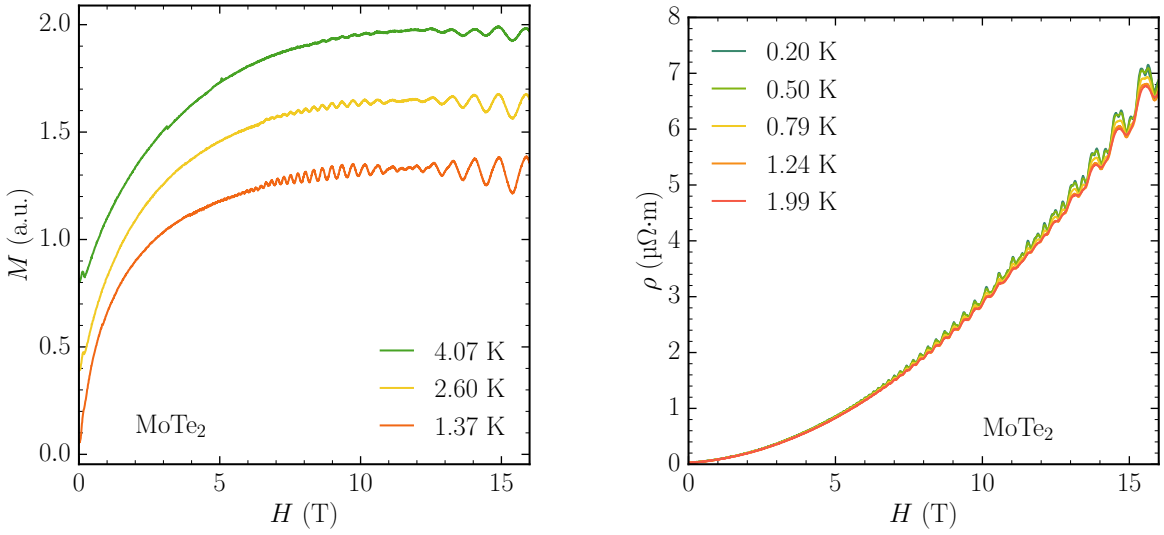

Figure B.2: Left: field dependence of the magnetization signal (in arbitrary units) between 0 and 16 T for three temperatures between 1.37 and 4.07 K. Right: field dependence of the resistivity between 0 and 16 T for temperatures between 0.2 and 2 K.

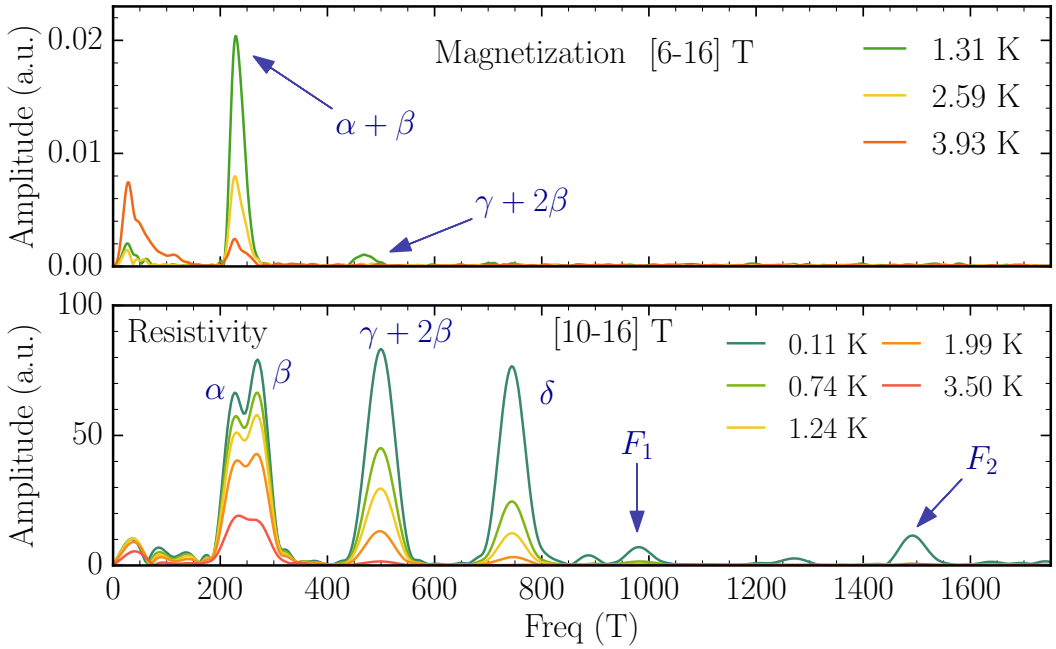

Figure B.3: FFT spectra from dHvA (top) and SdH (bottom) with peaks labeled as in [120]. The field windows used for the FFT calculations are [6-16] T and [10-16] T respectively. A + sign indicates two branches unresolved into a single peak.

From the dHvA spectrum, we can see the first peak corresponding to both α and β around 250 T, with both frequencies too close to be distinguished. This is true for all the FFT field windows studied. Another peak at around 500 T can be observed at 1.37 K, corresponding to γ. By comparison with the SdH FFT spectrum, one can see the higher frequency peaks appear at lower temperature. In the SdH spectrum, α and β are resolved. γ is clearly observed, as well as δ. We also observe the newly reported frequencies at 970 T and 1490 T respectively. The two frequencies however, only appear for $T < 0.5$ K, and thus only visible for the 0.11 K data in the figure.

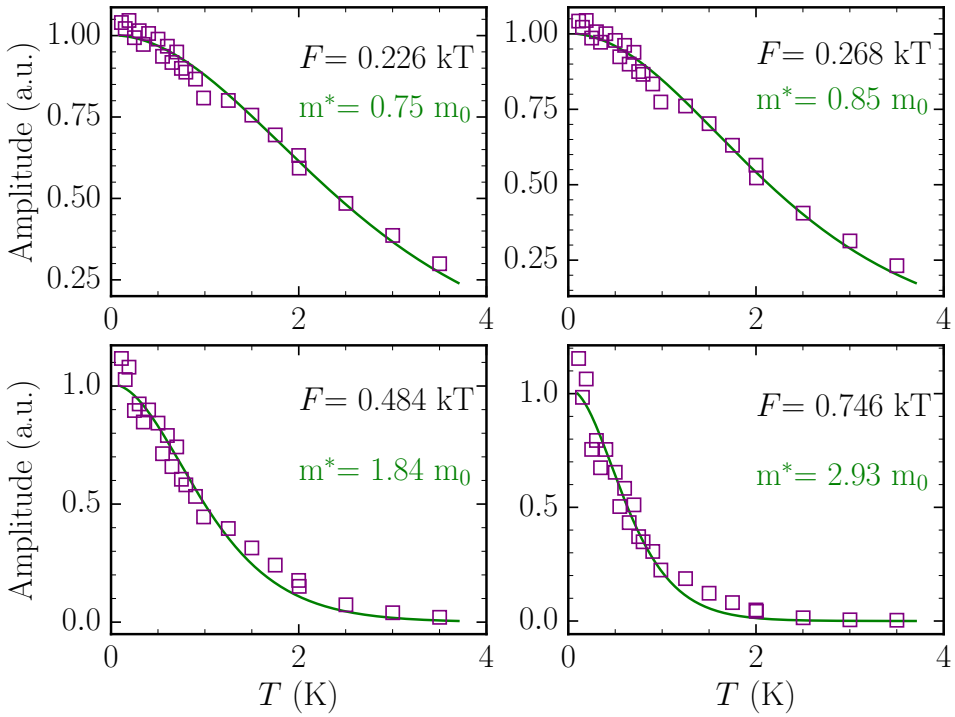

Figure B.4: Amplitude of the SdH peaks as a function of temperature (squares) fitted with the Lifshitz-Kosevich formula (green), for branches $F_\alpha = 0.226$ kT, $F_\beta = 0.268$ kT, $F_{\gamma+2\beta} = 0.484$ kT and $F_\delta = 0.746$ kT. The amplitudes are normalized with respect to the maximum amplitude of the fit. The fitted values of the effective masses are indicated.

Despite being observed in the FFT spectrum, the $F_1 = 970$ T and $F_2 = 1490$ T peaks have not yielded successful effective mass calculations due to the small amplitude and the low temperatures. The amplitude of the other peaks, on the other hand, have been fitted with the Lifshitz-Kosevich formula to recover the effective masses. The resulting temperature dependencies are shown in figure B.4. Each plot corresponds to a frequency, the LK formula fit is the green curve and the squares are the peak amplitudes. The amplitudes have been renormalized by the maximum amplitude of the fit in the low-temperature limit.
The recovered effective masses are in good agreement with the works of Hu et *al.* for the α and β peaks. Our calculations yield masses 0.75 m_0 and 0.85 m_0 respectively, compared to 0.69 m_0 and 0.82 m_0, from [123]. The γ peak at $F = 484$ T however yields $m^* = 1.84\ m_0$ which is much larger than 1.37 m_0 in the literature. Even by considering the influence of the 2β harmonic mixed with γ, the mass for the 2β peak was estimated at 1.65 m_0, which

is also smaller than our measurements suggest. The same observation is made for the δ peak with $F_\delta = 746$ T in our measurement. The corresponding mass is 2.93 m_0 compared to 1.99 m_0 in the literature.
Because our measurements of the dHvA and the SdH quantum oscillations were limited by the low temperatures for the higher frequency peaks, we now turn to oscillations in the thermoelectric power. For a given frequency, the maximum amplitude is not at 0 K and instead for a temperature $T_{\max} = \frac{0.11 H_{\text{eff}}}{pm^*}$. H_{eff} is the effective field and p is the harmonic of the frequency.

Thermoelectric power quantum oscillations measurements

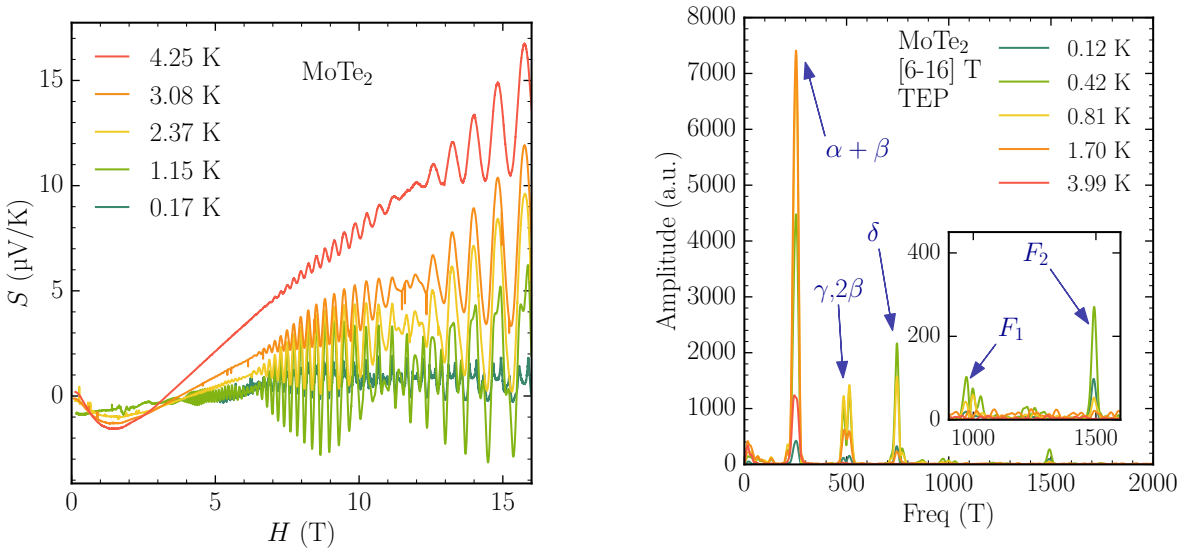

Figure B.5: Left: field dependence of the thermoelectric power up to 16 T for temperatures between 0.17 and 4.25 K. Right: resulting FFT spectrum calculated between 6 and 16 T with labeled peaks. The inset shows a close-up between 800 and 1600 T with the newly observed frequencies $F_1 = 970$ T and $F_2 = 1490$ T.

The Seebeck coefficient field-dependence for $MoTe_2$ is shown in the left panel of figure B.5 between 0 and 16 T for temperatures between 0.17 and 4.25 K. For the whole temperature range, quantum oscillations are clearly observed with a very large amplitude reaching almost 10 μV/K, or ten times the background signal, at 16 T and 1.15 K. The corresponding FFT spectrum calculated for a [6-16] T field window is shown on the right panel, with peaks labeled as per [120]. The inset is a close-up between 800 and 1600 T to show the higher frequencies. We can note, however that the α and β peaks are unresolved and instead a single peak is observed at $F = 252$ T. Using the Pantsulaya-Varlamov formula (see section 1.2.3), we have analyzed the temperature dependence of the amplitude of the quantum oscillations in the thermoelectric power. The results for each peak are represented in figure B.6. The PV fits (blue curves) are renormalized with respect to the maximum amplitude at $T_{\max}$. The data points are in red.
For the α and β mixed peak at $F = 252$ T, the corresponding effective mass is 0.80 m_0, which lies between the 0.75 m_0 and 0.85 m_0 values for α and β in SdH. The γ peak at

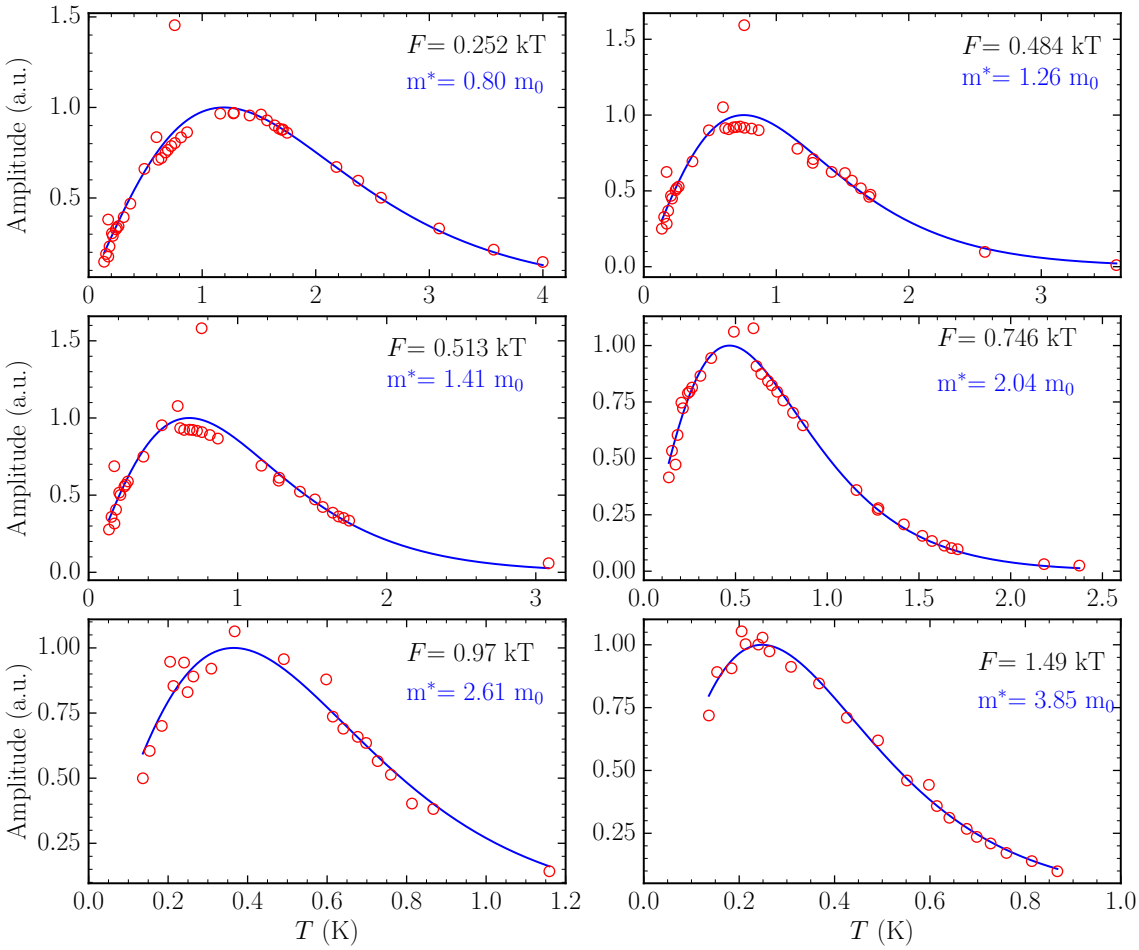

Figure B.6: Amplitude of the FFT peaks from quantum oscillations in the thermoelectric power as a function of temperature (circles) fitted with the Pantsulaya-Varlamov formula (blue), for all the observed branches. The amplitudes are normalized with respect to the maximum amplitude of the fit. The fitted values of the effective masses are indicated.

$F = 484$ T yields an effective mass of 1.26 m_0, significantly less than the SdH result of 1.84 m_0, and in better agreement with 1.37 m_0 from [123]. The peak at $F = 513$ T corresponding to $2 \times \beta$ yields $m^* = 1.41$ m_0 with $p = 1$, i.e. for a first harmonic calculation. Taking $p = 2$ recovers $m^* = 0.75$ m_0 for the β peak.
At $F = 746$ T for the δ peak, we have $m^* = 2.04$ m_0, corresponding very well with the 1.99 m_0 from the literature. Comparing the thermoelectric power results with those from our SdH experiment, we can note that the thermoelectric power yields results very close to the literature whereas our SdH experiment overestimates the masses considerably as the frequency is increased. For the available peaks in every probe, the results are reported in table B.1.

TEP, this work			SdH, this work			SdH from [120]		
Branch	F (T)	m_c^* (m_0)	Branch	F (T)	m_c^* (m_0)	Branch	F (T)	m_c^* (m_0)
$\alpha + \beta$	252	0.80	α	226	0.75	α	226	0.69
			β	268	0.85	β	263	0.82
γ	484	1.26	$\gamma + 2\beta$	484	1.84	γ	484	1.37
2β	513	1.41				2β	518	1.65
δ	746	2.04	δ	746	2.93	δ	758	1.99
F_1	970	2.61				F_1	988	1.50
F_2	1490	3.85				F_2	1513	2.77

Table B.1: Effective carrier masses m_c^* and the corresponding frequencies F for $MoTe_2$, from thermoelectric power and Shubnikov-de Haas results from this work, and SdH results from [120, 123]. A + sign indicates two branches unresolved into a single peak.

For the peaks with frequencies $F < 900$ T, the results so far seem to confirm what is found in the literature. The newly observed peaks at higher frequencies, however, differ in the results. For the $F_1 = 970$ T peak, the PV fit yields a mass $m^* = 2.61$ m_0. For the $F_2 = 1490$ T peak, the effective mass is 3.85 m_0. These values are significantly higher than 1.50 m_0 and 2.77 m_0 from the literature. Taken as second harmonics, i.e. dividing the masses and the frequencies by 2, the results are very close to the γ and δ peaks. From our results, the possibility of the newly observed frequencies being harmonics instead of the hole pockets predicted by DFT calculations can not be excluded.

Appendix C

Résumés en français

C.1 Résumé de la thèse

Dans cette thèse, j'ai étudié les propriétés de transport électrique et thermique du composé non centro-symétrique EuPtSi, à basse température et fort champ magnétique.
La première partie des résultats porte sur l'étude à bas champ ($H < 5$ T) des phases magnétiques observées dans EuPtSi en dessous de la température de Néel $T_N = 4.1$ K, pour les trois directions principales: $H \parallel [110]$, $H \parallel [111]$ et $H \parallel [100]$. Grâce à la dépendance angulaire de la résistivité sous champ, j'ai confirmé la présence de phases exotiques: la phase A skyrmionique pour $H \parallel [111]$, et les phases A' et B supposées skyrmioniques pour $H \parallel [100]$. En étudiant ces phases à l'aide de différentes sondes de transport, j'ai établi le diagramme de phase magnétique avec précision. J'ai aussi mis en évidence la présence à basse températures de nouvelles anomalies liées aux phases skyrmioniques. Les résultats de mesures dépendantes en température pour les directions $H \parallel [111]$ et $H \parallel [100]$ mettent en évidence le caractère métastable des phases A, A' et B en refroidissant sous champ. En préparant le système dans l'état métastable A' ou B, les variations en champ de la résistivité montrent que les deux phases sont créées simultanément par le même processus. Grâce aux résultats en température, j'ai également montré la présence d'un comportement différent d'un liquide de Fermi dans l'état conique de EuPtSi.
La deuxième partie de mes résultats se concentre sur la surface de Fermi de EuPtSi, étudiée grâce aux oscillations quantiques dans le pouvoir thermoélectrique, pour des champs intenses ($H > 6$ T). La dépendance en température de l'amplitude des oscillations permet d'obtenir des valeurs de masses effectives de porteurs de charge en accord avec la littérature pour chaque orbite de la surface de Fermi. En étudiant la dépendance en champ des oscillations quantiques, j'ai obtenu la température de Dingle et le libre-parcours moyen des porteurs en utilisant une nouvelle méthode d'analyse propre au pouvoir thermoélectrique.

C.2 Introduction en français

En 2009, la découverte d'un réseau de skyrmions magnétiques (SkL) dans la phase A de MnSi a prouvé l'existence d'un objet prédit il y a plus de 40 ans. Un skyrmion magnétique est une pseudo-particule qui est protégée topologiquement et qui permet un large panel d'applications technologiques potentielles. Grâce à leur petite taille, des mémoires

magnétiques à haute densité d'information peuvent être imaginées, et des skyrmions individuels peuvent être déplacés avec un faible courant d'excitation, c'est à dire une faible consommation énergétique. Les skyrmions sont donc intensément étudiés pour leurs potentielles applications et leurs propriétés fondamentales, pour beaucoup étant encore des questions ouvertes.

Bien qu'il existe maintenant des skyrmions dans des systèmes possédant une symétrie d'inversion, il a premièrement été pensé qu'un ingrédient majeur de la formation de skyrmions vient du manque de symétrie d'inversion de la structure cristalline. Depuis la découverte de la SkL dans MnSi, d'autres composés du groupe d'espace $P2_13$ ont été étudiés comme candidats pour des phases skyrmioniques. L'un d'eux est EuPtSi. EuPtSi a un ordre magnétique hélical en dessous de la faible température de Néel $T_N = 4.1$ K, et présente un diagramme de phase sous champ avec différents ordres magnétiques. La phase A pour un champ appliqué $H \parallel [111]$ a été confirmé comme étant une SkL en 2018, une première pour un composé $4f$ [3]. De plus, le vecteur d'ordre hélical est très court, avec une période de 18 Å, et donc est très fortement ancré au réseau cristallin. Sous champ magnétique, cela produit une forte anisotropie du diagramme de phase. La phase A a été observée autour de la direction $H \parallel [111]$ alors que la direction $H \parallel [110]$ ne présente aucune phase exotique. La direction $H \parallel [100]$, par contre, présente deux phase différentes appelées A' et B, qui pourraient être des SkL. Une faible excitation thermique est nécessaire pour induire la phase A. Cela nous permet de l'observer pour des températures aussi basses que 450 mK, ce qui nous donne l'opportunité rare d'étudier les réseaux de skyrmions proches de leur état fondamental [4]. Les phases A' et B, cependant, existent pour un très faible gamme angulaire et jusqu'à 250 mK [5]. Leur étude est compliquée d'un point de vue expérimental et leur mécanisme de formation ainsi que leur structure n'ont pas encore été confirmés. De plus, il a récemment été montré qu'il est possible de stabiliser les phases skyrmioniques dans un état métastable à des températures plus faibles en refroidissant le système sous champ [4].
Le diagramme de phase température-champ magnétique de EuPtSi est étudié par le biais de mesures de transport électrique et thermique à basses températures et fort champ pour les trois directions principales. Nous avons comparé les anomalies correspondant aux SkL en résistivité longitudinale et transverse avec nos mesures de pouvoir thermoélectrique. Le pouvoir thermoélectrique présente des résultats prometteurs, aussi bien dans les mesures liées aux ordres magnétiques et pour l'analyse de la surface de Fermi de EuPtSi grâce aux oscillations quantiques.

Cette thèse est divisée en quatre chapitres. Le premier correspond aux concepts de théorie nécessaires pour comprendre les travaux expérimentaux des chapitres suivants. Le pouvoir thermoélectrique et la théorie sous-jacente sont présentés, en se concentrant principalement sur sa sensibilité aux changements de la densité d'état électronique et aux propriétés de la surface de Fermi. Le principe des oscillations quantiques est ensuite présenté d'après la théorie Lifshitz-Kosevich pour l'aimantation et la résistivité, et d'après la théorie Pantsulaya-Varlamov pour le pouvoir thermoélectrique. Enfin, nous introduisons différents ordres magnétiques, le concept de skyrmions et le composé prototype MnSi. Le second chapitre décrit les méthodes expérimentales utilisées pour les mesures de transport des chapitres suivants. Dans le troisième chapitre, nous introduisons EuPtSi en détail et nous présentons les résultats de mesures de transport électrique et thermique

obtenus. Les mesures en fonction du champ magnétique sont premièrement décrites pour les trois directions principales, $H \parallel [110]$, $H \parallel [111]$ et $H \parallel [100]$, en s'intéressant particulièrement aux phases SkL A, A' et B. Une deuxième partie du chapitre décrit les mesures en fonction de la température et l'étude du comportement métastable des phases SkL jusqu'à 100 mK. Le quatrième et dernier chapitre présente les mesures d'oscillations quantiques dans EuPtSi, principalement dans le pouvoir thermoélectrique.
Durant ces trois années de thèse d'autres composés ont été étudiés, comme $MoTe_2$ dont les résultats principaux sont présentés brièvement dans l'annexe B.

C.3 Résumé de chaque chapitre

Chapitre 1 - Elements de théorie

Dans ce chapitre, des éléments théoriques sont rappelés pour aider à la compréhension des chapitres suivants. Premièrement, le concept de thermoélectricité est développé afin d'introduire le coefficient Seebeck, ou pouvoir thermoélectrique, ainsi que le coefficient Nernst, son pendant transverse. Les relations liant le Seebeck à la densité d'état électronique g, au temps caractéristique de diffusion τ et à la géométrie de la surface de Fermi sont explicitées. Dans une seconde partie, la notion d'oscillations quantiques est introduite, et la théorie sous-jacente est rappelée dans le cas de l'aimantation (effet de Haas-van Alphen), la résistivité (effet Shubnikov-de Haas), ainsi que le pouvoir thermoélectrique. Les deux premiers sont analysés dans le cadre de la théorie Lifshitz-Kosevich, permettant de calculer la masse effective des porteurs d'après la dépendance en température de l'amplitude des oscillations. Pour le coefficient Seebeck, cependant, ce cadre ne peut être utilisé, et la théorie de Pantsulaya-Varlamov (PV) est utilisée. L'utilisation de la théorie PV est également développée pour l'analyse de la dépendance en champ magnétique des oscillations, remontant ainsi à la détermination de la température de Dingle T_D et au libre-parcours moyen l. La troisième partie introduit les ordres magnétiques qui sont rencontrés dans le composé phare de cette thèse, EuPtSi. Les ordres hélicaux et conicaux sont décrits, ainsi que le concept de skyrmion magnétique. Un bref état de l'art de MnSi est établi en tant que composé prototype d'un système skyrmionique. Enfin, les applications potentielles des skyrmions dans l'industrie sont brièvement présentées.

Chapitre 2 - Méthodes expérimentales

Ce second chapitre porte sur les méthodes expérimentales utilisées dans cette thèse. Un premier point décrit le réfrigérateur à dilution sur lequel la majorité des mesures ont été effectuées ainsi que les améliorations faites pour descendre de 100 mK jusqu'à 50 mK sur les étages froids. Les méthodes de mesures de la résistivité longitudinale et transverse (effet Hall) sont présentées, suivi du principe de fonctionnement de la balance de Faraday pour l'aimantation. Le pouvoir thermoélectrique est ensuite abordé avec une description du montage expérimental et du protocole de mesure spécifique à cette sonde. Enfin, le protocole de traitement et d'analyse des oscillations quantiques est décrit.

Chapitre 3 - Etudes des phases skyrmioniques de EuPtSi

Le troisième chapitre présente le composé EuPtSi et les mesures bas champ ($H < 5$ T) de transport pour caractériser les ordres magnétiques. La dépendance angulaire de la résistivité sous champ est présentée, confirmant la présence de la phase A pour la direction $H \parallel [111]$, et des phases A' et B dans un petit angle autour de la direction $H \parallel [100]$. Ces directions, ainsi que $H \parallel [110]$, sont ensuite étudiées, premièrement en fonction du champ magnétique puis de la température. Les mesures de la résistivité selon $H \parallel [110]$ nous permettent d'établir le signal de l'ordre conique sans la présence de phases skyrmioniques. Nous observons également le comportement différent d'un liquide de Fermi dans la phase conique pour les trois directions principales. Le diagramme de phase $H - T$ est établi précisément pour chaque direction à partir de la résistivité, du pouvoir thermoélectrique et de la conductivité thermique. Pour la direction $H \parallel [111]$, nous avons observé la signature de l'effet Hall topologique dans la phase A, dont la forte amplitude est liée à la petite taille des skyrmions, induisant un fort champ effectif opposé au champ appliqué. Pour la direction $H \parallel [100]$, les phases A' et B sont observées jusqu'à basse température où une nouvelle anomalie est présente pour $T < 0.25$ K. Cette dernière est possiblement liée à une nouvelle phase magnétique ou bien une combinaison des autres phases. Les mesures de transport en fonction de la température présentent une forte hystérèse entre le chauffage et le refroidissement sous champ. Cela met en évidence le caractère métastable des phases A, A' et B que l'on peut alors observer jusqu'à 100 mK. Pour la direction $H \parallel [100]$, nous avons montré que des variations du champ magnétique permettent de passer d'une phase métastable à l'autre, indiquant ainsi que leur mécanisme de formation est similaire et simultané. Une anomalie additionnelle est aussi observée, liée aux résultats en fonction du champ.

Chapitre 4 - Oscillations quantiques dans le pouvoir thermoélectrique de EuPtSi

Ce dernier chapitre présentes les mesures d'oscillations quantiques sur le composé EuPtSi. Les oscillations quantiques sont un moyen direct d'observer la surface de Fermi d'un composé métallique et leur analyse permet de remonter à un certain nombre de propriétés des porteurs de charge. Dans la littérature, seules les mesures de l'effet de Haas-van Alphen (dHvA) par Kakihana et *al*. [5] ont été rapportées. Nos mesures d'oscillations quantiques dans le pouvoir thermoélectrique sous fort champ magnétique (H entre 5 et 15 T) sont présentées pour les trois orientations principales d'EuPtSi, les directions $H \parallel [110]$, [111] et [100]. L'amplitude des oscillations est analysée d'après la théorie de Pantsulaya-Varlamov (PV) en fonction de la température, et les masses effectives de porteurs correspondantes sont en accord avec les mesures de dHvA. Nous présentons également nos mesures d'oscillations quantiques en aimantation et en résistivité. En utilisant la théorie PV, nous avons également étudié la dépendance en champ de l'amplitude des oscillations du pouvoir thermoélectrique. Cette méthode d'analyse nouvelle nous permet de remonter à la température de Dingle et au libre-parcours moyen des porteurs. Une comparaison entre les mesures du coefficient Seebeck et de la résistivité confirme nos résultats et valide l'approche utilisée.

C.4 Conclusion en français

Depuis l'observation d'un réseau de skyrmions dans MnSi en 2009, de nombreux composés ont également montré la présence de skyrmions. Un de ces composés est EuPtSi, dont la phase A dans la direction $H \parallel [111]$ a été confirmée comme étant skyrmionique en 2018. Dans cette thèse, EuPtSi a été étudié selon ses trois directions principales: [110], [111] et [100], via des mesures de transport à basse température (jusqu'à 90 mK) et fort champ magnétique (jusqu'à 16 T). Nous avons établi le diagramme de phase magnétique pour les trois direction, confirmant la présence de la phase A pour $H \parallel [111]$, et les phases A' et B pour $H \parallel [100]$. La phase A correspond à une augmentation de la diffusion des électrons de conduction, donnant lieu à une contribution anormale de la résistivité. Le champ magnétique effectif induit par la texture de spin de la phase A donne lieu à l'effet Hall topologique dont l'amplitude importante reflète le petit diamètre des skyrmions de 18 Å. En refroidissant le système sous champ appliqué, une hystérèse en température s'ouvre dans la phase A et cette dernière peut être maintenue à très basses températures, prouvant les faibles fluctuations thermiques nécessaires pour stabiliser le réseau de skyrmions. La phase A métastable est très irréversible vis à vis des fluctuations de champ magnétique. Nos mesures pour la direction $H \parallel [100]$ montrent une forte ressemblance entre les phases A' et B et la phase A décrite précédemment. Des mesures précises à basse température, jusqu'à 100 mK, de la résistivité montrent la présence d'anomalies liées aux phases magnétiques, potentiellement attribuées à un état mixte d'ordres magnétiques. Par refroidissement sous champ, nous avons montré que les deux phases A' et B peuvent apparaître sous forme métastable. Dans cet état, les deux phases sont créées simultanément via le même mécanisme. Une structure additionnelle est observée dans l'état métastable.

Malgré les limites en température du pouvoir thermoélectrique, ce dernier s'est révélé être une sonde très puissante pour EuPtSi. Les phases magnétiques sont clairement observées et en accord avec les autres sondes. Les mesures du coefficient Seebeck mettent en évidence la présence de deux échelles d'énergies nouvelles dans l'état paramagnétique et l'état polarisé. Sous fort champ, nous avons mesuré les oscillations quantiques dans le pouvoir thermoélectrique et retrouvé les orbites de la surface de Fermi. Pour chaque orbite, la masse effective des porteurs a été déduite de la dépendance en température de l'amplitude des oscillations en utilisant la théorie Pantsulaya-Varlamov. Les résultats sont en bon accord avec les mesures d'aimantation de la littérature. Nous avons analysé la dépendance en champ des oscillations, et développé pour cela un nouveau cadre de calcul de la température de Dingle par les mesures de pouvoir thermoélectrique. Le temps caractéristique de diffusion et le libre-parcours moyen des porteurs a été calculé, et nous avons mis en évidence la présence d'un effet Zeeman non linéaire pour les orbites à haute fréquence.

EuPtSi est un système métallique complexe qui n'a pas encore révélé tous ses mystères. Les mesures de ses propriétés magnétiques à basses températures pourraient mener à une nouvelle compréhension de la physique des skyrmions proche de l'état fondamental.

Bibliography

[1] S. Mühlbauer, B. Binz, F. Jonietz, C. Pfleiderer, A. Rosch, A. Neubauer, R. Georgii, and P. Böni, "Skyrmion Lattice in a Chiral Magnet," *Science*, vol. 323, pp. 915–919, Feb. 2009.

[2] T. Skyrme, "A unified field theory of mesons and baryons," *Nuclear Physics*, vol. 31, pp. 556–569, Mar. 1962.

[3] M. Kakihana, D. Aoki, A. Nakamura, F. Honda, M. Nakashima, Y. Amako, S. Nakamura, T. Sakakibara, M. Hedo, T. Nakama, and Y. Ōnuki, "Giant Hall Resistivity and Magnetoresistance in Cubic Chiral Antiferromagnet EuPtSi," *Journal of the Physical Society of Japan*, vol. 87, p. 023701, Feb. 2018.

[4] T. Sakakibara, S. Nakamura, S. Kittaka, M. Kakihana, M. Hedo, T. Nakama, and Y. Ōnuki, "Magnetic Phase Transitions of the 4 f Skyrmion Compound EuPtSi Studied by Magnetization Measurements," *Journal of the Physical Society of Japan*, vol. 90, p. 064701, June 2021.

[5] M. Kakihana, D. Aoki, A. Nakamura, F. Honda, M. Nakashima, Y. Amako, T. Takeuchi, H. Harima, M. Hedo, T. Nakama, and Y. Ōnuki, "Unique Magnetic Phases in the Skyrmion Lattice and Fermi Surface Properties in Cubic Chiral Antiferromagnet EuPtSi," *Journal of the Physical Society of Japan*, vol. 88, p. 094705, Sept. 2019.

[6] K. Behnia, D. Jaccard, and J. Flouquet, "On the thermoelectricity of correlated electrons in the zero-temperature limit," *Journal of Physics: Condensed Matter*, vol. 16, pp. 5187–5198, July 2004. arXiv:cond-mat/0405030.

[7] H. B. Callen, "The Application of Onsager's Reciprocal Relations to Thermoelectric, Thermomagnetic, and Galvanomagnetic Effects," *Physical Review*, vol. 73, pp. 1349–1358, June 1948.

[8] L. Onsager, "Reciprocal Relations in Irreversible Processes. I.," *Physical Review*, vol. 37, pp. 405–426, Feb. 1931.

[9] L. Onsager, "Reciprocal Relations in Irreversible Processes. II.," *Physical Review*, vol. 38, pp. 2265–2279, Dec. 1931.

[10] N. W. Ashcroft and N. D. Mermin, *Solid state physics*. Fort Worth: Saunders College Publ. [u.a.], internat. ed., 21. print ed., 1995.

[11] S. N. F. Mott and H. Jones, *The Theory of the Properties of Metals and Alloys*. Dover Publications, Jan. 1958. Google-Books-ID: LIPsUaTqUXUC.

[12] J. M. Ziman, *Electrons and Phonons: The Theory of Transport Phenomena in Solids*. Clarendon Press, 1960. Google-Books-ID: 2SMIAQAAIAAJ.

[13] P. Sun, K. R. Kumar, M. Lyu, Z. Wang, J. Xiang, and W. Zhang, "Generic Seebeck effect from spin entropy," *The Innovation*, vol. 2, p. 100101, May 2021.

[14] L. Shubnikov and W. J. De Haas, "New phenomena in the change in resistance of bismuth crystals in a magnetic field at the temperature of liquid hydrogen (II)," *Proceedings of the Royal Netherlands Academy of Arts and Science*, vol. 33, pp. 418–432, 1930.

[15] L. Shubnikov and W. J. De Haas, "New phenomena in the change in resistance of bismuth crystals in a magnetic field at the temperature of liquid hydrogen (I)," *Proceedings of the Royal Netherlands Academy of Arts and Science*, vol. 33, pp. 363–378, 1930.

[16] W. J. De Haas and P. M. Van Alphen, "The dependence of the susceptibility of diamagnetic metals upon the field," *Proc.Acad.Sci.Amst.*, vol. 33, pp. 1106–1118, 1930.

[17] A. M. Kosevich and I. M. Lifshitz, "The de Haas-van Alphen effect in thin metal layers," *Soviet physics JETP6USSR*, vol. 2, no. 4, pp. 646–649, 1956.

[18] D. Shoenberg, *Magnetic oscillations in metals*. Cambridge monographs on physics, Cambridge [Cambridgeshire] ; New York: Cambridge University Press, 1984.

[19] A. A. Abrikosov, *Fundamentals of the Theory of Metals*. North-Holland, 1988. Google-Books-ID: mKHvAAAAMAAJ.

[20] Dingle, "Some magnetic properties of metals I. General introduction, and properties of large systems of electrons," *Proceedings of the Royal Society of London. Series A. Mathematical and Physical Sciences*, vol. 211, pp. 500–516, Mar. 1952.

[21] A. B. Pippard, "Magnetic Breakdown in a dislocated lattice," *Proceedings of the Royal Society of London. Series A. Mathematical and Physical Sciences*, vol. 287, pp. 165–182, Aug. 1965.

[22] A. B. Pippard, *Magnetoresistance in metals*. No. 2 in Cambridge studies in low temperature physics, Cambridge [England] ; New York: Cambridge University Press, 1989.

[23] C. Capan, L. Balicas, T. P. Murphy, E. C. Palm, R. Movshovich, D. Hall, S. W. Tozer, M. F. Hundley, E. D. Bauer, J. D. Thompson, J. L. Sarrao, J. F. DiTusa, R. G. Goodrich, and Z. Fisk, "Unusual metamagnetism in CeIrIn 5," *Physical Review B*, vol. 80, p. 094518, Sept. 2009.

[24] R. C. Young, "Quantum oscillations in the thermal transport properties of tin," *J. Phys. F: Met. Phys.*, vol. 3, no. 721, 1973.

[25] R. Fletcher, "An experimental study of the quantum oscillations in the high field thermopower of zinc," *Journal of Physics F: Metal Physics*, vol. 11, pp. 1093–1106, May 1981.

[26] R. Fletcher, "Further experiments on the quantum oscillations in the transport properties of aluminum," *Physical Review B*, vol. 28, pp. 6670–6676, Dec. 1983.

[27] H. J. Trodahl and F. J. Blatt, "Quantum Oscillations in the Peltier Effect of Zinc," *Physical Review*, vol. 180, pp. 706–715, Apr. 1969.

[28] O. V. Kirichenko, I. V. Kozlov, D. Krstovska, and V. G. Peschanskiĭ, "Quantum oscillations of the thermomagnetic coefficients of layered conductors in a strong magnetic field," *Low Temperature Physics*, vol. 34, pp. 538–542, July 2008.

[29] A. V. Pantsulaya and A. A. Varlamov, "Possibility of observation of giant oscillations of thermoelectric power in normal metal," *Physics Letters A*, vol. 136, pp. 317–320, Apr. 1989.

[30] R. Fletcher, "On the amplitude of the quantum oscillations in the thermopower of metals," *Journal of Low Temperature Physics*, vol. 43, pp. 363–370, May 1981.

[31] S. Blundell, *Magnetism in condensed matter*. No. 4 in Oxford master series in condensed matter physics, Oxford: Oxford Univ. Press, reprint ed., 2014.

[32] S. Zhang, *Chiral and Topological Nature of Magnetic Skyrmions*. Springer Theses, Cham: Springer International Publishing, 2018.

[33] R. Skomski, *Simple models of magnetism*. Oxford ; New York: Oxford University Press, 2008. OCLC: ocn138342362.

[34] I. Dzyaloshinsky, "A thermodynamic theory of "weak" ferromagnetism of antiferromagnetics," *Journal of Physics and Chemistry of Solids*, vol. 4, pp. 241–255, Jan. 1958.

[35] T. Moriya, "Anisotropic Superexchange Interaction and Weak Ferromagnetism," *Physical Review*, vol. 120, pp. 91–98, Oct. 1960.

[36] S. M. Stishov and A. E. Petrova, "Itinerant helimagnet MnSi," *Physics-Uspekhi*, vol. 54, pp. 1117–1130, Nov. 2011.

[37] Y. Yamasaki, D. Morikawa, T. Honda, H. Nakao, Y. Murakami, N. Kanazawa, M. Kawasaki, T. Arima, and Y. Tokura, "Dynamical process of skyrmion-helical magnetic transformation of the chiral-lattice magnet FeGe probed by small-angle resonant soft x-ray scattering," *Physical Review B*, vol. 92, p. 220421, Dec. 2015.

[38] S. Seki, J.-H. Kim, D. S. Inosov, R. Georgii, B. Keimer, S. Ishiwata, and Y. Tokura, "Formation and rotation of skyrmion crystal in the chiral-lattice insulator Cu 2 OSeO 3," *Physical Review B*, vol. 85, p. 220406, June 2012.

[39] Y. Ōnuki, M. Kakihana, W. Iha, K. Nakaima, D. Aoki, A. Nakamura, F. Honda, M. Nakashima, Y. Amako, J. Gouchi, Y. Uwatoko, S. Nakamura, T. Sakakibara, T. Takeuchi, Y. Haga, H. Ikeda, H. Harima, M. Hedo, and T. Nakama, "Unique Skyrmion Phases and Conduction Electrons in Cubic Chiral Antiferromagnet EuPtSi and Related Compounds," in *Proceedings of the International Conference on Strongly Correlated Electron Systems (SCES2019)*, (Okayama, Japan), Journal of the Physical Society of Japan, Mar. 2020.

[40] A. Bauer and C. Pfleiderer, "Magnetic phase diagram of MnSi inferred from magnetization and ac susceptibility," *Physical Review B*, vol. 85, p. 214418, June 2012.

[41] Y. Tokura and N. Kanazawa, "Magnetic Skyrmion Materials," *Chemical Reviews*, vol. 121, pp. 2857–2897, Mar. 2021.

[42] B. Kaviraj and J. Sinha, "Review—Magnetic Skyrmions in Chiral Ferromagnets: Electrical Transport Properties and Device Applications," *ECS Journal of Solid State Science and Technology*, vol. 11, p. 115003, Nov. 2022.

[43] T. Lancaster, "Skyrmions in magnetic materials," *Contemporary Physics*, vol. 60, pp. 246–261, July 2019. arXiv:2202.11019 [cond-mat].

[44] R. Juge, *Nucléation et dynamique de skyrmions magnétiques dans des films ultraminces*. PhD thesis, Université Grenoble Alpes, 2020.

[45] T. Hesjedal, "Magnetic skyrmions, https://www.youtube.com/watch?v=YPxbcRrzj6M by Oxford University Physics Society," 2021.

[46] Y. Ishikawa, K. Tajima, D. Bloch, and M. Roth, "Helical spin structure in manganese silicide MnSi," *Solid State Communications*, vol. 19, pp. 525–528, July 1976.

[47] C. Pfleiderer, D. Reznik, L. Pintschovius, H. v. Löhneysen, M. Garst, and A. Rosch, "Partial order in the non-Fermi-liquid phase of MnSi," *Nature*, vol. 427, pp. 227–231, Jan. 2004.

[48] B. Lebech, P. Harris, J. Skov Pedersen, K. Mortensen, C. I. Gregory, N. R. Bernhoeft, M. Jermy, and S. A. Brown, "Magnetic phase diagram of MnSi," *Journal of Magnetism and Magnetic Materials*, vol. 140-144, pp. 119–120, Feb. 1995.

[49] A. Neubauer, C. Pfleiderer, B. Binz, A. Rosch, R. Ritz, P. G. Niklowitz, and P. Böni, "Topological Hall Effect in the A Phase of MnSi," *Physical Review Letters*, vol. 102, p. 186602, May 2009.

[50] C. Pfleiderer, S. R. Julian, and G. G. Lonzarich, "Non-Fermi-liquid nature of the normal state of itinerant-electron ferromagnets," *Nature*, vol. 414, pp. 427–430, Nov. 2001.

[51] C. Pfleiderer, A. Neubauer, S. Mühlbauer, F. Jonietz, M. Janoschek, S. Legl, R. Ritz, W. Münzer, C. Franz, P. G. Niklowitz, T. Keller, R. Georgii, P. Böni, B. Binz, A. Rosch, U. K. Rößler, and A. N. Bogdanov, "Quantum order in the chiral magnet MnSi," *Journal of Physics: Condensed Matter*, vol. 21, p. 164215, Apr. 2009.

[52] R. Ritz, M. Halder, M. Wagner, C. Franz, A. Bauer, and C. Pfleiderer, "Formation of a topological non-Fermi liquid in MnSi," *Nature*, vol. 497, pp. 231–234, May 2013.

[53] H. Watanabe, S. A. Parameswaran, S. Raghu, and A. Vishwanath, "Anomalous Fermi liquid phase in metallic Skyrmion crystals," *Physical Review B*, vol. 90, p. 045145, July 2014. arXiv:1309.7047 [cond-mat, physics:hep-ph].

[54] N. Doiron-Leyraud, I. R. Walker, L. Taillefer, M. J. Steiner, S. R. Julian, and G. G. Lonzarich, "Fermi-liquid breakdown in the paramagnetic phase of a pure metal," *Nature*, vol. 425, pp. 595–599, Oct. 2003.

[55] A. Fert, N. Reyren, and V. Cros, "Advances in the Physics of Magnetic Skyrmions and Perspective for Technology," *Nature Reviews Materials*, vol. 2, p. 17031, June 2017. arXiv:1712.07236 [cond-mat].

[56] K. Everschor-Sitte, J. Masell, R. M. Reeve, and M. Kläui, "Perspective: Magnetic skyrmions—Overview of recent progress in an active research field," *Journal of Applied Physics*, vol. 124, p. 240901, Dec. 2018.

[57] H. Yang, A. Thiaville, S. Rohart, A. Fert, and M. Chshiev, "Anatomy of Dzyaloshinskii-Moriya Interaction at Co/Pt Interfaces," *Physical Review Letters*, vol. 115, p. 267210, Dec. 2015.

[58] A. Soumyanarayanan, M. Raju, A. L. G. Oyarce, A. K. C. Tan, M.-Y. Im, A. P. Petrovic, P. Ho, K. H. Khoo, M. Tran, C. K. Gan, F. Ernult, and C. Panagopoulos, "Tunable Room Temperature Magnetic Skyrmions in Ir/Fe/Co/Pt Multilayers," *Nature Materials*, vol. 16, pp. 898–904, Sept. 2017. arXiv:1606.06034 [cond-mat].

[59] F. Jonietz, S. Mühlbauer, C. Pfleiderer, A. Neubauer, W. Münzer, A. Bauer, T. Adams, R. Georgii, P. Böni, R. A. Duine, K. Everschor, M. Garst, and A. Rosch, "Spin transfer torques in MnSi at ultralow current densities," *Science (New York, N.Y.)*, vol. 330, pp. 1648–1651, Dec. 2010.

[60] X. Z. Yu, N. Kanazawa, W. Z. Zhang, T. Nagai, T. Hara, K. Kimoto, Y. Matsui, Y. Onose, and Y. Tokura, "Skyrmion flow near room temperature in an ultralow current density," *Nature Communications*, vol. 3, p. 988, Aug. 2012.

[61] G. Frossati, "OBTAINING ULTRALOW TEMPERATURES BY DILUTION OF ^{3} He INTO ^{4} He," *Le Journal de Physique Colloques*, vol. 39, pp. C6–1578–C6–1589, Aug. 1978.

[62] F. Pobell, *Matter and methods at low temperatures*. Berlin ; New York: Springer-Verlag, 2nd ed ed., 1996.

[63] M. C. Runyan and W. C. Jones, "Thermal Conductivity of Thermally-Isolating Polymeric and Composite Structural Support Materials Between 0.3 and 4 K," *Cryogenics*, vol. 48, pp. 448–454, Sept. 2008. arXiv:0806.1921 [astro-ph, physics:physics].

[64] T. Sakakibara, H. Mitamura, T. T. Takashi Tayama, and H. A. Hiroshi Amitsuka, "Faraday Force Magnetometer for High-Sensitivity Magnetization Measurements at

Very Low Temperatures and High Fields," *Japanese Journal of Applied Physics*, vol. 33, p. 5067, Sept. 1994.

[65] S. Borisenko, "99 years of ARPES," *Nature Reviews Physics*, vol. 3, pp. 539–539, Aug. 2021.

[66] J. Barros and R. Diego, "On the Use of the Hanning Window for Harmonic Analysis in the Standard Framework," *IEEE Transactions on Power Delivery*, vol. 21, pp. 538–539, Jan. 2006.

[67] G. Knebel, D. Aoki, and J. Flouquet, "Antiferromagnetism and superconductivity in cerium based heavy-fermion compounds," *Comptes Rendus Physique*, vol. 12, pp. 542–566, June 2011.

[68] I. Kawasaki, M. Kobata, S.-i. Fujimori, Y. Takeda, H. Yamagami, M. Hedo, T. Nakama, and Y. Ōnuki, "Electronic structure of the intermediate-valence compound ${\mathrm{EuNi}}_{2}{\mathrm{P}}_{2}$ studied by soft x-ray photoemission spectroscopy," *Physical Review B*, vol. 104, p. 165124, Oct. 2021.

[69] Y. Homma, M. Kakihana, Y. Tokunaga, M. Yogi, M. Nakashima, A. Nakamura, Y. Shimizu, D. Li, A. Maurya, Y. J. Sato, F. Honda, D. Aoki, Y. Amako, M. Hedo, T. Nakama, and Y. Ōnuki, "Magnetic Fluctuation and First-Order Transition in Trillium Lattice of EuPtSi Observed by ^{151} Eu Mössbauer Spectroscopy," *Journal of the Physical Society of Japan*, vol. 88, p. 094702, Sept. 2019.

[70] J. M. Hopkinson and H.-Y. Kee, "Geometric frustration inherent to the trillium lattice, a sublattice of the B20 structure," *Physical Review B*, vol. 74, p. 224441, Dec. 2006.

[71] S. V. Isakov, J. M. Hopkinson, and H.-Y. Kee, "Fate of partial order on trillium and distorted windmill lattices," *Physical Review B*, vol. 78, p. 014404, July 2008.

[72] T. E. Redpath and J. M. Hopkinson, "Spin ice on the trillium lattice studied by Monte Carlo calculations," *Physical Review B*, vol. 82, p. 014410, July 2010. arXiv:0912.3795 [cond-mat].

[73] D. T. Adroja, B. D. Padalia, S. K. Malik, R. Nagarajan, and R. Vijayaraghavan, "Magnetic susceptibility and 151Eu Mössbauer studies on cubic ternary compounds: EuPtSi and EuPdSi," *Journal of Magnetism and Magnetic Materials*, vol. 89, pp. 375–378, Oct. 1990.

[74] D. G. Franco, Y. Prots, C. Geibel, and S. Seiro, "Fluctuation-induced first-order transition in Eu-based trillium lattices," *Physical Review B*, vol. 96, p. 014401, July 2017.

[75] C. D. Cao, R. Klingeler, H. Vinzelberg, N. Leps, W. Löser, G. Behr, F. Muranyi, V. Kataev, and B. Büchner, "Magnetic anisotropy and ferromagnetic correlations above the Curie temperature in Eu 2 CuSi 3 single crystals," *Physical Review B*, vol. 82, p. 134446, Oct. 2010.

[76] W. Simeth, A. Bauer, C. Franz, A. Aqeel, P. J. Bereciartua, J. A. Sears, S. Francoual, C. H. Back, and C. Pfleiderer, "Resonant Elastic X-Ray Scattering of Antiferromagnetic Superstructures in EuPtSi 3," *Physical Review Letters*, vol. 130, p. 266701, June 2023.

[77] T. Matsumura, K. Kurauchi, M. Tsukagoshi, N. Higa, H. Nakao, M. Kakihana, M. Hedo, T. Nakama, and Y. Ōnuki, "Distorted triangular skyrmion lattice in a noncentrosymmetric tetragonal magnet," Tech. Rep. arXiv:2306.14767, arXiv, June 2023. arXiv:2306.14767 [cond-mat].

[78] M. Gen, R. Takagi, Y. Watanabe, S. Kitou, H. Sagayama, N. Matsuyama, Y. Kohama, A. Ikeda, Y. Ōnuki, T. Kurumaji, T.-h. Arima, and S. Seki, "Rhombic skyrmion lattice coupled with orthorhombic structural distortion in EuAl$_{4}$," *Physical Review B*, vol. 107, p. L020410, Jan. 2023. arXiv:2209.12751 [cond-mat].

[79] M. Kakihana, K. Nishimura, Y. Ashitomi, T. Yara, D. Aoki, A. Nakamura, F. Honda, M. Nakashima, Y. Amako, Y. Uwatoko, T. Sakakibara, S. Nakamura, T. Takeuchi, Y. Haga, E. Yamamoto, H. Harima, M. Hedo, T. Nakama, and Y. Ōnuki, "Unique Electronic States in Non-centrosymmetric Cubic Compounds," *Journal of Electronic Materials*, vol. 46, pp. 3572–3584, June 2017.

[80] A. K. Mishra and V. Ganesan, "A -phase, field-induced tricritical point, and universal magnetocaloric scaling in EuPtSi," *Physical Review B*, vol. 100, p. 125113, Sept. 2019.

[81] T. Sakakibara, S. Nakamura, S. Kittaka, M. Kakihana, M. Hedo, T. Nakama, and Y. Ōnuki, "Fluctuation-Induced First-Order Transition and Tricritical Point in EuPtSi," *Journal of the Physical Society of Japan*, vol. 88, p. 093701, Sept. 2019.

[82] N. Higa, T. U. Ito, M. Yogi, T. Hattori, H. Sakai, S. Kambe, Z. Guguchia, W. Higemoto, M. Nakashima, Y. Homma, A. Nakamura, F. Honda, Y. Shimizu, D. Aoki, M. Kakihana, M. Hedo, T. Nakama, Y. Ōnuki, and Y. Tokunaga, "Critical slowing-down and field-dependent paramagnetic fluctuations in the skyrmion host EuPtSi: μ SR and NMR studies," *Physical Review B*, vol. 104, p. 045145, July 2021.

[83] K. Kaneko, M. D. Frontzek, M. Matsuda, A. Nakao, K. Munakata, T. Ohhara, M. Kakihana, Y. Haga, M. Hedo, T. Nakama, and Y. Ōnuki, "Unique Helical Magnetic Order and Field-Induced Phase in Trillium Lattice Antiferromagnet EuPtSi," *Journal of the Physical Society of Japan*, vol. 88, p. 013702, Jan. 2019.

[84] C. Tabata, T. Matsumura, H. Nakao, S. Michimura, M. Kakihana, T. Inami, K. Kaneko, M. Hedo, T. Nakama, and Y. Ōnuki, "Magnetic Field Induced Triple- q Magnetic Order in Trillium Lattice Antiferromagnet EuPtSi Studied by Resonant X-ray Scattering," *Journal of the Physical Society of Japan*, vol. 88, p. 093704, Sept. 2019.

[85] T. Takeuchi, M. Kakihana, M. Hedo, T. Nakama, and Y. Ōnuki, "Angle Dependence of the Magnetic Phase Diagram in Cubic Chiral Antiferromagnet EuPtSi," *Journal of the Physical Society of Japan*, vol. 89, p. 093703, Sept. 2020.

[86] R. Prozorov and V. G. Kogan, "Effective Demagnetizing Factors of Diamagnetic Samples of Various Shapes," *Physical Review Applied*, vol. 10, p. 014030, July 2018.

[87] T. Yokouchi, N. Kanazawa, A. Tsukazaki, Y. Kozuka, A. Kikkawa, Y. Taguchi, M. Kawasaki, M. Ichikawa, F. Kagawa, and Y. Tokura, "Formation of In-plane Skyrmions in Epitaxial MnSi Thin Films as Revealed by Planar Hall Effect," *Journal of the Physical Society of Japan*, vol. 84, p. 104708, Oct. 2015.

[88] R. G. Chambers, *Electrons in metals and semiconductors*. No. 1 in Physics and its applications, London New York Tokyo [etc.]: Chapman and Hall, 1990.

[89] A. Neubauer, C. Pfleiderer, R. Ritz, P. Niklowitz, and P. Böni, "Hall effect and magnetoresistance in MnSi," *Physica B: Condensed Matter*, vol. 404, pp. 3163–3166, Oct. 2009.

[90] D. Hirobe, M. Sato, Y. Shiomi, H. Tanaka, and E. Saitoh, "Magnetic thermal conductivity far above the Néel temperature in the Kitaev-magnet candidate RuCl 3," *Physical Review B*, vol. 95, p. 241112, June 2017.

[91] N. Prasai, A. Akopyan, B. A. Trump, G. G. Marcus, S. X. Huang, T. M. McQueen, and J. L. Cohn, "Spin phases of the helimagnetic insulator Cu 2 OSeO 3 probed by magnon heat conduction," *Physical Review B*, vol. 99, p. 020403, Jan. 2019.

[92] I. I. Lobanova, V. V. Glushkov, N. E. Sluchanko, and S. V. Demishev, "Macroscopic evidence for Abrikosov-type magnetic vortexes in MnSi A-phase," *Scientific Reports*, vol. 6, p. 22101, Feb. 2016.

[93] K. Behnia and H. Aubin, "Nernst effect in metals and superconductors: a review of concepts and experiments," *Reports on Progress in Physics*, vol. 79, p. 046502, Apr. 2016.

[94] M. Lee, Y. Onose, Y. Tokura, and N. P. Ong, "Hidden constant in the anomalous Hall effect of high-purity magnet MnSi," *Physical Review B*, vol. 75, p. 172403, May 2007.

[95] A. Fert and A. Hamzić, "Hall Effect from Skew Scattering by Magnetic Impurities," in *The Hall Effect and Its Applications* (C. L. Chien and C. R. Westgate, eds.), pp. 77–98, Boston, MA: Springer US, 1980.

[96] J. Smit, "The spontaneous hall effect in ferromagnetics II," *Physica*, vol. 24, pp. 39–51, Jan. 1958.

[97] H. Ishizuka and N. Nagaosa, "Spin chirality induced skew scattering and anomalous Hall effect in chiral magnets," *Science Advances*, vol. 4, p. eaap9962, Feb. 2018.

[98] L. Berger, "Side-Jump Mechanism for the Hall Effect of Ferromagnets," *Physical Review B*, vol. 2, pp. 4559–4566, Dec. 1970.

[99] B. Binz and A. Vishwanath, "Theory of helical spin crystals: Phases, textures, and properties," *Physical Review B*, vol. 74, p. 214408, Dec. 2006.

[100] B. Binz and A. Vishwanath, "Chirality induced anomalous-Hall effect in helical spin crystals," *Physica B: Condensed Matter*, vol. 403, pp. 1336–1340, Apr. 2008. arXiv:0706.1841 [cond-mat].

[101] J. Ye, Y. B. Kim, A. J. Millis, B. I. Shraiman, P. Majumdar, and Z. Tešanović, "Berry Phase Theory of the Anomalous Hall Effect: Application to Colossal Magnetoresistance Manganites," *Physical Review Letters*, vol. 83, pp. 3737–3740, Nov. 1999.

[102] P. Bruno, V. K. Dugaev, and M. Taillefumier, "Topological Hall Effect and Berry Phase in Magnetic Nanostructures," *Physical Review Letters*, vol. 93, p. 096806, Aug. 2004.

[103] R. Ritz, M. Halder, C. Franz, A. Bauer, M. Wagner, R. Bamler, A. Rosch, and C. Pfleiderer, "Giant generic topological Hall resistivity of MnSi under pressure," *Physical Review B*, vol. 87, p. 134424, Apr. 2013.

[104] K. Karube, J. S. White, N. Reynolds, J. L. Gavilano, H. Oike, A. Kikkawa, F. Kagawa, Y. Tokunaga, H. M. Rønnow, Y. Tokura, and Y. Taguchi, "Robust metastable skyrmions and their triangular–square lattice structural transition in a high-temperature chiral magnet," *Nature Materials*, vol. 15, pp. 1237–1242, Dec. 2016.

[105] T. Nakajima, H. Oike, A. Kikkawa, E. P. Gilbert, N. Booth, K. Kakurai, Y. Taguchi, Y. Tokura, F. Kagawa, and T.-h. Arima, "Skyrmion lattice structural transition in MnSi," *Science Advances*, vol. 3, p. e1602562, June 2017.

[106] H. Oike, A. Kikkawa, N. Kanazawa, Y. Taguchi, M. Kawasaki, Y. Tokura, and F. Kagawa, "Interplay between topological and thermodynamic stability in a metastable magnetic skyrmion lattice," *Nature Physics*, vol. 12, pp. 62–66, Jan. 2016.

[107] T. Kawai, H. Muranaka, T. Endo, N. Duc Dung, Y. Doi, S. Ikeda, T. D. Matsuda, Y. Haga, H. Harima, R. Settai, and Y. Ōnuki, "Split Fermi Surface Properties of $LaTGe_3$ (T: Transition Metal) and $PrCoGe_3$ with the Non-centrosymmetric Crystal Structure," *Journal of the Physical Society of Japan*, vol. 77, p. 064717, June 2008.

[108] Y. Ōnuki, A. Nakamura, T. Uejo, A. Teruya, M. Hedo, T. Nakama, F. Honda, and H. Harima, "Chiral-Structure-Driven Split Fermi Surface Properties in $TaSi_2$, $NbSi_2$, and VSi_2," *Journal of the Physical Society of Japan*, vol. 83, p. 061018, June 2014.

[109] A. Nakamura, Y. Hiranaka, T. Uejo, T. Takeuchi, F. Honda, H. Harima, K. Matsubayashi, Y. Uwatoko, M. Hedo, T. Nakama, and Y. Ōnuki, "Magnetic and Fermi Surface Properties of Antiferromagnet $EuCd_{11}$," *Journal of the Physical Society of Japan*, vol. 83, p. 074714, July 2014.

[110] A. Nakamura, Y. Hiranaka, M. Hedo, T. Nakama, Y. Miura, H. Tsutsumi, A. Mori, K. Ishida, K. Mitamura, Y. Hirose, K. Sugiyama, F. Honda, R. Settai, T. Takeuchi,

M. Hagiwara, T. D. Matsuda, E. Yamamoto, Y. Haga, K. Matsubayashi, Y. Uwatoko, H. Harima, and Y. Ōnuki, "Magnetic and Fermi Surface Properties of EuGa $_4$," *Journal of the Physical Society of Japan*, vol. 82, p. 104703, Oct. 2013.

[111] G. Lu, K. Yu, Z. Wen, and J. Chen, "Semiconducting graphene: converting graphene from semimetal to semiconductor," *Nanoscale*, vol. 5, pp. 1353–1368, Feb. 2013.

[112] N. Armitage, E. Mele, and A. Vishwanath, "Weyl and Dirac semimetals in three-dimensional solids," *Reviews of Modern Physics*, vol. 90, p. 015001, Jan. 2018.

[113] M. Trescher, E. J. Bergholtz, and J. Knolle, "Quantum oscillations and magnetoresistance in type-II Weyl semimetals: Effect of a field-induced charge density wave," *Physical Review B*, vol. 98, p. 125304, Sept. 2018.

[114] Y. Qi, P. G. Naumov, M. N. Ali, C. R. Rajamathi, W. Schnelle, O. Barkalov, M. Hanfland, S.-C. Wu, C. Shekhar, Y. Sun, V. Süß, M. Schmidt, U. Schwarz, E. Pippel, P. Werner, R. Hillebrand, T. Förster, E. Kampert, S. Parkin, R. J. Cava, C. Felser, B. Yan, and S. A. Medvedev, "Superconductivity in Weyl semimetal candidate MoTe2," *Nature Communications*, vol. 7, p. 11038, Apr. 2016.

[115] Y. Sun, S.-C. Wu, M. N. Ali, C. Felser, and B. Yan, "Prediction of the Weyl semimetal in the orthorhombic MoTe2," *Physical Review B*, vol. 92, p. 161107, Oct. 2015. arXiv:1508.03501 [cond-mat].

[116] J. Jiang, Z. K. Liu, Y. Sun, H. F. Yang, C. R. Rajamathi, Y. P. Qi, L. X. Yang, C. Chen, H. Peng, C.-C. Hwang, S. Z. Sun, S.-K. Mo, I. Vobornik, J. Fujii, S. S. P. Parkin, C. Felser, B. H. Yan, and Y. L. Chen, "Signature of type-II Weyl semimetal phase in MoTe2," *Nature Communications*, vol. 8, p. 13973, Jan. 2017.

[117] S. Thirupathaiah, R. Jha, B. Pal, J. S. Matias, P. K. Das, P. K. Sivakumar, I. Vobornik, N. C. Plumb, M. Shi, R. A. Ribeiro, and D. D. Sarma, "MoTe2 : An uncompensated semimetal with extremely large magnetoresistance," *Physical Review B*, vol. 95, p. 241105, June 2017. arXiv:1705.07217 [cond-mat].

[118] K. Deng, G. Wan, P. Deng, K. Zhang, S. Ding, E. Wang, M. Yan, H. Huang, H. Zhang, Z. Xu, J. Denlinger, A. Fedorov, H. Yang, W. Duan, H. Yao, Y. Wu, S. Fan, H. Zhang, X. Chen, and S. Zhou, "Experimental observation of topological Fermi arcs in type-II Weyl semimetal MoTe2," *Nature Physics*, vol. 12, pp. 1105–1110, Dec. 2016.

[119] A. Crepaldi, G. Autès, A. Sterzi, G. Manzoni, M. Zacchigna, F. Cilento, I. Vobornik, J. Fujii, P. Bugnon, A. Magrez, H. Berger, F. Parmigiani, O. V. Yazyev, and M. Grioni, "Persistence of a surface state arc in the topologically trivial phase of MoTe 2," *Physical Review B*, vol. 95, p. 041408, Jan. 2017.

[120] Y. Hu, W. Yu, K. T. Lai, D. Sun, F. Balakirev, W. Zhang, J. Xie, K. Yip, E. P. Aulestia, R. Jha, R. Higashinaka, T. D. Matsuda, Y. Yanase, Y. Aoki, and S. K. Goh, "Detection of Hole Pockets in the Candidate Type-II Weyl Semimetal MoTe 2 from Shubnikov–de Haas Quantum Oscillations," *Physical Review Letters*, vol. 124, p. 076402, Feb. 2020.

[121] Q. Zhou, D. Rhodes, Q. R. Zhang, S. Tang, R. Schönemann, and L. Balicas, "Hall effect within the colossal magnetoresistive semimetallic state of MoTe 2," *Physical Review B*, vol. 94, p. 121101, Sept. 2016.

[122] I.-L. Liu, C. Heikes, T. Yildirim, C. Eckberg, T. Metz, S. Ran, W. Ratcliff II, J. Paglione, and N. P. Butch, "Quantum oscillations from networked topological interfaces in a Weyl semimetal," May 2019. arXiv:1905.02277 [cond-mat].

[123] Y. J. Hu, W. C. Yu, K. T. Lai, D. Sun, F. F. Balakirev, W. Zhang, J. Y. Xie, K. Y. Yip, E. I. P. Aulestia, R. Jha, R. Higashinaka, T. D. Matsuda, Y. Yanase, Y. Aoki, and S. K. Goh, "Supplemental Material for "Detection of hole pockets in the candidate type-II Weyl semimetal MoTe2 from Shubnikov-de Haas quantum oscillations"," *Physical Review Letters*, p. 7, 2020.